Development and Construction of a Large TPC Prototype for the ILC
and
Study of τ Polarisation in $\tilde{\tau}$ Decays with the ILD Detector

Dissertation zur Erlangung des Doktorgrades
des Departments Physik der Universität Hamburg

vorgelegt von Peter Schade
aus Attendorn

Hamburg
2009

Gutachter der Dissertation:	Prof. Dr. R.-D. Heuer Dr. P. Bechtle
Gutachter der Disputation:	Dr. P. Bechtle JProf. Dr. J. Haller
Datum der Disputation:	28. August 2009
Vorsitzender des Prüfungsausschusses:	Dr. G. Steinbrück
Vorsitzender des Promotionsausschusses:	Prof. Dr. R. Klanner
Leiter des Departments Physik:	Prof. Dr. J. Bartels
Dekan der MIN-Fakultät:	Prof. Dr. H. Graener

Abstract

Today high-energy physicists agree that the next accelerator to be built should be an electron positron (e^+e^-) linear collider with a centre of mass energy in the one-TeV regime [1, 2]. Such a lepton collider would be complementary to the Large Hadron Collider (LHC), which has currently the highest discovery potential for new physics at highest energies. For a start, the mechanisms behind discoveries made at the LHC can be studied precisely in the clean environment of an e^+e^- machine. Moreover, many fundamental measurements are feasible only with the well defined initial state of an electron positron collision.

The International Linear Collider [3] (ILC) is currently the most advanced concept of such a machine. Many research groups are working on the development of the accelerator and the detectors, with the aim to be prepared for the construction at the beginning of the next decade.

This thesis presents two studies which have been made in the framework of the detector development for the International Large Detector (ILD). ILD is one of three proposed detector concepts for the ILC [4, 5, 6]. In the preparation phase for the ILD, prototype studies are performed to develop and optimise the sub-detector technologies which will come into operation. Complementary to these hardware studies, expected physics scenarios are being investigated in full detector simulations. These simulations demonstrate the physics potential of the detector concept and are a benchmark for the detector and the accelerator design.

The first part of this thesis gives an introduction to the physics questions addressed to the ILC. Also, the machine and the ILD detector concept are presented.

The second part is dedicated to the development and the construction to a large Time Projection Chamber (TPC) prototype (LP). A TPC is foreseen as one of ILD's sub-detectors and shall measure the trajectories of charged particles with an accuracy unprecedented by TPCs operated before. The new prototype offers an infrastructure for the development of modern TPC readout structures which can fulfil the required criteria. Before construction, the design plans of the LP have been optimised for a low material budget of the structure and a very homogeneous drift field. Both are crucial parameters for the TPC to be operated in the ILD detector. During the manufacturing of the LP, experience with construction techniques has been gained for the construction of the ILD TPC.

The third part deals with a simulation study for a polarisation measurement of τ leptons in the process $e^+e^- \rightarrow \tilde{\tau}_1\tilde{\tau}_1 \rightarrow \chi_1^0\chi_1^0\tau\tau$. Here, the $\tilde{\tau}_1$ is the supersymmetric partner of the τ lepton. Supersymmetry (SUSY) is a scenario of new physics which could solve major shortcomings of the Standard Model of particle physics. It could be investigated in detail with the ILD. The polarisation measurement is sensitive to key parameters of the SUSY theory. This simulation study shows the feasibility of the measurement in the chosen SUSY scenario and estimates the accuracy to be expected.

Both studies address in particular the track reconstruction capabilities of the ILD detector. Conclusions of the discussed studies and an outlook are presented in part IV.

Kurzfassung

Diese Arbeit stellt zwei Studien vor, die im Rahmen der Detektorentwicklung für den International Large Detector (ILD) durchgeführt wurden. ILD ist eines von drei vorgeschlagenen Detektorenkonzepten für den ILC [4, 5, 6]. In der Vorbereitungsphase für den ILD werden einerseits Prototypstudien durchgeführt, um die Detektortechnologien zu entwickeln und zu optimieren, die zum Einsatz kommen sollen. Andererseits werden physikalische Prozesse im Detektor simuliert, um die Sensitivität des Detektors zu demonstrieren. Darüberhinaus sind die Simulationen geeignete Tests für das Design des Detektors und des Beschleunigers.

Der erste Teil dieser Arbeit gibt eine Einführung in die physikalischen Fragen, die der ILC beantworten soll. Weiterhin wird die Maschine in ihren Grundzügen erklärt und das ILD Detektorkonzept vorgestellt.

Der zweite Teil ist der Entwicklung und dem Bau eines großen Prototypen einer Zeit Projektions Kammer (TPC) gewidmet. Eine TPC soll im ILD zum Einsatz kommen und mit einer, im Vergleich zu vorangegangenen TPCs, unerreichten Genauigkeit Teilchenspuren vermessen. Der neue Prototyp stellt eine Infrastruktur zur Verfügung, mit der moderne Auslesestrukturen entwickelt werden, welche die geforderten Kriterien erfüllen können. Vor dem Bau der Kammer wurden die Konstruktionspläne des Prototypen optimiert um eine möglichst geringe Materialdichte der Wände und ein sehr homogenes elektrisches Feld in der Kammer zu erreichen. Beides sind auch kritische Parameter der TPC, die im ILD Detektor betrieben werden soll. Weiterhin wurden mit dem Bau der Kammer Erfahrungen mit Konstruktionstechniken für den Bau der finalen TPC gesammelt.

Ein dritter Teil befasst sich mit einer Simulationsstudie zur Messung des Polarisationsgrad von τ Leptonen, die in Prozess $e^+e^- \to \tilde{\tau}_1\tilde{\tau}_1 \to \chi_1^0\chi_1^0\tau\tau$ erzeugt werden. Hierbei ist $\tilde{\tau}_1$ der supersymmetrische Partner des τ Leptons. Supersymmetrie (SUSY) ist ein Szenario neuer Physik, das viele Mängel des Standardmodells der Teilchenphysik beheben kann. Supersymmetrie könnte am ILC untersucht werden. Die vorliegende Messung ist sensitiv auf Schlüsselparameter dieser Theorie. Mit der Simulation wird die Machbarkeit der Messung im gewählten SUSY Szenario demonstriert und die mögliche Präzision abgeschätzt.

Beide Studien beziehen sich insbesondere auf die Spurrekonstruktionsfähigkeiten des ILD Detektors. Ergebnisse der präsentierten Studien und Ausblicke werden in Teil IV präsentiert.

Contents

"Nothing is impossible. Not if you can imagine it.
That's what being a scientist is all about." - Professor Hubert Farnsworth

Preface

Since the earliest times, humans have tried to understand the universe on the largest as well as on the smallest scales.

In the very beginning of human research, people speculated about the striking questions of the universe and the atoms rather independently. Since then, the image of the universe evolved from holes in the celestial sphere to a complete picture describing stars and galaxies - the latest striking questions are related to dark matter and energy. In parallel, the understanding of the smallest structures developed from first atomic models of the ancient Greeks, to a quantum mechanic description of atoms and their interaction and finally to even smaller substructures, the quarks and leptons.

In the last few hundred years, both fields of research have made impressive advancements compared to the long times before. The accelerated growth of knowledge has been triggered by innovative new techniques. On the largest scales, this has been the introduction of the telescope by Galileo. Today modern telescopes orbit the earth, but the very basic principle still prevails. The exploration of the microcosm had to wait longer for the appropriate tool, which is the particle accelerator. People like Robert J. Van de Graaff, Rolf Wideröe and Lawrence Livermore launched first accelerators and started an evolution, which is about to peak - currently - with the Large Hadron Collider at CERN.

In recent years, these two somewhat disconnected fields of research developed an increasing interplay. Today, the striking questions of the universe about dark matter and energy are addressed to modern particle accelerators. Physicists are about to develop comprehensive theories to describe the evolution of the universe from its beginnings until today - with the help of particle accelerators. Telescopes and space observations will complement and falsify the predictions of these models.

To reveal the basic principles of nature, the most precise and most energetic particle accelerators are needed, completed by precision detectors operated at these machines.

This work aims to contribute a little piece to these developments....

Part I
Physics at Terascale Energies

In the 1940s, physicists started to operate particle accelerators and collided protons with fixed targets. These early machines discovered a multitude of yet unknown particles, which were believed to be elementary and became infamous as the 'particle zoo'. First attempts to give the discoveries an ordering scheme were made by Murray Gell-Mann [7] and George Zweig [8] in 1964. They proposed the existence of quarks, even more fundamental constituents of matter. Today these early proposals have found their place in the Standard Model of particle physics (SM). Completed by a description of fundamental forces, the SM became a coherent collection of theories to describe the world on the smallest scales. The model has been developed from the 1960s on and it was recurrently tested with experiments at increasingly powerful particle accelerators. Almost every new generation of accelerators made new discoveries, unexpected or predicted ones, which could be included into the SM. To these days, even the latest and most energetic particle colliders confirmed the SM in collisions of elementary particles with up to a few 100 GeV. However, the SM is not completed yet.

One of its constituents is still undiscovered, the Higgs boson. This particle is expected to have a mass of 115 GeV to 1 TeV and it is still being searched for. Today, the Higgs boson is already an inherent part of the model - if it is not found in the expected mass window, the probability interpretation of the SM calculations breaks down at high energies of 1 TeV. Moreover, the SM as such cannot explain all observations of the universe. The mystery of dark matter is out of its scope. Several scenarios of possible SM extensions are currently under discussion, in first place so-called Supersymmetry (SUSY), to solve these shortcomings and to put SM calculations on a more sound base. Irrespective whether SUSY is reality or not, high-energy physicists are convinced that some completely new physics phenomena have to show up in the energy range up to 1 TeV. This scale defines the energy frontier for next-generation particle colliders.

The following chapter 1 discusses the SM and its deficiencies. Two complementary colliders are foreseen to look beyond the SM: the Large Hadron Collider (LHC) and the International Linear Collider (ILC). The LHC will start nominal operation in autumn 2009 whereas the ILC is in the planning phase. Chapter 2 presents the ILC, explains the physics motivation to build it and the interplay between ILC and LHC. In addition, the International Large Detector (ILD) concept, a proposed ILC detector, is discussed. Development studies for the ILD are in the main focus of this work. They are outlined at the end of this introductory part I and presented in part II and III.

1 The Standard Model

Today the Standard Model (SM) [9, 10, 11] defines a solid base for high energy physics research. It describes the matter particles discovered so far and three fundamental forces. The dynamics of these particles is described in terms of quantised fields while the forces are derived form the a gauge invariance principle. This mathematical framework allows for the calculation of the cross section of particle interactions, which is the most important observable in high-energy physics.

In this introductory chapter the basic principles of the SM are outlined. In addition, the major theoretical and experimental shortcomings of the model are discussed. To solve these problems of the SM, deeper studies at new particle accelerators are mandatory.

1.1 Overview of the Matter Particles and Forces

According to the SM, the basic constituents of matter are six leptons and six quarks (see table 1.1). The elementary particles have a hierarchy in three generations and the particle masses increase with the generation number. Only the neutrinos and first-generation particles are stable. Higher-generation particles can be produced in particle interactions but they decay gradually to first-generation particles. Thus the known stable matter is entirely made up of the electron, the up and the down quark. Unlike the leptons, quarks have not been observed as free particles. They are confined in groups of three quarks, the baryons, or in bound states of a quark and an anti-quark, the mesons. Each of these elementary particles has an antimatter counterpart of equal mass but opposite charge.

While the matter particles carry half integer spin (fermions), forces are mediated by particles of integer spin (bosons). The SM bosons are summarised in table 1.2 with the associated forces, namely the electromagnetic, the weak and the strong force. In the table, also the Higgs-boson is listed, which does not mediate a force. This particle is introduced to explain the appearance of mass [13, 14], as explained in the next section. The mediators of the weak force have the peculiarity that they are massive and the W-bosons are electromagnetically charged, whereas the photon and the gluon are massless and electrically neutral.

Figure 1.1 illustrates in an overview the possible interactions of the particles. A line connects particles which are able to interact with one another and q denotes the quarks, l the charged leptons and ν the neutrinos, respectively. The gluons (g), the Higgs and W bosons (H, W) couple to themselves, which means several W-bosons can interact in a three or four-leg vertex in a Feynman diagram (see below).

	1st	2nd	3rd	em. charge	spin
lepton (mass)	e-neutrino ν_e ($< 3\,\text{eV}$)	μ-neutrino ν_μ ($< 0.19\,\text{MeV}$)	τ-neutrino ν_τ ($< 18.2\,\text{MeV}$)	$Q = 0$	$1/2$
	electron e ($511\,\text{keV}$)	muon μ ($105.7\,\text{MeV}$)	tau τ ($1.777\,\text{GeV}$)	$Q = -1$	$1/2$
quark (mass)	up ($1.5 - 3.3\,\text{MeV}$)	charm ($1.27\,\text{GeV}$)	top ($171.2\,\text{GeV}$)	$Q = +2/3$	$1/2$
	down ($3.5 - 6\,\text{MeV}$)	strange ($104\,\text{MeV}$)	bottom ($4.2\,\text{GeV}$)	$Q = -1/3$	$1/2$

Table 1.1: *Fermions described in the Standard Model* [12]

		mass	em. charge	spin
strong	gluon g	0	0	1
electromagnetic	photon γ	0	0	1
weak	$W^\pm$	$80\,\text{GeV}$	± 1	1
	Z^0	$91\,\text{GeV}$	0	1
(mass)	Higgs	$> 114.4\,\text{GeV}$	0	0

Table 1.2: *Bosons described in the Standard Model* [12]

1.2 The Gauge Symmetry and Symmetry Breaking

The SM describes particles and their dynamics in terms of quantum fields, whose equations of motion are derived from a Lagrangian density function $\mathcal{L}$ (e.g. [16, 17]). If, for example, ψ denotes the electron field, the according Lagrangian is

$$\mathcal{L}_{\text{electron}} = i \underbrace{\bar{\psi}\gamma^\mu \partial_\mu \psi}_{\text{dynamic term}} - \underbrace{(mc^2)\bar{\psi}\psi}_{\text{mass term}}. \tag{1.1}$$

The 'dynamic term' in this equation describes the evolution of the electron field, the mass term accounts for its mass, $\bar{\psi}$ is the adjoint of ψ and the γ^μ are the so-called γ-matrices.

The Lagrangian $\mathcal{L}_{\text{electron}}$ is invariant under a global gauge transformation. This means exchanging the original field ψ by the modified field

$$\psi \to e^{-i\alpha}\psi \qquad \text{(global gauge transformation)}$$

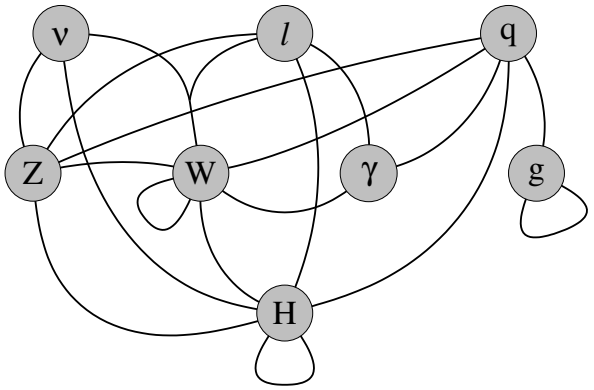

Figure 1.1: *Force couplings between the different particles* [15]

neither changes the Lagrangian nor the equation of motion. The parameter α is free and could be chosen differently by different observers. Thus it is natural to demand gauge invariance with α being a function of space time $\alpha(x^\mu)$:

$$\psi \to e^{-i\alpha(x)}\psi \qquad \text{(local gauge transformation)}$$

However, $\mathcal{L}$ contains differential operators which generate additional terms when acting on $\alpha(x)$. Initially these terms do not cancel out, but a locally gauge invariant Lagrangian can be constructed with the extensions

$$\mathcal{L} \to \mathcal{L} - \underbrace{i(q\bar{\psi}\gamma^\mu\psi)A_\mu}_{\text{electron to field coupling}} + \underbrace{\frac{1}{16\pi}F^{\mu\nu}F_{\mu\nu}}_{\text{dynamic term for the field}} . \tag{1.2}$$

Here a gauge field A_μ and the field-strength tensor $F^{\mu\nu} = \partial^\mu A_\nu - \partial^\nu A_\mu$ are introduced. The Lagrangian is invariant under a local gauge transformation, if A_μ is transformed at the same time via

$$A_\mu \to A_\mu + \partial_\mu \alpha(x).$$

The gauge field A_μ in this example can be identified with the electromagnetic field. Hence, the requirement for local gauge invariance automatically introduces an interaction into the model.

To derive an equation of motion for ψ, $\mathcal{L}$ is subjected to the Euler-Lagrange equations. The result - in this case the Dirac equation - is solved by quantising the field ψ. From the solutions, Feynman diagrams are derived which define a set of rules to calculate a reaction cross section of any electromagnetic process. The 'dynamic term' in (1.1) is connected to the electron propagator in such a diagram. The 'electron to field coupling' term in the extension (1.2) describes the interaction of the electron with the electromagnetic field, whereas the 'dynamic term' accounts for the photon propagator. The electromagnetic interaction in this example arises from an $U(1)$ gauge symmetry requirement, because $e^{-i\alpha(x)}$ is the generator of an $U(1)$ transformation.

In a similar manner, the weak and the strong force are included into the SM Lagrangian. The final symmetry structure of the SM is

$$\underbrace{SU(3)_C}_{\text{strong}} \times \underbrace{SU(2)_L \times U(1)_Y}_{\text{electroweak}}$$

The strong force is described in the QCD theory, and a cause of a $SU(3)_C$ symmetry requirement. The weak and the electromagnetic force are combined consistently in the GWS model. Together they are derived from $SU(2)_L \times U(1)_Y$ symmetry requirement, which must be augmented with an additional field, because the gauge principle is not applicable straight forward.

The Lagrangian in (1.1) includes a mass term which consists of a product of the fields. This term can describe the masses of the fermions under $SU(1)$ and $SU(3)$ symmetry, but it is not entirely $SU(2)$ invariant. Moreover, the W and Z bosons are massive. If B_μ denotes the field of such a boson, also the naive mass term for the field

$$\mathcal{L} \rightarrow \mathcal{L} + m_{\mathrm{B}} \bar{B}^\nu B_\nu \quad \text{is not gauge invariant.}$$

To preserve gauge invariance, the existence of an additional field is postulated, namely the Higgs field Φ. This field is introduced by the Higgs potential:

$$\mathcal{L} \rightarrow \mathcal{L} - \mu^2 |\Phi|^2 + \lambda^2 |\Phi|^4$$

with $\lambda > 0$ and $\mu^2 < 0$. The Higgs potential has its minimum at $v = \sqrt{\mu^2/\lambda} \neq 0$. Hence, the field does not vanish in the lowest energy states and it is omnipresent. This phenomenon is called spontaneous symmetry breaking - in a completely symmetric vacuum state, all fields would vanish. Massive particles couple to the Higgs field and thereby acquire their masses. This principle can be adopted to all particles in an entirely gauge-invariant way. For the Lagrangian (1.1) this means, that the mass term is reinterpreted as a coupling term between the field ψ and the Higgs field. The coupling strength is mass.

If the Higgs mechanism is realised in nature, it would manifest itself in the existence of the yet undiscovered Higgs boson. Figure 1.2 shows the SM fit to the available data from colliders operated so far with the Higgs boson mass m_{Higgs} as the fit parameter. The best fit predicts a m_{Higgs} around 90 GeV, but measurements done at the Large Electron Positron ring (LEP) set a lower limit $m_{\mathrm{Higgs}} > 114.4\,\mathrm{GeV}$ with a 95-% confidence level [18].

Currently the Tevatron collider performs searches for the Higgs particle, but the physics processes at this machine do not provide a high sensitivity in the most probable mass range around 120 GeV. Up to now, Higgs searches could exclude a region around 170 GeV. Thus the Higgs is to be expected 'just around the corner', between 115 GeV to about 160 GeV and it is among the first targets of high-energy colliders in the TeV energy range.

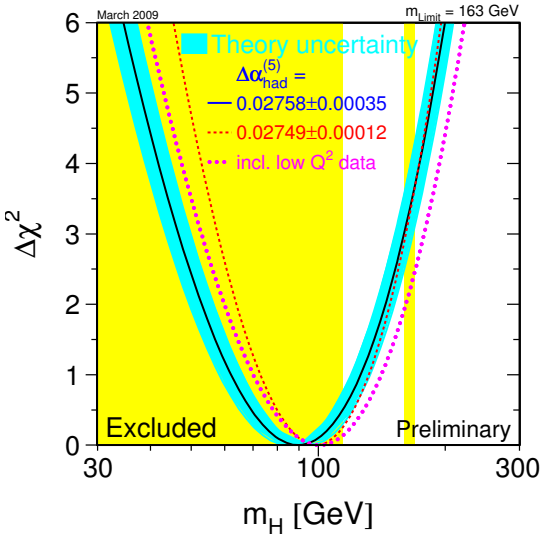

Figure 1.2: *Current Higgs-mass exclusion limits* [19]

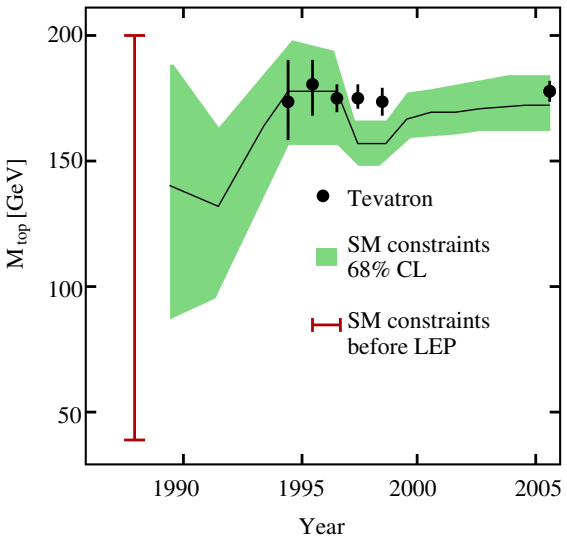

Figure 1.3: *Top mass predictions during LEP runtime* (adapted from [20])

1.3 Successes and Problems of the SM

Today the standard model is considered to be very successful as it withstands all experimental test without significant deviations. Moreover, the model has proven a remarkable predictive power. One example is connected to the discovery of the top quark. Figure 1.3 illustrates the development of top mass predictions, which have been made on the basis of precision measurements on the Z-peak at 91 GeV, to which the top quark give virtual contributions without showing up as a physical particle. In 1989, when LEP started the search, the top mass was expected to be in the range 150 ± 50 GeV. The prediction got finetuned in the following years of LEP runtime on the basis of the taken data. In 1995, the top quark was discovered at the Tevatron Collider, precisely within the predicted mass window.

Up to today, LEP and the Tevatron have almost reached an energy close to the expected spontaneous symmetry breaking scale. Although these colliders have not discover the Higgs particle yet, there are no major doubts that it exists.

However, even if the missing piece is found, the SM will still have major shortcomings. On the experimental side, it can not explain the abundance of energy in the universe (e.g. [21]). Only 5 % of the observed energy seem to consist of SM particles. The 95-%-rest is dark matter (25 %) and dark energy (70 %), which are completely out of the SM scope.

Another example for a SM incompleteness is given in the neutrino sector. In the last years several experiments have proven neutrino oscillations (e.g. [22, 23]), which are a clear sign for non-zero neutrino masses. Yet, in its current form the SM describes massless neutrinos.

On the theory side, the hierarchy problem is one of SM's most striking problems.

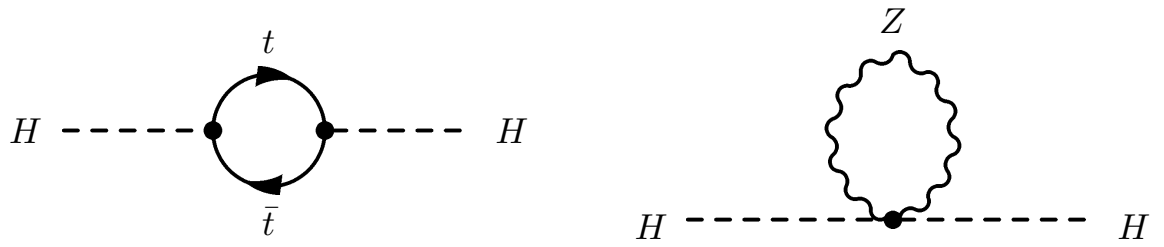

(a) fermionic loop **(b)** bosonic loop

Figure 1.4: *Divergent loop corrections to the Higgs mass*

Like other SM particles, the Higgs particle acquires self energy contributions from loop diagrams (see figure 1.4). For example, in figure 1.4(a) the Higgs couples to a top pair while the dominant bosonic contributions come from Z or W loops shown in figure 1.4(b). Such contributions to particle masses cause divergences that have to be cancelled in the calculations. The technique is called renormalisation. In case of the Higgs particles, the contributions are quadraticlly divergent,

$$\Delta m_{\mathrm{H}}^2 \sim \Lambda^2,$$

while for other SM particles they are only logarithmically divergent. Here Λ is a parameter in the calculation that defines the energy scale to which the SM shall be valid. Initially, it is set to an arbitrary cut-off value and arising divergences are corrected with a renormalisation parameter. Finally, the SM shall be valid to the Planck scale of $\Lambda_{\mathrm{P}} \approx 10^{19}\,\mathrm{GeV}$. To arrive at the expected or measured masses, the renormalisation parameter has to be chosen in a range of the actual mass, except for the Higgs boson. The quadratic divergence needs to be renormalised by a fine-tuned parameter far above the Higgs mass range of $m_{\mathrm{Higgs}} < 1\,\mathrm{TeV}$. Although this is theoretically possible, it is disfavoured, as the level of relative precision of the parameter choice is ${}^{m_{\mathrm{H}}}/_{\Lambda} > 10^{16}$. The upper limit on m_{Higgs} of about 1 TeV is set by the calculated cross sections of W fusion processes. These processes would violate unitarity above $\sqrt{s} \approx 1.2\,\mathrm{TeV}$ unless either a SM Higgs particle exists below the one-TeV limit or an additional strong force acts on the W bosons.

The hierarchy problem does not occur in a standard model that is extended by Supersymmetry (SUSY), as explained in chapter 8. Thus this can be understood as a hint that the SM could be a low-energetic approximation to a more comprehensive theory of nature. Besides SUSY, other expansions of the model are discussed, but all predict that new physics will show up in the energy range up to one TeV. This will be addressed by the next generation colliders, the Large Hadron Collider (LHC) and the International Linear Collider (ILC).

The final goal of the ongoing research is a theory of everything, including gravity. The latter could not be included into the SM framework yet. This is currently another of SM's shortcomings.

2 The International Linear Collider

The majority of particle accelerators have operated either with hadron or lepton beams. Hadron machines have often pushed the energy frontier to higher values and discovered new particles. Their counterparts, the lepton accelerators, are precision machines. They allow for precise studies of particle properties and are sensitive to virtual effects produced by particles that are even above their energy range.

The first section of this chapter discusses key parameters of colliders and explains the interplay between hadron and lepton machines. Section 2.2 introduces the ILC and its physics programme. The subsequent section 2.3 is dedicated to the ILD detector concept which is a proposed detector for the ILC. In the main focus of this work are the development of a prototype tracking detector (part II) and a physics performance study for the ILD (part III).

2.1 Collider Principle

A particle accelerator produces a highly energetic particle beam and delivers it to a detector of an experiment. Inside the detector, the beam particles are brought to collision with particles of an opposite beam (particle collider) or with a fixed target. The centre-of-mass energy of this collision, $\sqrt{s}$, is one of the key performance parameters of an accelerator. High centre-of-mass energies are needed to produce heavy particles and resolve small structures and in particular today, highest energies are required to explore the physics of the TeV energy scale. The highest centre-of-mass energies can be reached with a particle collider because in a fixed target experiment $\sqrt{s}$ increases only with the square root of the beam energy ($\sqrt{s} \propto \sqrt{E_{\text{beam}}}$), while the full beam energy becomes available in the collision of two beams with equal energies ($\sqrt{s} = 2\,E_{\text{beam}}$) . Therefore, today's accelerator facilities with highest centre of mass energies are exclusively particle colliders.

The second figure of merit of the machine is its luminosity $\mathcal{L}$. The luminosity describes the number of particles which are brought to collision per unit time and area and determines the rate n of a physics process to take place. The rate is

$$n = \mathcal{L} \cdot \sigma,$$

where σ is the cross-section of the reaction. The cross-section can be calculated from the Feynman diagram of the process.

Rare signal processes at TeV energies have cross-sections of a few ten femtobarn ($10^{-39}\,\text{cm}^2$), which is valid for example for many supersymmetric processes. Their

study requires luminosities in the range of $10^{34}\,\mathrm{cm}^{-2}\mathrm{s}^{-1}$ to get a sufficient amount of signal processes in a typical running period of a collider. This used to be in the order of a few years.

2.1.1 Hadrons versus Leptons - Circular versus Linear

The LHC will collide protons with protons and is designed to reach centre-of-mass energies of 14 TeV at a luminosity in the order of $10^{34}\,\mathrm{cm}^{-2}\mathrm{s}^{-1}$. The energy is about a factor of ten higher than the highest energy reached at a running hadron collider, namely the Tevatron with $\sqrt{s} \approx 1.9\,\mathrm{TeV}$. Although both machines have centre-of-mass energies above one TeV, only a fraction is available in the collision of two elementary particles. This is because protons are not point-like but have a substructure of quarks and gluons and interesting physics events happen when two of these constituents collide. Moreover, the energy of the proton constituents is not fixed and particles collide with all possible energies. Thus a hadron collider covers a wide energy range while running at a fixed beam energy which makes them well suited as discovery machines. But they do not allow highest precision measurements. Firstly, the centre of mass energy is not adjustable and so the initial energy of an interaction is unknown, as well as the precise kinematics. Secondly, the proton-proton interaction cross-sections are dominated by elastic background QCD processes. This means that each interesting signal event is overlaid with large backgrounds produced by the interactions of other proton collisions.

Contrary to protons, electrons and positrons are point-like. Therefore an e^+e^- collider produces well defined initial states and offers a clean environment. Also, the centre-of-mass energy is tunable via the beam energy. This allows for threshold scans and resonant production of interesting particles. These two features allow for high precision measurements.

But lepton colliders cannot compete with hadron colliders in terms of maximum centre-of-mass energies. The reason is that the particle colliders used to be operated in circular rings. In these storage rings, the beams run around in opposite direction and collide in the detectors. Electrons and positrons are comparably light particles and suffer from energy losses by synchrotron radiation when running around. These losses ΔE are (e.g. [24])

$$\Delta E \propto \frac{1}{R}\left(\frac{E}{m}\right)^4 \qquad \text{and for electrons} \qquad \Delta E_{e^\pm}\,[\mathrm{MeV}] \approx 8.85 \cdot 10^{-2}\frac{(E\,[\mathrm{GeV}])^4}{R[\mathrm{m}]}.$$

Here, R is the radius of the collider and E the beam energy. So far, the Large Electron-Positron Collider (LEP) was the highest-energetic e^+e^- collider in operation. It ran between 1989 and 2000 in a 27-km-long circular tunnel at the European laboratory for particle physics CERN and reached $\sqrt{s} = 209\,\mathrm{GeV}$ in the final period of operation. In the end, the centre-of-mass energy was limited by the beam energy losses due to synchrotron radiation. They accumulated to 2.5 GeV per electron and turn. Nowadays, the LHC has replaced LEP in the same tunnel. Since protons are about 2000 times

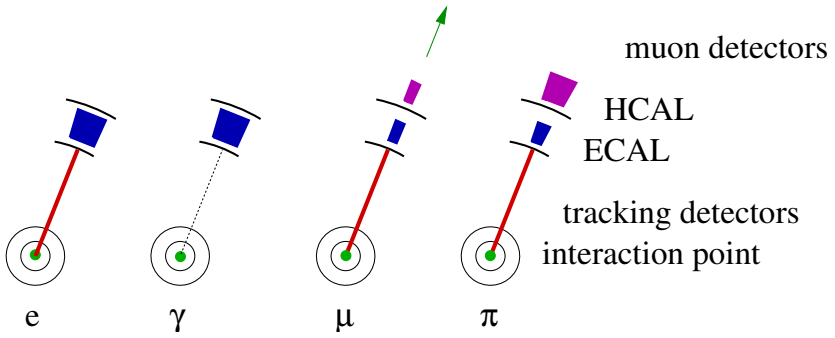

Figure 2.1: *Signatures of different particles in a detector*

heavier than electrons, synchrotron radiation does not limit the LHC energy but the strength of the magnetic fields needed to bend the protons on the circular course.

To reach a higher energy with a lepton collider, the radius of the machine could be increased to mitigate the synchrotron radiation losses. However, the reduction is only linear while the losses rise with E^4. Hence a circular lepton collider needs to be unrealistically large if it was supposed to run beyond $\sqrt{s} = 300\,\text{GeV}$. Therefore the ILC is planned as a linear machine which means that energy losses due to synchrotron radiation losses are avoided.

2.1.2 Particle Detectors

A particle detector is the tool for studies of the physics processes, which take place in collisions of beam particles. For this, the detector measures particles which are produced in the interaction or their decay remnants. The reconstruction of particle momenta and energies allows for a reconstruction of the kinematics of the physics process.

A particle detector typically consist of different detector layers which are in most cases installed hermetically around the interaction point of a collider. Each of these sub-detector layers performs a dedicated measurement. Figure 2.1 illustrates this principle for three particle species. Tracking detectors are installed closest to the IP and measure space points along the trajectories of charged particles, like muons or electrons. They are followed by a calorimeter system consisting of an electromagnetic (ECAL) and a hadronic calorimeter (HCAL). The ECAL absorbs electrons and photons completely and measures their energies. Hadrons can punch through to the hadronic calorimeter before being absorbed. Muons typically escape completely and are measured also in a muon system outside the HCAL.

In the data analysis, the detector data are processed with dedicated software tools in an event reconstruction: Particle momenta and energies can be determined with the measurements of the tracking detectors and the calorimetric systems, while the distinct detector signatures of different particles allow for a particle identification. The data analysis yields reconstructed events which are used in physics analysis to deter-

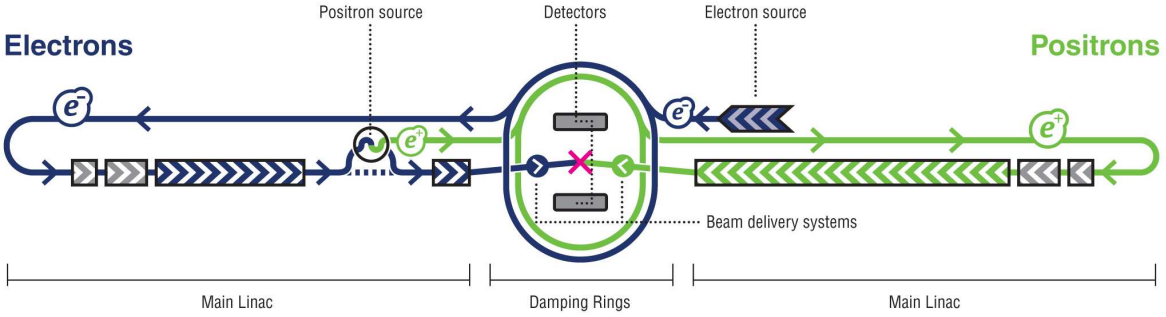

Figure 2.2: *Footprint of the ILC in the baseline design* [25]

mine cross sections or particle lifetimes. These measured quantities are compared with physics model predictions.

2.2 The ILC Baseline Design

In the baseline design, the ILC will consist of two eleven kilometre long superconducting linear accelerators, called linacs. The linacs are directed on a central interaction region where collisions take place at an angle of 14 mrad. Figure 2.2 shows the schematic ILC layout in more detail.

In operation, firstly beam particles are filled into damping rings with a circumference of 6.7 km. Therein, they circulate at an energy of 5 GeV and the beam size is reduced. The prepared beams are guided to the linacs which accelerate them towards the interaction point. In between, the electrons pass an undulator where they produce high energetic photons. These photons are shot onto a target and produce positrons which are filled back into the positron damping ring. This way, positrons are created permanently on runtime, while electrons can be extracted from a conventional electron source.

Both accelerator arms work at a nominal acceleration gradient of 31.5 MeV/m and allow for a maximal centre of mass energy of $\sqrt{s} = 500\,\text{GeV}$ with energy fluctuations due to the machine of less than 0.1 %. The gradient can be adjusted to steer the beam energy and operate the ILC at lower $\sqrt{s}$. Currently, runs at $\sqrt{s} = 91\,\text{GeV}$ on the Z resonance and at 161 GeV at the W^+W^- threshold are under discussion. These are called Giga-Z and Mega-W options, respectively.

Figure 2.3 illustrates the bunch structure of the ILC. In nominal operation, the machine will collide bunch trains with a repetition rate of 5 Hz. Each bunch train contains 2625 bunches with $2 \cdot 10^{10}$ particles per bunch. With the nominal beam parameters, the ILC will reach a peak luminosity of $\mathcal{L} = 2 \times 10^{34}\,\text{cm}^{-2}\text{s}^{-1}$.

The beams will be provided with a beam polarisation of up to 80 % for the electron beam and 30 % for the positron beam. Beam polarisation an instrument well suited to enhance signal rates since the cross sections of many signal processes depend on the

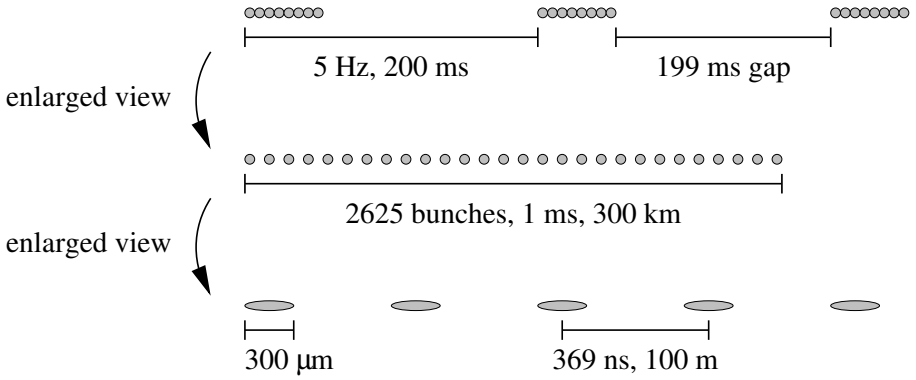

Figure 2.3: *Beam structure of the ILC: 2625 bunches with* 2×10^{10} *particles in each bunch are arranged in a bunch train. The train repetition rate is* 5 Hz. [15]

polarisation state of the initial particles.

At a later stage, an optional upgrade is foreseen to extend the ILC energy range up to $\sqrt{s} = 1\,\text{TeV}$, if this is required by physics. In addition, the positron beam polarisation could be increased to 60 %.

Besides the mentioned International Large Detector (ILD), two other detector concepts have been proposed for operation at the ILC. These are the Silicon Integrated Detector (SiD) [5] and the so-called 4^{th}-concept detector [6]. The ILC will host two detectors, which are operated in push-pull operation. That means, alternating one detector is off the beam in a packing position while the other one takes data.

2.2.1 ILC Physics Programme

In the first stage, the ILC could focus on the exploration of the Higgs boson. This particle is expected in the mass range between 115 GeV to $\lesssim$ 750 GeV and it is likely to be found at the LHC. The LHC will be able to determine its mass m_{Higgs} with an expected precision of about 500 MeV (e.g. [26]). However, a full characterisation of the Higgs includes a measurement of its total decay width, the spin, the production cross-sections and the couplings to the known Standard Model (SM) particles. These measurements are very difficult or impossible to do at the LHC. But they are mandatory to prove that a discovery is exactly the Higgs boson which is expected in the SM and among these key measurements foreseen for the ILC.

As an example, figure 2.4(a) depicts the Feynman diagram of the Higgs-strahlungs process, one of the optimal channels for the study of the Higgs boson. The electron and the positron annihilate with a known $\sqrt{s}$ and produce an exited Z^0. This radiates off a Higgs boson. The Z^0 decays, to a fermion anti-fermion pair. If the two produced fermions are measured, m_{Higgs} and the total $e^+e^- \rightarrow HZ^0$ cross section can be determined, independent of the Higgs decay mode. Moreover, this measurement is independent of the Higgs model as only the decay products of the Z^0 need to be measured. The optimal event topology appears in the detector when the Z decays to

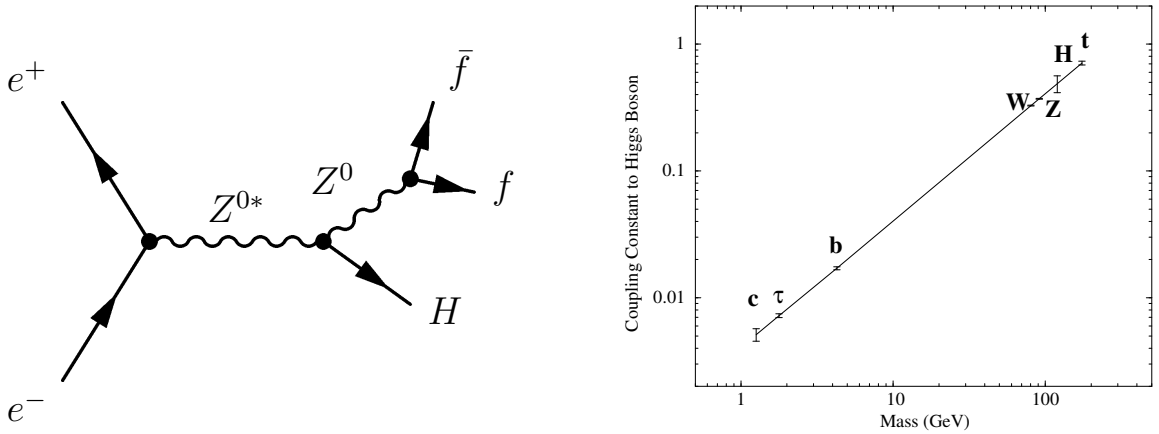

(a) Feynman diagram of the Higgs-strahlung process

(b) Coupling of the Higgs boson to different SM particles [27]

Figure 2.4: *Higgs studies at the ILC*

a muon pair. Such an event, coming from an ILD detector simulation, is illustrated in figure 2.5. The two muons have produce clear detector signature and can be identified and measured most precisely. In this final state, the mass determination is possible with a precision in the 100-MeV-regime (see below). In the further analysis, the decay of the Higgs will be studied and its absolute decay branching ratios be measured. As said before, a SM-like Higgs boson couples to SM particles with a strength proportional to the particle mass, as illustrated in figure 2.4(b). The measurement of the Higgs decay branching ratios is one curial input to the determination of these coupling strengths which is the essential measurements to proof that the Higgs mechanism is the source of mass generation.

Besides the Higgs boson, the ILC will be able to study a variety of other SM processes: it will measure the top quark mass with an unprecedented precision, also in the 100-MeV-regime. The dedicated Giga-Z and Mega-W runs will allow for precision studies of the W and Z bosons. These measurements will in particular benefit from the possibility to finely adjust the centre of mass energy because they require threshold scans and resonant production of the interesting particles.

If SUSY exists, the ILC will determine the properties of supersymmetric particles in its energy range. Many proposed SUSY scenarios have complex particle spectra with many overlapping decays that the LHC may not be able to distinguish or to identify correctly. Again, with the tunable beam energy, the ILC will be able to exactly point to the energy range where the LHC measured new particles and resolve possible substructures.

An broader overview over the potential of a TeV e^+e^--collider can be found in [29, 30, 31].

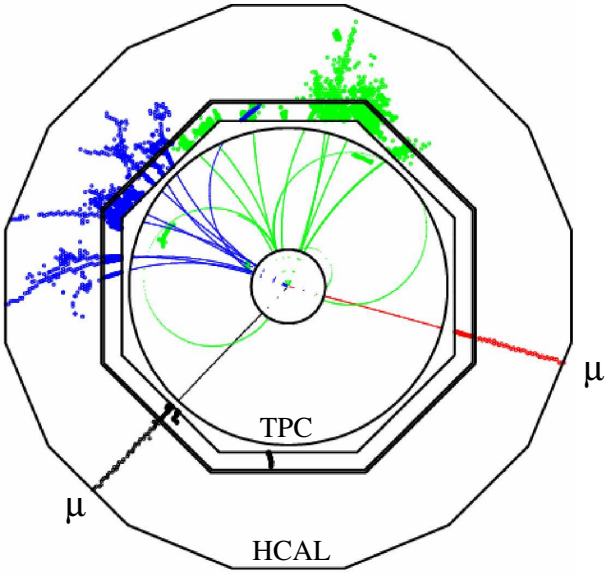

Figure 2.5: *Simulated event $e^+e^- \rightarrow H + \mu\mu$ in the ILD detector* [28]

2.3 The ILD Detector Concept

The comprehensive physics programme for the ILC puts high demands on the proposed ILC detectors. One of the most challenging tasks is the separation of $Z \rightarrow q\bar{q}$ from $W \rightarrow q\bar{q}$ final states. This is needed for example to distinguish between $H \rightarrow ZZ$ and $H \rightarrow WW$ decays or to study $WW \rightarrow WW$ scattering. The latter is the process which is responsible for the violation of the unitary bound at energies of 1.2 TeV, if no Higgs or new interaction is introduced into the SM.

The quarks being created in a Z or W decay hadronise further and produce a bundled jet of particles in the detector. To reach a clear separation between the two decay modes, the jet energies have to be measured with a resolution better than $\sigma_E/E \sim 3-4\,\%$ (equivalent to $^{30\,\%}/\sqrt{E[\mathrm{GeV}]}$). This is unprecedented by detectors so far - the detectors operated at LEP reached $^{60\,\%}/\sqrt{E[\mathrm{GeV}]}$ at most (e.g. [32]).

2.3.1 The Particle Flow Approach

Particle flow is the proposed concept to satisfy the jet energy resolution requirement for the ILD detector. This paradigm foresees to reconstruct the full four-momentum vector of each particle in the detector with the optimal set of sub-detector measurements, instead of performing only a calorimetric measurement.

The momentum p of charged particles can be measured most precisely with the tracking detectors. When the momenta and particle energies are determined, energy deposits in the calorimeters are associated to the trajectories of the charged particles and removed from the calorimeter measurements. The leftover calorimeters signal belong to neutral particles, whose energy can then be determined accurately.

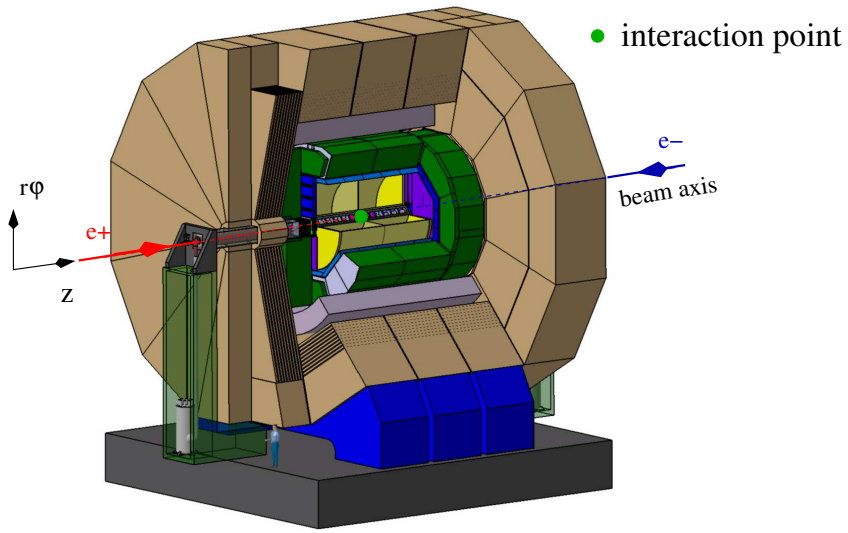

Figure 2.6: *Schematic view of the ILD detector concept with cylindric reference coordinate system* [4]

Finally, the achievable energy resolution is a sum of the energy resolutions of the different sub-detectors and a confusion term:

$$\frac{\sigma(E)}{E} = \underbrace{\frac{\sigma(E_{\text{charged}})}{E} \oplus \frac{\sigma(E_{\text{hadron}})}{E} \oplus \frac{\sigma(E_{\text{em.}})}{E}}_{\sim 20\,\%\sqrt{E}} \oplus \frac{\sigma(E_{\text{confusion}})}{E})$$

The latter describes the systematic uncertainties associated with the allocation of calorimeter energy deposits to the particles. Current calorimeter and tracking detector performances allow for an ideal jet energy resolution in the order of $20\,\%/\sqrt{E}$.

Thus, the additional contribution due to the confusion term must be kept below about $20\,\%/E$ to fulfil the aspired jet energy resolution. This imposes dedicated requirements to the overall detector design:

- the detector must be as hermetic as possible to minimise the number of particles which escape undetected
- the tracking system must be highly efficient and allow for a precise momentum measurement
- the material budget of the tracking system must be minimised to reduce multiple scattering and conversation of particles before they reach the calorimetric system, which would spoil the momentum measurement
- the calorimeter must be fine segmented to allow for allow for a correct assignment of calorimeter clusters to particles, even in the high particle densities of a jet

The performance of the particle flow event reconstruction is closely connected to the sub-detector performances and the reconstruction software algorithms.

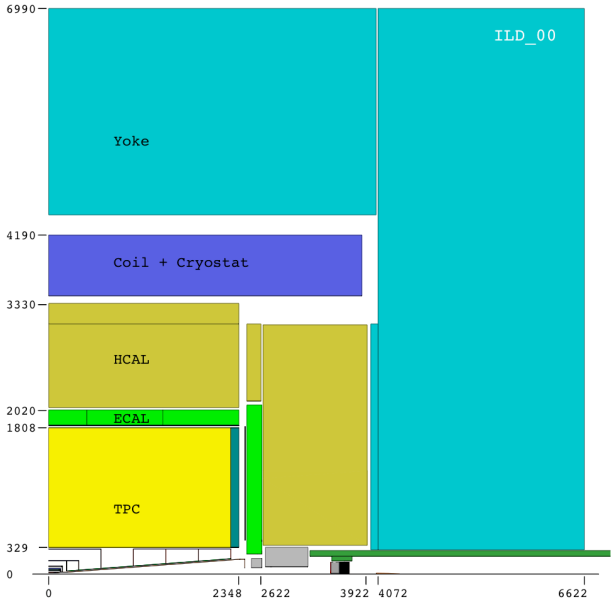

Figure 2.7: *Quadrant of the ILD detector concept with dimensions in millimetres* [4]

2.3.2 The ILD Detector Layout

The ILD detector (see figure 2.6) is optimised for the particle flow concept. Figure 2.7 shows a schematic view of a quadrant of the ILD detector. Here the interaction point is located at the lower left corner of the figure. The foreseen tracking system consists of pixel-vertex detectors and silicon strip detectors (VTX, SIT). These detectors measure about 10 points per particle trajectory with a precision in the 10-μm region. In the forward region, a system of silicon detector disks provides the low angle coverage. The VTX and SIT systems are surrounded by a large-volume Time Projection Chamber (TPC). The TPC records up to 224 three-dimensional space points per particle and provides quasi-continuous tracking. The aspired resolution for the TPC is 100 μm per measured point in the $r-\varphi$-plane and 500 μm in the z-direction. A development study for this TPC is the main topic of part II of this thesis - there the detector principle is described in detail. To improve the tracking, the ILD detector concept foresees another layer of silicon strip detectors in front of the calorimeter system (SET).

Both calorimeters have very fine granularity and are optimised the particle flow principle. The ECAL cell size is planed to be $1 \times 1\,\mathrm{cm}^2$ in up to to 30 active layers whereas the HCAL is segmented in $3 \times 3\,\mathrm{cm}^2$ large cells and consists of 48 layers.

The calorimeter system is completed by a system of radiation hard detectors in the very forward region around the outgoing beam pipes. These specialised calorimeters measure the luminosity and monitor the beam quality. Of particular importance is the so-called beam calorimeter which is used to veto against backgrounds, for example in the simulation study that is discussed in part III.

The mentioned detector components are embedded in a solenoid magnet ('Coil +

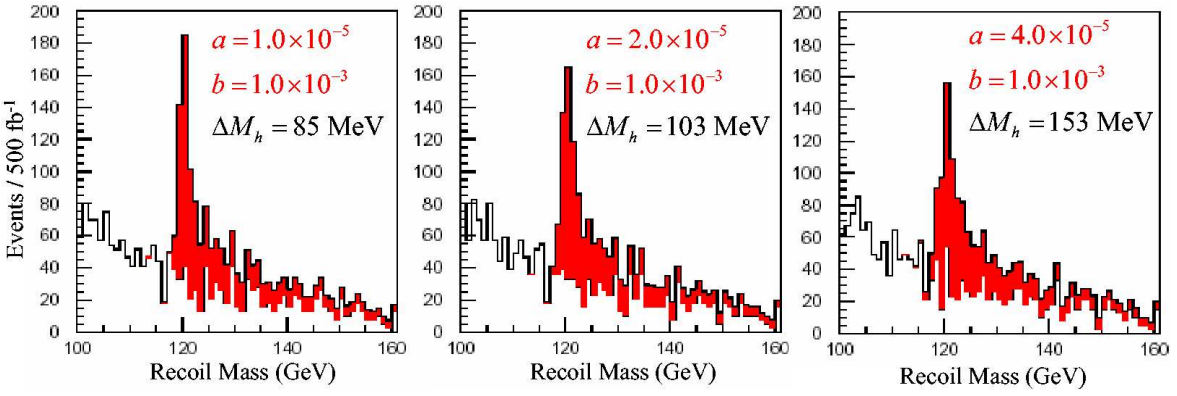

Figure 2.8: *Higgs recoil mass spectra for several momentum resolutions, parameterised as* $^{\delta p_\perp}/_{p_\perp^2} = a \oplus b\,(p_\perp \sin\Theta)^{-1}$ [33]

Cryostat' in figure 2.7) which produces an axial-magnetic field of 3.5 T in the detector, which forces charged particles on curved trajectories for the momentum measurement. An iron yoke returns the magnetic flux outside the magnet. At the same time, the iron is instrumented and serves as a muon detector. The detector is operated without trigger and read out by a sophisticated data acquisition system adapted to a trigger-less running mode.

Requirements to the Tracking System

The particle flow reconstruction is based to a great extent on the tracking system and hence the reconstruction accuracy depends crucially on the achieved momentum resolution.

To determine the momentum p of a charged particle, the angle θ between the reconstructed particle trajectory and the beam axis is measured. In addition, the trajectory is curved due to the magnetic field and from the measurements of the tracking system the radius of the trajectory ρ is determined, projected on the transversal plane $r-\varphi$-plane. Then p is calculated from

$$p_\perp = p\,\sin\theta \qquad \text{and} \qquad p_\perp\,([\text{GeV}]) \approx 0.3\;\rho\,[\text{m}]\;B\,[\text{T}]$$

Here, $p_\perp$ it the component of $\vec{p}$ perpendicular to the beam pipe ($r-\varphi$ - plane in figure 2.6), and ρ the trajectory radius.

The ILD concept aspires to a momentum resolution of $^{\delta p_\perp}/_{p_\perp^2} \approx 2\cdot 10^{-5}\,\text{GeV}^{-1}$ for the whole tracking system. This number is for example pushed by the mentioned Higgs recoil analysis, which closely relates the resolution to the achievable precision of m_{Higgs}. Figure 2.8 shows the reconstructed recoil mass distribution coming from a simulation of the measurement. This simulation has been made for the data of $500\,\text{fb}^{-1}$ at $\sqrt{s} = 350\,\text{GeV}$ and m_{Higgs} is assumed to be 120 GeV. The tracker momentum resolution is parametrised as $^{\delta p_\perp}/_{p_\perp^2} = a \oplus b\,(p_\perp \sin\Theta)^{-1}$. With the foreseen accuracy, ILD

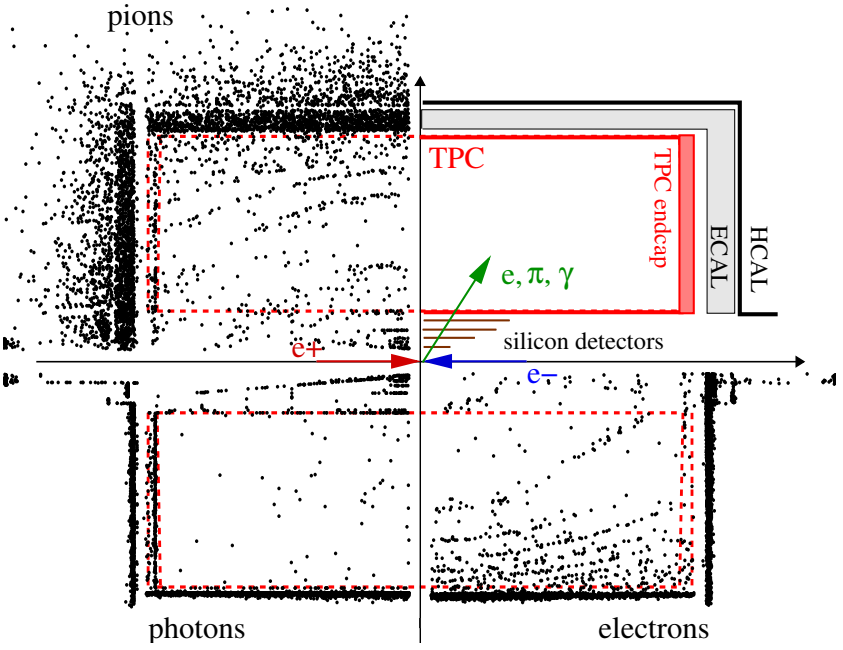

Figure 2.9: *Simulated points of the first hard interaction in the detector for electrons, pions and photons coming from the IP with energies of 0.1-10 GeV. (The 'round' shape of the distribution is a simulation artifact - a modified version of the diagram can be found in [34])*

can determine m_{Higgs} with an uncertainty better than 150 MeV. A better momentum resolution could reduce the uncertainty even further.

The TPC is foreseen to contribute to the overall particle momentum measurement accuracy with ${}^{\delta_{pt}}/_{p_t^2} \sim 9 \cdot 10^{-5}\,\text{GeV}^{-1}$. Via the Glückstern formula [35]

$$\frac{\delta p_\perp}{p_\perp^2} = \frac{\sigma_\perp}{0.3\,B^2\,L}\sqrt{\frac{720}{N+4}}\left(\frac{\text{T m}}{\text{GeV / c}^2}\right)$$

this requirement can be transformed into a resolution requirement $\sigma_\perp$ for the coordinates of a measurement point with respect to the $r-\varphi$-plane. Here, L is the length of the trajectory piece in the TPC and N the number of measured space points. With $L = 1.5\,\text{m}$ and 150 robustly measured points in the 3.5-T magnetic field, $\sigma_\perp$ comes out to be about $100\,\mu\text{m}$, as stated above.

Table 2.1 summarises further design goals for the TPC. A second challenge is the reduction of the material budget of the TPC structure, measured in radiation lengths X_0. One radiation length corresponds to the mean distance over which an electron looses all except ${}^1/_e$ of its initial energy due to interactions with matter - in this case the detector material. Figure 2.9 illustrates the need to reduce the material budget of the tracking system. This illustration shows the simulated point of the first hard interaction, in which a particle is converted or a charged particle radiates of a photon, in the detector. It is made for 10000 electrons, pions and protons each. These particles

Size	diameter: 3.6 m, length $2 \cdot 2.15$ m
point resolution in $r\varphi$	$< 100\,\mu$m
point resolution in z	< 0.5 mm
TPC material budget	$\lesssim 0.01\,\mathrm{X}_0$ of the inner barrel
	$\lesssim 0.04\,\mathrm{X}_0$ to the outer barrel
	$\lesssim 0.15\,\mathrm{X}_0$ to the end caps in z
${}^{\mathrm{d}E}/_{\mathrm{d}x}$ resolution	$\sim 5\,\%$

Table 2.1: *Design goals for the ILD TPC* [4]

have been shot from the IP into one detector quadrant at energies between 100 MeV and 10 GeV.

Ideally, all particles undergo a hard scattering process for first time in one of the calorimeters. However, occasionally particles are scattered in the TPC structure, and thereby lose energy, eventually get a new direction or even fragment to other particles. These encounters spoil the momentum measurement and thus the PFO reconstruction. Less critical are interactions inside the TPC, because the fragments are measured and the energy and momentum of the initial particle can still be reconstructed.

To reduce the rate of interaction in the tracking system, the tracking sub-detectors have to be optimised to a low material budget. For the TPC structure, the envisaged numbers are $X_{\mathrm{wall}} \lesssim 0.01\,\mathrm{X}_0$ for the inner wall, $X_{\mathrm{wall}} \lesssim 0.04\,\mathrm{X}_0$ to the outer wall and $\lesssim 0.15\,\mathrm{X}_0$ to the outer end caps.

Both the aspired resolution and the reduction of the material budget are topics of current development studies.

2.3.3 Magnetic Field Setup

Unlike in detectors operated for example at LEP, the beams do not collide head on in the ILD detector but under a 14-mrad crossing angle. Thus the beams are not directed into the opposite linac but can be dumped safely behind the IP. The crossing angle affects the design of the whole detector and particularly requires a modified magnetic field setup. As figure 2.10 shows, the magnetic field is not perfectly axial, but has a slightly bended shape. The modified field guides charged beam background particles with energies in the GeV regime into the outgoing beam pipes (e.g. [15]). Different field configurations are currently being studied, so-called DID or anti-DID fields. These setups are in particular challenging for the measurements in the TPC, because an inhomogeneous magnetic field produces a bias in the operation, which has to be corrected precisely to ensure the 100-μm resolution in the transversal plane.

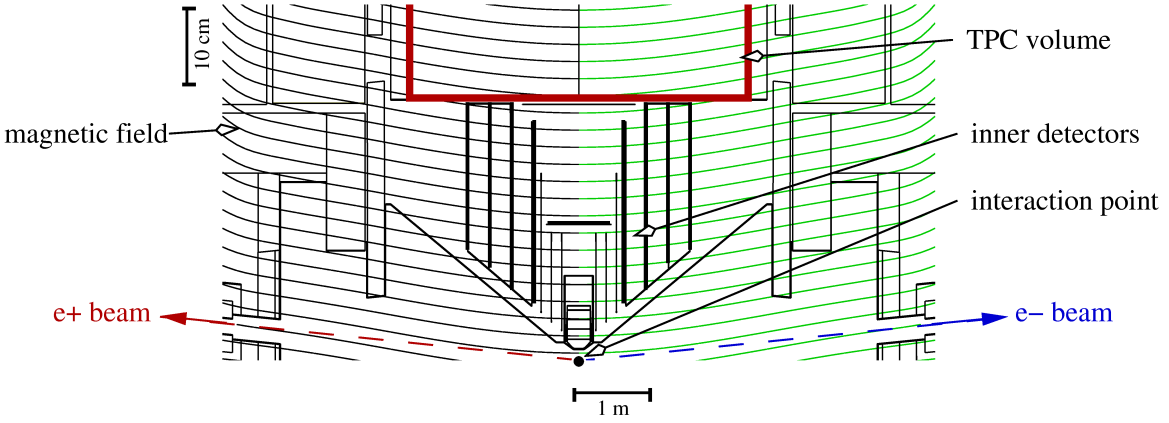

Figure 2.10: *Magnetic field in the ILD detector (1:10)* (modified from [36])

Short Summary - Development Studies for the ILD

The particle flow reconstruction heavily depends on the tracking systems of the ILD detector. In the development phase for the ILD, established detector technologies need to be developed further and their performances have to be improved significantly to meet the desired design goals.

This thesis presents two studies which are closely related to the tracking system and in particular to the main tracker - the TPC. In the following part II, the development and construction of a large TPC prototype is presented. Such prototypes are an essential infrastructure for the development of TPC readout structures, which are able to meet the 100-μm resolution design goal. In addition they are an appropriate test for the construction of the final ILD TPC. In particular the reduction of the material budget to the aspired design goal of 1 % of a radiation length per wall requires an optimisation of the TPC structure.

In part III, a measurement with the ILD detector is discussed in a simulation study, which heavily depends on the tracking performance. In this measurement, pions with energies between 0 and 43 GeV need to be detected and reconstructed efficiently. The analysis yields a result for the possible accuracy of the physics observable - in this case the degree of polarisation of τ-leptons - if the ILD is able to satisfy the desired performance goals. Moreover, it is possible to estimate the impact of changes in the detector layout on the measurement accuracy.

Part II
A Large TPC Prototype

The concept of the Time Projection Chamber (TPC) was first proposed by D.R. Nygren in 1975 [37] and was established for the first time at the PEP-4 collider at Standford (e.g. [38]). TPCs have been and are running in a variety of high energy-physics detectors, ranging from ion beam experiments with high multiplicity events [39] to detectors of low rate neutrino experiments [40]. One example is the TPC of the ALEPH experiment [41], which took data from 1989 until 2000 at LEP.

TPCs are used in collider experiments because of their quasi continuous tracking capabilities. Their measurements are free from ambiguities even in high multiplicity events. Furthermore, a TPC accounts for a moderate material budget. These features make a TPC the optimal main tracking detector for the particle flow concept and, as such, for the ILD detector. However, the ILD requirements on its TPC (see section 2.3.2) exceed anything accomplished with standard technology so far. Substantial improvements are needed to meet the ILD TPC design goals, in particular of the TPC readout technologies.

A traditional TPC readout is based on thin wires clamped parallel to each other with distances of a few millimetres (Multi Wire Proportional Chambers, MWPC) [42] above a so-called pad plane (see section 3). Due to the electrostatic forces, the wires cannot be placed closer and must be held under tension. Hence a stable support structure is needed which increases the material budget of the TPC. Moreover, the finite distance of the wires influences the achievable resolution.

Currently, new readout structures are under study as a replacement for the MWPCs. They are called Micro Pattern Gaseous Detectors (MPGD). During the last few years, different research groups have constructed small TPC prototypes with diameters of about 30 cm and operated MPGD structures on $10 \times 10\,\mathrm{cm}^2$ surfaces. Many operational studies show that a point resolution of $100\,\mu\mathrm{m}$ can be achieved with a MPGD readout, at least on the small surfaces. The next research and development (R&D) step intends to set up and test MPGD structures on larger surfaces, together with adapted readout electronics. As an infrastructure for this R&D work, a Large TPC Prototype (LP) has been constructed for this thesis. The LP has an usable inner diameter of 72 cm.

The following chapter 3 introduces the basic TPC principles and chapter 4 reflects on the status of the R&D for the ILD TPC. This thesis documents the construction of the major part of the LP, the so-called field cage. Chapter 5 discusses preparatory studies to optimise the design plans, and chapter 6 covers the construction and results of quality assurance measurements of the field cage.

3 The Working Principle of a TPC

A Time Projection Chamber (TPC) is a so-called gaseous drift chamber. Gaseous detectors (e.g. [43]) register the electrons which are released by ionisation when an energetic charged particle traverses a gas volume. In a drift chamber the electron drift times are measured in addition and used to reconstruct space points along the initial charged particle's trajectory. The first section of this chapter explains how this principle is realised in a TPC. In addition, the main components of a TPC setup are presented.

In a TPC, electrons drift over distances of up to some metres and physics processes are relevant for the TPC which dominate the stationary drift of electron charge clouds in the gas. These are explained in section 3.2.

Finally section 3.3 discusses how a TPC is installed in a detector at a collider and compares its properties to an alternative tracking detector, namely a silicon tracker.

3.1 TPC Principle

The sensitive gas volume of a TPC is located between an anode and a cathode surface which are aligned parallel. These electrodes span an electric field of some $100\,{}^{V}/_{\mathrm{cm}}$ in the gas. The anode surface is divided in conductive segments, so-called pads, which are made for example from gold plated copper. In the recent prototype studies, rectangular pads have been used with sizes of $4 - 21\,\mathrm{mm}^2$. Each pad is connected to a channel of a readout electronic.

Figure 3.1 illustrates the TPC measurement principle. When a highly energetic charged particle crosses the gas, it produces gas ionisation along its trajectory. This initial particle typically has a velocity close to the speed of light and is much faster than the released electrons. Driven by the electric field, the electrons separate from the gas ions and drift towards the pad plane. This means that the electric field shifts an image of the trajectory to the readout - in the best case without any deformations.

Directly in front of the pad plane, the electrons are multiplied in the amplification structures. The amplification is necessary because an initial particle creates only about 90 electron ion pairs per centimetre. The ionisation yield depends on the particle species, the particle momentum (see below) and the gas mixture, but it is in any case too small to produce sufficiently strong signals on the pad plane.

Finally, a signal density distribution is measured which represents a projection of the trajectory onto the pad plane. For the full three-dimensional reconstruction, also z-coordinates have to be known. They are calculated from the electron drift velocity

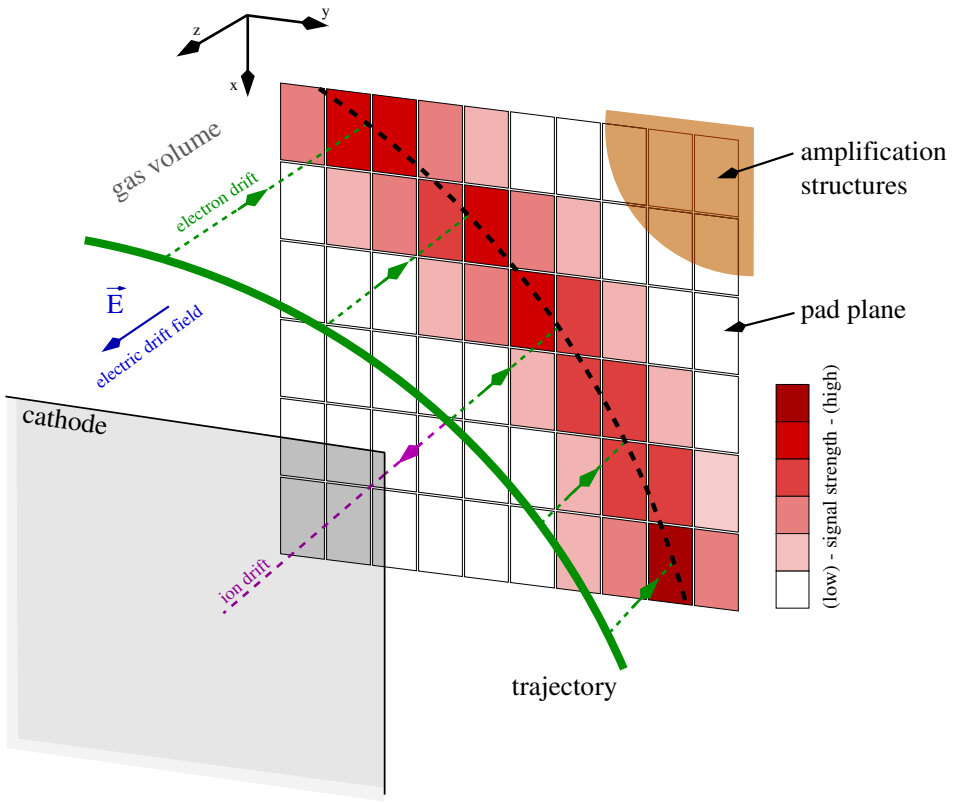

Figure 3.1: *Basic working principle of a TPC*

in the gas v_{drift} and the drift time t_{drift}:

$$z = v_{\text{drift}}\, t_{\text{d}} = v_{\text{drift}}(t_0 - t_1).$$

When the initial particle crosses the volume, it is registered by an external trigger. This event starts a clock and marks the point t_0 in time. The clock runs until the electrons arrive on the pads, which defines the point t_1. The measured time difference is the drift time t_{drift}. Typical electron drift velocities are of the order $5\,\text{cm}/\mu\text{s}$ and hence t_{drift} is in the range of some $20\,\mu\text{s}$ for drift lengths of about one metre. Ions drift about a factor of 1000 more slowely. They are not useful for the measurement and are collected on the cathode.

In the analysis, a computer algorithm reconstructs the trajectory from the signal distributions on the pads and the corresponding drift times.

3.1.1 TPC Setup and Amplification Devices

The basic TPC principle can be realised in different detector geometries. A common setup is illustrated in figure 3.2, which is also the standard layout for the prototypes that are used for R&D work and as such the basic layout of the Large Prototype. Here, the TPC is realised as a cylinder with one end cap being the cathode and the other

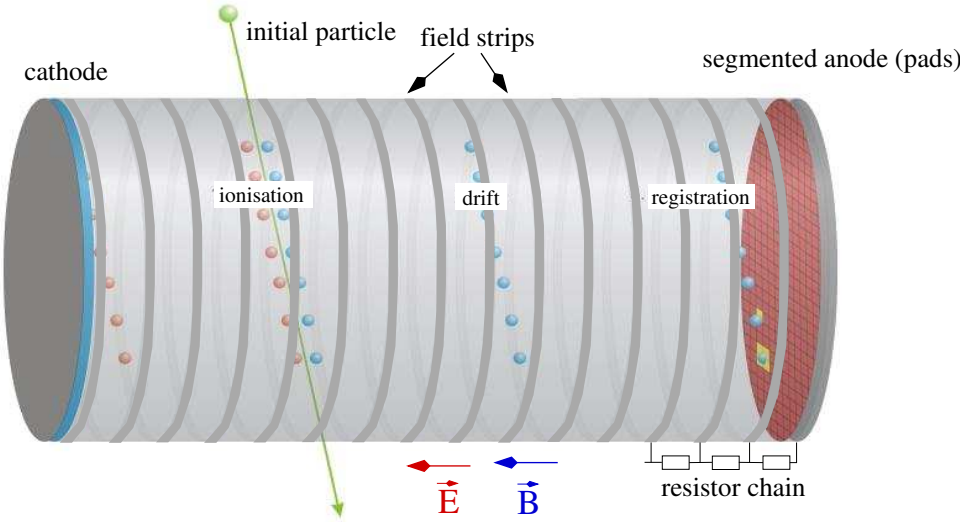

Figure 3.2: *Layout of a cylindrical TPC* (modified from [44])

serving as instrumented anode with the amplification devices and the pad plane. The cylinder is called field cage and contains the detector gas.

Inside the field cage, the electric drift field is spanned and commonly a TPC is operated with a magnetic field parallel to the electric one. As stated in section 2.1.2 this is needed for a momentum measurement. Moreover, it is also beneficial for the TPC operation and the following discussion refers to the according benefits.

The Field Cage

The homogeneity of the electric field is one of the most crucial parameters for the resolution of a TPC. To guarantee the field homogeneity in the TPC volume, conductive rings are attached to the inside wall of the field cage, so-called field strips. Their introduction is motivated in the following with figure 3.3.

Figure 3.3(a) shows the electric potential on a plane cut through a simplified TPC. This TPC consists only of an anode and a cathode. The cathode lies on a potential U_0 and the anode on a bias voltage of $0.2 \cdot U_0$, which is needed for the amplification devices. The drift field is rather inhomogeneous since the equipotential surfaces are not parallel to anode and cathode surfaces and, moreover, the field leaks out of the walls of the field cage. Outside it could disturb surrounding devices and thus the leakage must be suppressed.

A grounded shielding layer on the outside of the barrel provides the confinement for the field. Figure 3.3(b) depicts the potential distribution of the modified TPC setup. Here the electric field is contained, but its homogeneity is worse compared to figure 3.3(a). The shielding layer has a higher potential than the anode and attracts the drifting electrons more strongly. If no magnetic field is present, the electrons follow the potential gradient and many end up on the inner field cage wall.

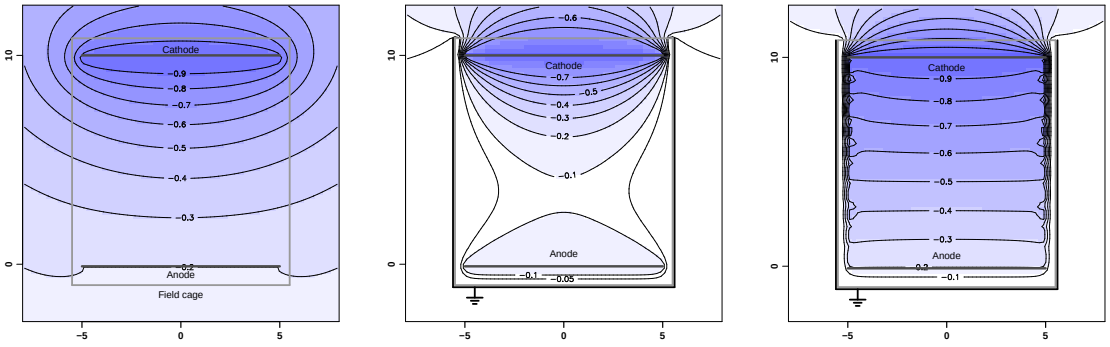

(a) TPC consisting only of anode and cathode

(b) TPC with additional shielding layer

(c) TPC with shielding layer and field strips

Figure 3.3: *Electric potential distributions for simplified TPC models*

The introduction of field strips allows for a recovery of the electric field homogeneity. The strips are equally wide and equidistant, as sketched in figure 3.2. They are interconnected by a resistor chain which applies them with stepwise descending potentials. This way, the field strips provide an almost linear decreasing electric potential along the inside wall, which is an improved boundary condition for the electric field. Figure 3.3(c) illustrates the electric potential for the setup with additional field strips. Here, the equipotential surfaces are almost parallel to the end plates all over the sensitive volume and the field is homogeneous.

This field strip layout can still be improved, and this is one central aspect for the optimisation of the Large TPC Prototype. Detailed in-depth studies are presented in chapter 5.2.

3.1.2 Amplification Devices

A traditional MWPC amplification structure is illustrated schematically in figure 3.4. Here, two types of wires are installed in front of the pads - the sense wires are held on a positive potential compared to the field wires. Drifting electrons are attracted by the sense wires and multiplied in an avalanche close to the wire surface. The electrons are quickly collected by the wire and the sudden appearance of an ion cloud induces signals on the underlying pads. Both the direct electron signal on the wire and the induction signals on the pads are registered.

This technique worked robustly, for example in the ALEPH chamber, but has some major drawbacks which make it unattractive for usage in a detector at the ILC:

- The wires apply electrostatic forces on each other because they are on different potentials. Thus they have to be tightened with high tension to reduce deflections. This requires stable structures which increase the material budget.

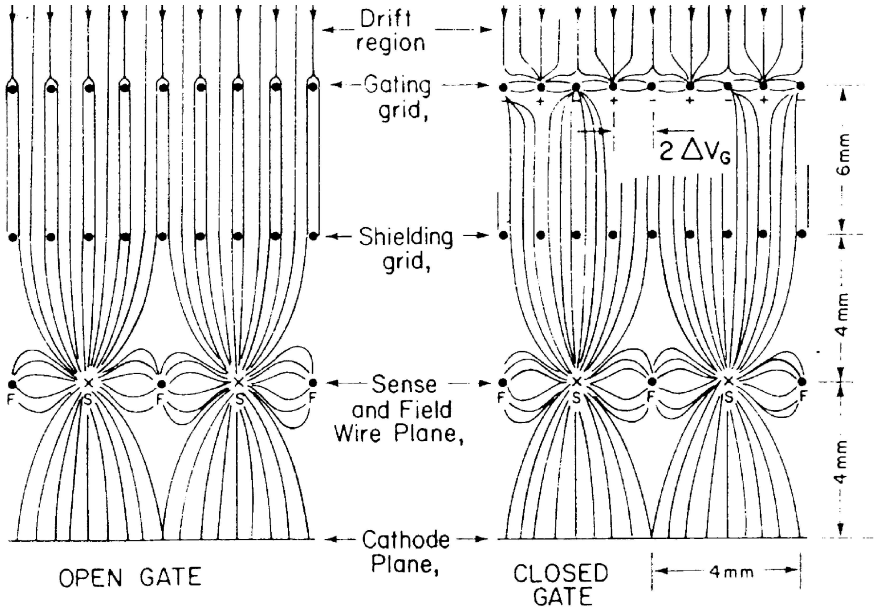

Figure 3.4: *MWPC amplification structure with ion gate to catch back-drifting ions* [45, 46]

- The ions created in the avalanche at the wire can directly drift back into the sensitive volume of the TPC. There they disturb the drifting electrons coming from subsequent trajectories to be read out. Thus the ions need to be caught with an additional gating grid (see figure 3.4), which makes the setup as a whole more complicated.

- The wires distort the electrical field in front of the pad plane, which causes $\vec{E} \times \vec{B}$ effects (see below) that limit the achievable resolution.

Micro Pattern Gas Detectors (MPGDs) provide the prospect to solve the problems of the MWPC technique. Among them are Gas Electron Multipliers (GEMs) [48] and MicroMEGAS [49].

A standard GEM[1] consists of a 50-μm-thick polyimide carrier foil which is covered on both sides with 5-μm-thick copper layers. This foil is perforated with a hexagonal hole pattern, as shown in figure 3.5(a). The holes have a diameter of 70 μm and a pitch of 140 μm.

Operated in a TPC, the GEM is installed some millimetres in front of the pads. Then a voltage of some hundred volts is applied between the copper layers, which produces a strong electric field in the holes. This is shown in figure 3.5(b). The upper copper layer is directed towards the drift volume. Electrons which arrive from there are pulled into the holes. In the passage through the hole, their number is multiplied by avalanche processes that are induced by the strong electric field.

[1]produced at CERN [47]

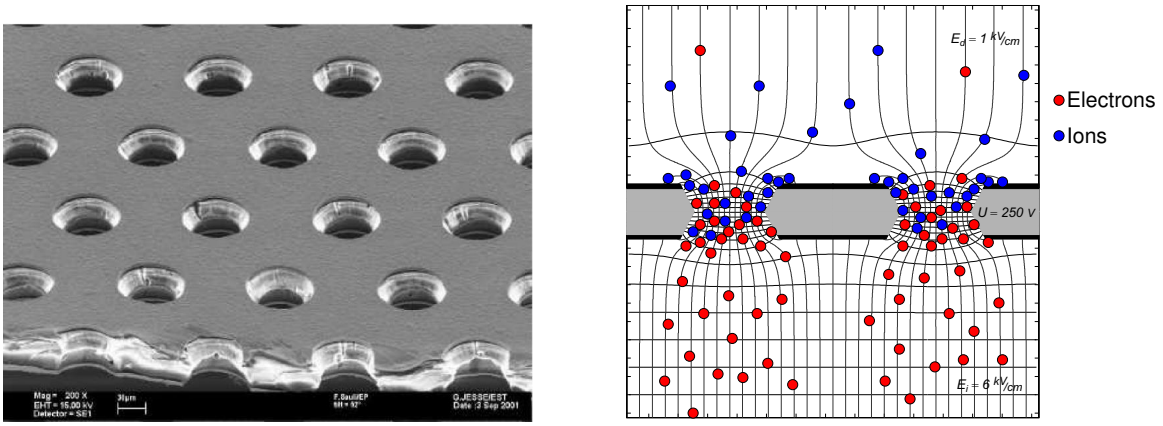

(a) raster electron microscope image of a GEM [47]

(b) electric field in the GEM [15]

Figure 3.5: *Gas Electron Multiplier (GEM) layout*

Also here, ions are created that could drift back into the sensitive volume. However, the GEM has an intrinsic ion back drift suppression which works best if GEMs are operated in multiple layers, for example in a stack of two or even tree GEMs in series. In such a setup, the topmost GEM operates with a moderate amplification and produces only few ions that could drift back. At the same time, most of the ions coming from a lower GEM are caught on the bottom layer of an upper GEM.

Contrary to a MWPC setup, a GEM foil provides a homogeneous surface which reduces $\vec{E} \times \vec{B}$ effects close to the readout. Moreover, the pitch of the holes is an order of magnitude smaller than the distance of the wires in MWPC which allows for an improvement of the resolution. Until today GEMs have been operated successfully in high-energy physics experiments [50] and also in TPC prototypes.

A possible MPGD alternative are the MicroMEGAS, which consist of a very fine mesh placed some 100 μm in front of the pads. The mesh is supported by insulation pillars and applied with a voltage of about 400 V. Here, electrons are multiplied in strong electric field between the mesh and the pads.

3.1.3 Detector Gas

Typically noble gases are used for TPC operation, mostly Argon. These gases require a relative low ionisation energy and are chemically inert. For the operation, the pure gas is enriched with so-called quencher gases in a ratio of about 10 %. The molecules of the additives catch photons that are created in the amplification devices and could ionise other gas molecules and create free electrons. The photon energy is absorbed in rotational and oscillation degrees of freedom of the quencher molecules. In addition, the quencher gases can improve the electron drift properties of the gas, as they influence, for example, the electron drift velocity.

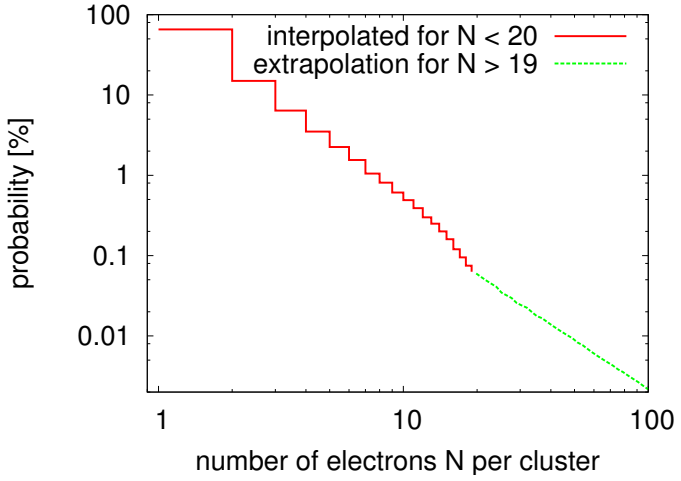

Figure 3.6: *Cluster size distribution for Argon* (according to [51])

			Ar	Ne	Xe
clusters created per centimetre	Λ	[cm^{-1}]	~ 28	12	44
ionisation energy	I	[eV]	15.8	21.6	12.1
avr. energy to create a e^--ion pair	W	[eV]	26.3	36.4	21.9

Table 3.1: *Parameters for gases used in TPCs* (e.g. [43])

3.2 Physics of the Time Projection Chamber

The basic principles of a TPC and the chamber setup are described in the previous section. This section goes into more detail on the main physical principles exploited in a TPC. The discussion follows the measurement procedure, from the signal creation by ionisation, the drift of charge clouds in the detector gas to the readout (see figure 3.2). In addition, one standard reconstruction method is discussed together with the determination of the resolution.

3.2.1 The Ionisation Process

Highly energetic particles ionise a gas in distinct ionisation clusters. Such a cluster is formed when an initial particle interacts with a gas molecule and releases an electron. These encounters are called primary ionisation and are mainly inelastic scattering processes. Frequently the electron from the primary ionisation acquires sufficient energy to ionise further molecules. This produces a larger cluster and is called secondary ionisation.

The cluster distance and cluster size follow along the course of the initial particle follow statistical distribution: The number of ionisation processes n per track length

L is Poisson distributed

$$P(\Lambda, n) = \frac{\Lambda^n}{n!} \cdot e^{-L/\Lambda}.$$

Λ is the average number of clusters created per track length. Numbers for this parameter are given in table 3.1 for different gases.

The cluster sizes follow a cluster size distribution which describes the probability to find a cluster with a certain number of electrons. Such a distribution depends in first place on the gas mixture. As an example figure 3.6 shows the cluster size distribution for ionising particles crossing Argon. Qualitatively the distributions for typical gases used in TPCs have a similar shape.

Most clusters contain only a few electrons and represent a homogeneous ionisation along the trajectory. In this example, 95 % are smaller than ten electrons. Larger clusters have up to a few hundred secondaries and are created when the initial particle transfers a large amount of energy to a single electron. These are called δ-electrons.

According to the cluster size distribution in figure 3.6 in total only 0.25 % of the clusters have a size of 100 electrons or more. These larger clusters appear with an average distance of some 10 cm. Thus the ionisation can look very inhomogeneous on a short piece of a trajectory. To determine a mean cluster size or an averaged ionisation density, a sufficiently long piece of a trajectory - of the order 50 cm - has to be measured.

Energy Loss and Particle Identification

Due to the ionisation processes, the initial particle suffers from a permanent energy loss on its way through the gas volume. The mean energy loss per track length is described by the Bethe-Bloch formula (e.g. [52, 53]):

$$-\frac{\mathrm{d}E}{\mathrm{d}x} = 4\pi\, N_\mathrm{A}\, r_\mathrm{e}^2\, m_\mathrm{e}\, c^2\, z^2\, \frac{Z}{A}\, \frac{1}{\beta^2} \left[\ln\left(\frac{2 m_\mathrm{e}\, c^2\, \gamma^2\, \beta^2}{I} \right) - \beta^2 - \frac{\delta}{2} \right]. \tag{3.1}$$

- $^{\mathrm{d}E}/_{\mathrm{d}x}$ - energy loss per distance
- N_A - Avogadro constant
- z - charge of the incident particle in units of the electron charge
- m_e - mass of the electron
- r_e^2 - the classical electron radius
- Z, A - charge and mass of the gas atoms
- I - Ionisation energy of the detector gas
- β and γ - Lorentz factors for the particle
- c - speed of light
- δ - parameter of the Fermi density and the shell correction

In this form, the Bethe-Bloch formula is valid for all charged particles heavier than the electron. In the derivation of the formula, the binding energy of the electrons in the gas molecules is neglected and it is assumed that the gas molecules are at rest.

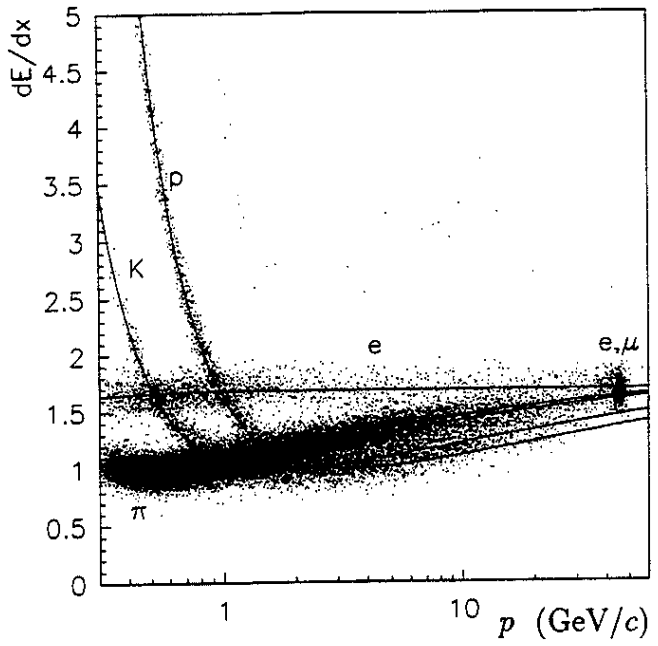

Figure 3.7: *Measured energy loss of charged particles in the ALEPH TPC with appropriated curves calculated with the Bethe-Bloch formula* [32]

Figure 3.7 shows the mean energy loss for different particle species as a function of particle momentum. Overlaid are according measurement points. A particle with $\beta\gamma \approx 3-4$ deposits a minimum of energy per unit length and is therefore called minimal ionising particle. For higher momenta, the energy loss rises logarithmically whereas for slower particles it increases with $1/\beta^2$.

The Bethe-Bloch formula offers a possibility to identify a particle that produced a trajectory in a TPC. For this purpose, the particle's specific energy loss is determined from the produced number of electrons n_t released per unit length. This number, n_t, cannot be measured directly but it can be determined from the measurements of the trajectory on the pad plane.

With n_t at hand, the specific energy loss of the primary particle is calculated by:

$$n_\mathrm{t} = \frac{1}{W}\int_{l_0}^{l_0+l} \frac{\mathrm{d}E}{\mathrm{d}x}\,\mathrm{d}x \quad \rightarrow \quad \frac{\mathrm{d}E}{\mathrm{d}x} = \frac{n_\mathrm{t}\cdot W}{l}.$$

Here l is the length of the measured trajectory and W the mean energy necessary to produce an electron-ion pair in the gas. The latter has a value higher than the ionisation energy of a gas molecule I because tighter bound electrons in deeper shells of the gas atoms are released as likely as electrons from the upper shells. In addition, the free electrons gain kinetic energy in the ionisation process. Numbers for W and I are listed in table 3.1 for different gases.

In parallel to the energy loss also the momentum of a particle is measured in a particle detector. In their combination, both measurements can be used to compare

the measured energy loss to a prediction coming from the Bethe-Bloch formula, which allows for a identification of the particle. The data points in figure 3.7 demonstrates this measurement. Here, the measurement points are focused on the curves for certain particle species in certain momentum ranges and especially low momentum protons and kaons can be identified robustly.

3.2.2 Drift of Electrons in Gases

After an electron cluster has been created in the gas, the individual free electrons start to drift independently and in an undisturbed way between between the gas molecules. However, like the initial particle, they also interact with the gas molecules. In such an encounter an electron gets a new direction of flight and the electric forces re-accelerate it towards the anode. Thus the individual electrons drift on zigzag courses and only the average motion of a cluster can be described analytically.

Drift of the Centre of Gravity

The drift velocity of a cluster's centre of gravity v_{drift} is described by the Langevin equation [54]:

$$m_{\text{e}} \frac{\mathrm{d}\vec{v}_{\text{drift}}}{\mathrm{d}t} = e\vec{E} + e(\vec{v}_{\text{drift}} \times \vec{B}) + \vec{Q}(t). \tag{3.2}$$

The change of $\vec{v}_{\text{drift}}$ is dominated by the local electric drift field $\vec{E}$ and an additional magnetic field $\vec{B}$. The time dependent term $\vec{Q}(t)$ describes the average scattering of the electrons with the gas molecules.

The Langevin equation has the stationary solution

$$\vec{v}_{\text{drift}} = \mu\vec{E} + \tau\vec{v}_{\text{drift}} \times \vec{\omega} \tag{3.3}$$

which is valid if the fields are constant on scales of the mean free path of an electron in the gas. Here τ is the associated mean time between two encounters, $\mu = {}^{e\tau}/_{m}$ is called electron mobility and $\vec{\omega} = {}^{e\vec{B}}/_{m}$ is the cyclotron frequency.

Rearranging (3.3) for $\vec{v}_{\text{drift}}$, one finds

$$\vec{v}_{\text{drift}} = \frac{\mu E}{1 + (\omega\tau)^2} \left[\hat{E} + \omega\tau\hat{E} \times \hat{B} + (\omega\tau)^2(\hat{B} \cdot \hat{E}) \cdot \hat{B}\right] \tag{3.4}$$

with $\hat{E}$ and $\hat{B}$ being unit vectors along $\vec{E}$ and $\vec{B}$. A TPC is typically operated with both fields aligned perpendicular to the pad plane. Then the term $\vec{E} \times \vec{B}$ vanishes and the absolute value of the drift velocity $\vec{v}_{\text{drift}}$ takes the simple form

$$v_{\text{drift}} = \mu E \qquad \text{if} \qquad \vec{E} \times \vec{B} = \vec{0}.$$

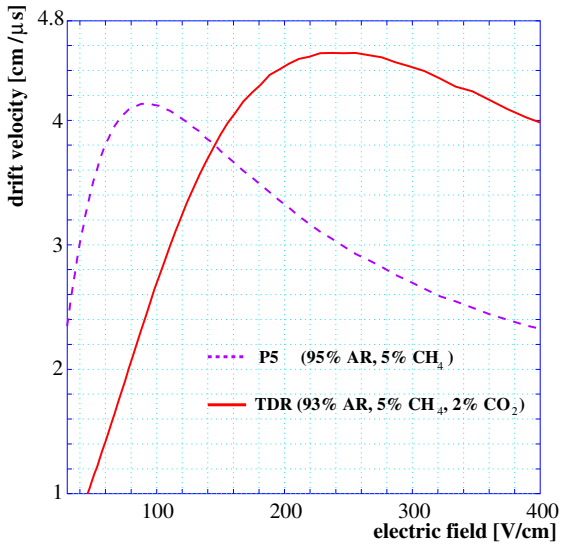

Figure 3.8: *Simulated drift velocity in dependence of the electric drift field strength for two gases* [55]

Otherwise, it yields

$$\begin{aligned} v_{\text{drift}} &= \frac{\mu E}{1+(\omega\tau)^2}\sqrt{1+(1+\cos^2\alpha)\cdot(\omega\tau)^2+(\omega\tau)^4\cdot\cos^2\alpha} \\ &\approx \frac{\mu E}{1+(\omega\tau)^2}\cdot(1+(\omega\tau)^2\cdot|\cos\alpha|) \end{aligned}$$

with α being the angle between $\vec{E}$ and $\vec{B}$, or $|\cos\alpha| = |\hat{B}\cdot\hat{E}|$. The approximation is correct within a few percent for angles $\alpha \lesssim 45\,\text{deg}$.

Via μ, the drift velocity depends also on gas composition, the gas pressure, the water content and other gas parameters. As an example, figure 3.8 depicts $v_{\text{drift}} = \mu \cdot E$ versus E for two gases. The optimal working point for a TPC is in the maximum of $v_{\text{drift}}(E)$, which is in the range of $\approx 90 - 240\,{}^{V}/_{\text{cm}}$ for most gas mixtures. In the maximum ${}^{\partial\mu(E)}/_{\partial E}$ is small and $\vec{v}_{\text{drift}}$ stays constant if the field strength E fluctuates in a small range. Such fluctuations cannot be avoided under realistic operation conditions.

Besides having a constant drift speed, the clusters should drift parallel to $\vec{E}$. This is the case if the chamber is operated without magnetic field or if $\vec{B}$ and $\vec{E}$ are collinear, that means parallel or anti parallel:

$$\vec{v}_{\text{drift}} = \mu\vec{E} \quad \text{for} \quad \vec{B}=0 \quad \text{or} \quad \vec{B}\uparrow\uparrow\vec{E} \quad \text{or} \quad \vec{B}\uparrow\downarrow\vec{E}.$$

If in addition $\vec{E}$ is constant and perpendicular to the readout surface in the whole drift volume, trajectories are projected without distortions onto the readout surface.

In volumes where $\vec{E}$ and $\vec{B}$ are not collinear, the drift velocity has a component in the direction of $\vec{E}\times\vec{B}$. Hence clusters are deflected in this direction and arrive in displaced

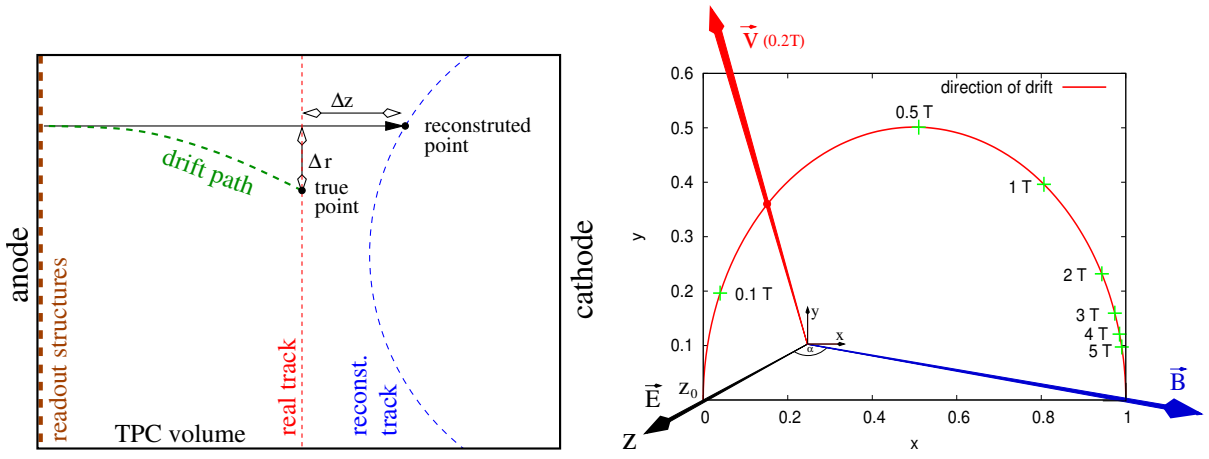

(a) false hit reconstruction

(b) direction of the velocity vector $\vec{v}_{\text{drift}}$

Figure 3.9: *Effect of a non parallel alignment of the $\vec{E}$ and $\vec{B}$ field*

points on the anode, as illustrated in figure 3.9(a). In the consequence their origin is reconstructed at a false position. If many points along a trajectory are displaced, the whole trajectory can be reconstructed inaccurately.

Figure 3.9(b) shows the dependency of $\vec{v}_{\text{drift}}$ on B and and the angle between the fields. In this diagram it is assumed that $\vec{E}$ and $\vec{B}$ include an angle $\delta\alpha \approx \sin\delta\alpha \lesssim 30\,\text{deg}$ in the origin of the coordinate system. $\vec{E}$ is parallel to the z-axis and $\vec{B}$ lies in the z-x plane. The distance between the z-axis and the magnetic field vector at z_0 is set to unity and the curve labelled 'direction of drift' depicts the point where the velocity vector intersects with the y-z plane.

In the optimal case of $\delta\alpha = 0$ or if B vanishes, the intersection point lies on the z-axis. In very strong magnetic fields, the electrons almost follow the magnetic field vector. For the intermediate case $B = 0.2\,\text{T}$ to $5\,\text{T}$, the drift velocity has a significant component in the direction $\vec{E} \times \vec{B}$, parallel to the y axis.

In the reconstruction it is possible to apply a correction which compensates for $\vec{E} \times \vec{B}$ effects. For this, the magnetic field has to be measured accurately and $\mu(E)$ of the gas needs to be known. The electric field however cannot be measured, because a measuring device would by itself modify the field. Thus the TPC setup has to guarantee a sufficient electric field homogeneity by design. The evaluation of a correction algorithm and a requirement on the field homogeneity are discussed in [56].

Diffusion

Overlaid to the average motion of the cluster is a random diffusive movement which broadens the charge cloud. The diffusion is caused by the mentioned interaction of the electrons with the gas and the initial energy they gain in the ionisation process.

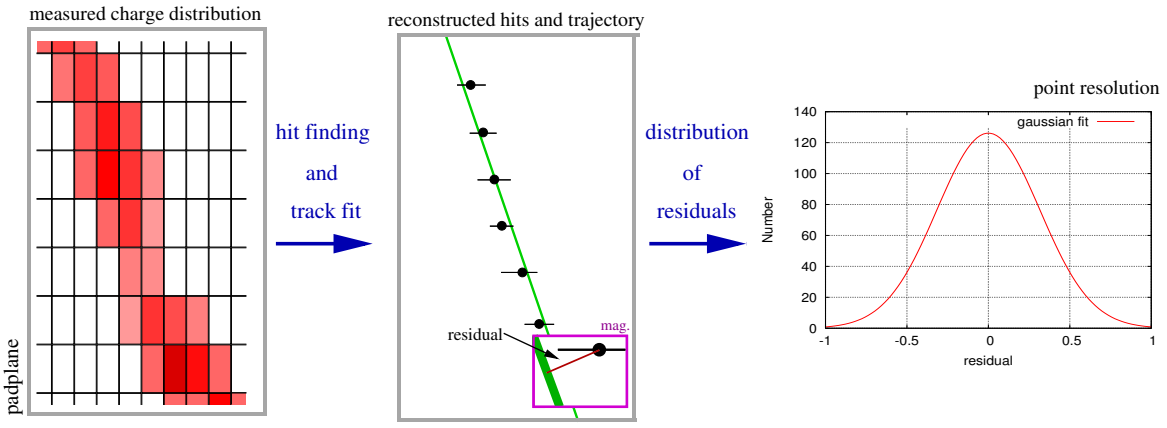

Figure 3.10: *Track reconstruction and determination of the single point resolution*

If a cluster is point-like when it is created, it adopts Gaussian shape after a certain drift length. The width σ of this Gaussian depends on the gas and is described by a diffusion coefficient D

$$\sigma^2 = D^2 \cdot z.$$

Here z is the drift distance. Typical values for D are in the range of $0.005 - 0.08\,\sqrt{\text{cm}}$. If a magnetic field is present in the TPC volume, aligned parallel to the electric field, it reduces the diffusion perpendicular to the direction of drift. The electrons spiral around the magnetic field lines and their transversal movement is suppressed. The suppression factor is $1/(1+\omega^2\tau^2)$.

3.2.3 Track Reconstruction and Resolution

Trajectories, which have been measured in a TPC, can be reconstructed using different approaches (e.g. [57]). A standard method is a χ^2 fit which is presented here and referred to in the following.

Figure 3.10 illustrates the reconstruction procedure and the subsequent method to calculate the resolution. At the beginning, a computer algorithm[2] searches for charge accumulations in the measurements for each row of the pad plane. Then it calculates the respective centres of gravity with their uncertainties. The MPGD amplification structures spread the charge homogeneously over several pads and hence the mean values of charge accumulations can be determined significantly more precisely than the pad width. For each accumulation also a z component is calculated from the drift time measurement. The result is a space point in the TPC volume, which is called a hit. When all hits are reconstructed, a trajectory reconstruction algorithm groups them to together to form trajectories. Finally, a χ^2 fit of an analytic curve to the combined points is performed.

[2]for example MultiFit [57]

The resolution is typically given in two numbers, namely a resolution in the transversal plane parallel to the pad plane ($\sigma_\perp$) and in direction of drift (σ_z). In the following, the calculation of $\sigma_\perp$ is discussed, σ_z can be determined in an analogue way. For this, the distances are calculated between the reconstructed points to the fitted trajectory on the pad plane, as illustrated in figure 3.10. The distribution of these residuals is a Gaussian and $\sigma_\perp$ is defined as its standard deviation. Here it is assumed that enough hits are reconstructed along a trajectory, so that the fit result is stable even if a single hit is left out. This requirement is fulfilled for about 20 points and will be reached in the LP. The resolution $\sigma_\perp$ depends on the drift length z of the clusters and can be parametrised by

$$\sigma_\perp(z) = \sqrt{\sigma_0^2 + D_\mathrm{T}^2 \cdot z}$$

The contribution σ_0^2 defines a lower limit for the achievable resolution which is caused by the physics of the exploited processes and the readout setup, like the pad size. The second term, $D_\mathrm{T}^2 \cdot z$, describes a linear rise with the drift distance, due to the transverse diffusion. As stated, this can be suppressed by a magnetic field.

To give an example, within simulation studies for the ILD detector $\sigma_\perp$ has been parametrised by [4]

$$\sigma^2_{\perp,\mathrm{ILD\ sim.}} \,/\, [\mu\mathrm{m}^2] = 50^2 + 455 \,/\, (B[\mathrm{T}])^2 \cdot z\,[\mathrm{cm}]\, \sin\Theta + 900^2 \sin\phi$$

Here σ_0 is 50 μm and $D_\mathrm{T} = {}^{455}/_{B[\mathrm{T}]}$. The angle Θ is the trajectory angle with respect to the axis perpendicular to the pad rows, while the angle ϕ is the angle between the trajectory and the pad rows. This parametrisation is motivated by resolution measurements performed in smaller TPC prototypes which are discussed in the next chapter.

The ILD TPC has a 2.15-m-long drift distance and is operated in a 3.5-T magnetic field. In the simulation $\sigma_\perp$ reaches 102 μm for $\theta = 0$ and $\phi = 0$ which is the aspired limit.

3.3 A TPC operated in a Collider Experiment

A TPC for a collider experiment is adapted to the overall detector layout. Thus it has a more sophisticated shape than described previously. Figure 3.11 illustrates the setup. The field cage is again cylindrical, but intersected by a tube with the beam pipe and the inner silicon tracking detectors inside. The interaction point (IP) of the beams lies in the centre of this tube. A cathode membrane separates the gas volume, slightly displaced with respect to the IP. With this modification, a charged particle coming from the IP crosses at least one of the two half volumes. Its trajectory is measured on the instrumented anode that belongs to the drift volume. This means that two independent TPCs are operated at the same time. In a standard detector without a beam crossing angle, a magnetic solenoidal field is spanned over the TPC volume to

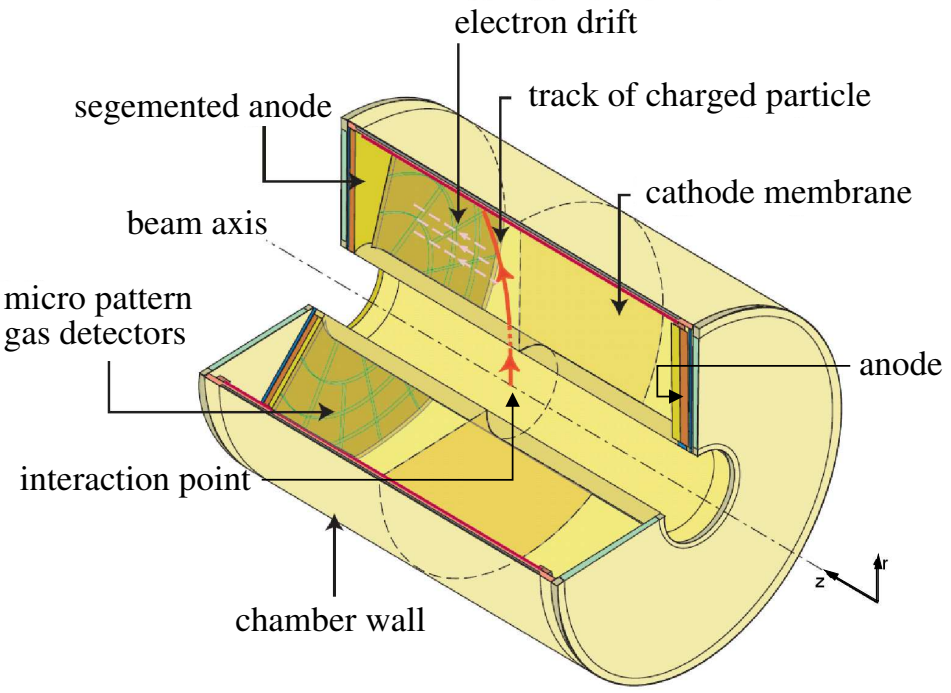

Figure 3.11: *A TPC operated in a collider experiment* (modified from [33])

allow for the momentum measurement. It is parallel to the beam pipe and thus parallel to the electric field.

A TPC measures points with a resolution that is about a factor of ten worse compared to a silicon detector. However, it provides one measurement point per pad-row - in the ILD these are about 200 points compared to about 10 points in the SiD detector. The number of points compensates for the worse point resolution of a single point. An additional benefit of TPCs compared to silicon tracking is the $^{dE}/_{dx}$-measurement, the lower material budget and a more robust pattern recognition. The latter means that points can be combined without ambiguities to trajectories.

One of the major drawbacks of a TPC is its slow readout compared to silicon detectors. The TPC foreseen for the ILD has a drift length of about 2.15 m. The tracks of an event in the TPC can be read out completely in about 35 μs. In this time, the ILC produces some hundred bunch crossings (see figure 2.3). Thus trajectories from the different events are overlaid in the readout and need to be disentangled in the event reconstruction. The time between the bunch trains is used to remove the ions from the drift volume. However, in such high rate environments, the ions cause significant problems. They are not removed during a bunch train and cause space charges that can disturb the electron drift. Therefore it is mandatory to assure that the amplification structures suppress the ion back drift efficiently.

Short Summary - The optimal Field Cage

The construction of the best possible TPC for the ILD detector requires a sophisticated chamber design and a high manufacturing accuracy. To meet the resolution goals, the design of the field cage has to be optimised to achieve the highest possible electric field homogeneity. This requires an optimised layout of the field forming elements, in particular the field strips, and defines stringent requirements to the mechanical accuracy of the field cage. An imperfect alignment, for example, of the anode and cathode surfaces will cause field distortions and possibly spoil the resolution.

At the same time, the chamber walls - especially of the inner tube in a TPC of a collider - should be as lightweight as possible, to reduce the material budget. However, the demand for highest accuracy and lowest material budget are conflictive, because a thin chamber is less stable and could deform under mechanical loads. This could displace the field forming elements.

Besides the optimisation of the readout structures, these design aspects of the field cage have to be studied for the preparation of the ILD TPC. These aspects are also addressed with the development and the construction of the LP which is presented in the chapters 5 and 6.

4 Research and Development towards a TPC at the ILC

Around the year 2000, several research groups started first prospect studies for the application of MPGD readout techniques for a linear collider TPC. At that time MPGDs were a comparably new technique but already used in high energy physics experiments (e.g. [50]). Since then, research and development (R&D) work was carried out in a loose collaboration of the different groups. In 2007, the efforts were officially joined within the Linear Collider TPC collaboration (LC TPC). The new collaboration plans the ongoing R&D towards the construction of the ILD TPC in the first half of the next decade [58]. The commissioning and operation of the Large Prototype is among the first collaborative activities.

The first section of this chapter gives an overview of R&D studies on MPGDs so far. The Large Prototype (LP) is an infrastructure for advanced R&D work which is outlined in section 4.2. These future development studies require an extended test setup and pose certain requirements on the field cage which is discussed in section 4.3.

4.1 Basic MPGD Studies - Demonstration Phase

The R&D research activities on MPGDs began with a variety of basic studies. The primary goal was to gain experience with the new techniques and to demonstrate that they offer a substantial improvement compared to MWPCs. This included for example GEM ion back drift suppression measurements which have been performed in small test chambers (e.g. [59, 60]). In the following, different pad designs and gas mixtures have been tested and many basic operational parameters have been investigated, like GEM voltage settings and its connection to the amplification (e.g. [61]).

The first major milestone was to demonstrate that it is possible to reach a resolution of $100\,\mu$m over a significant drift length of about a metre. For this, appropriate TPC prototypes have been constructed, to operate readout surfaces of about $10 \times 10\,\mathrm{cm}^2$. Major efforts also went into the development of software reconstruction tools.

In this context, the MediTPC has been set up at the Deutsches Elektronen Synchrotron (DESY) [55]. This prototype has been operated with pad planes that have $2{\times}6$-cm^2-large pads in six rows in magnetic fields. With this setup, a resolution of $\sigma_\perp \lesssim 100\,\mu$m was measured, but only for tracks created very close in front of the GEM (e.g. [57]). The resolution was limited by the width of the pads.

A new readout setup has been developed in the scope of this thesis. This includes

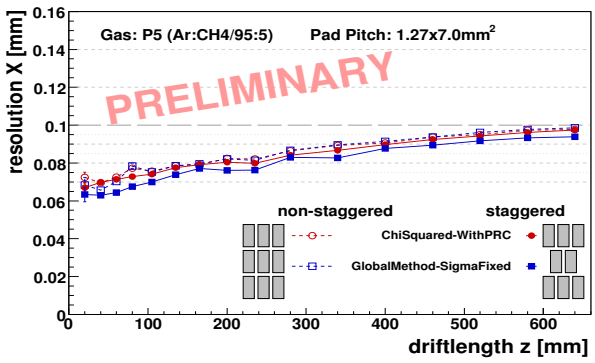

(a) single point resolution measured with the MediTPC [62]

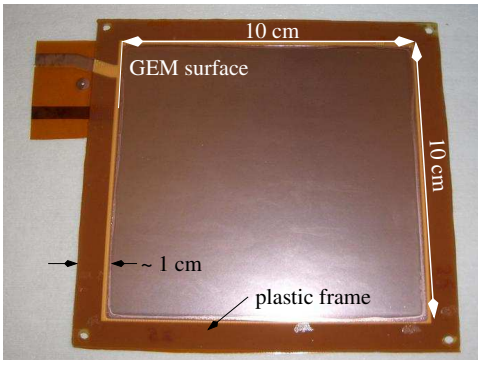

(b) image of a GEM type operated in the MediTPC

Figure 4.1: *Results of MediTPC studies*

two new pad planes with 1.27 mm × 7 mm large pads arranged in eleven rows and 48 columns. Figure 4.1(a) shows a resolution plot for MediTPC measurements performed in 2008 with these new readout structures. The resolution shows the expected $\sqrt{\sigma_0^2 + D \cdot z}$ dependence (see section 3.2.3), while it stays below the aspired value of 100 μm over the whole drift length. For this measurement, the MediTPC was operated with a triple GEM structure and two different pad planes: one has the pads arranged non-staggered, a second in a staggered design, as illustrated in the figure. The data has been analysed with two reconstruction techniques. The 'ChiSquared' method is discussed in section 3.2.3. An alternative approach is called 'GlobalFitMethod'. However, the measured resolution curves have a very similar shape, independent of pad layout and underlying reconstruction algorithm. Thus, the operation and reconstruction techniques are considered as very robust, also because comparable studies by various other groups came to similar conclusions (e.g. [63, 64]). In summary, these results confirmed that MPGDs are a well suited readout technique for a TPC at a future ILC detector.

Another field of prototype studies has been the mechanical construction of the chamber. In the focus were the minimisation of the field cage's radiation length. Like other prototypes of similar size (e.g. [65]), the MediTPC has been constructed from lightweight composite materials with a low radiation length.

These preparatory research efforts are summarised as 'Demonstration Phase'.

4.2 Motivation for the Large Prototype - Consolidation Phase

In the next step, the research work is planned to focus on technical realisation of large-scale MPGD readout structures and preparations for the TPC operation in the ILC environment. The main questions under study are:

- How could a GEM or MicroMEGAS readout structure be constructed that covers the end plate of the ILD TPC ($\mathcal{O}(10\,\mathrm{m}^2)$) homogeneously and with as little dead area as possible?

- How can appropriate electronics be designed to read out several thousand channels on the end plate?

- How can the TPC be operated in slightly inhomogeneous magnetic field configurations?

- How can the material budget of the field cage and the end plate of the ILD TPC kept minimal, including the readout electronics?

The LP is planned as an infrastructure for studies on these questions. Its construction marks the beginning of the so-called 'Consolidation Phase'.

While smaller chambers are still being used for basic studies like gas tests, they are not adequate for the ongoing R&D work. As stated, they offer only a limited readout surface of typically $10\times10\,\mathrm{cm}^2$. Among the first goals is the development of significantly larger readout surfaces than this, which needs designated design studies. Firstly, the amplification structures need to be scaled. In the case of GEMs, this requires a new way to implement them in a detector. The photograph in figure 4.1(b) illustrates how a GEM is supported in the MediTPC. It is mounted in a plastic frame of about 1 cm width. The frame keeps the GEM flat, allows for a simplified handling and a staggering of GEMs in the readout structures. But this support is not suited for larger readout surfaces - if two GEMs are operated side by side, their frames will introduce a sizable dead area. If the size of the GEMs is increased, they have to be supported and stacked differently to ensure the flatness. The Large Prototype offers a sufficiently larger readout surface for investigations on how GEMs can be joint to larger areas. Currently alternative GEM support structures are being studied [34].

In parallel, new and larger pad planes are developed and tested in the LP. The R&D work will aim to reduce the size and the power dissipation of the electronics.

A challenge for a future TPC is the operation environment in the ILD. As stated in section 2.3.3, the magnetic field is planed to be slightly inhomogeneous in the TPC volume and thus not parallel to the electric field. The inevitable $\vec{E}\times\vec{B}$ effects will systematically displace reconstructed hits and can spoil the resolution. Adequate reconstruction algorithms shall correct for these effects and guarantee the aspired resolution in the full TPC volume. They can be supplemented by additional calibration techniques, like laser beams, that produce trajectories at well defined places in the TPC. The correction algorithms and calibration techniques will be developed and tested with the LP.

Finally, in the construction of the LP, materials are used which offer the prospect to reduce the material budget of the field cage walls. Thereby, the experience gained in the construction of the smaller prototype chambers can be tested on a larger scale. In addition, low material budget end plates could be developed and tested with the new

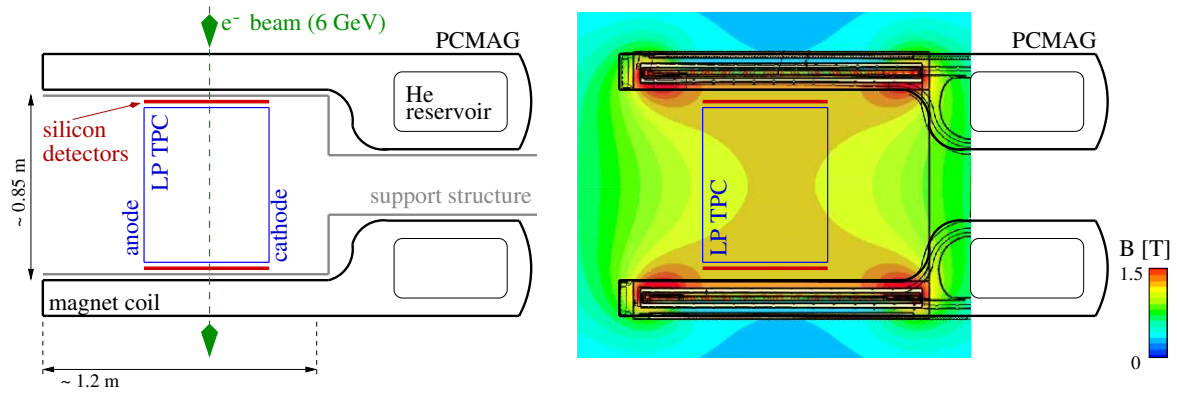

(a) schematic view of the test setup **(b)** magnetic field strength of PCMAG

Figure 4.2: *Large Prototype operated in the PCMAG*

prototype. The cathode plates of the smaller prototypes used to be produced from aluminium. A significant lower material budget end plate could also be produced from composite materials.

4.3 Infrastructure for the Consolidation Phase

The planned R&D programme for the consolidation phase requires a dedicated test setup. For the development of correction algorithms, the LP needs to be operated in an inhomogeneous, but well measured magnetic field [66]. In addition, external reference detectors are mandatory that provide independent points of passing particles. Then it is possible to compare a reconstructed trajectory with the external reference and test the accuracy of the correction.

An appropriate setup has been installed during 2008 in the electron test beam at DESY. It is a part of the EUDET programme [67] that supports infrastructure for detector R&D.

4.3.1 The Magnet Facility at the DESY Electron Test Beam

Figure 4.2(a) sketches the main parts of the EUDET setup. Its main components are a superconducting magnet, called PCMAG, the LP and two layers of silicon detectors. The magnet has a bottle-like shape and offers a cylindrical volume of about 1.2 m length with an inner diameter of 85 cm. It has a lightweight structure and its wall a comparably low material budget. Figure 4.2(b) shows the magnetic field strength distribution of the magnet. The field shown here is the result of a finite element calculation[1]. As the

[1] CST EM-Studio has been used for this calculation

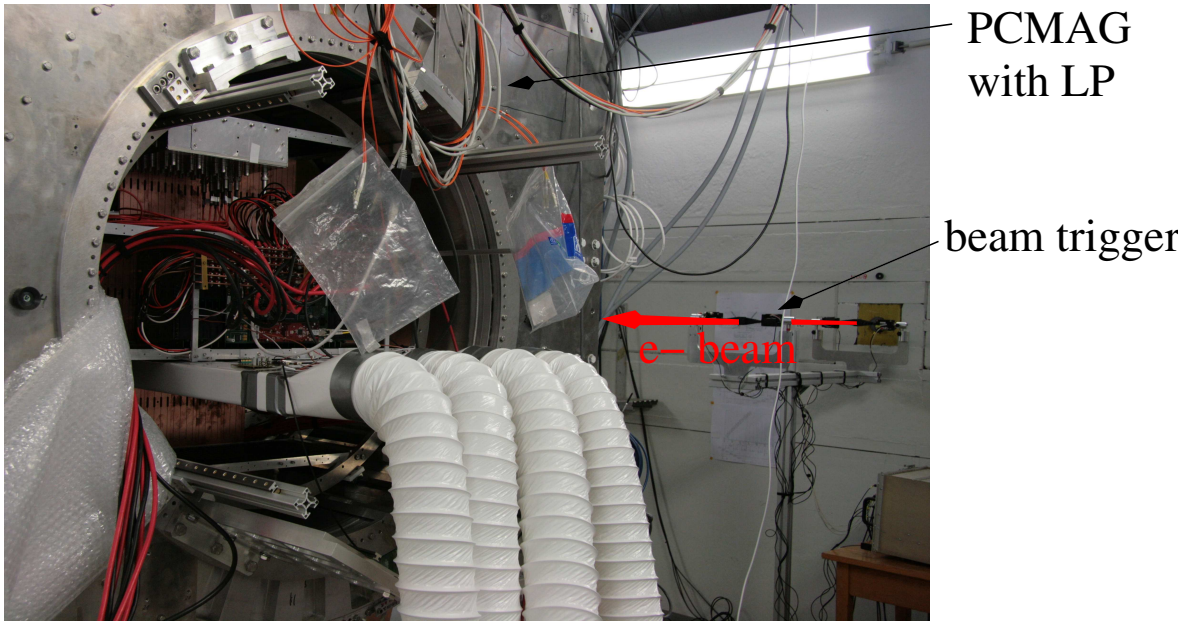

Figure 4.3: *Magnet setup at the DESY electron test beam (July 2009)*

colour coding illustrates, it has a strength of up to 1.2 T in the centre of the magnet and it is slightly inhomogeneous because the magnet is not instrumented with a return yoke. Complementary to the calculation, the field has also been measured in 2007. An analytic description of the field, derived from the measurement, is available for the data analysis [68, 69].

The LP TPC is operated inside PCMAG. The chamber is 61 cm long with an outer diameter of 77 cm. It is supported by a special mounting structure inside the magnet which allows to shift the TPC in different positions. When the chamber is placed in the very centre of the magnet, as sketched in Figure 4.2(b), the field strength varies only by three percent over the sensitive volume. The chamber can also be placed at the entrance or the back of the magnet to perform studies at a higher magnetic field gradient.

Besides the LP, the mounting structure also carries two layers of silicon detectors. They can measure reference space points of test beam particles traversing the TPC with a spatial resolution of better than 20 μm [70].

As sketched in figure 4.2(a), electrons are shot through this setup from the 6-GeV DESY test beam. In the walls of the magnet electrons can undergo scattering processes and get lost from the beam. However, the two silicon detector layers are installed between the outer wall of the LP and the inner surface of the PCMAG and only the LP with the chamber gas inside lies between them. Thus beam electrons could scatter in the LP walls before passing the second silicon detector. The field cage has a low material budget of only 1.24 % of a radiation length per wall (see section 5.5). Hence multiple scattering will be rare enough for a comparison between the reference points and TPC measurement.

Relative to the test beam area, the electron beam has a fixed position. To exploit the full LP volume in any beam configuration, the whole setup is installed on a movable platform. This can lift the magnet in the vertical direction and rotate it horizontally. At the same time, the silicon detectors can be adjusted to different beam positions.

Figure 4.3 depicts a picture of a test beam run in July 2009. Here, the movable platform and the silicon detectors are still missing - they are planned to been added by the end of 2009.

4.3.2 Anode End Plate

The LP consists of two major components: an anode end plate and the field cage with a cathode, whose construction is discussed in the following chapters. A first anode plate was manufactured in parallel to the field cage at the University of Cornell [71]. Figure 4.4(a) shows this part in a schematic view. It is produced from aluminium and has an outer diameter of 770 mm. The seven module windows have a size of about 23 cm × 17 cm and can be equipped with prototype readout devices. Their shape is adapted to a possible modular design of a future TPC end plate in the ILD detector, as sketched in the figure. This modular design offers a high flexibility: it is possible to instrument only a part of the seven windows and to cover the remaining with blind dummy modules. It is also possible to operate different readout techniques in different module windows at the same time.

At the end of 2008, a first test run has been performed with one readout module assembled on the end plate. Figure 4.4(b) shows an image of this setup in the PCMAG.

4.3.3 Requirements to the Field Cage of the Large Prototype

The envisaged R&D programme for the LP and the operation in the EUDET setup define basic requirements to the field cage:

- The electric field inside the chamber has to be homogeneous enough to allow for a point resolution of $\sigma_\perp < 100\,\mu$m. For this, any distortions of the electric field $^{\Delta E}/_{E}$ have to be reduced to the order of about 10^{-4}.

- For the operation of the Large Prototype and with regard to the final TPC, the material budget of the walls should be kept minimal to reduce multiple scattering of electrons in the field cage walls. It should be around the aspired value of $1\%\,X_0$ for the inner tube of the ILD TPC.

- The mechanical structure of the field cage has to be robust enough for the handling in the test beam area.

- The field cage has to allow for operation with various gases and drift fields of up to $350\,^{V}/_{\mathrm{cm}}$.

The requirement for the electric field homogeneity is the most challenging aspect for the design of the field cage, which is discussed in the next chapter. It is derived from a possible correction to cope with the inhomogeneous magnetic field setups. The idea is to correct displacements caused by the $\vec{E} \times \vec{B}$ effects with a correction vector field. If a hit is reconstructed at a biased position $\vec{r}_{\text{reco.}}$, a correction vector is added,

$$\vec{r}_{\text{origin}} = \vec{r}_{\text{reco.}} + \vec{R}_{\text{correct}}(\vec{r}_{\text{reco.}})$$

that shifts it to the corrected position $\vec{r}_{\text{origin}}$. The shifted position complies to the space point where the measured cluster was produced.

A possible method to calculate the correction vector field is proposed in [56]. Its accuracy depends primarily on the precise knowledge of the magnetic field and the homogeneity of the electric field. If the electric field is homogeneous better than $^{\Delta E}/_{E} \lesssim 10^{-4}$, it is possible to determine $\vec{R}_{\text{correct}}$ with an accuracy of $\Delta R_{\perp} < 30\,\mu\text{m}$ in the transversal plane, which is parallel to the pad plane. Thus, the resolution $\sigma_{\perp}$ of a single point would rise to

$$\sigma_{\perp} \rightarrow \sqrt{\sigma_{\perp}^2 + \Delta R_{\perp}^2} \leq 105\,\mu\text{m} \quad \text{for} \quad \sigma_{\perp} = 100\,\mu\text{m}.$$

In this estimation it is assumed that the magnetic field is known significantly better than the achieved homogeneity of the electric field. In addition, $\vec{R}_{\text{correct}}$ will be accurate at least within $^{\Delta E}/_{E} \cdot l \leq 60\,\mu\text{m}$ in the z-direction. Here it is assumed that the drift velocity is directly proportional to the electric field strength. As stated in section 3.2.2, the drift field strength is typically chosen at the maximum of $\mu(E)$. Therefore, the connection between v_{drift} and E is weaker and smaller displacements along z are expected.

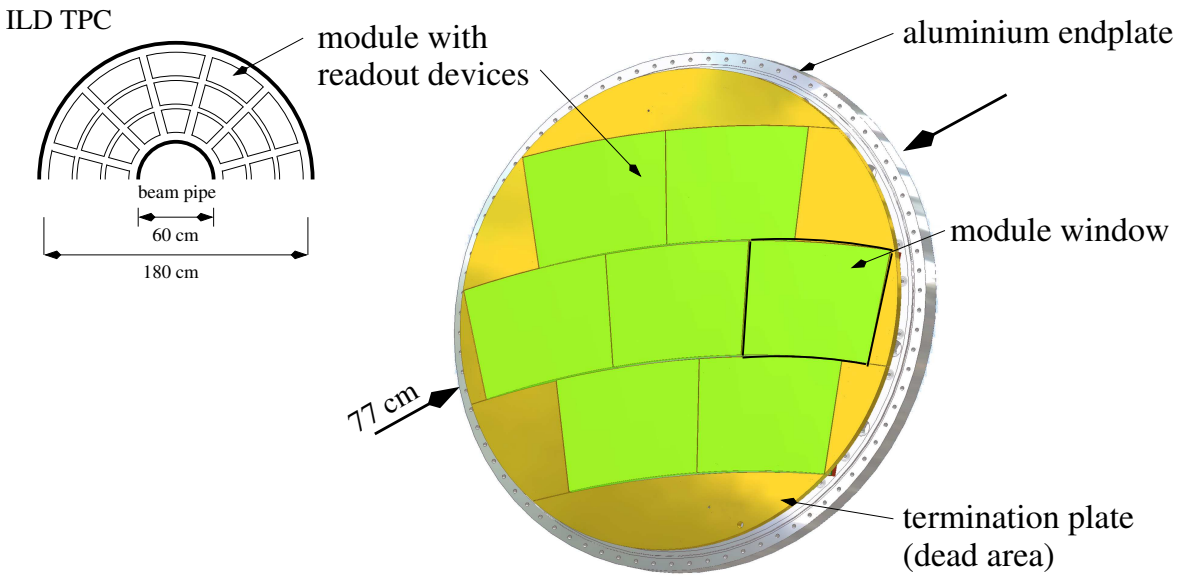

(a) schematic view of the anode end plate (adapted from [71])

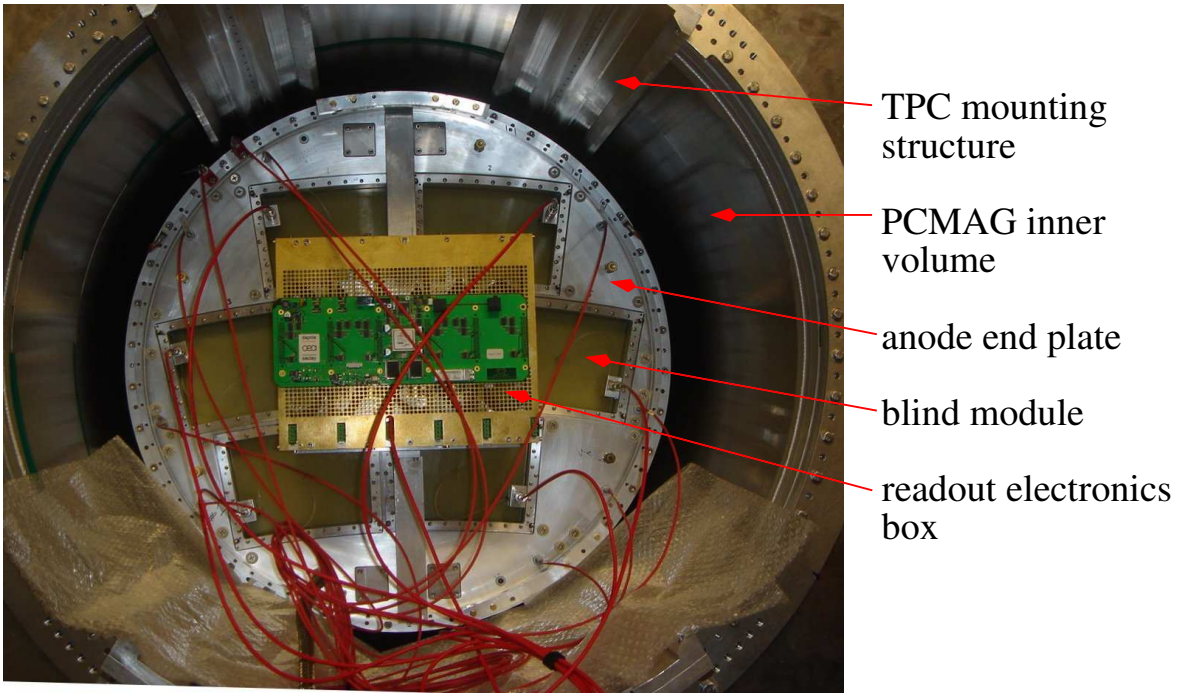

(b) end plate mounted on the field cage in the PCMAG

Figure 4.4: *First anode end plate for the LP*

5 Design Studies for the Field Cage of the Large Prototype

In a design phase the construction plans for the field cage have been optimised with the aim that the Large Prototype (LP) can meet the requirements defined in section 4.3.3. This chapter presents these design studies and the evolving field cage construction plans. The basic mechanical and electrostatic setup of the field cage are summarised in section 5.1 and the underlying design studies are presented in the subsequent sections. An optimised arrangement of the field strips has been developed and is discussed in section 5.2. Systematic effects which worsen the drift field quality in the LP, are studied in section 5.3. These results define the mechanical tolerances of the field cage. Studies on mechanical aspects and results of tests on sample pieces are summarised in section 5.4.

5.1 Field Cage Layout

The field cage was planned to be 610 mm long, with an inner diameter of 720 mm, an outer diameter of less than 770 mm and about 25-mm-thick walls. This layout is sketched in figure 5.1(a). The outer dimensions are limited by the EUDET setup that is described in section 4.3: the field cage diameter fills out the available space in the PCMAG after the installation of the mounting structure and the silicon detectors, the length allows a shifting of the LP to different positions inside the magnet. Detailed engineering drawings for the field cage can be found in figure 5.38 at the end of this chapter.

A cathode end plate was developed and constructed, adapted to the field cage. It is mounted on an intermediate flange, which is attached to the cathode side of the field cage. On the flange, the cathode can be aligned relative to the anode.

Mechanical design

The walls of the field cage barrel are produced from lightweight composite materials. Figure 5.1(b) sketches their cross-section in detail. The main component is an aramid honeycomb material sandwiched between two layers of 300-μm-thick glass fibre reinforced plastic (GRP). Due to technical requirements in the construction (see chapter 6) an additional layer of aramid paper was introduced on the outer side of the honeycomb. At both ends the honeycomb sandwich is terminated by massive end flanges of a hard foam material. Each of these flanges bears 40 specially made M6-threaded inserts for

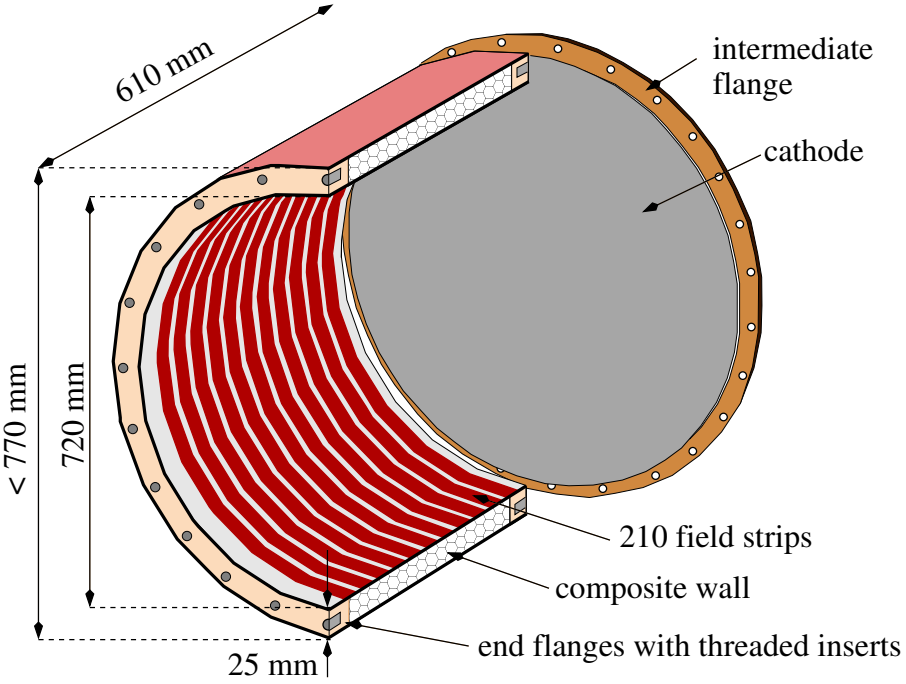

(a) cut view of the field cage with the cathode

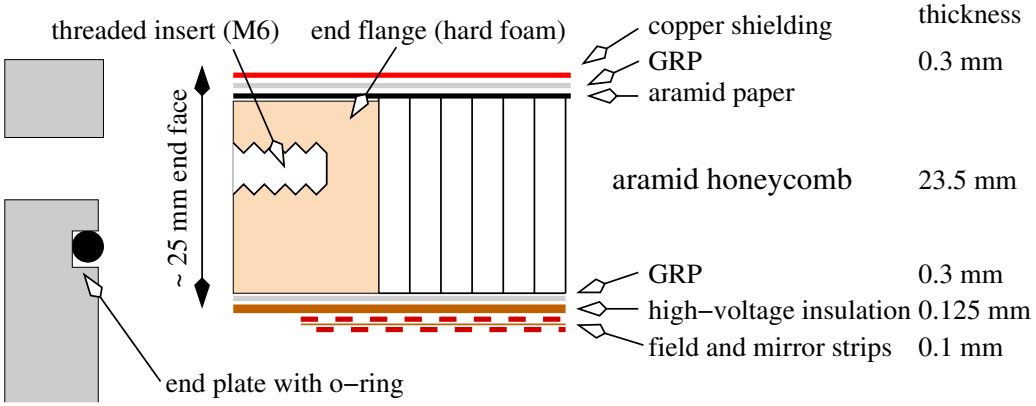

(b) cross-section of the field cage wall and the end flanges

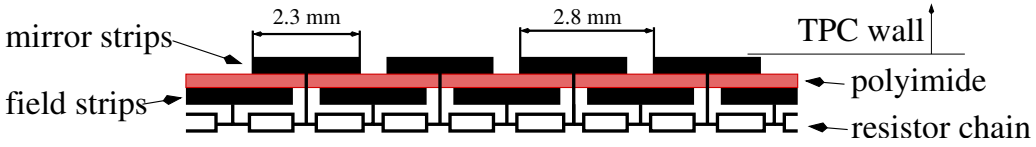

(c) layout of the field strips

Figure 5.1: *Schematic view of the field cage*

manufacturer of the field cage	DESY in cooperation with Haindl, Individuelle Kunststoff-Verbundbauweise
field strip board	Optiprint, Innovative PCB Solutions
insulation layer	DuPont™, Kapton® 500HN
aramid honeycomb	Hexel, HexWeb®,HRH 10/OX-3/16-1.8
hard foam end flanges	SP, Corecell™ S-Foam
aramid paper	DuPont™, Nomex® 410

Table 5.1: *Materials and vendors involved in the construction of the field cage*

the installation of the end plates. These end flanges are 23.5 mm thick - adapted to the honeycomb material - and offer sufficient space for the threaded inserts and an o-ring. The total thickness of the wall and the outer diameter of the field cage are not dimensioned precisely, because these are not critical parameters. The mounting structure, which holds the LP in the PCMAG, supports the LP on anode and cathode end plates and is thus independent from the precise diameter of the barrel. Therefore the outer diameter of the field cage is only limited to the available space in the PCMAG of 770 mm.

On the outside of the field cage barrel, an electric shielding layer of 35-μm-thick copper is attached, whereas the inside is covered by field strips and a high-voltage insulation layer. This wall has an estimated radiation length of about 1.24 % (see section 5.5). The materials used and the manufacturer of the different field cage components are listed in table 5.1.

Electrostatic design

To guarantee the electric field homogeneity of $^{\Delta E}/_{E} \lesssim 10^{-4}$ during operations, 210 copper field strips are installed on the inside wall of the field cage. These are amended by a second layer, so called mirror strips. Figure 5.1(c) shows the complete layout. The strips of both layers are 2.3 mm wide and separated by 0.5-mm-wide gaps. Thus the pitch is 2.8 mm. The mirror strips are displaced to the field strips by half the pitch and cover the gaps between the field strips from the outside. A 50-μm-thick polyimide insulation foil separates the two layers.

This setup is realised on a flexible circuit board, which is installed on the inside of the field cage barrel. Section 5.2.4 discusses the detailed layout of this field strip board.

When a voltage is applied, each mirror strip lies on the intermediate potential of the two field strips in front. These potentials are distributed by two resistor chains that interconnect the field and mirror strips.

The desired field homogeneity imposes requirements on the mechanical accuracy of the LP chamber, namely on the alignment of anode and cathode and the orientation of the chamber axis with respect to the anode surface. The acceptable mechanical tolerances (see figure 5.38) are derived from a study of the electric field deviations that are caused by an imperfect geometry of the LP. This is presented in section 5.3.

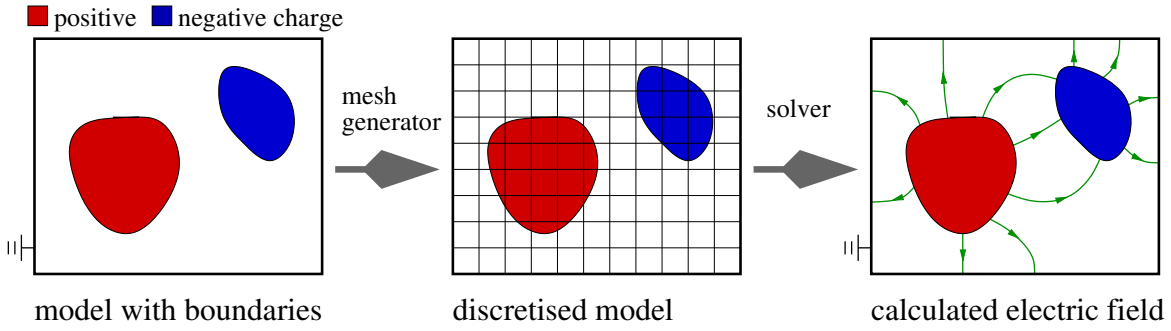

Figure 5.2: *Different steps of a finite element calculation*

5.2 Electrostatic Design Studies for the Field Cage

The layout of the field-forming elements has been developed with electro static finite element field calculations[1]. That means that the electric field in computer model of the LP was calculated for different configurations of the field strips. For each calculated field, the corresponding field homogeneity was derived, which is the crucial figure of merit for the corresponding strip layout. This way, different layouts could be compared and the optimal solution determined.

5.2.1 Finite Element Field Calculations

The finite element method (FEM) (e.g. [72, 73]) is an established and common approach to find approximate solutions of differential equations. It has its main applications in technical engineering problems. Besides the calculation of electrostatic fields which require the solution of the Poisson equation, this includes electrodynamic processes using the full Maxwell equations. Moreover, modern FEM software packages exist also for mechanical or thermal problems.

An FEM calculation comprises three steps that are illustrated in figure 5.2. In the first step, the geometry of the investigated setup is transferred into a computer model. The model is embedded into a calculation volume with defined boundary conditions. The modelling is closely connected to the second step: the volume is discretised by a mesh. A simple rectangular mesh is indicated in figure 5.2. Common FEM calculation programs support triangular meshes, which adapt better to round surfaces. Finally a solver algorithm calculates the electric field and the potential in the defined volume on the basis of the chosen mesh.

In the following the calculation principle is discussed with the example of the Poisson equation. This is given by

$$\Delta\Phi(\vec{x}) = \rho(\vec{x})$$

[1] with the software CST EM-Studio®

with $\Phi(\vec{x})$ being the electric potential and $\rho(\vec{x})$ a given charge density distribution. $\Phi(\vec{x})$ is to be calculated approximatively in the volume V - for example the sensitive volume of a TPC. In the first step of the calculation procedure, the Poisson equation is multiplied by a yet undefined function v, called test-function. The test-function is continuous in the volume and vanishes at the borders. The product is integrated and transformed with the help of differential geometric relations:

$$\int_V \rho(\vec{x})\, v \, \mathrm{d}V = \int_V \Delta\Phi(\vec{x})\, v \, \mathrm{d}V = -\int_V \vec{\nabla} v \cdot \vec{\nabla}\Phi(\vec{x}) \, \mathrm{d}V \tag{5.1}$$

This form of writing the differential equation is called the weak form. The right side of (5.1) is correct if $\rho(\vec{x})$ vanishes at the borders of the volume. That means that the volume is grounded on the outside. In the next step, the potential $\Phi(\vec{x})$ is approximated by a power series with basis functions ϕ_i:

$$\Phi(\vec{x}) \approx \tilde{\Phi} = \sum_{i=1}^{N} a_i \, \phi_i(\vec{x}) \qquad \text{with development coefficients } a_i.$$

The approximation, put in the the weak form (5.1), yields

$$\sum_{i=1}^{N} a_i \int_V \vec{\nabla} v \cdot \vec{\nabla}\phi_i \, \mathrm{d}V = \int_V \rho(\vec{x})\, v \, \mathrm{d}V$$

The number of basis functions N is equal to the number of knots in the mesh (see below). Now, the trick is to choose for the v one of the basis functions ϕ_j. With $v = \phi_j$, the above equation can be rewritten as

$$A_{ij} = \int_V \vec{\nabla}\phi_i \cdot \vec{\nabla}\phi_j \, \mathrm{d}V \quad \text{and} \quad F_j = \int_V \rho(\vec{x})\, \phi_j \, \mathrm{d}V \quad \text{with} \quad j = 1, ..., N. \tag{5.2}$$

This way the initial differential equation is transformed to the matrix equation

$$\sum_{i=1}^{N} a_i \, A_{ij} = F_j \qquad j = 1, ..., N. \tag{5.3}$$

This equation is solved by the solver for the coefficients a_i and with the a_i being calculated, the approximation $\tilde{\Phi}(\vec{x})$ is known.

The mesh is used to choose an appropriate set of basis functions for the calculation. One possible set are N basis functions such that each $\phi_j(\vec{r})$ is unity at exactly one knot j and vanishes at all others. In this case

$$A_{ij} = \int_V \vec{\nabla}\phi_i \cdot \vec{\nabla}\phi_j \, \mathrm{d}V \neq 0 \qquad \text{only if the knots } i \text{ and } j \text{ are adjacent.}$$

Here adjacent means that they are connected by a single mesh line with no intermediate knot. In this case, $A_{ij} = 0$ if $|i - j| > 1$ and only the diagonal and the two secondary

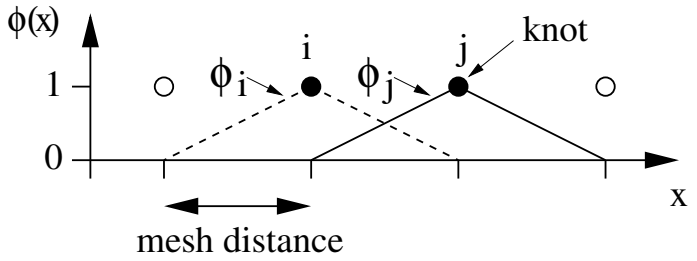

Figure 5.3: *One dimensional mesh with linear approximative basis functions* $\phi_{i,j}$

diagonals of are non-zero in the matrix A (see equation 5.2). Figure 5.3 shows a simplified one-dimensional example of this case. The basis functions ϕ_i rise linear between the two neighbouring knots and vanish elsewhere.

The knots of the mesh define the supporting points of the calculation - in these points the local charge density $\rho(\vec{x})$ is folded with the basis function (see equation (5.2)). Hence the result will in general get more accurate if the mesh density is increased. It is particularly important to adapt the mesh to the smallest structures of the model and the scales on which $\rho(\vec{x})$ variates.

However, an increase of the mesh density implies a higher computing time. There are two basic methods to keep the number of mesh cells moderate: firstly, a symmetric model can be simplified by replacing a symmetry with a boundary condition. In the example above, the boundary condition is fixed to being on ground potential. But, the discussed example reflects only the basic calculation principle. Most FEM implementations use more sophisticated techniques and allow for a setting of different boundary conditions. Secondly, the mesh can be refined only locally, where the model exhibits small structures.

In the following section both methods are used with the example of a model for the LP.

5.2.2 TPC Modelling and Model Discretisation

Figure 5.4(a) illustrates a simplified computer model of a TPC. The anode is not instrumented and, like the cathode, modelled as a plane surface. Apart from the resistor chain, the model is rotational symmetric around the axis of the field cage. This rotational symmetry is exploited to simplify the model: as figure 5.4(b) illustrates, it is sufficient to calculate the electric field in a two-dimensional plane. This calculation plane ranges along the cylinder axis to the outer shielding layer. By rotating the plane around the axis, the electric field can be evaluated in every point of the three-dimensional TPC model.

This simplification of the model requires a boundary condition for the electric field: the field vectors must become parallel to $\vec{e}_z$ along the axis and be parallel to the $r-z$ plane.

The LP has been modelled in this two-dimensional way. The calculation plane is

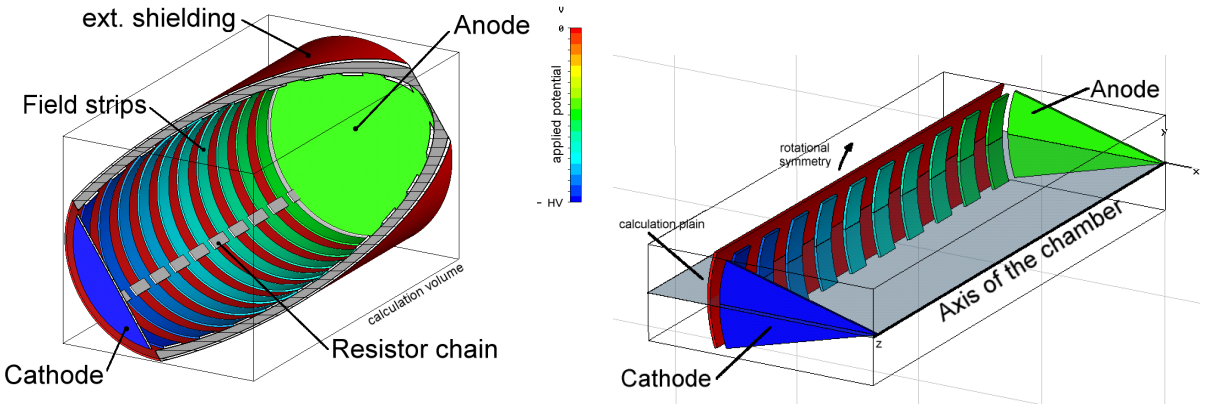

(a) simplified computer model of a TPC

(b) rotational symmetry of the model and calculation plane

Figure 5.4: *TPC model in the FEM calculation software with rotational symmetry*

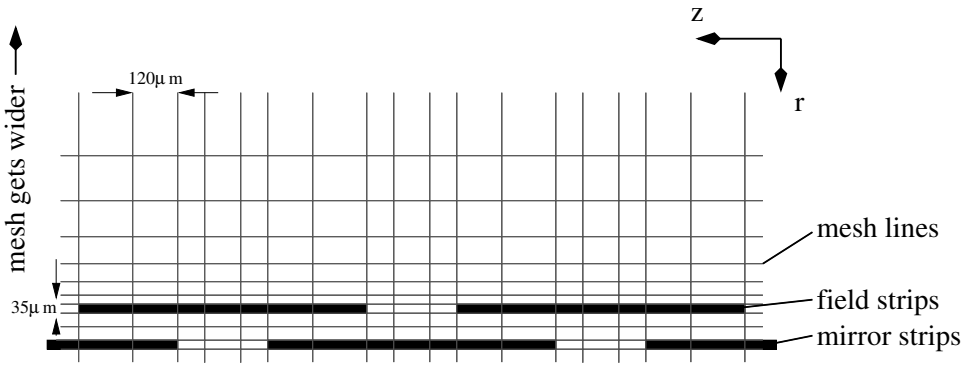

Figure 5.5: *Mesh in the vicinity of the field strips (schematically)*

600 mm long and 385 mm wide - in agreement with the outer radius of the LP. Along the outside edge of the model, behind the field strips, the grounded shielding layer is included into the model and set to a ground potential. Behind the cathode, the potential is not defined by external volumes but forced to ground in a large distance. This boundary condition is called 'open'. According to the construction plans of the LP, the inner radius of the field cage is modelled to be 360 mm. The cathode is put at $z = 599.2\,\text{mm}$.

This calculation plane is discretised in about $4.6 \cdot 10^6$ rectangular mesh cells. Hence an average cell has a size of $0.05\,\text{mm}^2$ and a side length of about $220\,\mu\text{m}$.

The TPC model has its smallest structures in the vicinity of the field strips. To increase the accuracy of the calculation, here the mesh has been refined as illustrated schematically in figure 5.5. About 20 mesh lines are introduced per 2.8 mm along the z-axis - this distance corresponds to the width of a strip and a gap. Thus the mesh

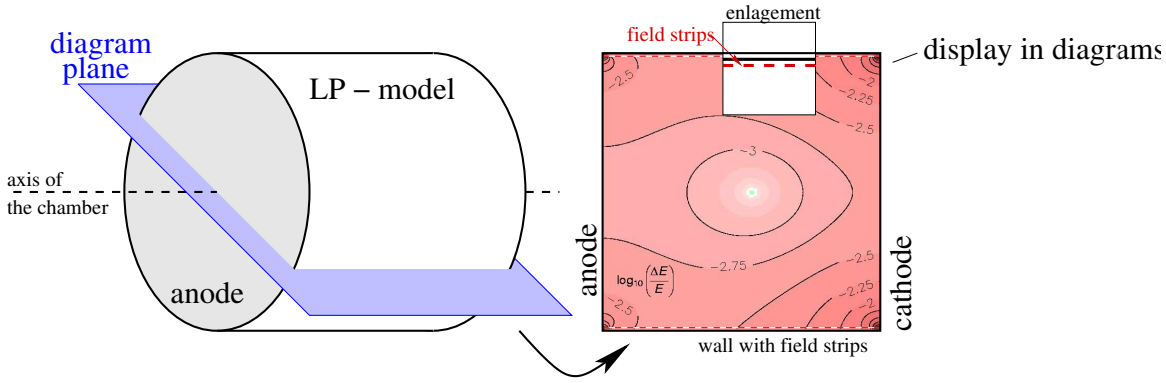

Figure 5.6: *Display of calculated field deviations in the following diagrams*

lines have an average distance of about 120 μm in this direction. In the radial direction, the mesh lines have a minimal distance of about 35 μm around the field strips. Going to smaller radii, the scale on which the field shows significant variations is expected to increase. Thus the mesh is widened and the lines reach a distance of 0.5 mm at the other border of the calculation plane, which corresponds to the centre of the TPC.

Presentation of Calculation Results

After the field distribution $\vec{E}_{\text{calculated}}(\vec{r})$ has been calculated for a given setup, the field deviations $^{\Delta E}/_{E}$ are evaluated by

$$\frac{\Delta E}{E}(\vec{r}) = \frac{|\vec{E}_{\text{calculated}}(\vec{r}) - \vec{E}_{\text{nominal}}|}{|\vec{E}_{\text{nominal}}|}$$

in the whole plane of the model. Here $\vec{E}_{\text{nominal}} = -E_{\text{nominal}} \cdot \vec{e}_z$ is the nominal field strength and $\vec{e}_z$ the unit vector in the z-direction, normal to the anode (see figure 5.4(b)). E_{nominal} is set to 220 $^{V}/_{\text{cm}}$, which is in the range of a typical field strength for TPC operation. The anode is set on a bias potential of -2500 V, which defines the cathode potential to be -15680 V.

In the figures of the following pages, the magnitude of $^{\Delta E}/_{E}$ is displayed on a full plane cut through the LP model, as illustrated in figure 5.6. Red areas in the diagrams denote regions where the magnitude of $^{\Delta E}/_{E}$ exceeds the aspired value of 10^{-4}. White areas mark the transition to values below 10^{-4} and in the green coloured regions the field deviations are significantly smaller than 10^{-4}. In addition, contour lines illustrate the magnitude of the field deviations.

Basic Design of the Field Strips - Pitch

Before the calculations of different field strip models are presented in detail a basic parameter for the following calculations is fixed, namely the field strip pitch.

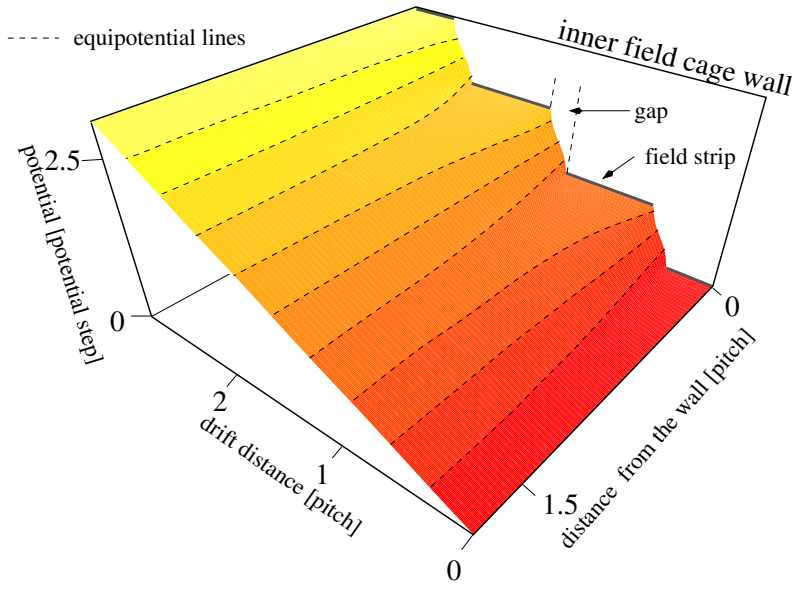

Figure 5.7: *Adaption of the linear decrease of the electric potential in the centre of the TPC to a stepwise decrease close to the chamber wall*

In the centre of a TPC-chamber, the electric potential drops linearly along the field cage axis from the anode to the cathode, while the field strips define a stepwise descent of the potential along the inner wall. In between, it adapts form the linear to the stepwise decay, as illustrated in figure 5.7 for the nominal LP strip layout (e.g. figure 5.1(c)) along three field strips. The diagram shows the magnitude of the potential in the vertical direction. The horizontal is spanned by the distance from the wall and the drift direction, respectively.

The adaption takes place within a distance of two pitches from the wall, as illustrated by the shape of the potential surface. Studies on small calculation models show, that this distance is constant even if the width of the strips is varied. Thereby only the gap between the strips must be kept sufficiently wide to guarantee the electric insulation and small enough that field and mirror strips are overlapping.

In a distance closer than two pitches to the wall, the electric field is very inhomogeneous and hence this volume is lost for nominal TPC operation. To keep this loss as small as possible, the minimal pitch should be chosen. At the same time, the strips have to be interconnected with resistors. In the LP, this is done with surface mount (SMD) resistors that are soldered in a specially designed footprint on the field strips. This layout requires a minimal pitch and the chosen 2.8-mm pitch is the smallest pitch that is technically feasible. All following studied field strip layouts refer to this 2.8-mm pitch.

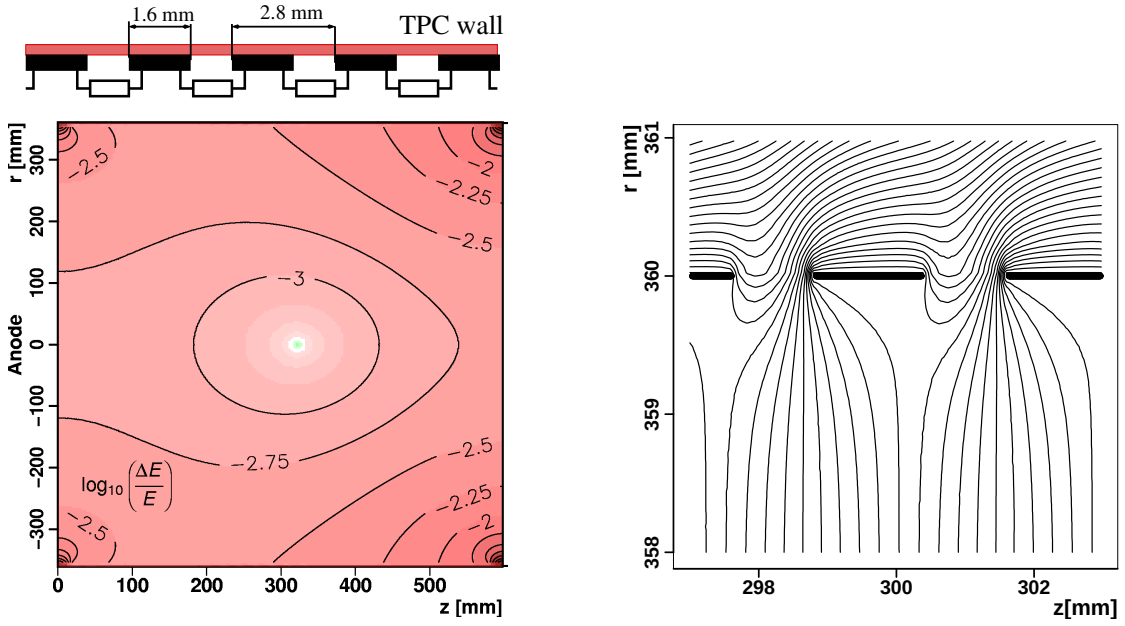

(a) strip layout and calculated field distortions

(b) punch-through the gaps between the strips

Figure 5.8: *Calculation results for a layout with a single layer of 1.6-mm-wide strips and 1.2-mm-wide gaps*

5.2.3 Evaluation of Different Field Strip Layouts

To motivate the introduction of the additional mirror strips, a design with a single layer of field strips is discussed first in the following. It turns out that such layouts cannot guarantee a sufficiently homogeneous field because the outer shielding influences the electric field in the drift volume through the gaps between the strips. This 'punch-through' is prevented by the mirror strips. Three different field arrangements with mirror strips have been investigated and the results are presented subsequently.

Single Layer of Field Strips - Punch-through

A basic design of the field strips is motivated in section 3.1.1 and used as a starting point for the following discussion. The discussed setup features single layer of field strips and is illustrated in figure 5.8(a) together with the calculated field deviations. Here the field strips are 1.6 mm wide and separated by 1.2-mm-wide gaps, which corresponds to the layout realised in the MediTPC transfered to the LP geometry. The field deviations are insufficiently high and have magnitudes between 10^{-3} and 10^{-2} in a large part of the LP model. As said, the reason for the large distortions is the influence of the grounded shielding layer onto the electric field inside the TPC. This is illustrated in figure 5.8(b). Here the equipotential levels in the vicinity of two field strips at $z \approx 300\,\text{mm}$ are

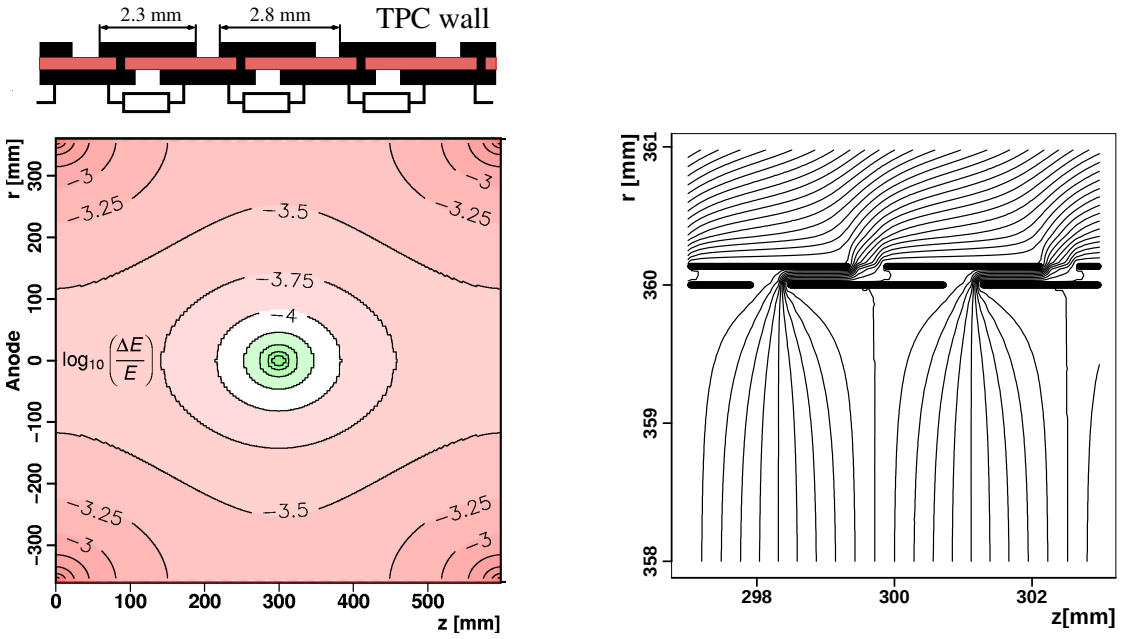

(a) layout of the strips and calculated field deviations

(b) equipotential lines in the vicinity of the wall

Figure 5.9: *Calculation results for a setup with connected field and mirror strips*

drawn. The lower potential of the shielding layer reaches through the gaps and bends the equipotential lines in the TPC-volume towards the anode. The field deviations increase towards the cathode (see figure 5.8(a)) because in this direction the potential difference between field strips and grounding layer increases continuously and, at the same time, the distance between the strips and the shielding layer is constant.

One possibility to minimise the effect is widening the strips and reducing the gaps. Yet the gaps cannot be made too narrow because the neighbouring strips are on different potentials. If the insulation between them becomes unstable an undisturbed operation of the field cage is not guaranteed because, for example, dust particles could short-circuit two strips.

Tests with sample pieces show that 2.3-mm-wide strips that are separated by 0.5-mm gaps allow a stable operation. With these broadened field strips the deviations could be reduced by a factor of ten compared to figure 5.8(a) but would still be insufficiently high. A further reduction of the gaps is too delicate if the LP is operated with up to 100 V between two neighbouring strips.

Layouts with mirror strips

In combination with the field strips, mirror strips can provide a complete shielding against the 'punch-through'. In addition, they serve another purpose. Free charges

can be deposited on the insulation between the field strips and disturb the electric field locally. Because of the insulator's low conductivity they are not removed quickly. The charges invoke mirror charges on mirror strips which reduce the field distortions[2]. For this to work, the insulation layer between field and mirror strips needs to be thin compared to the strip's width. The insulation is modelled to be 100 μm thick, while in the real LP it is only 75 μm thick. In addition, the 2.3-mm-wide strips cover about 80 % of the inner field cage barrel with conductive copper. This keeps a possible charging of the insulation in the 0.5-mm-wide gaps minimal.

The first studied setup with mirror strips is shown in figure 5.9(a) together with the calculated field deviations. Here, each field strip is directly connected to the following mirror strip in the direction towards the cathode. The setup is technically simple to realise because the mirror strips do not require an extra setup for their electrical connections. But the calculated field shows unsatisfactorily high distortions, in the range of $10^{-4} \lesssim {}^{\Delta E}/_{E} \lesssim 10^{-3}$. Unlike figure 5.8(a), the deviation map is symmetric to the centre of the LP model in the z direction. This demonstrates that the punch-through is prevented.

The reason for the large deviations can be seen in figure 5.9(b). This diagram shows the course of the equipotential lines around the field strips at $z \approx 300\,\mu$m and is the equivalent to figure 5.8(b). In-between a field strip and the connected mirror strip, the electric potential is constant. Hence all equipotential lines are guided through the gaps where the two strips are on a different potential. This defines a privileged direction close to the walls - all equipotential lines are bended towards the cathode. This inhomogeneity causes the electric field deviations in the whole volume. They are equally high in a reversed design, where a field strip is connected to the next mirror strip in the direction to the anode. In that case, the equipotential lines are bended in the direction of the anode.

The setup finally chosen for the LP is sketched in figure 5.10(a). In this layout, each mirror strip is applied with the intermediate potential of the two field strips in front. Sizable field distortions occur only in a band of about 5 mm along the wall and the field is homogeneous to a level better than 10^{-5} in the rest of the LP model. Therefore, the field deviation diagram is restricted to the vicinity of the wall. The volume affected by the distortions has a thickness of about two times the pitch.

To apply the potentials to the mirror strips, the number of SMD resistors in the resistor chain needs to be doubled compared to the layout of figure 5.9(a). One possible layout of the resistor chain is indicated in figure 5.10(a) . Two neighbouring field strips are connected by two resistors in series with an intermediate connection to the mirror strip behind. Thus each mirror strip lies on the intermediate potential of the two field strips in front. Here, figure 5.10(b) illustrates the equipotential lines around the field strips. Coming from the inside field cage, the lines run homogeneously into the gaps and are guided to the outside.

This setup is commonly installed in TPCs, like for example the ALEPH TPC [41].

[2]This is why the additional strips are called mirror strips.

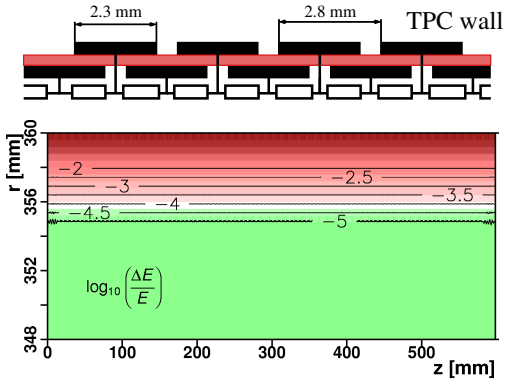

(a) field deviations for mirror strips on intermediate potential

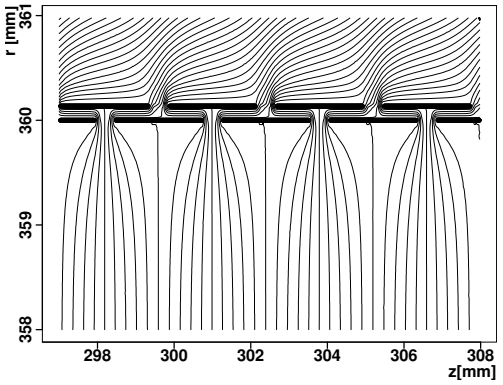

(b) equipotential lines for mirror strips on intermediate potential

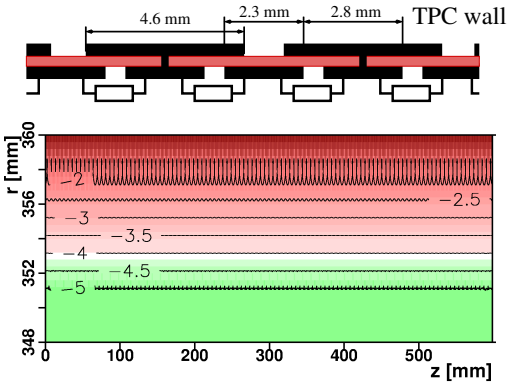

(c) field deviations for broadened parallel mirror strips

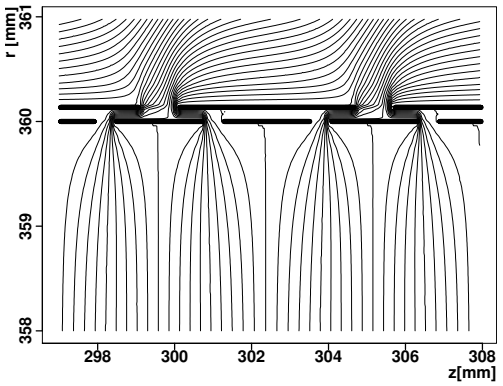

(d) equipotential lines for broadened parallel mirror strips

Figure 5.10: *Calculation results for optimised field strip layouts*

However, the technical realisation is sophisticated, because two resistors have to be installed between two neighbouring field strips.

In the scope of this thesis, an alternative configuration of field and mirror strips has been evaluated. This is a layout with broadened parallel mirror strips, illustrated in figure 5.10(c). An extended mirror strip covers two gaps on the outside and only every second field strip connects to a mirror strip. Similar to the previously discussed nominal layout, the field distortions are limited to a band of about 9 mm along the wall, while the field is homogeneous to a level better than 10^{-5} in the rest of the LP model. With this field strip configuration, the volume affected by the distortions has a thickness of three times the pitch. Figure 5.10(d) depicts the calculated equipotential lines around the field strips in this setup. The equipotential lines are again strongly bundled between a mirror strip and the field strips in front - as in the layout in figure 5.9 - but the direction in which the lines are guided to the outside alternates and

no overall privileged direction exists. Averaged over many field strips, this boundary condition is symmetric along the z-axis.

In this layout, only one resistor is needed to connect two neighbouring field strips. Hence it is technically simple to realise. At the same time, the lost volume along the wall is not significantly larger than in figure 5.10(a). Although this setup offers these advantages, it has not been chosen for the LP. The field strips boards, which are presented in the following, were already in production when the alternative setup was developed.

5.2.4 Field Strip Board

The field and mirror strips have been realised on a special flexible printed circuit board, as mentioned in the field cage design summary above. Figure 5.11 sketches the basic layout of this field strip board. It is 61 cm wide and 2262 mm long, according to the field cage's length and inner circumference, respectively.

In 2007, the manufacturer[3] could not produce a 61-cm-wide printed circuit board in a single piece. Thus a board of half the required width was designed and several pieces were ordered. These half boards are 29.4 cm wide and carry 105 strips. Two of them can be combined, as sketched in figure 5.11. The combination gives one 58.8-mm-wide board with 210 field strips. To this, additional spacer stripes have been attached at both sides. These spacers extend the width of the combined boards to the field cage's length of 61 cm.

The boards consist of a 75-μm-thick polyimide carrier foil that is covered on both sides with 35 μm of copper. On the top side, the field strips are etched into the copper, together with specially designed places to solder the resistors (see below). The mirror strips are installed on the opposite bottom side.

The top side with the resistors represents the inside of the field cage and hence the resistors are accessible for repairs. Two resistor chains have been assembled, for the sake of redundancy: if only one resistor fails in a single chain design, the full high-voltage would be applied at the affected gap. This could cause a spark and possible damage. Such an encounter is unlikely in a setup with two chains, as failures of resistors are expected to be rare.

The following chapter explains the production of the field cage in detail, together with the procedure of the field strip board installation into the field cage.

Detailed Layout of the Field Strip Boards

Going into more detail, figure 5.12 illustrates the layout of the field strip board, focused on a resistor chain at the central junction of the half boards. Figure 5.13 shows a corresponding photograph.

The field strips are 2.3 mm wide and separated by 0.5-mm gaps. A SMD resistor connects a field strip to an intermediate junction. Every of these 'islands' has a connection

[3] Optiprint, Innovative PCB Solutions

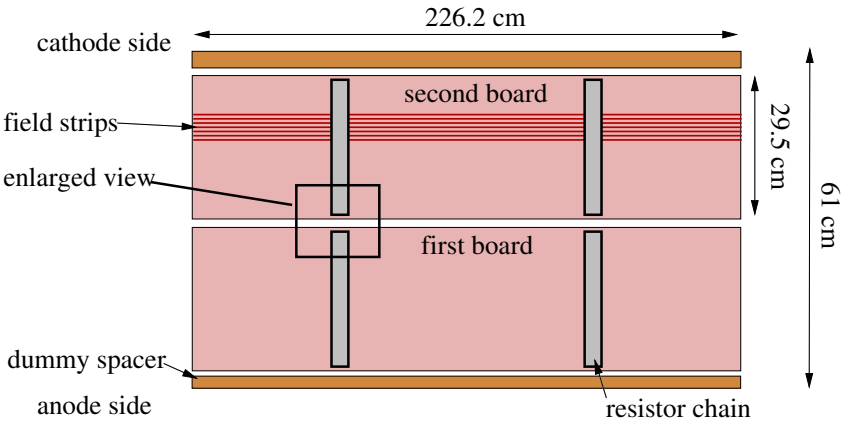

Figure 5.11: *Basic layout of the field strip boards*

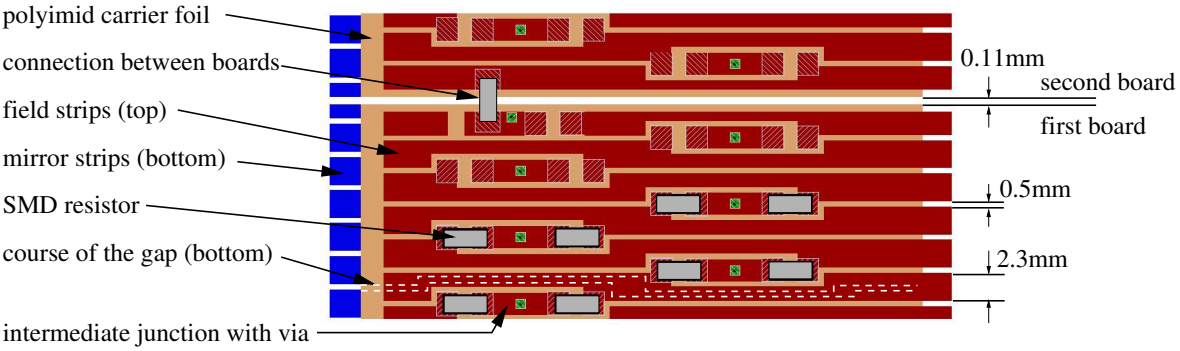

Figure 5.12: *Enlarged view on the field strips according to figure 5.11*

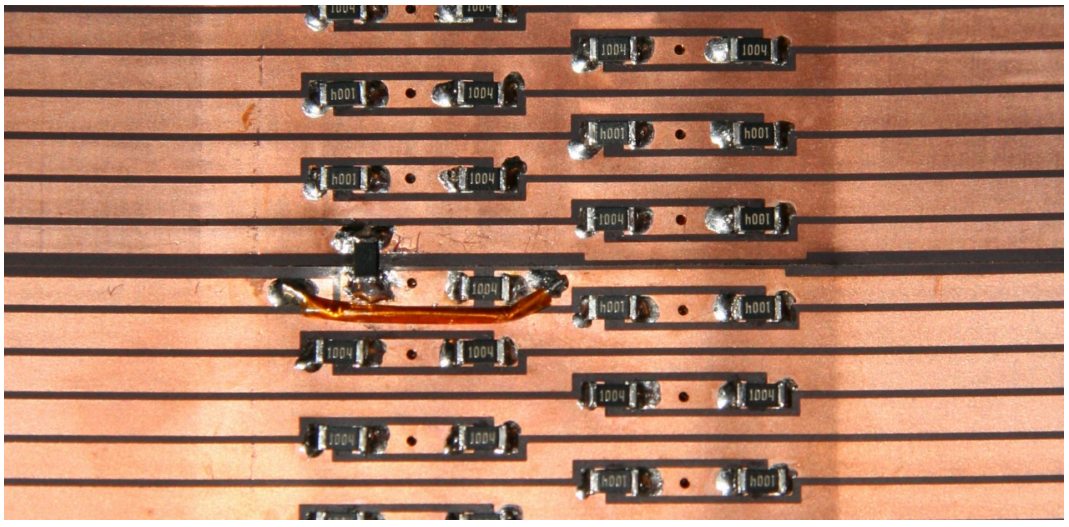

Figure 5.13: *Resistor chain in the field cage at the central connection between the half boards*

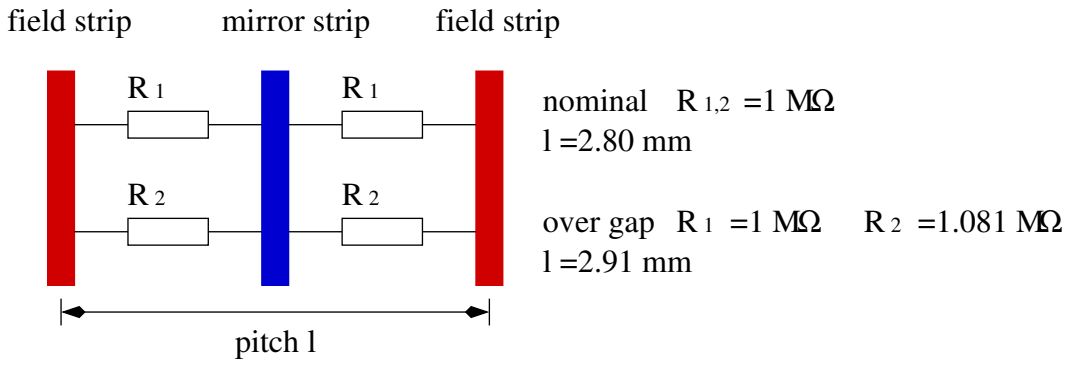

Figure 5.14: *Connections between the field strips and the mirror strips by the resistors*

through the board to the underlying mirror strip. This is called a 'via'. The layout corresponds to the optimised field strip design in figure 5.10(a) - two neighbouring field strips are connected by two resistors while the mirror strips are connected to the intermediate junction. Directly under the resistor chains, the mirror strips have a modified shape. This is done in such a way that all surfaces which are not covered with copper on the top side are covered on the bottom side. Hence, any punch-through around the resistor chains is prevented. The modified layout is exemplary indicated by the lines denoted 'course of the gap (bottom)' in the figure 5.12.

The outer mirror strip at the edge is specially modified for the connection between the two half-boards. It is only 1.8 mm wide, because the mirror strip below is cut over its full length. Such cuts through copper on polyimide are commonly prevented, because the edges tend to ripple. The broadened gap is supposed to ensure the safe insulation between the field and mirror strip. In addition, the last field strip is completely intersected by an extra island. A resistor is soldered on this island and the first strip of the second board. At the same time, an additional insulated wire is soldered onto the strip and closes the intersection. This is visible in the photograph of figure 5.13.

When the two halves are combined, the mottled mirror strips on the first and the second board are connected. Taken together, they combine to a full mirror strip.

Resistivity of the SMD Resistors

The SMD resistors assembled in the field cage have a nominal resistivity of 1 MΩ. The resistivity could be chosen in a wide range - in the MediTPC, 285 kΩ are installed between two strips and the TPC prototype built in Aachen [65] is assembled with 4.7-MΩ resistors. A too low resistivity would cause an increased heat dissipation into the gas volume. If a very high value is chosen, the field strips are not discharged quickly enough when they catch charges from the drift volume. These additional charges cause local field distortions.

The value of 1 MΩ produces a constant current of a few ten micro ampere that discharges the strips. This holds if the field strength is adjusted to $80 - 260\,V/cm$. Any

additional current caused by charged deposits is considered negligible compared to the permanent one. The heat dissipation over a whole resistor chain is 1 W at most and considered as not critical in operation.

The 1-MΩ resistors define the nominal potential difference between two strips for the 2.8-mm pitch. At the conjunction of the half boards the pitch is increased, because an additional gap between the two half-boards could not be avoided. This is also indicated in figure 5.12. To compensate for the increased pitch, two resistors of 1.081 MΩ have been soldered over the junction at both resistor chains. To illustrate the choice of this value, figure 5.14 sketches the connections between a field strip to the underlying mirror strip and the following field strip.

The additional gap between the two half-boards has been measured to be $110 \pm 20\,\mu$m wide, averaged over the complete circumference of the field cage. Thus, the pitch over the gap is increased to 2.91 mm, which is 3.9 % larger than nominal. Accordingly the resistivity between the strips at both sides of the gap must be increased by 3.9 % to 1.039 MΩ. The combination of both two nominal 1-MΩ resistors (R_1 in figure 5.14) with two 1.081-MΩ resistors (R_2 in figure 5.14) results in the required resistivity of $\approx 1.039\,\mathrm{M\Omega}$ between the strips.

The effect of a spread in the resistivity of the resistors on the field quality is discussed within the following section.

Operational Test

Prior to the production of the field cage, the prepared field strip board has been assembled with the SMD resistors and electrically tested. In the test, up to 21 kV were applied between both ends of the board. This corresponds to about 100 V between two neighbouring strips. The test was performed in air and the board showed an ohmic behaviour over the full voltage range.

The gas in a TPC consists mainly of argon which trips at electric field strengths of about 80 % compared to air. Thus the test certifies a safe operation of the LP only up to 18 kV or field strengths of up to $300\,{}^{V}/_{\mathrm{cm}}$.

5.3 Systematic Effects on the Field Quality

The installation of an optimised field strip layout is the precondition for a field quality of ${}^{\Delta E}/_{E} \lesssim 10^{-4}$ in the LP (see figure 5.10(a) or 5.10(c)).

In the LP calculation models of the previous section, the end plates, for example, are assumed to be parallel and aligned with respect to the field strips. In a realistic TPC setup, such perfect conditions are not feasible. Imperfections of the chamber geometry can cause field distortions in a locally limited volume of the TPC - as for example by a punch-through effect around a hole for a gas inlet - or over the whole drift volume. Locally limited effects can often be reduced by special additional setups. In this example, the hole for the gas inlet could be covered with a conductive mesh, which minimises the field deviations around, as also dedicated calculation studies show. More

severe are the global effects. They must be considered already in the construction of the field cage.

In this section, studies for three scenarios are discussed in detail. Field deviations can arise from

- an imperfect alignment of the end plates, because anode and cathode are not parallel.
- a tilt of the field cage axis, because the field strips are not aligned to the end plates.
- variations in the resistivity of the SMD resistors and a finite resistivity of the field cage walls, these effects alter the potentials on the field strips.

The alignment of the end plates can be adjusted with the cathode intermediate flange - at least within a certain range and accuracy. The other two points are most crucial for the construction, because these imperfections can not be corrected easily after the field cage is completed.

5.3.1 Evaluation of Field Deviations - Calculation of Systematic Displacements

To model an imperfect LP geometry, for example, the cathode end plate of the LP model is rotated by a small angle $\delta\alpha$. This is discussed below. The arising field deviations increase continuously with an increasing $\delta\alpha$. At a certain angle, they will spoil the point resolution more than the acceptable $30\,\mu$m (see section 4.3.3).

In the following, an additional method is used to evaluate the effect of the field deviations and to estimate the acceptable size of a deformation: it is assumed that an electron cluster is created in the sensitive volume of the LP. The cluster drifts in the inhomogeneous electric field towards the anode. Due to the field inhomogeneities, the cluster can drift in a radial direction and arrive radially displaced on the anode, compared to the nominal point of arrival if the electric field was homogeneous. The accumulated radial displacement is estimated as a function of where a cluster was created in the LP volume. For this, the drift path of the cluster through the TPC volume is reconstructed.

The according calculation method is illustrated in figure 5.15(a). Starting from a point $\vec{r}_0$ in the TPC volume where a cluster is assumed to be produced, the drift path $\vec{r}_{\mathrm{drift}}$ is calculated in steps:

$$\vec{r}_{\mathrm{drift}}(\vec{B},\vec{E}) = \vec{r}_0 + \sum_{\vec{r}_0}^{\mathrm{anode}} \frac{\vec{v}_{\mathrm{Drift}}}{|\vec{v}_{\mathrm{Drift}}|}(\vec{B},\vec{E}) \cdot \delta l$$

Here δl is the step width and $\vec{B}$ and $\vec{E}$ the magnetic and electric fields, respectively.

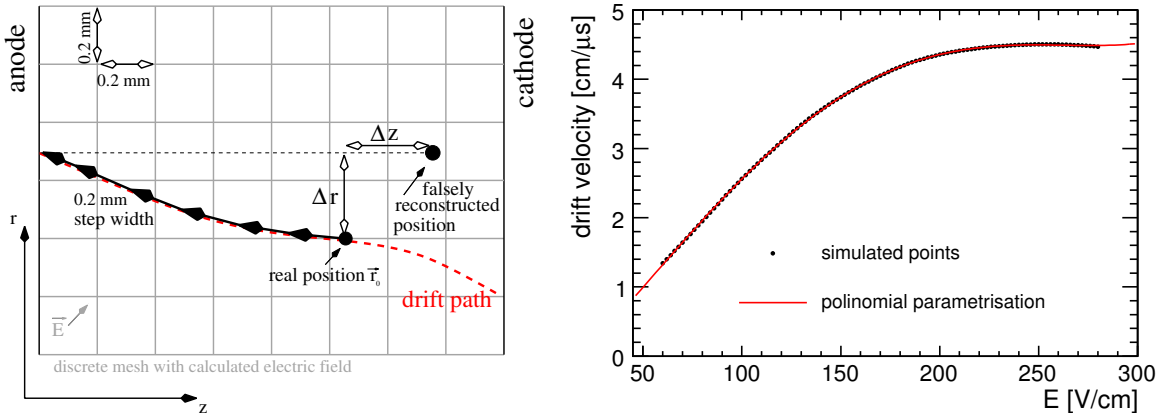

(a) iterative calculation procedure

(b) electron drift speed dependency used in the simulation

Figure 5.15: *Simulation of systematic deviations in the point reconstruction*

For the calculation, $\vec{B}$ is set to $-1\,\mathrm{T}\cdot\vec{e}_z$, which is about the field strength in the PCMAG and $\vec{E}$ is evaluated from the calculation result. The step width δl is chosen to be $200\,\mu$m.

In analytically constructed electric fields, it is possible to derive an analytic expression for a drift path. This analytic drift curve can be compared to the iteratively reconstructed drift path. Such studies have been performed with test fields that are similar to the calculated electric fields. They show that $\delta l = 200\,\mu$m is sufficiently small to calculate displacements with an accuracy of a few micrometres. The electric field is sampled with the same step width.

At a point $\vec{r}_i$ in the TPC volume the drift velocity vector $\vec{v}_{\mathrm{drift}}(\vec{r}_i)$ is parallel to:

$$\vec{v}_{\mathrm{drift}}(\vec{r}_i) \propto \left[\hat{E}_r + (\mu B)^2(\hat{\vec{B}}\cdot\hat{\vec{E}})\hat{B}_r\right]\vec{e}_r + \left[\mu B(\hat{B}_r\hat{E}_z - \hat{B}_z\hat{E}_r)\right]\vec{e}_\varphi + \left[\hat{E}_z + (\mu B)^2(\hat{B}\cdot\hat{E})\hat{B}_z\right]\vec{e}_z$$

The magnitude $v_{\mathrm{drift}}(\vec{r}_i)$ and the total drift time $t_{\mathrm{drift,\,i}}$ from $\vec{r}_0$ to the anode are

$$v_{\mathrm{drift}} = \frac{\mu E}{1+(\mu B)^2}\cdot(1+(\mu B)^2\hat{\vec{E}}\cdot\hat{\vec{B}}) \qquad \text{and} \qquad t_{\mathrm{drift,\,i}} = \sum_{\mathrm{i}=1}\frac{v_{\mathrm{drift}}(\vec{r}_i)}{\delta l}.$$

Figure 5.15(b) shows the drift velocity dependency used for the calculation. This curve has been simulated [55] for TDR gas[4] (see figure 3.8). From this, the electron mobility is calculated by $\mu = v_{\mathrm{drift}}/E$.

After a drift path has been reconstructed up to a point $\vec{r}_{\mathrm{Anode}}$ on the anode surface, the radial displacement is calculated by $\Delta\vec{r} = |(\vec{r}_{\mathrm{anode}} - \vec{r}_0)\cdot\vec{e}_r|$. The longitudinal displacement is $\Delta z_i = |(\vec{r}_i - t_{\mathrm{drift,\,i}}\cdot v_{\mathrm{nominal}})\cdot\vec{e}_z|$.

[4] 93 % AR, 5 % CH_4, 2 % CO_2

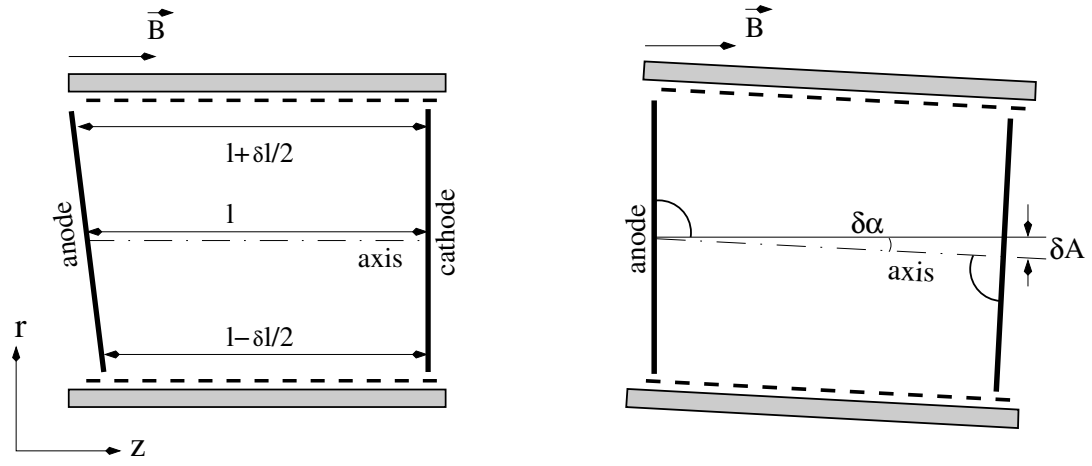

(a) anode tilted

(b) axis tilted

Figure 5.16: *Imperfect geometries of the LP*

5.3.2 Scenarios with Imperfect TPC Geometries

Figure 5.16 illustrates the studied imperfect TPC geometries. In the first setup, sketched in figure 5.16(a), the anode is slightly tilted while the cathode is aligned correctly to the field strips and perpendicular to the magnetic field. Here, the expected field deviations have a magnitude of

$$E = \frac{U_{\text{cathode}} - U_{\text{anode}}}{d} \qquad \rightarrow \qquad \frac{\Delta E}{E} \approx \frac{\delta l}{l}.$$

If the skew is $\delta l = 100\,\mu\text{m}$ this is of the order ${}^{\Delta E}/_{E} \approx 1.6 \cdot 10^{-4}$.

This scenario can also be looked at from another point of view. In figure 5.16(b) the anode is aligned perpendicular with respect to the magnetic field whereas the whole field cage is slightly rotated. If the angle between the magnetic field and the axis of the chamber is $\delta\alpha$, the expected field components in the radial direction are of the order

$$\Delta E \approx \delta\alpha \cdot E \qquad \rightarrow \qquad \frac{\Delta E}{E} \approx \delta\alpha \tag{5.4}$$

For an angle of $\delta\alpha = 1.7 \cdot 10^{-4}\,\text{rad} = 0.01\,\text{deg}$ the distance between the field cage axis to the nominal axis is $100\,\mu\text{m}$ at the cathode. This distance is labelled with δA in the figure.

Extension of the Calculation Model

The modified LP model geometries of figure 5.16 are not rotational symmetric with respect to the field cage axis and thus they require an extended calculation model compared to the one introduced above. Figure 5.17 illustrates the modified model for

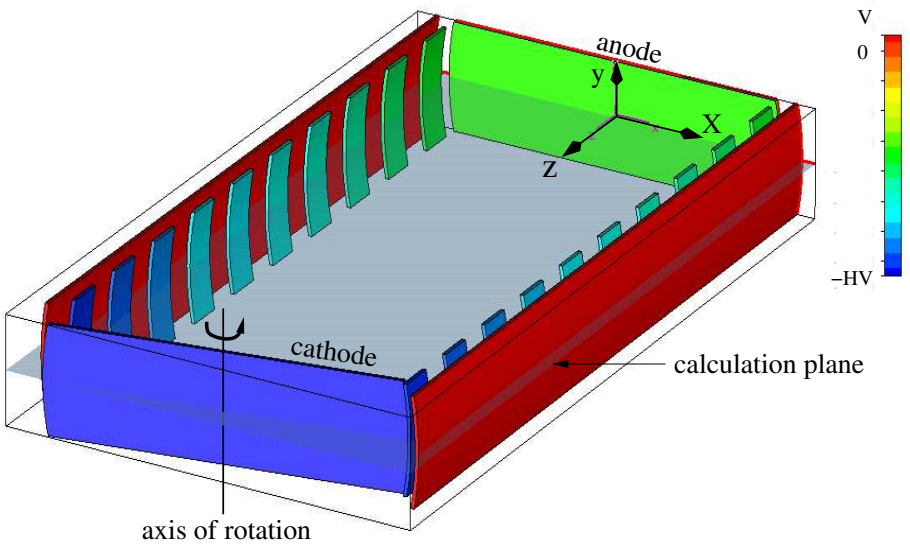

Figure 5.17: *Modified calculation model for the scenarios of figure 5.16*

a scenario where a sightly rotated cathode destroys the rotational symmetry. This model still features one symmetry plane: the axis of rotation for the cathode is parallel to the y axis and the $x - z$ plane separates the model in two mirror-inverted parts. The field has no $\vec{e}_y$ component in this $x - z$ plane and it can be calculated correctly in a two-dimensional model. For this, the calculation is extended over the full plane cut through the LP model. However, the result of a calculation is only valid in this plane and cannot be extended to the full three-dimensional model.

Results on studies of Imperfect Geometry

The figures 5.18 and 5.19 show as an example the results of calculations for a tilted cathode alone and for a tilt of the axis, respectively.

A tilt of the cathode, here by $\delta l = 100\,\mu$m (see figure 5.16(a)), causes field distortions in the back part of the LP model at $z > 350\,$mm. This result is displayed in figure 5.18(a). Towards the front part, the field strips cancel the distortions and in the vicinity of the anode the field is still perfectly homogeneous. Close to the cathode, the calculation results exhibits peculiar clusters. This is a calculation artifact: the rectangular mesh cannot adapt perfectly to the slightly rotated cathode surface.

Electron clusters being produced close to the cathode arrive with a small radial displacement of about $10 - 15\,\mu$m on the anode. The longitudinal displacements are equally small.

Figure 5.19(a) shows the equivalent results for a tilt of the axis by $\delta\alpha = 0.01\,$deg. The field deviations are of the expected magnitude of $1.7 \cdot 10^{-4}$, which would be indicated by a contour line labelled as -3.8 in figure 5.19(a) (see equation (5.4)).

The interplay between the field strips and the end plates produces a modified arrangement of the electric field lines and the equipotential surfaces that is illustrated

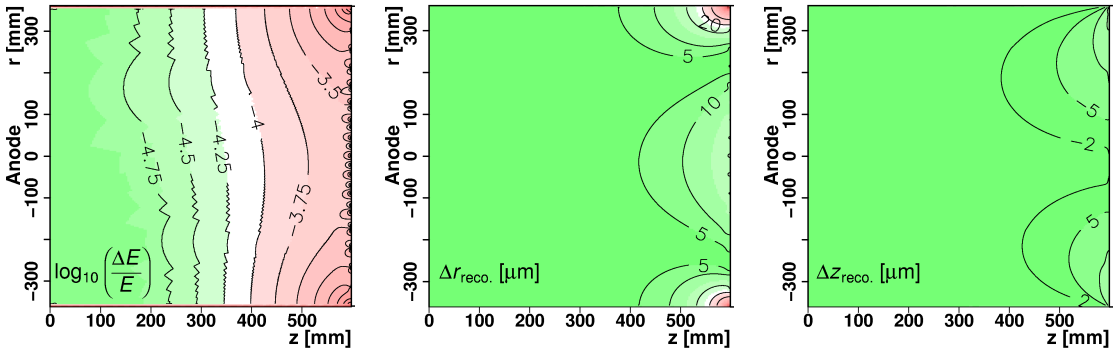

(a) field distortions **(b)** radial displacement **(c)** long. displacement

Figure 5.18: *Calculated field deviations and displacements for a tilted cathode*

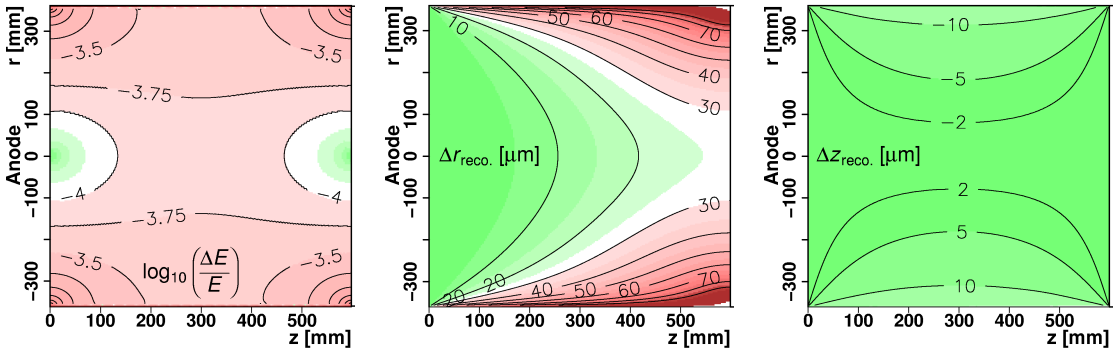

(a) field distortions **(b)** radial displacement **(c)** long. displacement

Figure 5.19: *Calculated field deviations and displacements in case of a tilted axis*

in figure 5.20. Close to an end plate the equipotential surfaces arrange parallel to the conductive surface. Hence, the field is perpendicular to the anode and the cathode and radial field components vanish in the vicinity of the end plates. But the field strength can be increased or decreased. At the same time, the field aligns parallel to the field cage axis in the very centre of the chamber. This is because the field strips dominate the field in this region: the strips are perpendicular to the axis and also fix the equipotential planes to be perpendicular. In the consequence, the clusters drift under the permanent influence of an $\vec{E} \times \vec{B}$-term, because the magnetic field is parallel to $\vec{e}_z$ over the whole length of the chamber.

Therefore the clusters accumulate sizable radial displacements while drifting, as shown in figure 5.19(b). The displacements rise up to 90 μm in the corners at the cathode. At the same time, the longitudinal displacements are still small (see figure 5.19(c)), because the electric field strength does not fluctuate greatly, only the field direction varies.

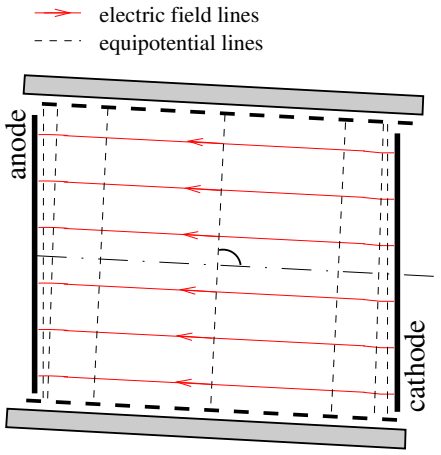

Figure 5.20: *Electric field lines in a TPC with tilted axis*

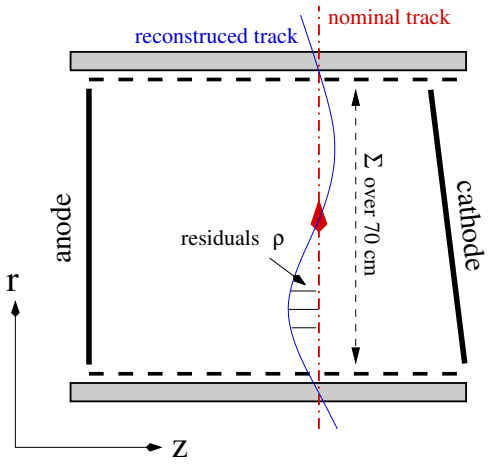

Figure 5.21: *Evaluation of the degradation in resolution*

Increase in Resolution

To evaluate the impact on the resolution due to the systematic displacements of the drifting clusters, it is assumed that a track is created in the LP and measured in an inhomogeneous drift field. Figure 5.21 illustrates the case, where the created trajectory is perpendicular to the z-axis and denoted 'nominal track'. The measured space points are distributed along the line called 'reconstructed track' and the difference between both lines are the residuals $\delta\rho$.

The sum of the squared residuals $\rho_\perp$ in the transversal plane,

$$\Delta\sigma_\perp = \sqrt{\frac{1}{N}\sum_{0}^{N}\rho_\perp^2(z)} \qquad (N \text{ denotes the number of points})$$

gives an additional contribution to the resolution $\sigma_\perp$ (see section 3.2.3).

The default method to calculate $\sigma_\perp$ is not sensitive to these systematic displacements, because residuals are evaluated with respect to the fitted trajectory and not with respect to the real one. If some points are displaced, the fitted curve could adapt to the change and hide the effect of systematic displacements. For the final ILD TPC, the resolution must be corrected with respect to the real trajectory. There, reference points are provided by the silicon detectors around the IP and outside the TPC field cage - in the EUDET setup these come from the external silicon detectors.

The equivalent sum where the residuals are substituted by the calculated radial displacements $\delta\vec{r}_{\text{reco.}}$ (see figure 5.18(b))

$$\Delta R^2_{\text{reco.}}(z) = \sqrt{\frac{1}{N}\sum_{-r}^{+r}\delta r^2_{\text{reco.}}(z)} \tag{5.5}$$

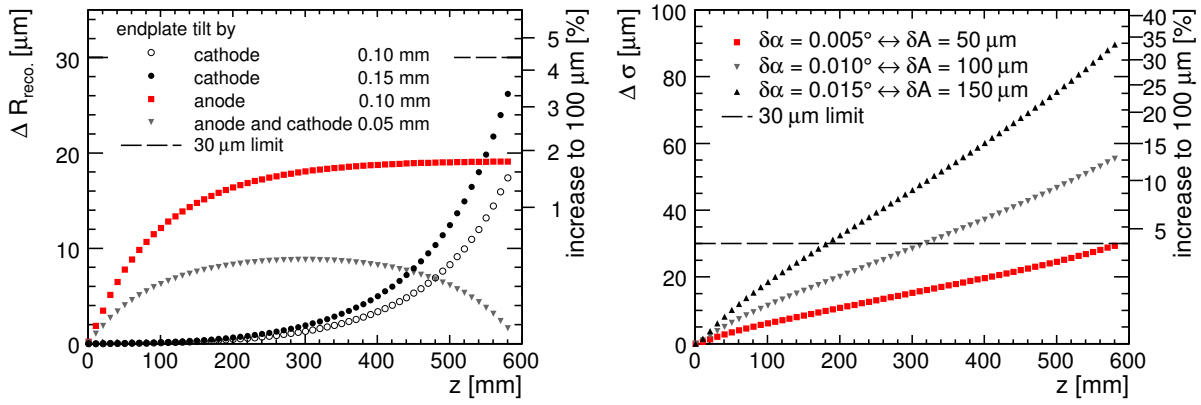

(a) tilted end plates with correctly aligned axis (see figure 5.16(a))

(b) parallel end plates and slightly rotated axis (see figure 5.16(b))

Figure 5.22: *Increase of the resolution due to field distortions for different studied imperfect geometries*

is an upper estimate for $\Delta\sigma_\perp$, because clusters can be displaced in the direction of the nominal trajectory. In this case, the residual is smaller than $\delta\vec{r}_{\text{reco.}}$. As stated, the goal is $\Delta R_{\text{reco.}} \lesssim 30\,\mu\text{m}$.

The sum in (5.5) extends over 700 residuals which are evaluated equally spaced by 1 mm along 70 cm of the the pseudo trajectory. In addition, it is assumed that the TPC is sensitive within a distance of 1 cm from the inside walls.

Figure 5.22(a) shows $\Delta R_{\text{reco.}}$ for geometries with tilted end plates. The magnitude of the tilt is $\delta l = 100\,\mu\text{m}$ and once also $\delta l = 150\,\mu\text{m}$ for the case of a slightly rotated cathode.

If only the cathode is affected by a misalignment, the resolution is worsened only in the back part of the TPC. This is expected from the result in figure 5.18(b). The increase is proportional to the magnitude of the tilt - the line for $\delta l = 150\,\mu\text{m}$ is 1.5 times the corresponding line for $\delta l = 100\,\mu\text{m}$. A misalignment of the anode affects the resolution over the whole drift length. In this case, the field distortions are as large as in case of a tilted cathode in figure 5.18(a), but located in front of the anode. Clusters from the whole the drift volume have to cross this region before arriving at the readout and accumulate a displacement. The displacements, $\Delta R_{\text{reco.}}$, saturate for $z \geq 300\,\mu\text{m}$ where the field distortions start to vanish. At the cathode, they approach the corresponding value of the tilted cathode. This is expected, because the field distortions are of the same magnitude in both cases.

If both end plates are tilted in opposite directions, the field distortions close to the cathode can compensate the distortions on the anode side. In this scenario, the $\vec{E} \times \vec{B}$ vector has a different sign at both ends of the LP model. The calculations show that the limit of $30\,\mu\text{m}$ is reached close to the cathode for a tilt of $\delta l = 150\,\mu\text{m}$. If the anode was misaligned by the same amount, the limit would be exceeded in the complete drift

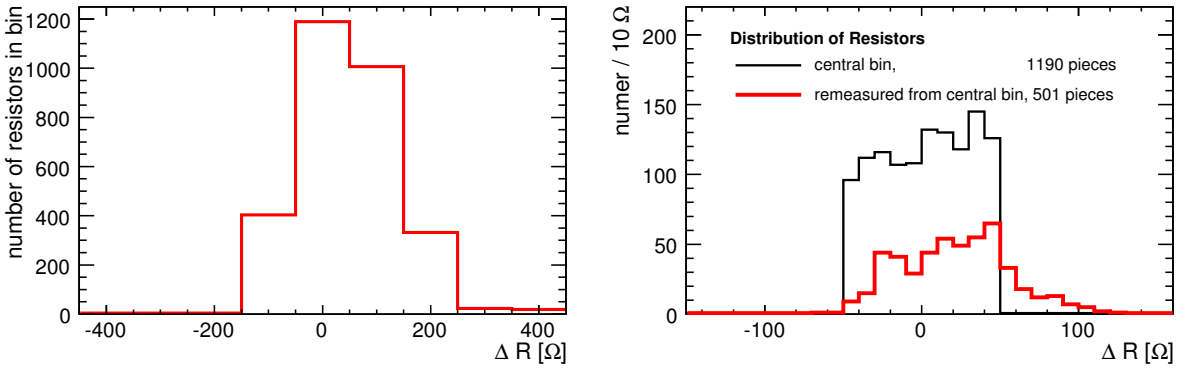

(a) 3000 one mega ohm resistors sorted into 50 Ω bins

(b) distribution of the central bin with the result of a re-measurement

Figure 5.23: *Measured resistivities of the SMD resistors soldered into the field cage*

volume.

Figure 5.22(b) illustrates the calculated $\Delta R_{\text{reco.}}(z)$ for geometries with a slightly rotated axis. The increase of resolution exceeds a value of 30 μm at the cathode already at a small rotation angle of $\delta\alpha = 0.005\,\text{deg}$. In this case, the axis of the field cage has a distance of about $\delta A = 50\,\mu\text{m}$ from its nominal intersection point with the cathode (see figure 5.16(b)). Similar to the case of a rotated cathode above, the resolution rises linearly with the magnitude of $\delta\alpha$.

In summary, the field cage has to be constructed such that its axis is defined within a tube with a diameter of 100 μm perpendicular to the anode and cathode end faces. At the same time, the end faces are required to be parallel within $\delta l \leq 150\,\mu\text{m}$.

5.3.3 Realistic Resistors and Finite Resistivity of the Field Cage Wall

The SMD resistors assembled in the LP have been chosen from a larger sample of 3000 resistors with a resistivity of 1 MΩ. Before, all 3000 resistors had been measured with an accuracy of $\pm 10\,\Omega$ and sorted into bins of 50 Ω. Figure 5.23(a) displays the resulting bin contents. For the the equipment of the field strip board 900 SMD resistors are needed. These have been taken from the central bin with $\Delta R = 1\,\text{M}\Omega \pm 50\,\Omega$. Prior to the soldering, a part of the selected resistors have been remeasured. Figure 5.23(b) compares the distribution for the central bin with the remeasured sample. The latter is shifted towards a higher R and broadened. The reason could be a change in the surrounding temperature - the resistors have a temperature coefficient of $25\,^{\text{ppm}}/_{^\circ\text{C}}$, as specified by the vendor. In operation, the temperature coefficient is not crucial, because temperature changes in the TPC affect all resistors equally. Thus they change their resistivity homogeneously. The resistivities fluctuate in a larger range, but they

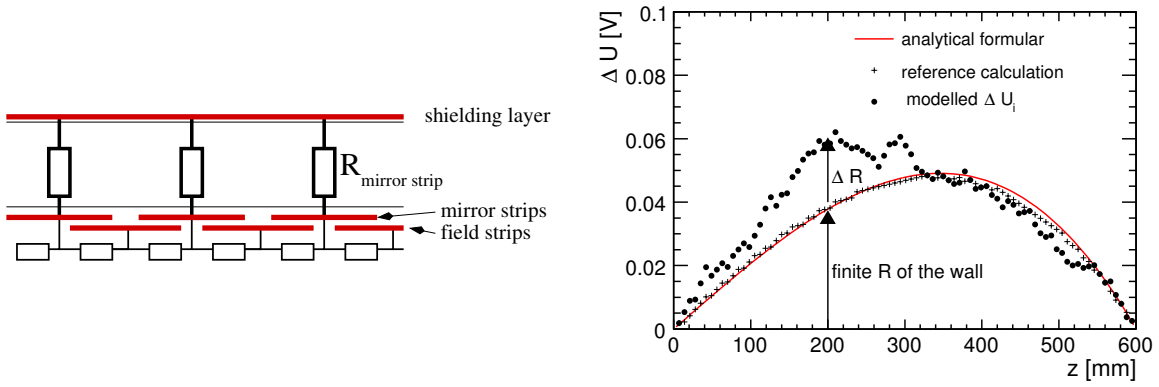

(a) finite resistivity of the wall

(b) additional potentials on the field strips

Figure 5.24: *Disturbances to the potentials on the field strips*

can be assumed to scatter in a range of

$$\frac{\Delta R}{R} \approx \frac{100\,\Omega}{1\,\mathrm{M}\Omega} = 10^{-4}. \tag{5.6}$$

Besides the fluctuating resistivities, a finite conductivity of the TPC wall modifies the potential on the field strips. This effect can be understood with the help of figure 5.24(a). Here, a small rest-conductivity of the wall is indicated by the resistors $R_{\text{mirror strip}}$. This causes a leakage current between the shielding and the mirror strips that rises the potential of the mirror strips. The disturbance to a potential ΔU_i of a strip at z is (mod. from [43])

$$\Delta U(z) = \frac{1}{6}\left[\frac{z}{l} - \left(\frac{z}{l}\right)^3\right] \cdot V_{\text{HV}} \cdot \frac{R_{\text{chain}}}{R_{\text{wall}}}. \tag{5.7}$$

In this formula, V_{HV} is the potential on the cathode of about $-15600\,\text{V}$. R_{chain} is the total resistivity of the resistor chain between anode and cathode and equal to $214\,\text{M}\Omega$. Finally, R_{wall} is the combined resistivity of the $R_{\text{mirror strip}}$ in figure 5.24(a), that are installed in a quasi-parallel circuit. $R_{\text{mirror strip}}$ has been estimated with the data sheets of the materials in the different layers and yields $R_{\text{wall}} = 5 \cdot 10^{12}\,\Omega$.

Figure 5.24(b) displays the additional potentials on the field and mirror strips according to equation (5.7). The points along the curve result from a reference calculation. For this, the setup in figure 5.24(a) has been evaluated with a software dedicated to electric circuits[5]. This calculation affirms formula (5.7).

The reference calculation has also been used to generate the modification potentials for one specific sample of resistors. For this, a set of resistors has been randomly chosen from the two central bins of the distribution in figure 5.23(a) and been included

[5] ngspice [74]

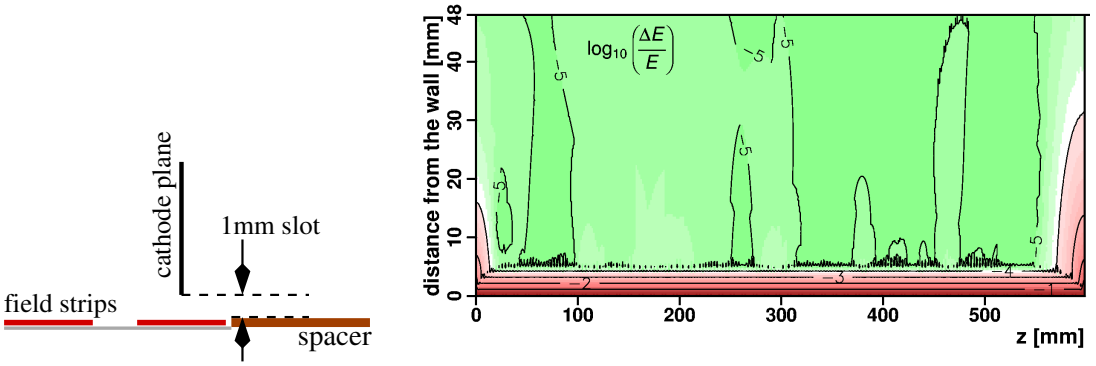

(a) slot between cathode and field strips

(b) calculated field distortions

Figure 5.25: *Field distortions along the inside wall due to imperfect resistors, a rest conductivity of the wall and a slot between the end plates and the strips*

into the reference calculation. The calculated additional potentials on the strips are illustrated in figure 5.24(b) ('modelled ΔU_{i}'). Both effects, the finite resistivity of the field cage wall and the imperfect resistors, account about equally to ΔU_i. The disturbance potential has a magnitude of 10^{-3} compared to the nominal potential of 60 V between two strips.

Slot between the End Plate and the Field Strips

The cathode plane, mounted on the intermediate flange, does not completely close the field cage. As illustrated in figure 5.25(a), it has a 1-mm smaller radius than the inner field cage. The slot is required for the installation and alignment of the cathode on the intermediate flange. Through the 1-mm-wide gap, the external undefined potentials (see section 5.2.2) can influence the field inside the field cage. These slots and a 100-μm gap in the mirror strip at the junction of the two half field strip boards have been introduced into the model.

Figure 5.25(b) displays the calculated field deviations with the modified potentials, and the additional modifications of the model. A punch-through at the slots between the end plates and the field cage causes local field distortions in the corners of the TPC. Their range is limited to a radius of 1 cm at the anode side and 3 cm at the cathode. The additional deviations due to the imperfect resistors are less severe and of the order of 10^{-5}, while the 100-μm gap between the two half-field strip boards does not cause significant additional distortions. Thus these effects are negligible compared to the effect of an imperfect geometry of the field cage.

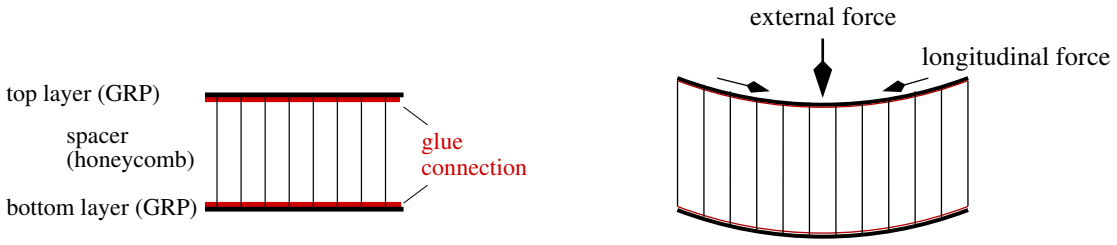

(a) cross-section of the structure

(b) application of an external force

Figure 5.26: *Basic principle of composite structure*

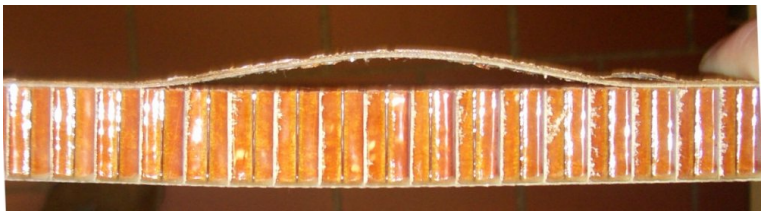

Figure 5.27: *Delamination due to over stressing of a composite structure*

5.4 Development of the Field Cage Structure

Composite materials, as they have been used for the construction of the field cage barrel, are lightweight but mechanically very robust. For this reason they are traditionally used for example in aircraft construction and today they find more and more applications in detectors of high energy physics.

Figure 5.26(a) sketches a cross-section of a composite structure, as it is used in the LP wall and figure 5.26(b) illustrates the reason for its high robustness. The central part of the wall consists of a material with a low density, but a high shear modulus. This layer is called spacer. This spacer is embedded between two layers of a thin but more massive material, typically glass or carbon fibre reinforced plastics. In the following, these are called top layers.

External forces on the structure are turned into longitudinal forces between the spacer and the top layers. These tractive forces stress the glue connection and if they become too strong the top layer detaches from the spacer. This is called delamination and shown in the photograph of figure 5.27. Hence, the stability depends mostly on the strength of the glue connection between the top layers and the spacer.

A big variety of spacer and top layer materials are used in composite constructions, depending on the field of application. A low material budget field cage wall requires low density spacer materials. The top layers should be electrically insulating because the field strips and the external shielding layer lie on different potentials during operations.

The spacer material in the LP field cage wall is a honeycomb structure made of aramid paper. This material has already been used for the construction of the MediTPC and

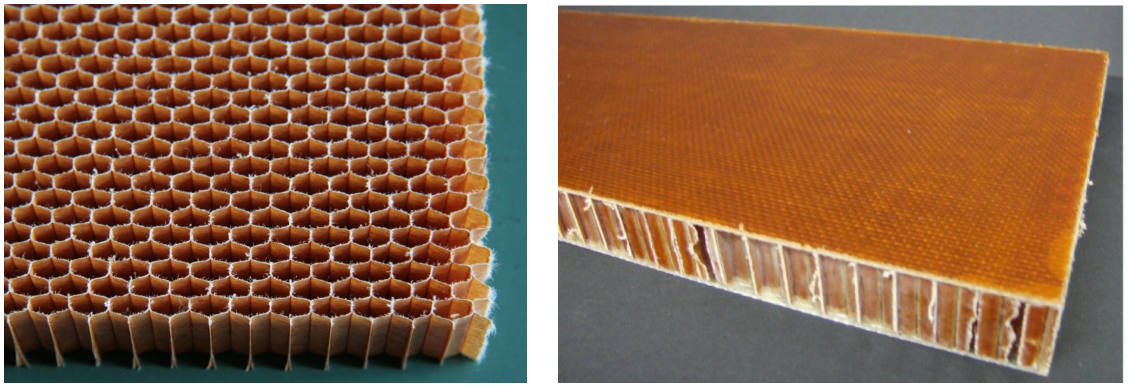

(a) aramid honeycomb spacer **(b)** sample piece of the wall structure

Figure 5.28: *Picture of sample pieces for the wall of the field cage*

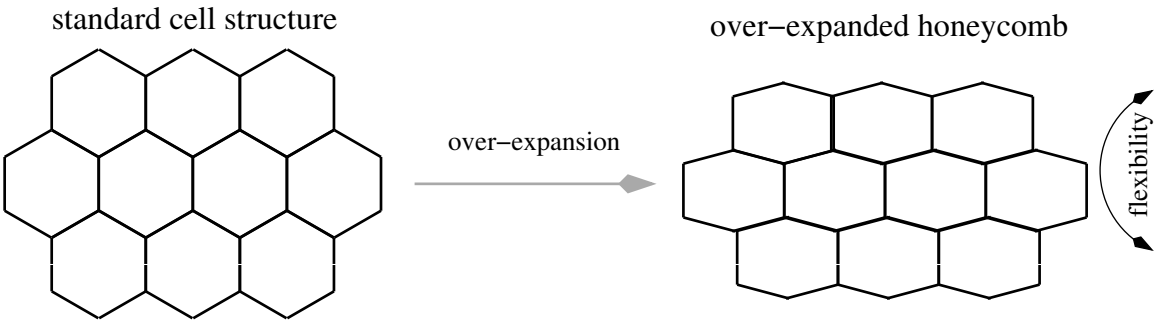

Figure 5.29: *Cell structure of standard and over-expanded of a honeycomb*

proved its robustness. Figure 5.28(a) displays a photograph of a material sample piece. The volume density of the material has been measured to less than $0.3\,{}^{g}/_{cm^3}$. This is less than discussed alternative materials like foams[6]. To build the honeycomb into the field cage wall, it must be bended around the cylinder. Therefore a special type has been used, so-called over-expanded honeycomb. This material has a modified cell structure compared to standard honeycomb material, as illustrated in figure 5.29 (see also figure 5.28(a)). It is more flexible in one direction and allows for the construction of the round shapes without putting extensive tension on the honeycomb.

The MediTPC has been constructed with conductive carbon fibre reinforced plastic as top layers on the honeycomb. This requires a good insulation between the field strips and the composite structure. Therefore a different top layer material, namely glass fibre reinforced plastic (GRP), has been used which is a good insulator.

[6]for example Evonik Rohacell®

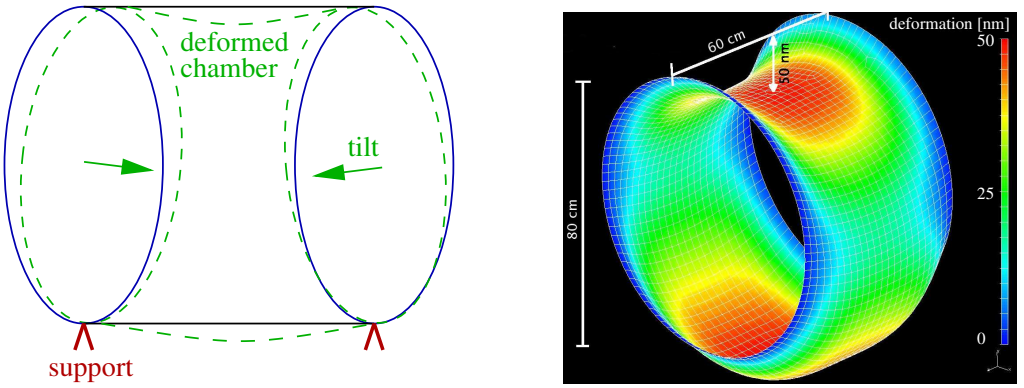

(a) boundary conditions for the calculation

(b) sagging of the field cage due to gravity

Figure 5.30: *Finite element calculations of the field cage statics*

5.4.1 Optimisation of the Wall - Simulations and Mechanical Tests on Sample Pieces

It is sophisticated R&D work to optimise a composite structure like the field cage wall for its field of application. To reach the lowest material budget possible, the massive GRP layers should be kept as thin as possible. At the same time the field cage must be sufficiently stable against high-voltages and robust during handling. Moreover, deformations of the chamber due to mechanical loads must stay below some 10 μm. Larger deformations could displace the end plates and worsen the electric field. Finally, the structure must be possible to construct.

For optimisation purposes, finite element calculations can be used, complemented by tests on sample pieces. However, FEM calculations are complicated for composite constructions, because the precise parameters of the different materials and the glue connections have to be known to get trustworthy results. Moreover, imperfections of a honeycomb can reduce the stability locally, which is difficult to account for in a calculation. Therefore FEM calculation results have to be validated with comparative mechanical tests of sample pieces.

In the following, FEM calculation results are discussed for a simple model of the LP. These are first example studies and not meant to optimise the field cage wall to the very lowest material budget. As the LP is a test chamber, in first place it has to be robust. In addition, results of tests are discussed that have been made with sample pieces of the type shown in figure 5.28(b). The samples have been developed in cooperation with the company that constructed the field cage.

GRP - honeycomb - GRP [mm]	max. deformation [nm]
1.5 - 17 - 1.5	57.5
1 - 18 - 1	55.2
0.5 - 19 - 0.5	53.1

Table 5.2: *Maximal deformation of the chamber due to gravity for different cross-sections of the wall*

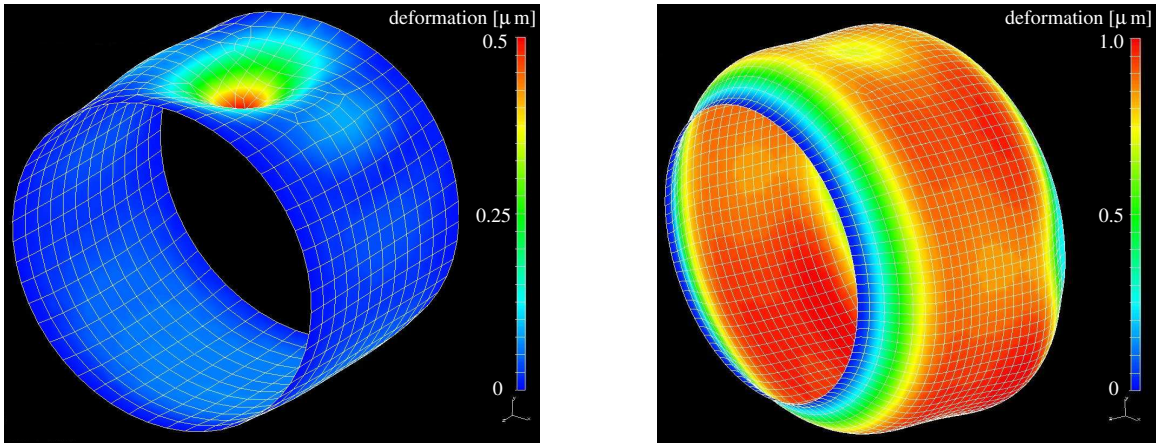

(a) deformation of the field cage under a 5 kg load

(b) deformation under overpressure of 100 mbar

Figure 5.31: *Deformation of the field cage under a five kilogramme load*

Simulations on the Statics of the Field Cage

The FEM studies of the LP statics have been performed with a software[7] for composite structure calculations. The LP model is a cylinder with an outer diameter of 80 cm and a length of 60 cm and sketched in figure 5.30(a). At the time when these studies have been done, the dimensions of the field cage have not been fixed yet. Therefore the diameter and the length of the model are different compared to the actual field cage. Also the thickness of the wall was modelled with 2 cm instead of 2.5 cm. As fixed boundary condition, the model cylinder has a circular shape at both end flanges, because the attached end plates are assumed not to deform. The end plates are supported in a single point and can tilt as illustrated in figure 5.30(a).

Figure 5.30(b) shows the calculated deformation of the chamber due to gravity. As no load is on the barrel, it sags by only 50 nm at most. Here the wall is modelled with 500-μm-thick GRP layers and a 19-mm-thick honeycomb spacer. The same calculation has been made for different thicknesses of the GRP, and the calculation results are

[7] module for UGS IDEAS

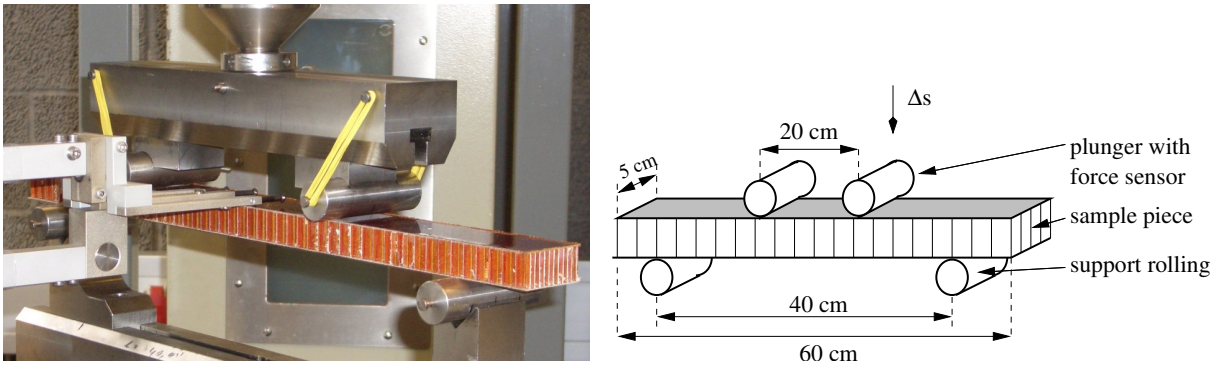

(a) photograph of the setup **(b)** schematic view

Figure 5.32: *Bending test of a wall sample piece*

summarised in table 5.2. The deviations are approximately constant and independent of the GRP thickness. If any, the results show a tendency that a reduction of the GRP-layers thickness also reduces the deformation. Making the GRP thinner decreases the weight of the structure and hence it is less deformed by gravity.

To simulate the handling of the LP, the deformation of the model under a dummy load of five kilogramme has been calculated. This is roughly the force that the chamber has to stand when being carried. The result of the calculation is displayed in figure 5.31(a). Here, the maximal deformation is 0.5 μm. Additionally the effect of a gas overpressure of 100 mbar in the chamber has been investigated. The overpressure balloons the chamber by about 1 μm as shown in figure 5.31(b) which is still in an acceptable range.

Following the results of these studies, the GRP layers could be thinned below 500 μm. However, the calculated deviations are very small and it is unclear whether they are reliable, because the parameters of the calculation have not been adapted to the materials of the field cage. For example the shear modulus of the honeycomb or the parameters of the glue have not been determined at the early stage of R&D work. Here, only preset default software parameter have been used.

These studies are a starting point for ongoing investigations of this kind. Such simulations will become necessary to optimise the final TPC for the ILD detector for a low material budget and a sufficient mechanical stability.

Bending Tests on Sample Pieces

A mechanical test gives an unbiased result on the stability of a composite structure and shows effects that could be modelled incorrect in the calculation. Figure 5.32 illustrates a standardised test setup. A sample piece rests on two supporting rollings with a diameter of 5 cm arranged in a distance of 40 cm. Two similar rollings, arranged in a distance of 20 cm, press centrally against the sample piece from the top until it eases. In parallel, a force sensor measures the force F and the bending Δs.

This four point bending test has been performed with two 5×60-cm^2-large sample

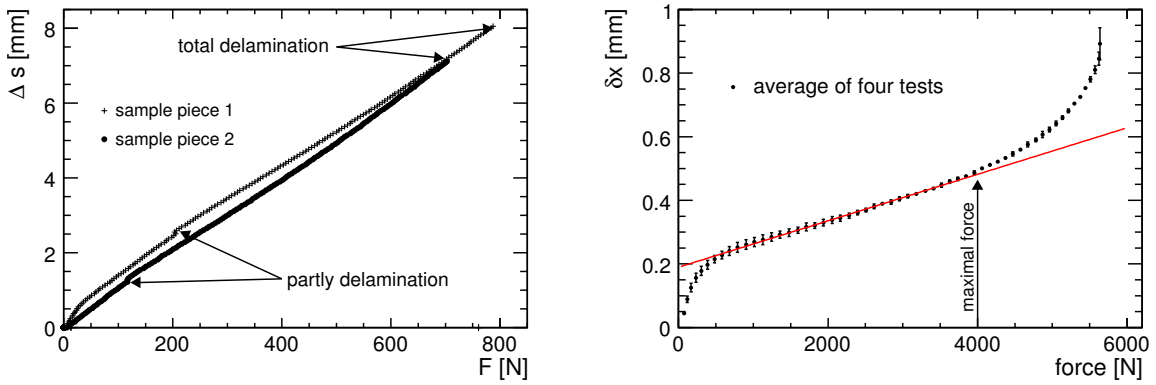

(a) results of bending test

(b) results of pull out tests of the inserts

Figure 5.33: *Results of mechanical tests with sample pieces of the field cage wall*

pieces[8]. Their walls consisted of 400-μm-thick GRP layers on a 20-mm-thick spacer. The diagram in figure 5.33(a) shows the measured bending versus the applied force. Both tests gave a similar result: the sample pieces could stand about $650 - 700\,\mathrm{N}$ until they completely delaminated. At the maximal force, the bending was around 8 cm. But, the samples incurred irreversible damage already at smaller forces. The characteristic curves exhibit unsteady points at about 150 N to 200 N. These indicate first delamination processes, that were accompanied by cracking noises.

The finite element calculation of the setup predicts a reduced bending and the results are incompatible with the measured curves. Currently, studies have started to determine the exact parameter of the used materials in the LP wall. The refined calculations will be compared with results from a new series of sample piece tests [75].

The test results give the impression that the structure is able to stand a local force of 100 N. This has been estimated as sufficient for the handling of the about 10-kg field cage. In addition, the laminate GRP surface turned out to be stiff enough not to crack immediately, if for example a screwdriver accidentally falls on the field cage.

After having consulted the manufacturer, the thickness of the GRP layers was fixed to 300 μm, based on the manufacturer's experience. This is a further reduction of 100 μm compared to the sample pieces.

Pull out Test of Threaded Inserts

The bending tests give an impression of the field cage robustness towards the handling in the test beam area. In addition, a recurrent mounting and demounting of the end plates should be possible without excessive abrasion. The threaded inserts that are installed in the end flanges, must be robust over the expected useful life of the field cage. They are produced from 25-mm-long stainless steel rods and have been tested in

[8] in collaboration with the Technische Universität Hamburg-Harburg

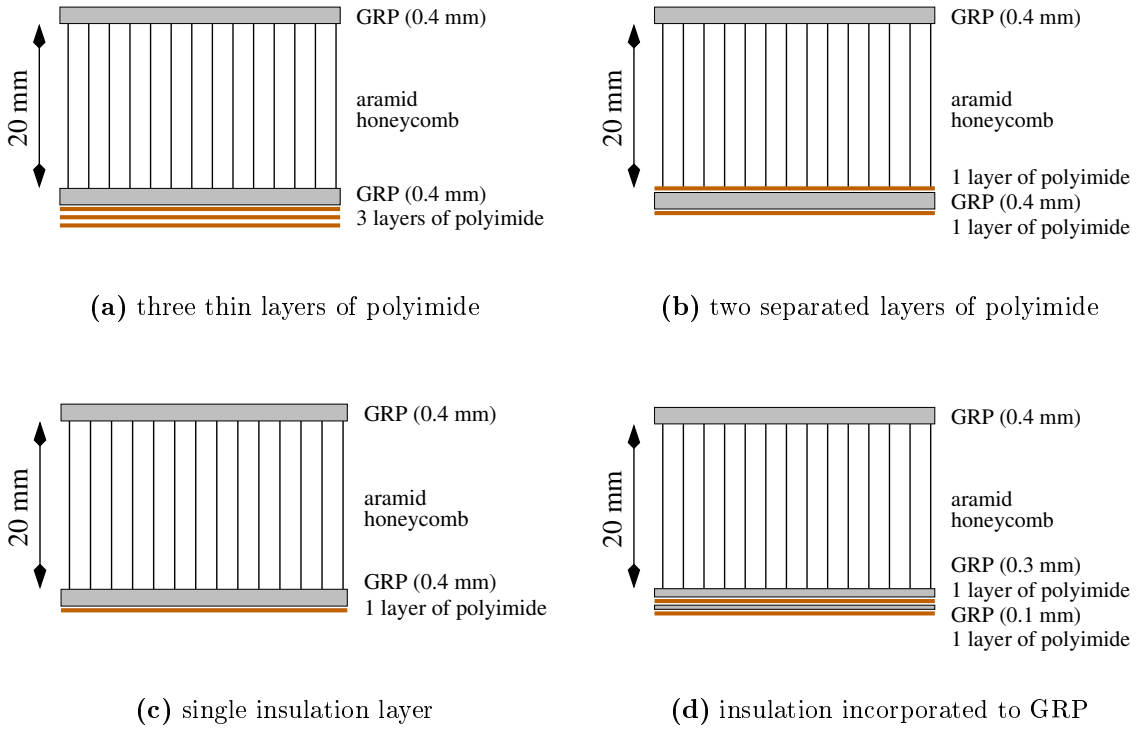

(a) three thin layers of polyimide

(b) two separated layers of polyimide

(c) single insulation layer

(d) insulation incorporated to GRP

Figure 5.34: *Cross-sections of the wall sample pieces*

a series of pull-out tests. For this, several inserts have been glued into a sample piece of the hard foam material. In a dedicated measurement apparatus, a pull out force was applied until the insert broke out. Such tests have been performed with five inserts. Figure 5.33(b) shows the average measured movement of an insert in the foam material δx versus the applied force. The uncertainties on δx are the standard deviations of the five test results.

In a range up to 450 N, the test apparatus got tightened. For increased forces up to 4 kN, δx rises linear. Above, an insert breaks out of the sample. Assumed the foam material behaves elastic in the linear range and assuming a safety factor of two, 2 kN is the maximal force that can be loaded on an insert.

5.4.2 High-Voltage Stability Test of the Field Cage Wall

At the maximal operational field strength of $350\,{}^{V}/_{\mathrm{cm}}$, the cathode and the last field strips lie on a potential of up to 23.5 kV. In this region, the voltage difference to the outer shielding applies an electric field of about $10\,{}^{kV}/_{\mathrm{cm}}$ in the field cage wall. To guarantee a safe operation of the LP with the highest drift fields, breakdown voltage tests have been performed with the sample pieces before the design of the field cage was finalised.

thickness [μm]	app. breakdown voltage [kV]	electric field strength $^{V}/_{\mu m}$
25	7.6	303
50	12	240
75	15.4	205
125	19.3	154

Table 5.3: *Breakdown voltages of different polyimide layers* [76]

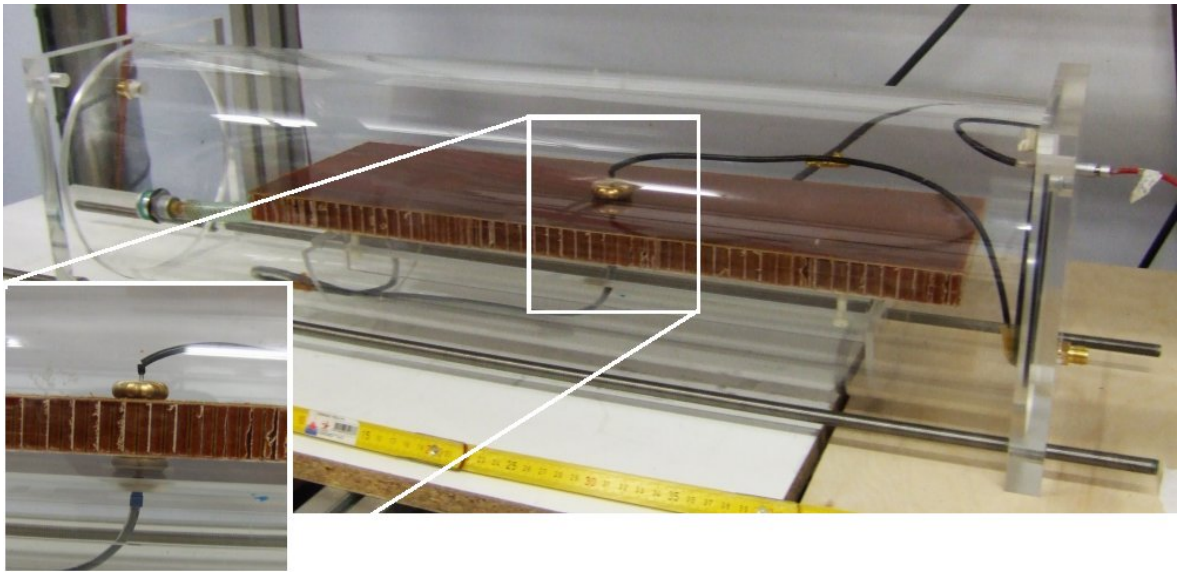

Figure 5.35: *High-voltage test setup*

Cross-sections of the Wall Sample Pieces

The high-voltage insulation of the field cage wall is provided by the 125-μm-thick polyimide insulation layer (see figure 5.1(b)) and by the honeycomb structure. To have a maximal operational safety, the insulation layer is dimensioned such that it alone can stand the voltage differences of about 20 kV.

According to the technical specifications, the breakdown stability of the used insulation material[9] is not proportional to the layer thickness. Breakdown voltages are listed in table 5.3 for different polyimide foil thicknesses. A 25-μm-thick foil is able to stand about twice the field strength than a 125-μm-thick one. Hence, the material budget could be reduced if the insulation layer is split up in many thin polyimide foils instead of a single thick one. To test several arrangements, four different sample pieces have been produced with the cross-sections illustrated in figure 5.34. In the samples, 50-μm-thick polyimide foils have been processed, because foils of different thicknesses have not been available for the production.

The setup of figure 5.34(a) the insulation is made up of three polyimide layers. If

[9] DuPont, Kapton^{TM} HN [76]

these were each 25 μm thick, the combined insulation could stand 22 kV and would be in total 75 μm thick. However, this design is disfavoured because additional gluing layers with an undefined thickness need to be introduced to connect the polyimide foils. Moreover, in the gluing process air bubbles are easily introduced between the layers. Such air bubbles could not be avoided in the sample piece. These air inclusions focus electric field lines in operations and possibly reduce the high-voltage stability of the foil sandwich.

The layout in figure 5.34(b) solves this problems partly. Instead of gluing the polyimide layers directly onto one another, they are separated by one of the GRP layers. To recover the 20-kV-breakdown voltage, one foil has to be 50 μm thick, while for the other 25 μm would be sufficient. The problem with air inclusions is solved, because the GRP is produced in a wet process and the air can be removed with an underpressure treatment. This procedure is discussed in chapter 6. However, the honeycomb is glued directly onto the polyimide surface. Polyimide is not very adhesive for epoxy glue and hence it does not allow for a strong connection to the honeycomb. Since this is one of the decisive connections, this layout has been rejected because of the possible loss of stability.

Figure 5.34(c) sketches the layout, which has finally been chosen for the LP. The insulation consists of a single polyimide foil only, which has to be 125 μm thick in order to stand about 20 kV. The thicker layer accounts for a higher material budget, but is optimal in terms of fabrication.

Finally in the design in figure 5.34(d) the insulation is again split in two polyimide foils. Contrary to the layout in figure 5.34(b), here the GRP is split up into a thin 100-μm layer and a 300-μm-thick one. In the production, the thin GRP is laminated onto the insulation foil while air inclusions are removed with the underpressure treatment. The second polyimide layer is attached onto the thin GRP and introduces new inclusions that are be removed as well. The production showed that this is not a good solution: the sample piece still showed larger air inclusions, in particular in the GRP layer between the two foils. These air bubbles could not escape at the edges when the underpressure was applied. Thus this design is disfavoured.

High-Voltage Tests of Wall Sample Pieces

The high-voltage stability of the four samples has been tested with the setup shown in figure 5.35. In the safety tube, a sample piece is placed between two circular electrodes of about 20 mm^2 size. During the test, the upper electrode was grounded and the lower one put on 30 kV. The current was monitored for 24 hours while a trip threshold limited it to a maximum of 20 μA.

All four sample pieces passed this test without trips and currents below the measurement sensitivity of 2 μA. Thus already the simplified cross-section in figure 5.34(c) with only one 50-μm-thick polyimide layer alone - as it was used in the sample piece - provides a sufficient operational safety for permanent operation with at least 25 kV.

As this layout is optimal in terms of fabrication, it has been chosen for the LP. Yet,

material	d [cm]	molecule	X_0 [g/cm^2]	ρ [g/cm^3]	X_0 [cm]	X_0^{material} [%]
copper	0.007	Cu	13.0	8.9	1.47	0.45
polyimide	0.016	$C_{22}\,N_2\,0_5\,H_{10}$	40.8	1.4	29.2	0.07
glass fibre	0.04	$Si\,O_2$	23.0	2.2	10.5	0.38
aramid paper	0.007	$C_{14}\,O_2\,N_2\,H_{10}$	41.5	1.4	29.7	0.02
honeycomb	2.35		41.5	0.03	1480	0.15
epoxy	≈ 0.06	$C_2\,N\,H_4$	42.5	≈ 1.2	≈ 35.4	≈ 0.17
					$\sum$	≈ 1.24

Table 5.4: *Radiation lengths and composition of the materials in the field cage wall* [77, 62]

the LP wall cross-section is modified compared to the sample piece. The GRP layers are thinned to 300 μm, potentially on the cost of HV stability. This is recovered by the thicker honeycomb of 23.5 mm, the additional layer of aramid paper on its outside and, finally, in the LP the polyimide layer is 125 μm thick.

In summary, the results of the voltage breakdown tests, extrapolated to the changed parameters of the field cage wall, guarantee a safe operation of the LP for voltages of up to 25 kV at the cathode.

5.5 Radiation Length of the Wall

The final field cage walls consist of nine different layers, including the field and mirror strips. Figure 5.36(a) illustrates the layer arrangement and the used materials. To estimate the wall's radiation length X_0^{wall}, the different materials and their effective layer thicknesses d_{i} have to be considered.

In table 5.4 the effective numbers are summarised and in the following they are discussed in detail. The field and mirror strips consist of copper and are 35 μm thick. Together with the about 30-μm-thick outer shielding layer, this sums up to 100 μm in total. Polyimide is used in the 125-μm-thick insulation layer and as carrier foil of the field strip board - this is 160 μm in total. The two GRP layers are together 600 μm thick - here it is assumed that GRP is effectively 2/3 glass fibre and 1/3 epoxy glue. Hence, the GRP is split up in a 400-μm-thick glass fibre canvas and effectively 200 μm of epoxy. In addition, six different epoxy layers are used in the wall laminate. Their thickness is undefined and estimated to 70 μm each. Thus, with the contribution in the GRP the epoxy sums up to 600 μm. The honeycomb and the additional layer of aramid paper have a defined thickness of 2.35 cm and 70 μm, respectively.

To estimate the different X_0^{material}, the radiation lengths X_0 of the individual materials need to be known. A formula for X_0 valid for raw materials layers, like copper, is (e.g. [12]):

$$X_0^{\text{raw material}} = \frac{716.4\,\text{g}\,\text{cm}^{-2} A}{Z(Z+1)\ln(287/\sqrt{Z})}. \tag{5.8}$$

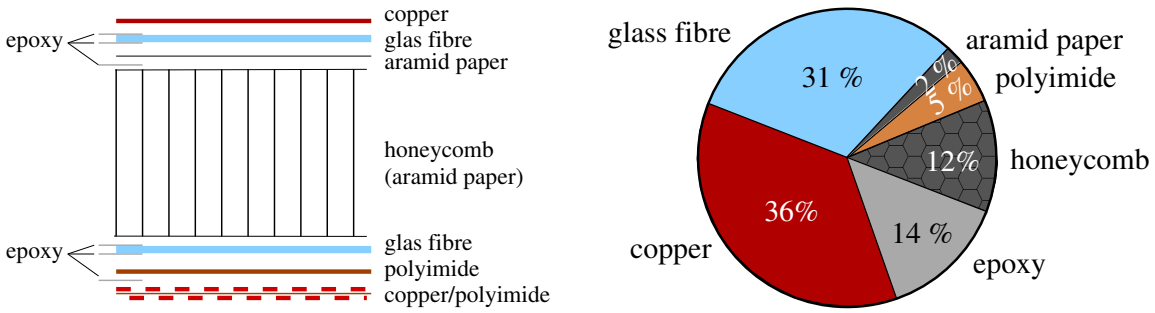

(a) material in the layers

(b) contributions to the radiation length

Figure 5.36: *Material layers and material budget in the field cage wall*

Z and A are the atomic and mass number of the material, respectively. Polyimide, aramid paper and GRP are compounds materials. Their radiation lengths need to be calculated in a weighted sum

$$X_0^{\text{compound}} = \left(\sum_i \frac{w_i}{X_{0,i}^{\text{raw material}}} \right)^{-1} \qquad \text{with the weights} \qquad w_i = \frac{n_i A_i}{\sum_j n_j A_j} \tag{5.9}$$

from the radiation lengths X_i of the elements in the compound. The weight factor w_i for an element is determined by the molecular composition [77] of the material: n_i is the abundance of the specific atom in the compound molecule and A_i the corresponding atomic number. The weight is normalised by sum over the whole molecule.

With X_0^{material} available the fraction of a total radiation length can be calculated which a layer accounts for (see table table 5.4):

$$X_0^{\text{material}} = \frac{X_0\,[\text{g/cm}^2]}{\rho\,[\text{g/cm}^3] \cdot d\,[\text{cm}]} = \frac{X_0\,[\text{cm}]}{d\,[\text{cm}]}.$$

Herein ρ and d are the density and the layer thickness, respectively. X_0^{material} is the radiation length of the material or compound and calculated with equation (5.8) or (5.9), respectively. The calculated numbers are given in table 5.4.

Summing up the contributions, the total radiation length of the wall is

$$X_0^{\text{total wall}} = \sum X_0^{\text{material}} \approx (1.24 \pm 0.30)\,\%.$$

The uncertainty is due to the estimations made in the calculation. For example, the composition of the GRP layer could be estimated differently or the thickness of the epoxy layers could be increased. Figure 5.36(b) illustrates the different contributions to $X_0^{\text{total wall}}$ in a pie chart.

5.6 Final Field Cage Construction Plans

The optimisation procedures define a field cage that can meet the demands for the LP. In summary, the key design points are

- the end faces of the field cage have to be parallel with deviations less than 150 μm
- the axis of the field cage has to be within a tube of 100 μm diameter over the whole length of the field cage, if it is defined being perpendicular to the anode end face
- field and mirror strips have to be installed on the field cage inner wall, in the optimal layout (see figure 5.1(c))
- the resistors between the field strips have to reach an accuracy of $^{\Delta R}/_{R} \lesssim 10^{-4}$
- the wall has to be made of a lightweight composite with an extra insulation layer and be able to withstand voltage differences of 20 kV

Figure 5.38 summarises the construction plans for the field cage in an engineering drawing. The two-dimensional overview drawings fix the outer dimensions of the field cage, while the five detail drawings define the end flanges.

Outer Dimensions of the Field Cage

In the longitudinal cut view (A-A in the drawing), the field cage's length is dimensioned to 610 mm with a comparably large tolerance of 1 mm. The length is not a critical parameter because the cathode can be adjusted relative to the anode and the field strips on the intermediate flange.

The field cage end faces are required to be parallel with deviations smaller than 100 μm, which is even more stringent than 150 μm (see section 5.3.1). When the end plates are installed properly, they will be parallel about the required level and a fine-adjustment of the cathode can be performed before operation. The construction plans define the anode end face to be perpendicular to the cylinder axis within 100 μm. That means that the axis could deviate by $\sim 80\,\mu$m from the normal axis of the anode plate at the cathode. This would be more than specified. The adequate tolerance has to be 60 μm because

$$60\,\mu\text{m} \cdot \frac{\text{length of the field cage}}{\text{diameter of the field cage}} \approx 60\,\mu\text{m} \cdot \frac{6}{7} \approx 50\,\mu\text{m}$$

The required 100-μm accuracy is already challenging in terms of the production. A refinement can be requested if a second field cage is to be built, which is currently under discussion.

Layout of the End Flanges

Four detail drawings in figure 5.38 are dedicated to the end flanges. The most important numbers are summarised in figure 5.37. The first field strip, viewed from the anode

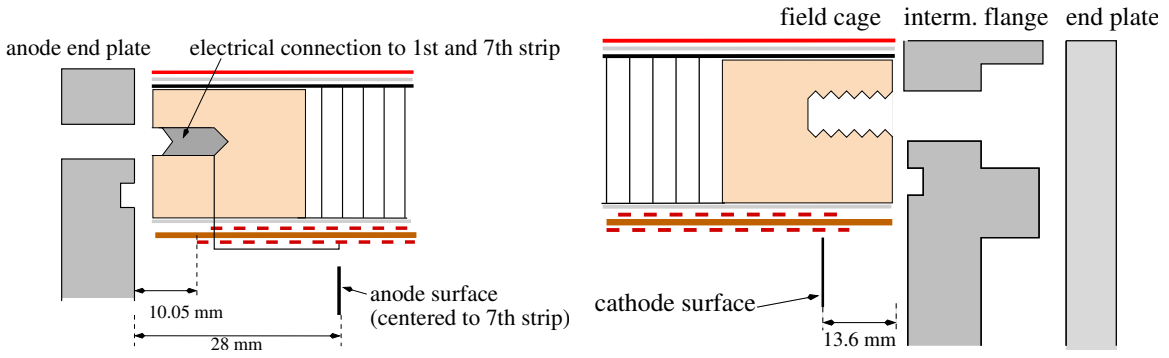

(a) anode side **(b)** cathode side

Figure 5.37: *Detailed layout of the field cage's end faces*

side, has a nominal distance of 10.05 mm to an anode end plate attached to the field cage. An adapted additional spacer strip has been installed at this side of the field strip board, as mentioned in section 5.2.4. The offset is chosen such that the centre of the seventh field strip has a distance of 28 mm to the anode end plate. Centred to this strip, the anode surface is installed [71]. The corresponding distance of the cathode surface to the other end of the field cage is 13.6 mm. One strip lies behind the cathode surface on this side. In the end, the nominal drift length is 568.4 mm.

Two high-voltage connections are installed in the end flange on the anode side. A first one connects to the seventh field strip, whereas the second is soldered to the first one. These strips can be put on different voltages during operations. Thus the potential gradient behind the anode can be chosen differently to the drift field.

Besides the mentioned reinforced M6-threaded inserts, four dowel pins are glued into the end flanges on both sides. These pins fit to dowel holes in the anode plate and the intermediate flange, respectively. They guarantee a reproduceable positioning of the end plates.

Field Strips Board and Resistor Chains

The front view on the field cage in figure 5.38 illustrates the position of the resistor chains. Initially, the field strip board has been designed for a diametrical placement of the resistors. After the board layout was finished, the planned outer circumference of the LP has been reduced to the final value of 77 cm. This was necessary because more space in the PCMAG was needed by the mounting structure as estimated before. The change reduced the available space for the field cage. The design of the field strip boards has not been completely adapted to this change - only the length of the boards was changed. Thus the resistors are not perfectly diametrical, but slightly displaced.

A diametrical placement is preferential, because charges which are deposited on the field strips have a minimal distance to one of the resistor chains and can discharge the quickest possible way.

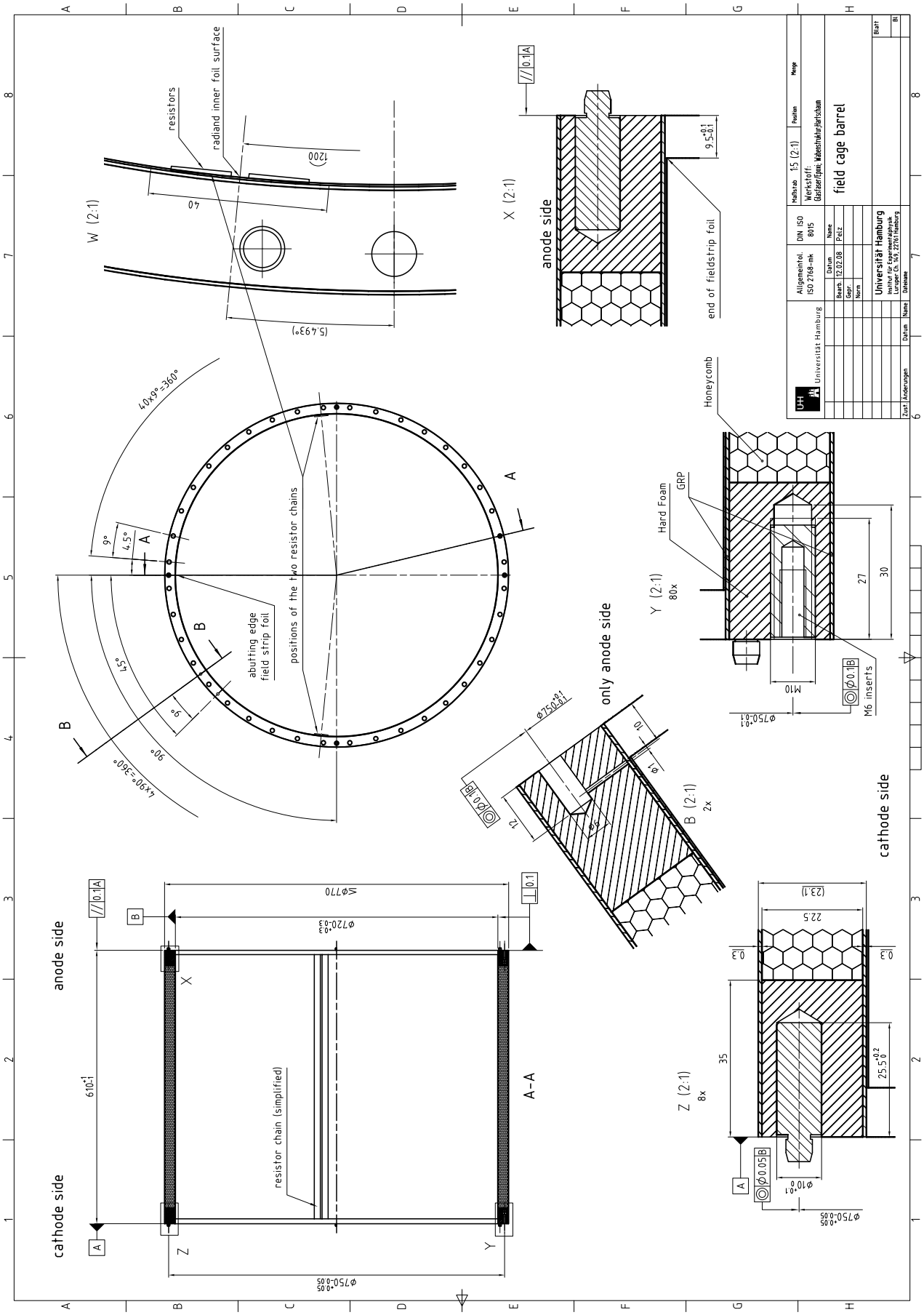

Figure 5.38: *Field cage construction plans*

6 Construction and Commissioning of the Field Cage for the Large Prototype

The field cage for the Large Prototype (LP) has been manufactured between May and July 2008. Like the preparatory design studies, the construction was performed in collaboration with a company specialised in composite materials[1]. This chapter describes in section 6.1 the manufacturing process which follows the design worked out in the previous chapter. After the field cage had been delivered to DESY, its outer dimensions have been measured in a quality survey. The results are reported in section 6.2. In the subsequent section the achieved drift field quality in the LP is estimated on the basis of the achieved accuracies,.

6.1 Production of the Field Cage on a Forming Tool

The field cage has been built in a common technique for composite constructions. For this, a forming tool has been designed and produced as a first step. The tool is a cylindric mandrel with a diameter of 72 cm, corresponding to the field cage's inner diameter, and its length is about 75 cm. The mandrel is made from aluminium and it is reusable for the production of another field cage. In the production process, the different layers of the field cage wall were laminated onto the mandrel surface. This procedure is illustrated in figure 6.1. After a new layer had been attached, the wet epoxy glue was cured at 60 °C. The curing temperature was kept comparably low, so that the aluminium in the mandrel does not expand too much and thereby put the field cage under tension.

The mandrel is furnished with an expansion slot which allows for a reduction of its diameter by a few millimetres. This way, the field cage could be taken off the mandrel without damage after it was finished.

6.1.1 Lamination of the Field Cage Wall

In the first production step, the combined field strip board was placed and aligned on the mandrel. As discussed in section 5.4, the board was assembled with the SMD resistors and electrically tested beforehand. The mandrel has two 1-mm-deep grooves

[1] Haindl, Individuelle Kunststoff-Verbundbauweise

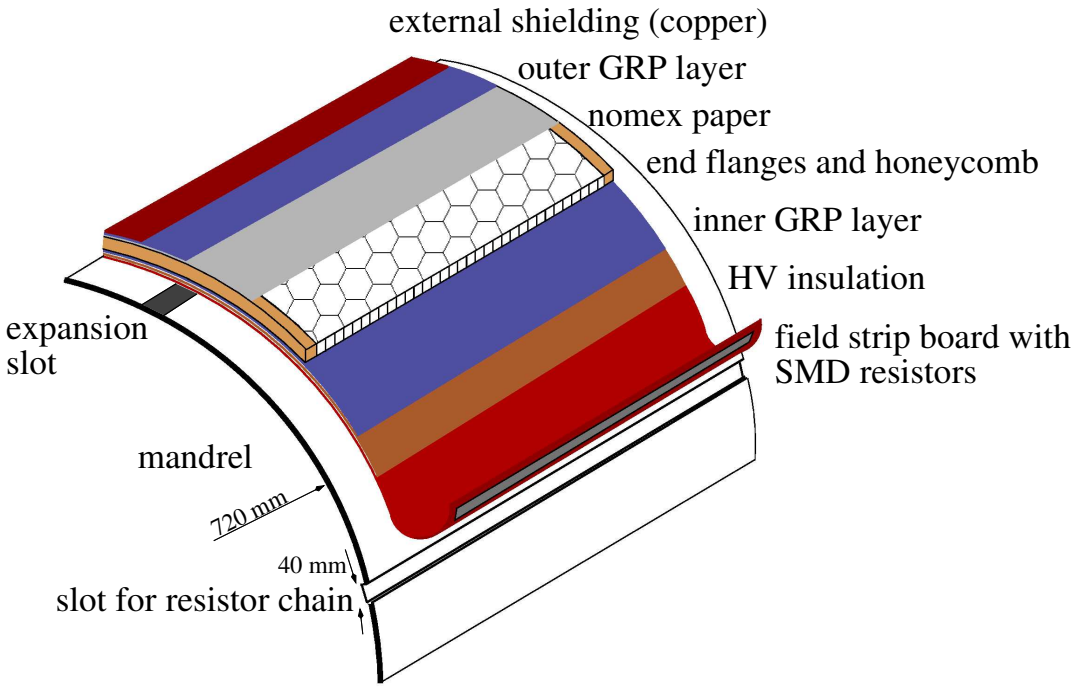

Figure 6.1: *Production of the field cage on the forming tool*

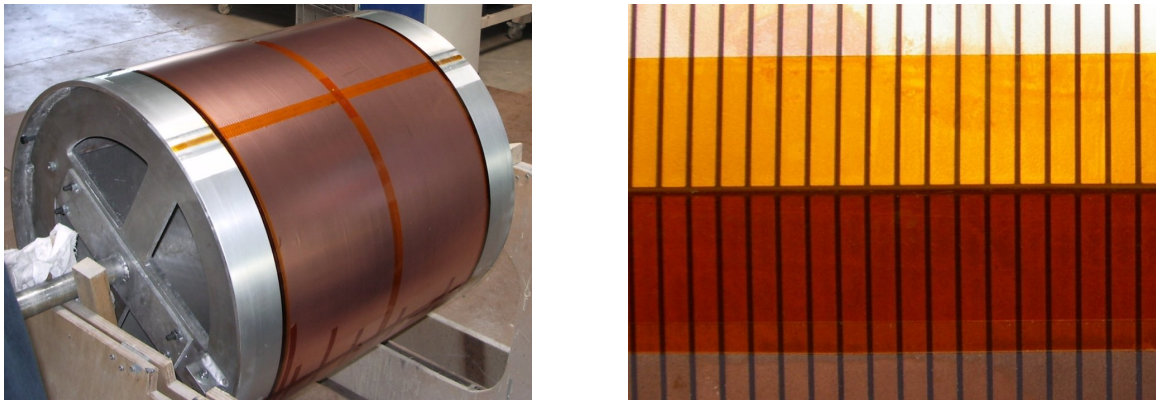

(a) photo of a the field strip foil mounted on the mandrel

(b) alignment of the field strips

Figure 6.2: *First step of the field cage production: placement of the field strip boards on the mandrel*

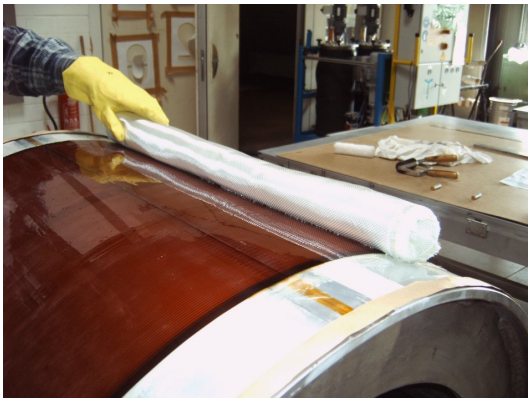

(a) application of the GRP

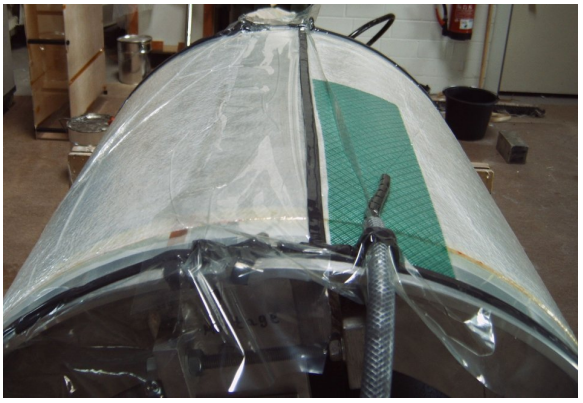

(b) vacuum treatment to reduce air inclusions in the inner GRP layers

Figure 6.3: *Lamination of the inner GRP layer*

machined into its surface which accommodated the resistors when the board was put on. Thereby, the correct alignment of the field strips was most crucial. The board had to be tightened to the mandrel in order to guarantee the flatness of the inner surface of the field cage barrel. At the same time, both ends of one field strip had to be jointed without displacement. Figure 6.2(a) shows a picture of the mandrel with the field strip board in place and figure 6.2(b) the junction of both ends. The field strip board's length was designed to fit the circumference of the mandrel and the gap at the junction was about 100 μm wide. As figure 6.2(b) shows, the alignment worked without obvious displacements.

In the next step, the high voltage insulation layer was glued onto the field strip board. During this process, the gaps between the mirror strips provided channels to remove air inclusions. Next, the inner GRP layer was laminated - 300 μm thick - onto the insulation layer, as shown in figure 6.3(a). In this step firstly a glass fibre canvas was laid onto the insulation layer. This was moisturised with epoxy and air inclusions were removed from the wet layer. Then an underpressure treatment was applied - the method is shown in figure 6.3(b). The whole mandrel and the wet laminate were covered air tight in a foil and the volume was evacuated. Thereby air bubbles were pressed out of the still wet epoxy glue. Successively the epoxy was cured. Figure 6.4(a) shows an image of the resulting GRP layer with the underlying mirror strips.

Afterwards, the hard foam end flanges were positioned at both ends of the field cage. Each of the two flanges was machined in three parts and these parts were joined on the mandrel to form the flange. Figure 6.4(b) shows a photograph of this production step. An adapted cut out of the honeycomb was laminated between the two end flanges, as figure 6.1 shows schematically. The thickness of the honeycomb was 23.5 mm and fitted the thickness of the flanges.

Typically, the next layer would have been the outer GRP layer, following the standard

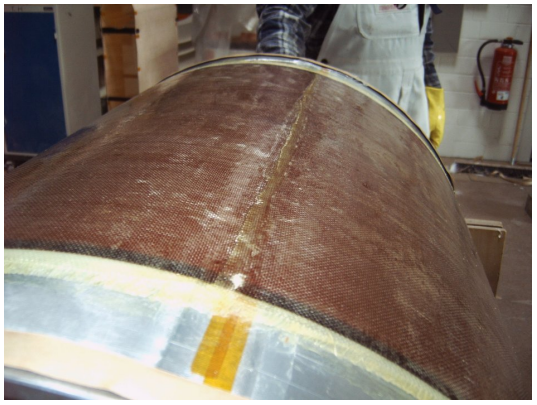

(a) first GRP layer cured

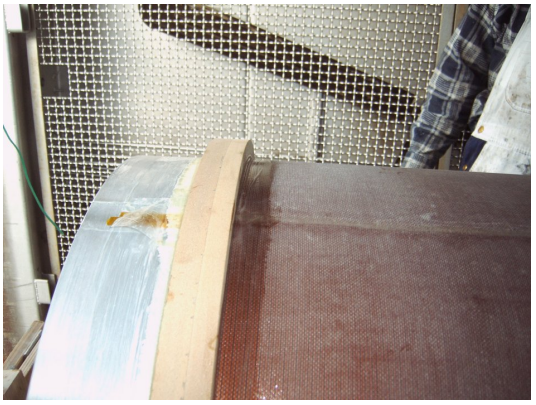

(b) lamination of the termination flanges

Figure 6.4: *Inner GRP layer and termination flanges*

cross section for a composite wall that is discussed in section 5.4. However, the lamination was done in a wet process and therefore the cells of the honeycomb could have been filled partly with glue. This would have resulted in an inhomogeneous material density of the field cage wall. To avoid this problem, an additional thin layer of aramid paper was introduced on the outer honeycomb. Aramid paper can be adhered with glue such that the wet epoxy does not drip down. This additional layer closed the cells and held back the wet epoxy when the second GRP layer was applied onto it. After the curing, the external copper shielding was attached as the last layer. Before the field cage was put off the mandrel, the dowel pins and the thread inserts were installed into the end flanges.

Figure 6.5 depicts an image of the completed field cage, viewed from the cathode side. Here, the anode plate is already attached and the module windows are closed with dummies.

6.1.2 Intermediate Flange and Cathode

In parallel to the field cage, the intermediate flange (see figure 5.1(a)) was constructed, which supports the cathode plane. It is produced from GRP, since this material provides a good voltage insulation. Figure 6.6 shows the flange attached to the field cage. Here it is also equipped with the cathode plate. A first-generation cathode is made from copper-plated aluminium. It is mounted on three adjustable points. Before operation, the anode is attached to the field cage and the cathode parallel-aligned with respect to its surface. Afterwards, a GRP end plate can be screwed onto the intermediate flange. It closes the field cage gas tight and without reasonable disturbance of the alignment. The end plate provides a high-voltage connection to the field strips and the cathode, as well as a gas inlet.

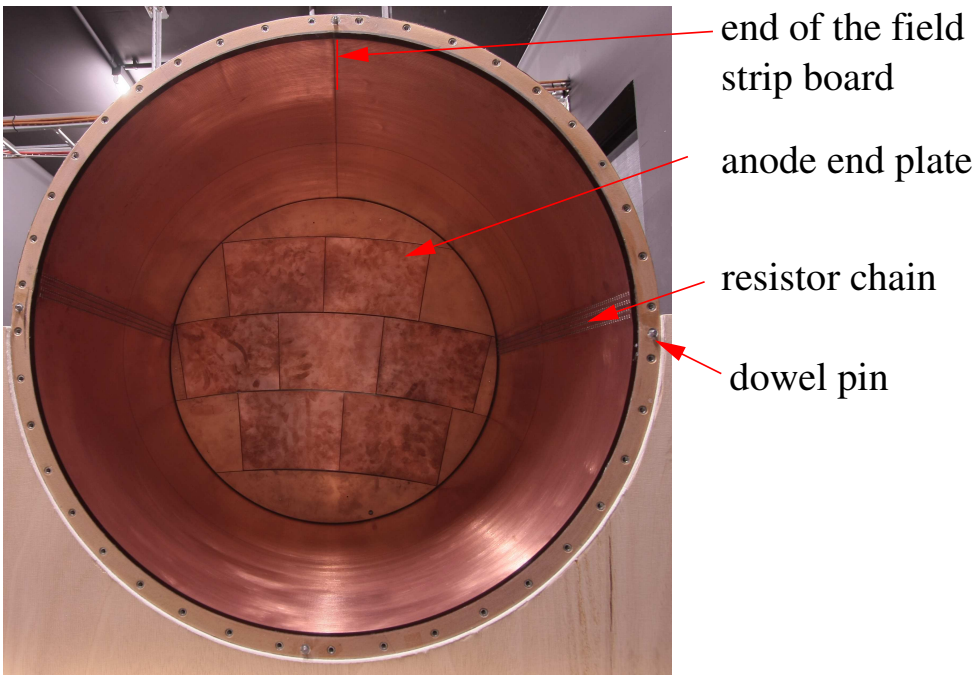

Figure 6.5: *Field cage of the LP*

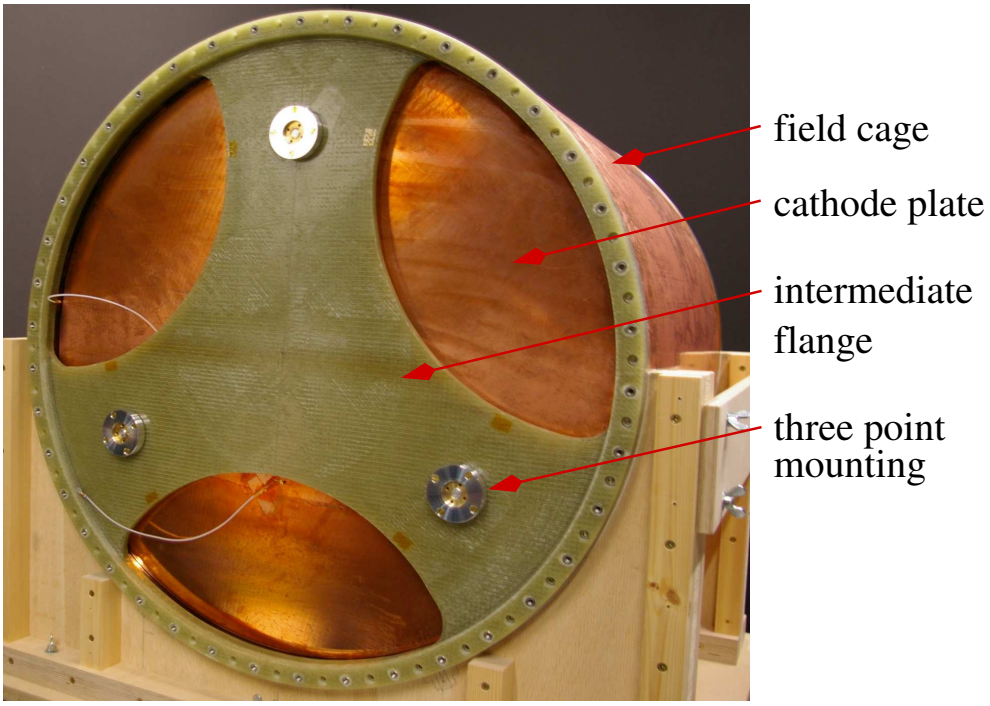

Figure 6.6: *Intermediate flange with the cathode assembled to the field cage*

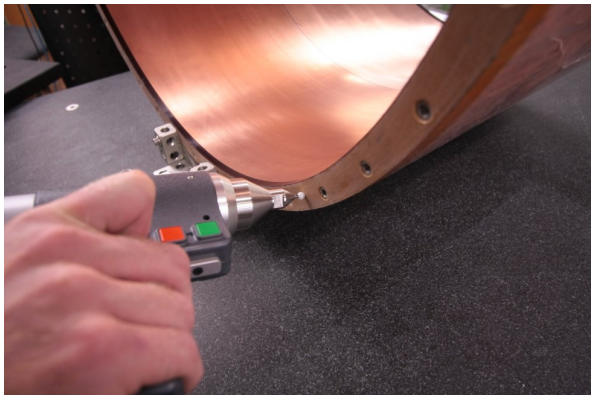

(a) measurement of a reference point

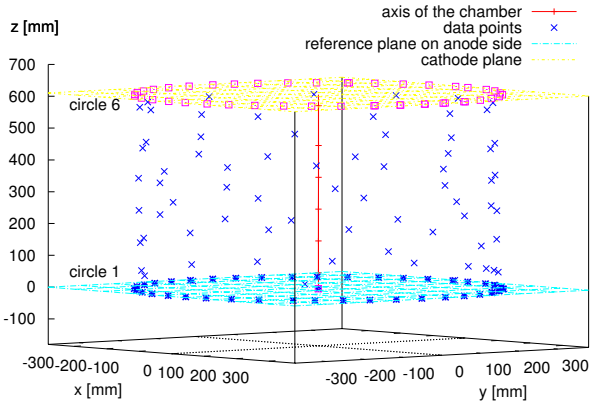

(b) data points taken over the field cage

Figure 6.7: *Measurement of reference points over the field cage*

6.2 Fabrication Quality Check of the Field Cage

In the fabrication survey, measurements have been done to check in particular the tolerance parameters that are crucial for the drift field quality. These are the alignment of the anode and cathode end faces and the axis of the barrel. For this, the field cage was measured with a special measurement device shown in figure 6.7(a). This test prod determines the location of space points relative to a fixed coordinate system with a spatial accuracy of 25 μm. With this tool, about 160 measurement points were taken on both end faces and inside the field cage barrel.

Figure 6.7(b) gives an overview over the whole data set. In total, these are about 80 measurement points on the end faces - Figure 6.7(a) shows the recording of such a point - and likewise about 80 points inside the barrel.

6.2.1 Alignment of the End Faces

The measurement points on the end faces allow to evaluate the alignment of the anode and cathode end faces with respect to one another. Figure 6.8(a) illustrates the relevant subset of points for this measurement. On both ends of the barrel, the points approximately follow the circle where the o-rings are pressed against the termination flange when the end plates are installed. The o-rings will balance the unevenness of the surface. Hence the end plates are assumed to arrange parallel to planes, which are fit to the measurement points (see figure 6.8(a)).

Written in Hesse normal form, the fitted plane on the anode side is

$$\left[\begin{pmatrix} 0 \\ 0 \\ 1 \end{pmatrix} \pm \begin{pmatrix} 18 \\ 17 \\ 0 \end{pmatrix} 10^{-6} \right] \cdot \vec{x} = (0 \pm 0.005)\,[\text{mm}]. \qquad \text{with} \qquad \chi^2/\text{ndf} = 46/43.$$

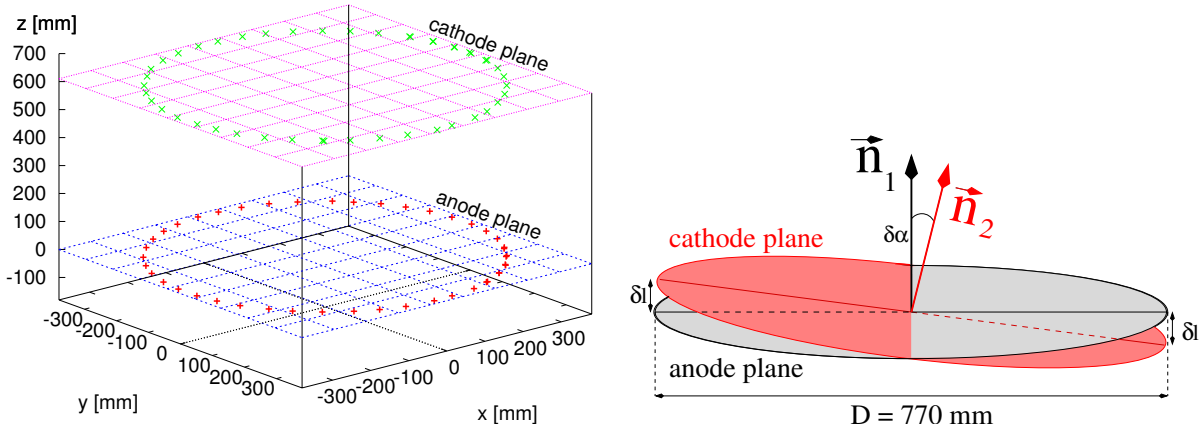

(a) measurement points on the anode and cathode end face

(b) evaluation of alignment of the end faces

Figure 6.8: *Determination of the parallelism between the end faces*

The coordinate system is arranged such that the normal is parallel to $\vec{e}_z$ and the anode plane defines the $x-y$ plane. In the same system, the fitted plane on the cathode side is

$$\left[\begin{pmatrix} -8\cdot 10^{-6} \\ 80\cdot 10^{-6} \\ 1 \end{pmatrix} \pm \begin{pmatrix} 20 \\ 21 \\ 0 \end{pmatrix} 10^{-6}\right] \cdot \vec{x} = (610.362 \pm 0.004)\,[\text{mm}] \quad \text{with} \quad \chi^2/_{\text{ndf}} = {}^{31}/_{42}.$$

The arrangement of the x and y axis is not fixed yet. The reference system could be rotated around $\vec{e}_z$ to make one more component of the normal vector vanish. However, the system is defined differently, namely relative to the axis of the field cage. This is explained in the next section. In addition, the vector that defines the plane is not exactly normalised. But its x and y components are very small and the z one set to unity. More precisely, the z-component would be 10^{-9} less than unity if the vector was a normal vector. This difference is neglected here.

The parallel alignment of the end planes can be read off from the angle $\delta\alpha$ between the their normal vectors (see figure 6.8(b)). In this case, the angle $\delta\alpha$ turns out to be almost zero:

$$\delta\alpha = \measuredangle(\vec{n}_1, \vec{n}_2) \approx 0 \qquad \text{, because} \qquad \vec{n}_1 \cdot \vec{n}_2 = 1.$$

with $\vec{n}_1$ and $\vec{n}_2$ being the normal vector of the anode and cathode plane, respectively. Thus the planes are parallel within the measurement accuracy. An upper limit for $\delta\alpha$ can be estimated from the fit uncertainties of $\delta\vec{n}_1$ and $\delta\vec{n}_2$. This is

$$\delta\alpha < \text{acos}\ (1 - \vec{n}_1 \cdot \delta\vec{n}_2 - \vec{n}_2 \cdot \delta\vec{n}_1) \approx 5 \cdot 10^{-5},$$

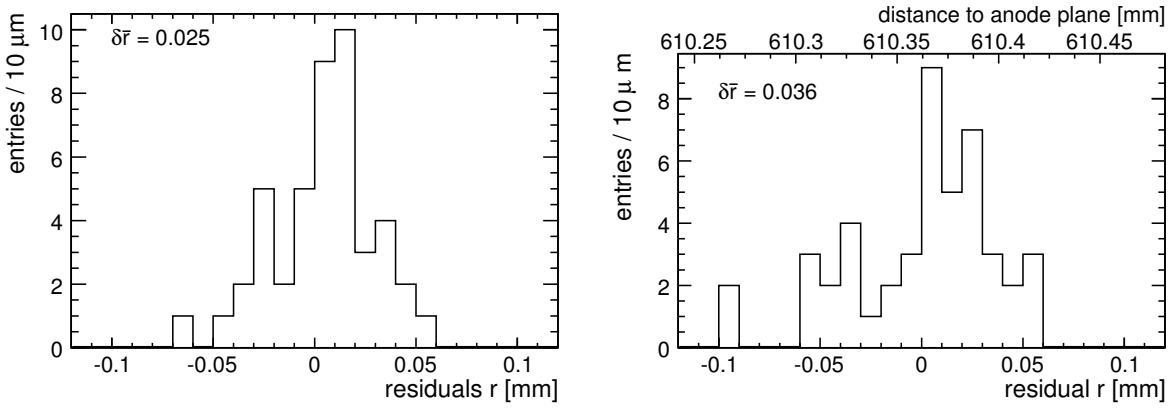

(a) anode side

(b) cathode side

Figure 6.9: *Distance of the measured points to the plane fit on both end faces*

If the two planes are superimposed as sketched in figure 6.8(b), the deviations δl would be

$$\delta l \lesssim R \cdot 6 \cdot 10^{-5} \approx 20\,\mu\text{m}.$$

Here $R = 385\,\text{mm}$ is the outer diameter of the field cage. This result fulfils the envisaged tolerance of $\delta l < 100\,\mu$m defined in the construction plans (see figure 5.38). The total length of the field cage is determined to $(610.362 \pm 0.004)\,\text{mm}$ and also is within the required range of $610 \pm 1\,\text{mm}$.

The diagrams in figure 6.9 show the residual distribution of measured points to the fitted planes for both sides. Within the diagrams, the calculated mean value is quoted with the standard deviation $\delta\bar{r}$ of the distribution. The mean value $\delta\bar{r}$ turns out to be $25\,\mu$m on the anode side, reflecting the 25-μm spatial accuracy of the single point measurement. On the cathode side, the standard deviation is $\delta\bar{r} = 36\,\mu$m which is square root of two times the value for the anode side. The increase is expected because the points on the cathode side are measured in the coordinate system defined by the points on the anode side. If the measurement accuracy of $25\,\mu$m is added to δl, the upper estimate for δl increases to about $30\,\mu$m, which is still in the allowed range.

6.2.2 Axis of the Field Cage Barrel

Two complementary methods were used to determined the orientation of the field cage axis relative to the anode plane. In the following, both are presented with figure 6.10.

Measurement Methods

Figure 6.10(a) sketches a simplified cross section of a TPC with a tilted axis. Since the alignment of the strips worked over the whole length of the field cage, it can be assumed

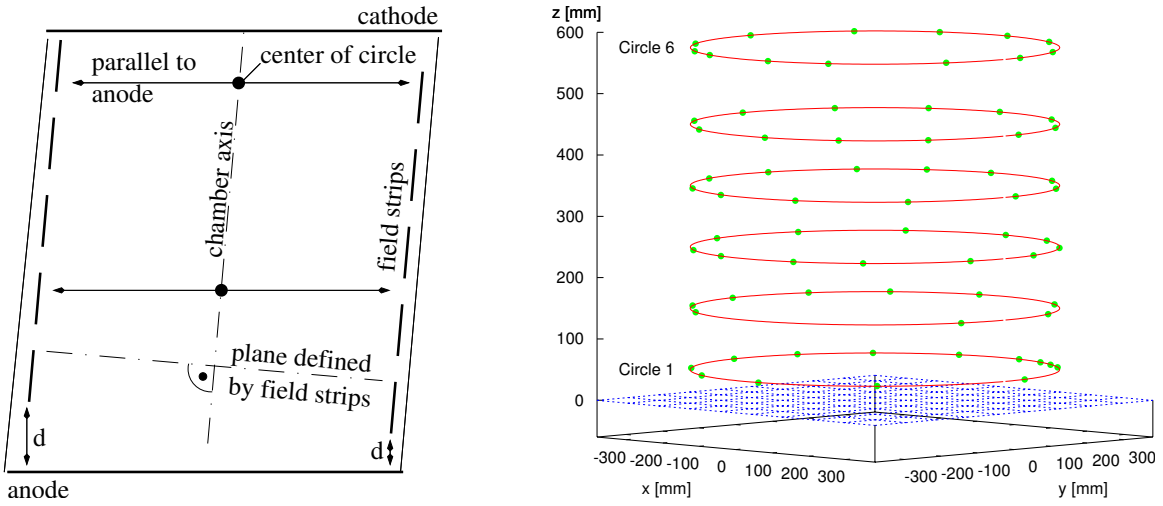

(a) determination of the field cage axis

(b) measured data points on the inside the field cage barrel

Figure 6.10: *Measurement of the field cage axis orientation relative to the anode plane*

that the field strips define parallel planes - at least with respect to the measurement accuracy of the test prod.

For the first method, the distance d was measured at several points around the inner circumference. d is the offset of the first field strip to the anode end of the field cage, as depicted in figure 6.10(a). If the axis and the anode end face are aligned correctly, d is constant and fixed to 10.05 mm. Otherwise, d varies sinus-like around the circumference.

The second method is more sophisticated and it allows for a determination of the axis' direction over the whole length of the field cage. For this, space points were taken on the inside of the barrel. These are in total 10 to 13 points around the circumference in six fixed distances to the fitted anode plane. Figure 6.10(b) depicts these points together with the anode reference plane.

If the axis is only slightly tilted, the points for a fixed distance define a circle - for an increased tilt, they lie on an ellipse. Here, the points belonging together are fitted with circles. Their centre points lie on the axis, as illustrated in figure 6.10(a). Thus six points can be determined in space that fix the orientation of the axis relative to the anode reference plane.

Measured Axis of the Field Cage

Firstly, the results are discussed of the second method using the measurement points on the inside field cage. Table 6.1 summarises the parameter of the six fitted circles together with their distances z_i to the anode end. The circles are numbered from one to six with increasing z_i. Figure 6.11(a) reflects a view from the top onto the $x-y$ plane

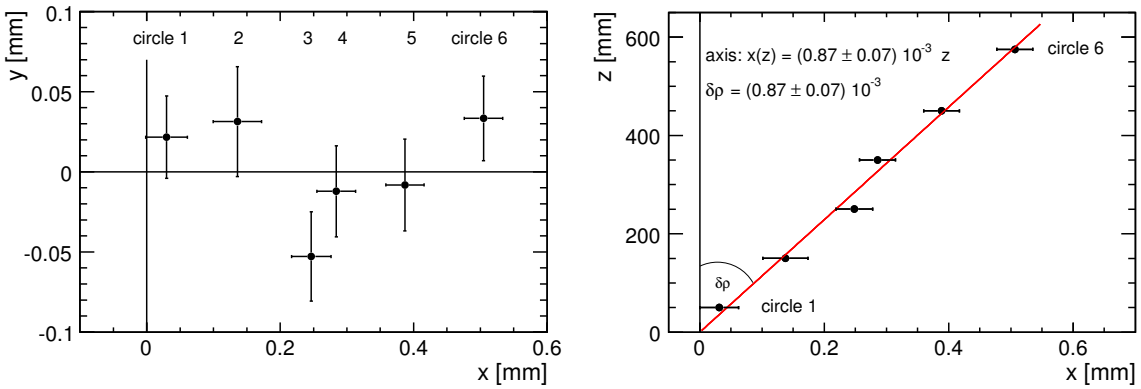

(a) circle centres in the $x - y$ plane

(b) fitted axis in the $x - z$ plane

Figure 6.11: *Orientation of the field cage axis*

circle	x_{centre} [mm]	y_{centre} [mm]	z_{i} [mm]	r [mm]	χ^2/ndf
1	0.03 ± 0.03	0.02 ± 0.02	50	360.13 ± 0.02	4.1
2	0.14 ± 0.04	0.03 ± 0.03	150	360.15 ± 0.03	1.7
3	0.25 ± 0.03	-0.06 ± 0.03	250	360.11 ± 0.02	1.0
4	0.29 ± 0.03	-0.02 ± 0.03	350	360.08 ± 0.02	3.4
5	0.39 ± 0.03	-0.01 ± 0.03	450	360.07 ± 0.02	4.2
6	0.51 ± 0.03	0.03 ± 0.03	575	360.01 ± 0.02	6.3
				$\bar{r} = 360.09 \pm 0.01$	

Table 6.1: *Centre points and radii of the six fitted circles*

and shows the fitted centre points projected onto this plane. The error bars reflect the fit uncertainties.

In the previous section the reference system is defined completely. Here the x axis is chosen such that the average of the y_{centre} vanish. Then the axis lies in the $x - z$ plane. As the assignment of the circle numbers to the points demonstrates, the axis is tilted and reaches an offset of about $500\,\mu\text{m}$ to the nominal axis at the last circle. Figure 6.11(b) shows the axis in the $x - z$ plane, fitted with a straight line. Here the origin of the system is put into the intersection point of the axis with the anode plane.

Likewise, the fitted axis intersects the cathode ($z \approx 600\,\text{mm}$) at $x_{\text{cathode}} \approx 500\,\mu\text{m}$. From this diagram, $\delta\rho$ can be read off, which is meant to be the angle between the normal of the anode plane and the field cage axis. This is

$$\delta\rho \approx \frac{x_{\text{cathode}}}{l_{\text{field cage}}} = 8.3 \cdot 10^{-4}\,\text{rad} = 0.05\,\text{deg}, \tag{6.1}$$

where the length is set to $l_{\text{field cage}} = 600\,\text{mm}$.

With the sketch in figure 6.12(a) it is possible to derive an expected result for the variation in d: the angle $\delta\rho$ is the included between the anode surface and the first

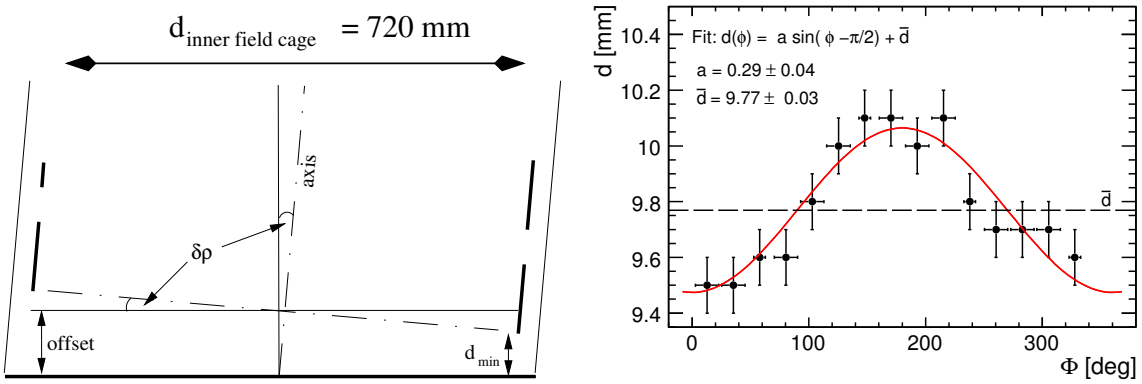

(a) comparison between the two measurements of the axis

(b) measured distance d around the circumference of the field cage

Figure 6.12: *Measurement of the distance of the first field strip to the anode plane*

field strip as well as between the axis and the normal of the anode plane. Therefore, d is expected to vary in a range of $d_{\max} - d_{\min} = \delta\alpha\, d_{\text{field cage}} = 0.3\,\text{mm}$.

Measured values d_i are displayed in figure 6.12(b). Here the starting point, 0 deg, denotes the x-axis. As expected, the distances d_i vary sinus-like. The fitted sinus has an amplitude of $a = 0.29 \pm 0.03$ - also in agreement with the expectation.

The fit also gives a result on the average distance d between the edge of the first strip and the end face, namely $9.77 \pm 0.02\,\text{mm}$. In the construction drawings, this is required to be $10.05 \pm 0.1\,\text{mm}$ (see figure 5.37(a)). This means that the nominal value lies in between the extrema of the sinus. Hence, when the anode plane is installed to the field cage, it is not aligned centred to a field strip.

6.2.3 Roundness of the Inner Field Cage

The roundness of the inner field cage is not a crucial parameter regarding the field homogeneity. Since the field and mirror strips define an optimised electrical boundary condition, they would also guarantee the field homogeneity, for example, in an oval field cage - given that the end plates and the axis are aligned. An imperfect roundness would become problematic when the independently manufactured end plates do not fit to the field cage. This is to be expected when the roundness is imperfect in the millimetre regime which is not the case. The radii of the fitted circles (table 6.1) scatter within $\approx 100\,\mu\text{m}$ over the full field cage length. Their weighted mean is $\bar{r} = 360.01 \pm 0.01\,\text{mm}$.

The measurement points on the inner surface of the field cage probe the roundness locally. For each point its radius r_i has been calculated with respect to the fitted circle it belongs to. Figure 6.13 illustrates the distribution of the r_i for all points in figure 6.10(b). The distribution has the same mean value $\bar{r}$ as quoted in table 6.1. Its width is $50\,\mu\text{m}$, calculated from the standard deviation of all points with respect to

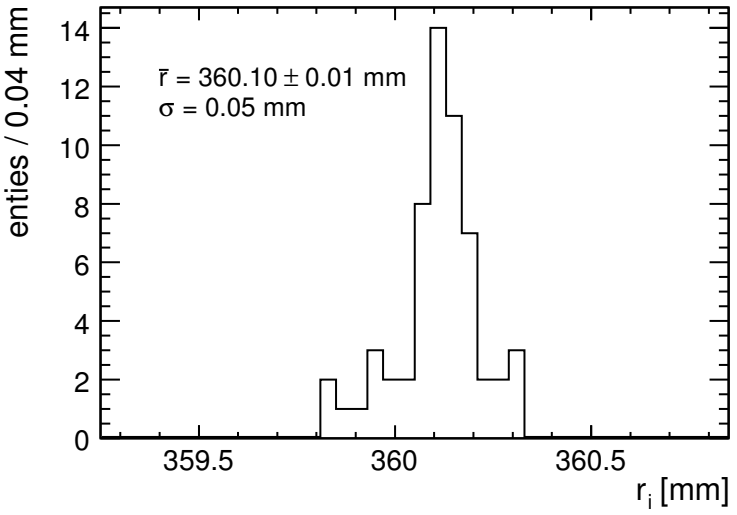

Figure 6.13: *Distribution of the distances r_i of the measured points from the centre of the corresponding fitted circle*

$\bar{r}$. From these results, the average diameter $\bar{d}$ of the field cage can be estimated to $720.02 \pm 0.07\,\mathrm{mm}$, because $\bar{d}$ is $2\,\bar{r}$ and $\delta\bar{d} = \sqrt{2}\,\delta\bar{r}$.

The construction plans define the inner diameter to $720.0 \pm 0.3\,\mathrm{mm}$. Thus, the field cage fulfils the requirement on the roundness over its whole length.

6.2.4 Summary of Quality Assurance Measurements and Final Drift Field Quality

The field cage fulfils the required mechanical accuracies, except that its axis is tilted sizably. For the same reason, the first field strip does not have the correct distance to the anode end. Thus, the field cage's end faces are perfectly parallel, the roundness of the cylinder is within the specification, but the it has a trapezoid side view.

Figure 6.14(a) illustrates the field cage's side view together with the measured dimensions. To evaluate the final electric field quality, an adapted LP-model model has been set up, based on the measured dimensions, and a field calculation been performed. The result is shown in figure 6.14(b). Due to the tilted axis, field deviations $^{\Delta E}/_{E}$ of about 10^{-3} are present in the large part of the drift volume. Thus the LP fails the aspired field quality by at least one order of magnitude. This model is calculated for perfectly parallel-aligned anode and cathode. In the commissioning phase of the field cage, it was possible to align the end plates parallel within $80\,\mu\mathrm{m}$. This would allow to reach the aspired end plate alignment accuracy.

Currently the reasons for the inaccurate axis alignment are under investigation. One possible explanation is that the axis of the mandrel was arranged incorrectly. In the post processing, the end faces have been machined over on a turning lathe while the field cage was still on the mandrel. Possibly, a misalignment was transfered from the mandrel to the field cage.

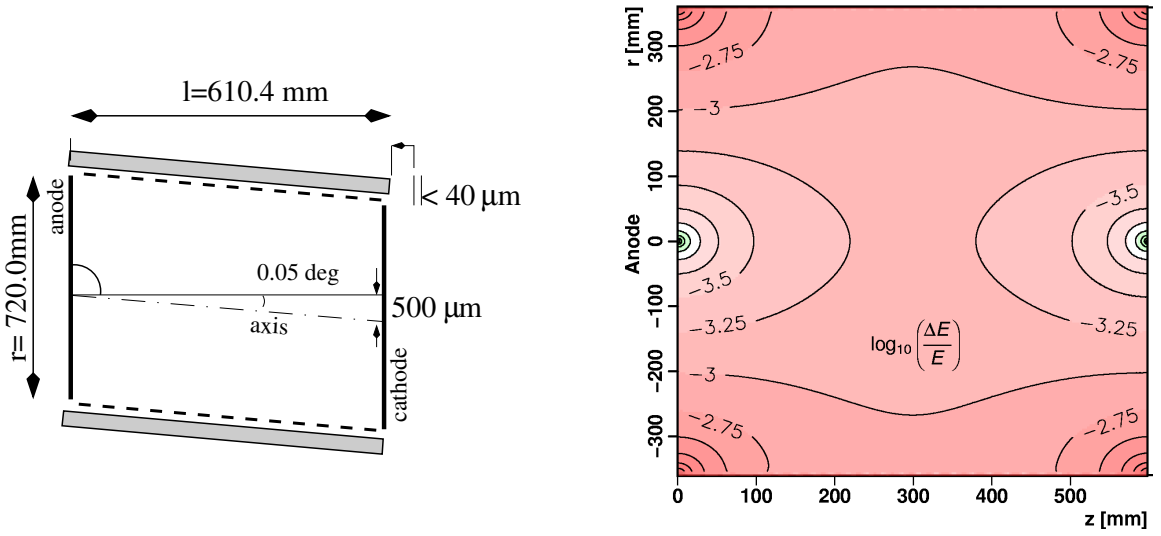

(a) measured dimensions of the field cage

(b) calculated drift field deviations

Figure 6.14: *Dimension of the field cage and electric field quality*

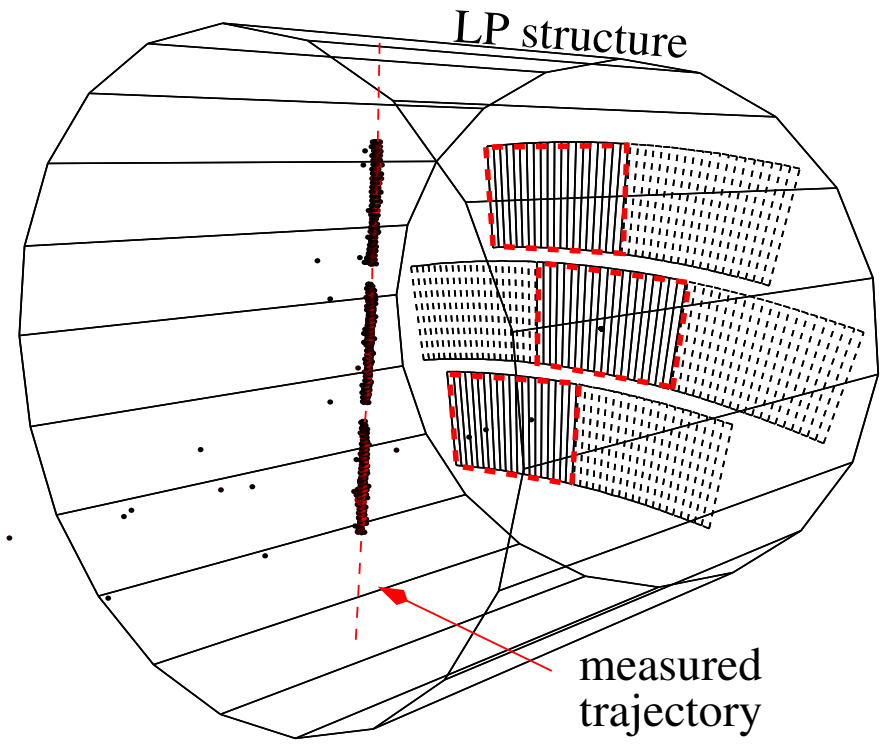

Figure 6.15: *Event display of a trajectory measured with three readout modules in the LP* [78]

7 Summary of the Large Prototype Development and Construction

Particle flow reconstruction (see section 2.3.1) puts high demands on ILD's sub-detectors and in particular on the Time Projection Chamber (TPC). The required measurement resolution for the TPC is 100 μm transversal to the beam axis, which exceeds anything accomplished in TPCs previously. Moreover, the material budget of the inner field cage wall should be as low as possible - less than 1 % of a radiation length.

To satisfy the requirements, the TPC has to be built from lightweight materials and has to be operated with a Micro Pattern Gaseous Detector readout, e.g. based on GEMs or MicroMEGAS. Novel composite construction techniques have been tested by various research groups in the construction of small TPC prototype chambers. These materials offer the prospect to fulfil the ambitious low material budget requirement for the ILD TPC. The TPC prototypes have been used for development work on MPGD readout techniques on surfaces of about $10 \times 10\,\mathrm{cm}^2$ size. Operational studies demonstrated a 'proof of principle' (e.g. [57]) and convinced people involved in TPC R&D work for the ILD that MPGWs are a suitable technique for the ILD TPC.

Construction of a the Field Cage for a Large TPC Prototype

In the next step of R&D work it is intended to develop a MPGD readout structure with an area comparable to a single readout module expected for the final TPC. In addition, composite construction techniques shall be tested on a larger scale. As an infrastructure for this, a new Large TPC Prototype (LP) was required. The LP consists of two components, a field cage and an anode end plate carrying MPGD prototype readout modules. The development and construction of the field cage is documented in part II of this thesis.

With an inner diameter of 72 cm, the field cage is significantly larger than the TPC prototypes available before, while its length is about 60 cm. The larger surface is well suited for the ongoing R&D work and the field cage diameter is comparable to the size of the inner field cage of the ILD TPC.

The LP is a part of a comprehensive test setup installed at the DESY electron test beam (EUDET infrastructure). The setup's dimensions define the outer dimensions of the LP, while the foreseen development studies set additional constraints: the electric field inside the LP is supposed to be homogeneous to a degree of $^{\Delta E}/_{E} \lesssim 10^{-4}$ and the material budget of the field cage wall as low as possible for the operation in the electron beam. In addition, the LP should allow for operation at highest electric drift fields of $300\,^{V}/_{\mathrm{m}}$ (see section 4).

An optimisation of the field cage design plans has been performed with finite element calculations and mechanical test with sample pieces. To achieve the desired field quality,

- two layers of the field strips are installed on the inside of the inner field cage in a defined layout (see figure 5.1(c)).
- the anode and cathode end plates have to be aligned with an accuracy of about $100\,\mu$m.
- the axis of the field cage has to be aligned with an accuracy of $50\,\mu$m over the field cage length.

The field strips in the LP are arranged in a common setup, which has been used in other TPCs operated before (e.g. [41]). In addition, an alternative design has been developed. This allows for an equally high homogeneity of the electric field and is technically simpler to realise (see figure 5.10(c)). This design could be tested in future TPC prototypes - it is not installed in the LP because the chamber was already under construction when the new design was developed. The composite wall structure has been optimised to allow for a safe operation with the required drift fields. In addition, mechanical tests on sample pieces demonstrated the robustness of the field cage. Although the wall structure is not optimised to the lowest possible material budget - in order not to risk the chamber's robustness - it has an estimated radiation length of $1.24\%\,X_0$.

The field cage was constructed in 2008 in cooperation with a company specialised in composite materials. Afterwards the achieved mechanical accuracies were evaluated. The requirements are satisfied except that the field cage axis is misaligned. Currently, the reason for this inaccuracy is being studied.

For the construction, a reusable forming tool has been produced. The production of a second field cage is under discussion for the end of 2009. This second iteration on the field cage shall meet all accuracy requirements. (see chapter 6)

In summary, the development of the LP demonstrates the possibility to construct a lightweight field cage for the ILD. The chamber is available as infrastructure for studies on MPGD modules and TPC operational aspects. The experience gained with the construction is a starting point for ongoing mechanical studies.

Operations of the Large Prototype

The LP was operated for the first time in November 2008. Since then, various research groups have used the EUDET infrastructure. Figure 6.15 depicts an example event display showing a trajectory measured in the LP. Here, three GEM readout modules have been operated on the anode end plate. The measured trajectory has a distance of about 30 cm from the anode end plate and is located almost centrally in the chamber. As of July 2009 the EUDET setup was still lacking the silicon detector layers, so no external reference points were measured. These detectors will be added in November 2009.

Part III
Measurement of τ Polarisation in $\tilde{\tau}_1$ Decays with the ILD Detector

The ILD detector will offer the possibility to measure a multitude of standard model (SM) physics observables and to reveal the nature of possible extensions of the SM. In the current detector preparation phase, many possible measurements are studied in detector simulations [4]. Such simulation studies demonstrate the physics potential of the detector and the achievable measurement accuracies. Moreover they are a key input to the optimisation of the detector concept.

For this, the complete analysis chain for a certain measurement is set up on the basis of fully simulated and reconstructed physics events. Then, certain parameters of the detector model, which is underlying the simulations, can be varied, for example the length of the TPC or the magnetic field strength. The parameter variations can improve or worsen the simulated measurement result. Finally, it is possible to tune the detector and the ILC beam parameters for the optimal measurement accuracy. A full and balanced detector optimisation requires many different simulation studies which address different properties of the detector.

The third part of this thesis presents one of these studies, namely the measurement of the τ polarisation in the decay $\tilde{\tau}_1 \rightarrow \tau\chi_1^0$. Here $\tilde{\tau}_1$ is a supersymmetric tau lepton which decays to a supersymmetric neutralino and a standard model tau lepton τ. If supersymmetry (SUSY) (e.g. [79]) is realised in nature, the exploration of the SUSY sector and precision measurements of SUSY parameters are among the main goals of the ILC. The following chapter 8 presents the motivation for SUSY and its phenomenology. In addition the measurement of the τ polarisation P_τ is outlined and it is discussed how the knowledge of P_τ could contribute to the understanding of SUSY.

Prior studies of this measurement used a simplified detector simulations and less challenging SUSY scenarios (e.g. [80, 81]). Here, realistically simulated events are used - chapter 9 presents the software framework used for these simulations. With these tools, the signal processes, significant SUSY and standard model backgrounds have been simulated. Two possible ways to measure P_τ are presented in chapter 10. The first one is based on the measurement of pions in the decay $\tau \rightarrow \pi\nu_\tau$, while the second is based on the the decay channel $\tau \rightarrow \pi\pi_0\nu_\tau$. For the former channel, statistical and systematical uncertainties are derived.

The signal pions from the τ decays appear isolated and with energies in a range between 0 and 43 GeV in the detector. Hence the measurement addresses in particular the achievable momentum resolution for low energetic particles, which is primarily affected by the TPC performance.

8 Supersymmetric Extension of the Standard Model

Today Supersymmetry (SUSY) (e.g. [79]) is the most elaborately studied extension of the Standard Model (SM), both on the theoretical as well as on the experimental side. SUSY is well appreciated by high energy physicists, because it offers solutions to many of SM's experimental and theoretical problems. Moreover, it can be introduced in complete agreement with precision measurements done at LEP, SLD [82] and the Tevatron which put tight bounds to any extension of the Standard Model (SM) (e.g. [83]). Finally SUSY contains the SM as a low-energy limit.

This chapter introduces SUSY and explains how it provides solutions to the problems of the SM mentioned in section 1.3. Section 8.3 discusses the measurement of the τ polarisation in the supersymmetric process $e^+e^- \to \tilde{\tau}_1\tilde{\tau}_1 \to \chi_1\chi_1\tau\tau$ and to what extend it can contribute to the understanding of SUSY.

8.1 Supersymmetry as a Solution to Standard Model Problems

Among the most striking shortcomings of the SM is hierarchy-problem (see section 1.3). To solve this problem, supersymmetry introduces a partner boson to each SM fermion and vice versa. In a SM augmented with SUSY, each SM contribution to the Higgs boson mass has a counter-diagram of the of the opposite spin-statistics. As an example, figure 8.1 illustrates this for the top quark. The bosonic loop of the supersymmetric partner of the top $\tilde{t}$, called stop, is the counter-diagram for the SM top loop. These two diagrams cancel each other in the calculation of Δm_{H}^2. In the consequence, Δm_{H}^2 is only logarithmic divergent,

$$\Delta m_{\mathrm{H}}^2 \propto \ln \Lambda \qquad \text{(with SUSY)},$$

and the calculation can be renormalised.

The new SUSY states are introduced with a spinor operator Q, which connects a SM state to its partnered SUSY state:

$$|\text{fermion}\rangle = \mathcal{Q}|\text{boson}\rangle \qquad |\text{boson}\rangle = \mathcal{Q}|\text{fermion}\rangle. \tag{8.1}$$

The partner of a SM boson is denoted by the extension 'ino' to its name, for example the 'Higgsino'-fermion is the partner of the SM Higgs-boson. In the case of the SM

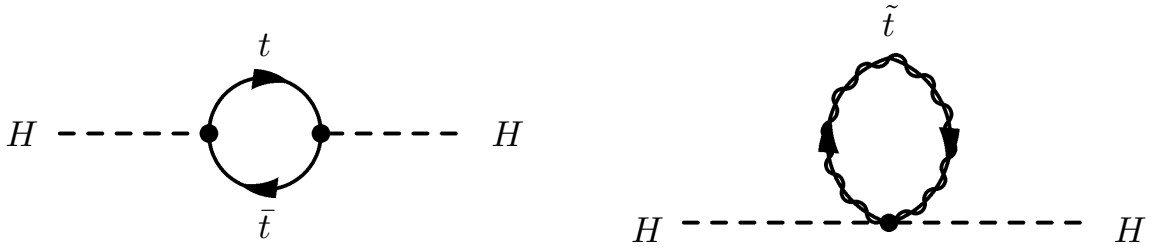

(a) top fermion loop **(b)** stop boson loop

Figure 8.1: *Loop correction to m_H and cancellation between the top and stop loops*

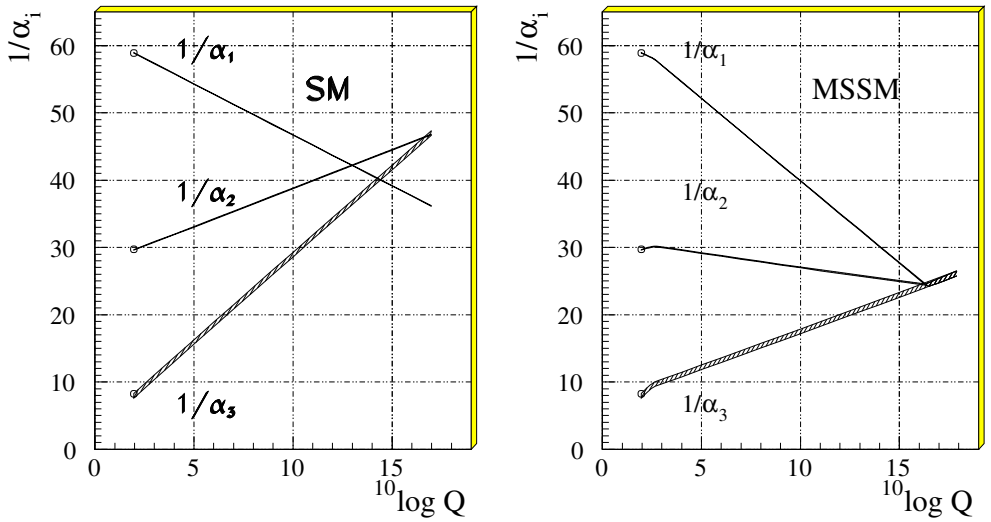

Figure 8.2: *Unification of forces with SUSY (Q is the momentum transfer in the interaction)* [84]

fermions, the partners are called 'sparticles', e.g. the selectron is the partner of the electron.

Besides solving the hierarchy problem, the introduction of supersymmetry offers further theoretical benefits. The new particles give contributions in loop corrections, which modify the energy dependence of the force couplings. Figure 8.2 compares the energy dependence of the couplings for the SM and the minimal supersymmetric standard model (MSSM, see below). With supersymmetry, the couplings unify in a single point [85]. Although this coincidence is not required by theoretical arguments, it is elegant. Finally supersymmetry is required by string theories, one of the attempts to include gravity into the theoretical framework.

In addition, SUSY could also provide solutions to some of SM's experimental problems. SUSY requires the lightest supersymmetric particle (LSP) to be stable and only weakly interacting. Thus the LSP is a possible candidate to account for the cold dark

SM SU(2) doublet	$\begin{pmatrix} e_{\mathrm{L}}^- \\ \nu_{el} \end{pmatrix}$	$\mathcal{Q}$ $\longleftrightarrow$	$\begin{pmatrix} \tilde{e}_{\mathrm{L}}^- \\ \tilde{\nu}_{el} \end{pmatrix}$	SUSY SU(2) doublet
SM SU(2) singlet	e_{R}^-	$\longleftrightarrow$	$\tilde{e}_{\mathrm{R}}^-$	SUSY SU(2) singlet

Table 8.1: *SUSY partner to the SM electron and electron-neutrino*

matter in the universe. However, this assumption must be in agreement with the expected rates of LSP annihilation processes to SM particles, like $\chi\chi \to gg$ or $\chi\chi \to \gamma\gamma$, in space. Here, the neutralino χ is the LSP. Currently such processes are under study together with their influence of the cosmic ray flux (e.g. [86]).

Although SUSY offers many advantages, its discovery is still an open issue. But, the required cancellations of the quadratic divergences only work out, if the lightest supersymmetric particles have masses below about 1 TeV. Thus, if SUSY exists, supersymmetric particles will be discovered with the next generation of collider experiments.

8.2 Supersymmetry Phenomenology

The operator $\mathcal{Q}$ in the relations (8.1) has a spinor character and fulfils certain commutation rules, namely

$$[\mathcal{Q}, \mathcal{H}] = 0 \quad [\mathcal{Q}, -P_\mu^2] = 0. \tag{8.2}$$

P_μ is a momentum operator and $\mathcal{H}$ a Hamiltonian for both SM and SUSY states. The vanishing of these commutators has two consequences: firstly the connected particle states have equal masses, because $\mathcal{Q}$ commutes with the mass operator $-P_\mu^2$, and secondly they have the same quantum numbers under $SU(2) \times U(1)$ symmetry, as $\mathcal{Q}$ commutes with the complete Hamiltonian $\mathcal{H}$. Hence the partnered states carry the same electroweak charges.

The SM electron appears in two electro weak states eigenstates - as left and right handed electron (e_{L} and e_{R}). As these behave differently under a $SU(2)$ transformation, each state is connected to a SUSY partner. Table 8.1 illustrates the transformation for the electroweak electron doublet and singlet. Thus, SUSY introduces two physical particles as partners to the standard model electrons, muons, taus and neutrinos. For the electrons, they are denoted by $\tilde{e}_{\mathrm{R}}$ and $\tilde{e}_{\mathrm{L}}$.

To give an overview, table 8.2 summarises the SM and the partnered SUSY states. Supersymmetry extends the Higgs sector to four states, because the existence of less Higgs-bosons would give rise to unrenormalizable anomalies.

This work refers to a minimal supersymmetric extension of the SM, called MSSM. In the MSSM, only one operator $\mathcal{Q}$ is introduced and thus the complete set of newly introduced SUSY states is already listed in table 8.2.

According to the discussion so far, two partnered states should be of equal mass. Hence the selectrons $\tilde{e}_{\mathrm{R}}$ and $\tilde{e}_{\mathrm{L}}$, the partners of the electron, should have masses of

SM particles	Supersymmetric partners interaction eigenstates		mass eigenstates	
$l = e, \mu, \tau$	$\tilde{l}_{\mathrm{L}}$, $\tilde{l}_{\mathrm{R}}$	slepton	$\tilde{l}_{\mathrm{L}}$, $\tilde{l}_{\mathrm{R}}$	Slepton
$\nu = \nu_{\mathrm{el}}$, ν_μ, ν_τ	$\tilde{\nu}$	sneutrino	$\tilde{\nu}$	Sneutrino
$q = u, d, s, c, b, t$	$\tilde{q}_{\mathrm{L}}$, $\tilde{q}_{\mathrm{R}}$	squark	$\tilde{q}_{\mathrm{L}}$, $\tilde{q}_{\mathrm{R}}$	Squarks
$W^\pm$	$\tilde{W}^\pm$	wino	$\tilde{\chi}_j^\pm$	Charginos
H_1^-	$\tilde{H}_1^-$	higgsino		
H_2^+	$\tilde{H}_2^+$	higgsino		
W_3	$\tilde{W}$	wino	$\tilde{\chi}_j^0$	Neutralinos
B	$\tilde{B}$	bino		
H_1^0	$\tilde{H}_0^1$	higgsino		
H_2^0	$\tilde{H}_0^2$	higgsino		
g	$\tilde{g}$	gluino	$\tilde{g}$	Gluino

Table 8.2: *SUSY particle states in the MSSM*

511 keV. These sparticles should have been in the energy reach of many of particle colliders operated so far and already been discovered. To explain the apparent absence of SUSY to the present date, it is assumed that supersymmetry is a broken symmetry in nature. Due to the breaking, the sparticles acquire masses above 100 GeV and above an energy range which is excluded by searches so far. Different options for the breaking mechanism are currently being discussed (e.g. [87, 88, 89]).

This work refers to a 'soft' SUSY breaking scheme. In such schemes, the unbroken SUSY Lagrangian $\mathcal{L}_{\mathrm{SUSY}}$ is extended to an effective one by additional terms that model the breaking and introduce logarithmic divergences at most.

$$\mathcal{L}_{\mathrm{effective}} = \mathcal{L}_{\mathrm{SUSY}} + \mathcal{L}_{\mathrm{soft}}$$

Moreover, it is necessary to introduce an additional quantum number into the model. The SUSY-Lagrangian $\mathcal{L}_{\mathrm{SUSY}}$ contains baryon- and lepton number violating terms. To eliminate these terms, a further discrete symmetry is proposed, connected to a quantum number R_P. This symmetry is called R-parity and R_P is calculated by

$$R_P = (-1)^{3(B-L)+2s}$$

with L being the lepton number, B the baryon number and s the particle spin. SM particles and the Higgs Boson have $R = 1$, whereas $R = 1$ for SUSY particles. The cancellation of the unwanted terms in $\mathcal{L}_{\mathrm{SUSY}}$ requires that the product of the R-parities of all particles in an interaction is conserved. This has the consequences that

- supersymmetric particles are produced pairwise in e^+e^- interactions and
- the lightest supersymmetric particle is stable due to R conservation and hence it is a promising dark matter candidate.

8.2.1 SUSY mixing

The SUSY partners to SM states are $SU(2) \times SU(1)$ interaction eigenstates. The soft SUSY breaking extension of the Lagrangian $\mathcal{L}_{\text{soft}}$ contains mass matrices which mix these interaction states. This means that the mass matrices are not diagonal in the basis of the interaction eigenstates. But the observable SUSY particles correspond to mass eigenstates of $\mathcal{L}_{\text{soft}}$ and they are mixtures of left-handed and right-handed interaction eigenstates.

Sfermions

The mixing terms for the sfermion states have the form

$$-(\tilde{f}_{\text{L}}^{\dagger}, \tilde{f}_{\text{R}}^{\dagger})\mathbf{M}_{\tilde{\mathbf{f}}}^{\mathbf{2}} \begin{pmatrix} \tilde{f}_{\text{L}} \\ \tilde{f}_{\text{R}} \end{pmatrix}.$$

Decomposed into its coefficients, the intermediate mass matrix looks like

$$\mathbf{M}_{\tilde{\mathbf{f}}}^{\mathbf{2}} = \begin{pmatrix} m_{\text{LL}}^2 & m_{\text{LR}}^2 \\ m_{\text{LR}}^2 & m_{\text{RR}}^2 \end{pmatrix} = \begin{pmatrix} m_{\text{LL}}^2 & m_f(A_f - \mu \tan\beta) \\ m_f(A_f - \mu \tan\beta) & m_{\text{RR}}^2 \end{pmatrix}$$

Here, m_f is the SM fermion mass, A_f is a coupling constant between the sfermion states and the Higgs state H_0^1 in the Lagrangian $\mathcal{L}_{\text{effective}}$ and $\tan\beta$ is the ratio between the two neutral Higgs expectation values ($\tan\beta = {}^{<H_0^2>}/_{<H_0^1>}$) (e.g. [81]). The parameter μ is called higgsino mass parameter and among others it is the analogue to $\mathbf{M}_{\tilde{\mathbf{f}}}^{\mathbf{2}}$ for the Higges. In table 8.3 values for these parameters are listed for the used SUSY scenario.

The SM electron and muon mass are comparably small and thus the selectron and smuon mass eigenstates are practically identical to the interaction eigenstates. A relevant mixing occurs only in the stau sector because of the higher tau mass. The following discussion is restricted to this case.

So far $\mathbf{M}_{\tilde{\mathbf{f}}}^{\mathbf{2}}$ is still written in the basis of the interaction eigenstates. Converted to the basis of the mass eigenstates, named $\tilde{\tau}_1$ and $\tilde{\tau}_2$, the matrix is diagonalised:

$$-(\tilde{\tau}_1^{\dagger}, \tilde{\tau}_2^{\dagger}) \begin{pmatrix} m_{\tilde{\tau}_1} & 0 \\ 0 & m_{\tilde{\tau}_2} \end{pmatrix} \begin{pmatrix} \tilde{\tau}_1 \\ \tilde{\tau}_2 \end{pmatrix} \quad \text{with} \quad \begin{pmatrix} m_{\tilde{\tau}_1} & 0 \\ 0 & m_{\tilde{\tau}_2} \end{pmatrix} = \mathbf{D} \begin{pmatrix} m_{\text{LL}}^2 & m_{\text{LR}}^2 \\ m_{\text{LR}}^2 & m_{\text{RR}}^2 \end{pmatrix} \mathbf{D}^{\dagger}$$

The matrix $\mathbf{D}$ describes the mixing of $\tilde{\tau}_{\text{R}}$ and $\tilde{\tau}_{\text{L}}$ to the mass eigenstates $\tilde{\tau}_1$ and $\tilde{\tau}_2$. As $\mathbf{D}$ is unitary, its components $\mathbf{D_{ij}}$ can be expressed in terms of a mixing angle $\Theta_{\tilde{\tau}}$

$$\begin{pmatrix} \tilde{\tau}_1 \\ \tilde{\tau}_2 \end{pmatrix} = \begin{pmatrix} \cos\Theta_{\tilde{\tau}} & \sin\Theta_{\tilde{\tau}} \\ -\sin\Theta_{\tilde{\tau}} & \cos\Theta_{\tilde{\tau}} \end{pmatrix} \begin{pmatrix} \tilde{\tau}_{\text{L}} \\ \tilde{\tau}_{\text{R}} \end{pmatrix}.$$

The naming convention is such that $\tilde{\tau}_1$ is lighter than $\tilde{\tau}_2$.

Neutralino mixing

Similar to the sfermion mixing, four neutralinos χ_i^0 are mixed states of the uncharged gauge and Higgs fields ($\tilde{B}$, $\tilde{W}_3$, $\tilde{H}_1^0$, $\tilde{H}_1^0$). The neutralino mass matrix $\mathbf{M}_{\chi_j}$ is a 4×4 matrix and it is diagonalised by the neutralino mixing matrix $\mathbf{N}$:

$$\mathbf{N}^\dagger \mathbf{M}_{\tilde{\chi}_j} \mathbf{N}^\dagger = \begin{pmatrix} m_{\chi_1} & 0 & 0 & 0 \\ 0 & m_{\chi_2} & 0 & 0 \\ 0 & 0 & m_{\chi_3} & 0 \\ 0 & 0 & 0 & m_{\chi_4} \end{pmatrix} \quad \text{and} \quad \chi_j = \mathbf{N} \begin{pmatrix} \tilde{B} \\ \tilde{W}_3 \\ \tilde{H}_0^1 \\ \tilde{H}_2^0 \end{pmatrix} \tag{8.3}$$

The four neutralinos are numbered in rising mass order, from χ_1 being the lightest to χ_4^0 being the heaviest neutralino.

8.2.2 SUSY point SPS1a'

The SUSY framework allows for a variation of parameters like mixings and couplings in a wide range and various SUSY parameters sets are currently under discussion. As stated, constraints on the parameter space can be deduced from cosmological and SM observations like, for example, CDM data or measurements of the branching ratio $\mathcal{B}(b \rightarrow s\gamma)$ (e.g. [91]). The SUSY parameter set SPS1a' [90] is compatible with all precision data and referred to in the work. Table 8.4 gives an overview of the SUSY particle masses in SPS1a' which are relevant for the analysis presented in the following chapters. In the SPS1a' parameter point, the neutralino χ_1^0 is the LSP. The following next to lightest sparticle is the $\tilde{\tau}_1$ and it decays exclusively via $\tilde{\tau}_1 \rightarrow \tau\chi_1^0$.

8.3 Polarisation of taus in the decay $\tilde{\tau} \rightarrow \tau\chi_1$

Among the simplest SUSY processes is the production of sfermions pairs in e^+e^- collisions, $e^+e^- \rightarrow \tilde{f}^+\tilde{f}^-$, with the adjacent decays $\tilde{f} \rightarrow f\chi_j$. From the turn-on curve of a specific sfermion pair production process, the sfermion mass can be determined. Moreover, the energy spectrum of the SM decay fermions is sensitive to the mass difference between neutralino χ_j and sfermion $\tilde{f}$. (e.g. [92]).

The decay of the stau $\tilde{\tau}_1 \rightarrow \tau\chi_1^0$ offers a unique additional insight, because the tau is not stable in a detector. By measuring the energy of its decay products, it is possible to determine the degree of τ polarisation P_τ [81, 80]. Before the measurement principle is explained, the term polarisation is introduced.

Polarisation

The degree of polarisation in a sample of N fermions is defined as

$$P = \frac{N_+ - N_-}{N_+ + N_-} = \frac{N_+ - N_-}{N} = p_+ - p_-,$$

	parameter	value	parameter	value
$<H_0^2>/<H_0^1>$	$\tan\beta$	10		
stau mixing	$\cos\Theta_{\tilde{\tau}}$	0.32	$\sin\Theta_{\tilde{\tau}}$	0.94
neutralino mixing	N_{11}	-0.989	N_{12}	0.050
	N_{13}	-0.131	N_{14}	0.045
trilinear coupling	A_τ	$-256\,\mathrm{GeV}$		
higgsino mass parameter	μ	$+1$		

Table 8.3: *SUSY parameter settings in SPS1a' (subset)* [90]

	particle	mass [GeV]	particle	mass [GeV]
neutralinos	χ_1^0	97.7	χ_2^0	183.9
	χ_3^0	400.5	χ_4^0	413.9
charginos	$\chi_1^\pm$	183.7	$\chi_2^\pm$	415.4
sfermions	$\tilde{\tau}_1$	107.9	$\tilde{\tau}_2$	194.7
	$\tilde{\mu}_\mathrm{R}$	125.3	$\tilde{\mu}_\mathrm{L}$	194.9
	$\tilde{e}_\mathrm{R}$	189.9	$\tilde{e}_\mathrm{L}$	125.3
sneutrinos	$\tilde{\nu}_\tau$	170.5	$\tilde{\nu}_\mu$	172.5
	$\tilde{\nu}_e$	172.5		
squarks	$\tilde{t}_1$	366.5	$\tilde{t}_2$	585.5
	$\tilde{b}_1$	506.3	$\tilde{b}_2$	545.7

Table 8.4: *Sparticle masses in SPS1a' (subset)* [90]

where N_+ is the sum of right handed fermions among N. This means that the particle spin of these fermions is oriented in the direction of flight. N_- the number of left handed fermions and thus $N = N_+ + N_-$.

The normalised quantities p_+ and p_- are the probabilities to find a randomly picked fermion from the sample being positively or negatively polarised, respectively. These probabilities fulfil the relations

$$p_+ = \frac{1+P}{2} \quad \text{and} \quad p_- = \frac{1-P}{2} \tag{8.4}$$

which are used frequently throughout the following chapters.

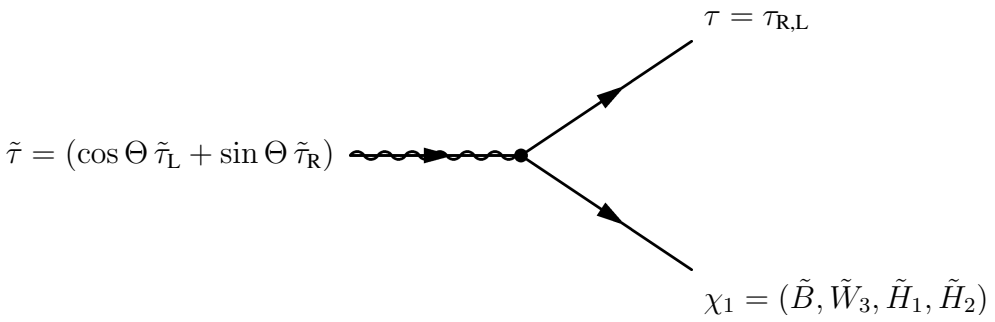

Figure 8.3: *Decay $\tilde{\tau}_1 \rightarrow \chi_1^0\tau$ in SPS1a'*

Polarisation in $\tilde{\tau} \rightarrow \tau\chi_1$

Figure 8.3 depicts the Feynman diagram of the decay process $\tilde{\tau} \rightarrow \chi_1^0 + \tau$. The SM taus come out of the process with certain degree of polarisation P_τ, which is influenced by the mixings of the of the $\tilde{\tau}_1$ and the χ_1^0.

The components $\tilde{\tau}_{\mathrm{R}}$ and $\tilde{\tau}_{\mathrm{L}}$ of the stau $\tilde{\tau}_1$ couple exclusively to right and left handed SM taus, respectively. If the mixing of the $\tilde{\tau}_1$ completely dominated the polarisation P_τ of the tau:

$$P_\tau|_{\text{only } \tilde{\tau} \text{ mixing}} = \sin^2\Theta_{\tilde{\tau}} - \cos^2\Theta_{\tilde{\tau}} \quad \text{(see figure 8.3).}$$

would be measured. The stau mixing angle is $\Theta_{\tilde{\tau}} \approx 72\,\mathrm{deg}$ in SPS1a' and the $\tilde{\tau}_1$ is predominately $\tilde{\tau}_{\mathrm{R}}$. Under this simplified assumption, P_τ would be about 80 %.

In the completed picture, the τ polarisation is also influenced by the neutralino mixing [93]:

- If χ_1^0 is gaugino like - that is the case if $\tilde{B}$ and $\tilde{W}_3$ contribute dominant to χ_1:
  $\rightarrow P_\tau$ is close to -1 if $\cos\Theta$ is 1.
  $\rightarrow P_\tau$ is close to $+1$ if $\cos\Theta$ is 0.
  This means that the mixing of the $\tilde{\tau}_1$ dominates the τ polarisation.

- If χ_1^0 is Higgsino like - that is the case if $\tilde{H}_1$ and $\tilde{H}_2$ contribute dominant to χ_1
  $\rightarrow P_\tau$ is close to $+1$ if $\cos\Theta$ is 1.
  $\rightarrow P_\tau$ is close to -1 if $\cos\Theta$ is 0.
  This means that the mixing of the χ_1 dominates the τ polarisation.

In the second case, the coupling between a sfermion and a Higgsino flips the polarisation of the tau in the decay. However, even if the $\tilde{\tau}_1$ is not purely $\tilde{\tau}_{\mathrm{R}}$ or $\tilde{\tau}_{\mathrm{L}}$ (e.g. $0 < \Theta_{\tilde{\tau}} < 1$), a gaugino-like neutralino favours $P_\tau \rightarrow +1$ and a higgsiono-like neutralino causes $P_\tau \rightarrow -1$. Hence the sign of P_τ alone can make a fundamental statement on the nature of the neutralino.

Moreover P_τ also depends on $\tan\beta$, because both $\tilde{H}_1$ and $\tilde{H}_2$ contribute to the χ_1^0. Figure 8.4 illustrates this dependency in the SPS1a' SUSY point and different variations of the mixings. The 'nominal' curve denotes the SPS1a' scenario. If the $\tilde{\tau}_1$ is

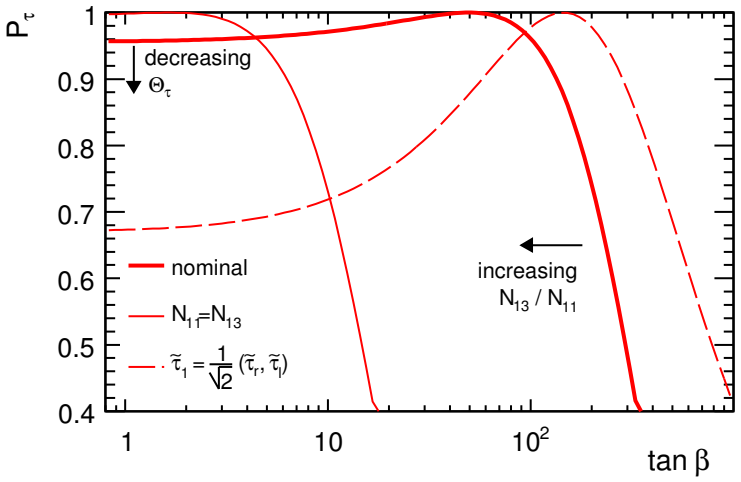

Figure 8.4: *P_τ in dependence of* $\tan\beta$ *under variation of SUSY mixing parameter*

predominantly $\tilde{\tau}_\mathrm{R}$, then it is possible to determine $\tan\beta$ by measuring P_τ. However a two fold ambiguity occurs if the $\tilde{\tau}_1$ has a $\tilde{\tau}_\mathrm{L}$ component, as 'decreasing Θ_τ' denotes in the diagram. Thus the measurement is most attractive if $\tilde{\tau}_1$ is very purely $\tilde{\tau}_\mathrm{L}$ or $\tilde{\tau}_\mathrm{R}$. In addition, the sensitivity rises, if the χ_1^0 has only a small $\tilde{H}_1$ component. In this case, the whole curve is shifted to smaller $\tan\beta$, denoted by 'increasing N_{11}/N_{13}'.

In SPS1a' $\tan\beta$ is 10 and P_τ is 97 %, derived from the 'nominal' curve in the diagram. SPS1a' happens to be a disfavoured scenario for the measurement of $\tan\beta$ via P_τ, because $P_\tau(\tan\beta)$ is very flat around 10 and exhibits the two fold ambiguity with $\tan\beta \approx 100$.

The Signal Process and Kinematics

The preferred process to measure the polarisation of taus in $\tilde{\tau}_1$ decays is the $t\tilde{a}u_1$ pair production process, whose Feynman diagram is shown in figure 8.5. This process has a cross-section in the 100 fb regime (see next section), which is among the highest SUSY cross-sections at the ILC. In addition, the interesting decay $\tilde{\tau} \to \tau\chi_1^0$ happens at two vertices, thus the cross-section is effectively doubled. Moreover, the process has a comparably simple kinematics: The decay $\tilde{\tau}_1 \to \tau\chi_1^0$ is a two body decay and hence the tau gets a fixed energy in the rest frame of the $\tilde{\tau}_1$, namely

$$E_\tau = \frac{m_{\tilde{\tau}}}{2}\left(1 - \frac{m_\chi^2 - m_\tau^2}{m_{\tilde{\tau}}^2}\right) = 9.55\,\mathrm{GeV}.$$

Thus it has a has a velocity of

$$\beta_{\tilde{\tau}\text{-sys}} = \frac{\sqrt{E_\tau^2 - m_\tau^2}}{E_\tau} = 0.983.$$

However, in the laboratory system, the tau can appear with an arbitrary angle with respect to its mother $\tilde{\tau}_1$. If it is emitted in the direction of the $\tilde{\tau}_1$, the tau acquires the

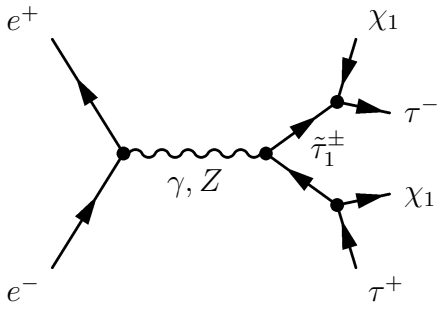

Figure 8.5: *Feynman diagram of* $e^+e^- \to \tilde{\tau}_1^+\tilde{\tau}_1^- \to \chi_1^0\chi_1^0\tau^+\tau^-$

maximum energy $E_\tau^{\max}$. In the opposite case, when the tau is emitted anti-parallel to the $\tilde{\tau}_1$, it has minimal energy of $E_\tau^{\min}$. The maximal and minimal τ energies can be evaluated by a Lorentz-transformation from the $\tilde{\tau}_1$ rest system back to the laboratory system of the detector:

$$E_\tau^{\min,\,\max} = \frac{m_{\tilde{\tau}}}{2}\left(1 - \frac{m_\chi^2 - m_\tau^2}{m_{\tilde{\tau}}^2}\right)\frac{1 \pm \beta\beta_{\tilde{\tau}}}{\sqrt{1-\beta^2}} \tag{8.5}$$

Here β is the velocity of a $\tilde{\tau}_1$ in the detector. This equation could be simplified by ignoring the term $m_\tau^2/m_{\tilde{\tau}}^2$, as a $\tilde{tau}_1$ is more than 50 times heavier than a SM tau. However, $\beta_{\tilde{\tau}}$ should only be neglected if a SUSY scenario is chosen with a sizable mass difference between χ_1^0 and $\tilde{\tau}_1$. In this case, the tau is highly relativistic in the $\tilde{\tau}_1$ rest frame and $\beta_{\tilde{\tau}}$ close to 1. In the SPS1a' parameter point and at the nominal ILC centre-of-mass energy of $\sqrt{s} = 500\,\text{GeV}$, the maximum energy is $E_\tau^{\max} = 42.6\,\text{GeV}$ ('+' in equation (8.5)) while the minimal τ energy is $E_\tau^{\min} = 2.54\,\text{GeV}$ ('-' in equation (8.5)).

8.4 Measurement of τ Polarisation in the Process $\tilde{\tau}_1\tilde{\tau}_1 \to \chi_1^0\chi_1^0\tau\tau$

The polarisation of a tau influences strongly the kinematic of its decay remnants. If the tau is positively polarised[1], the pion from a decay $\tau \to \pi\nu$ is emitted preferentially in the direction of flight in the decay $\tau \to \pi\nu$. (see figure 8.6). This is because neutrinos are left handed and the pion is a spin 0 particle. A negatively polarised, or left handed, τ^- emits the neutrino preferentially in the forward direction and then the pion gets a small energy share. For the τ^+ decay, the same arguments are true for the inverted handiness: A left handed or negatively polarised τ^+ emits the pion preferentially in forward direction, while a right handed τ^+ more often emits the neutrino in the forward direction in the single pion decay.

[1] right handed τ^- in the laboratory system

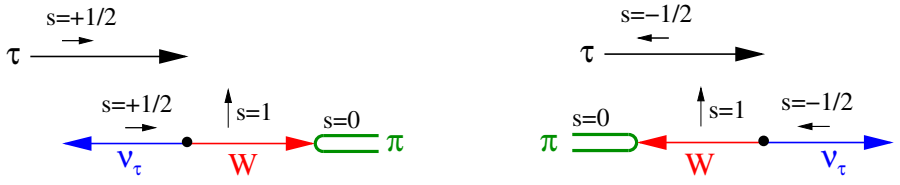

(a) visible decay products get a large energy share

(b) visible decay products get a small energy share

Figure 8.6: *Emission of the pion in τ decays in dependence of the τ polarisation: the W is transversely polarised and the W spin is transfered to an angular momentum of the ν_τ-π system.*

In the process $e^+e^- \to \chi_1^0\chi_1^0\tau^-\tau^+$, the polarisation of the two taus is linked via the two staus: if the τ^- is produced with a polarisation P_τ, then at the same time, the τ^+ is emitted with a polarisation $-P_\tau$, because the τ^+ is emitted by an 'anti'-stau $\tilde{\tau}_1^+$. All relevant quantum numbers, which determine P_τ, are reversed for the anti-stau compared to the stau $\tilde{\tau}_1^-$.

Thus it is possible to measure the average polarisation P_τ by observing the pions being produced in the decay of the tau. Here, no distinction between negative and positive pions is necessary, because a right handed τ^- appear as frequently as left handed τ^+. The former produces negative pions while the latter positive pions, but in both cases the pion is emitted with the same probability in forward or backward direction with respect to the tau.

In the analysis, which is presented in the following, this polarisation measurement in this single pion decay $\tau \to \pi\nu_\tau$ and in a second channel, the decay via an intermediate ρ-meson $\tau \to \rho\nu_\tau \to \pi\pi_0\nu_\tau$ are studied.

Decay $\tau \to \pi\nu_\tau$

Figure 8.7(a) shows the energy spectra of the pions in the decay $\tau \to \pi\nu_\tau$ in coming for the $\tilde{\tau}_1$ pair production process (see figure 8.5) for ILC's nominal centre-of-mass energy of $\sqrt{s} = 500\,\text{GeV}$. This spectrum denotes the cases $P_\tau = \pm 1$ and $P_\tau = 0$, respectively. The endpoint of the spectrum coincides with the maximum τ energy in the laboratory system E_τ^{max} (see equation (8.5)), independently of P_τ. In the case of $P_\tau > 0$ the spectrum has a triangular shape with a turnover point at E_τ^{min}. If P_τ decreases, also the average pion energy decreases, the turnover point vanishes and the spectrum starts to peak strongly towards zero.

These curves are evaluated from a theoretical description of the spectrum, given by (e.g. [81])

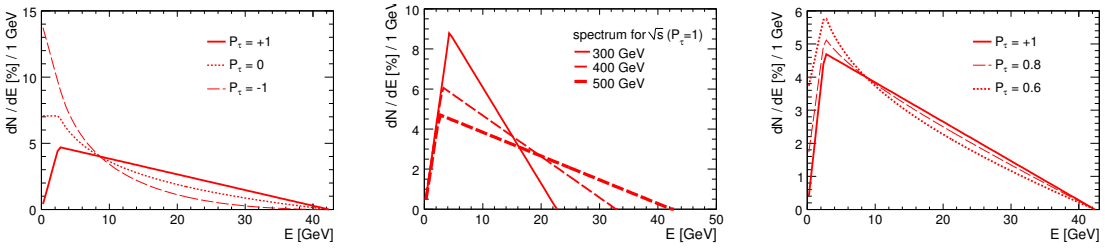

(a) $P_\tau = \pm 1$ and $P_\tau = 0$ for $\sqrt{s} = 500\,\text{GeV}$

(b) pion spectra for different $\sqrt{s}$

(c) pion spectra P_τ above 0.6

Figure 8.7: *Pion energy spectra in the process* $e^+e^- \to \tilde{\tau}_1\tilde{\tau}_1 \to \chi_1^0\chi_1^0\tau + \pi\nu_\tau$

$$\frac{1}{\sigma}\frac{\mathrm{d}N}{\mathrm{d}E_\pi} = \frac{\sqrt{s}(1-P_\tau)}{2(E^{\max}-E^{\min})} \begin{cases} \log\frac{E^{\max}}{E^{\min}} + 2P_\tau E_\pi(\frac{1}{E^{\min}} - \frac{1}{E_\tau^{\max}}) & 0 < E_\pi < E_\tau^{\min} \\ \log\frac{E^{\max}}{E_\pi} + 2P_\tau(1 - \frac{E_\pi}{E^{\max}}) & E_\tau^{\min} < E_\pi < E_\tau^{\max} \end{cases} \tag{8.6}$$

Here $^{\mathrm{d}N}/_{\mathrm{d}E_\pi}$ denotes the number of pions in a pion energy interval ΔE_π and σ is the effective cross-section for the process $e^+e^- \to \tilde{\tau}_1\tilde{\tau}_1 \to \chi_1^0\chi_1^0\tau + \pi\nu_\tau$.

Figure 8.7(b) shows the pion spectrum for different centre-of-mass energies $\sqrt{s}$ for a fixed $P_\tau = 1$. The turnover point moves to higher energies, if the centre-of-mass energy is decreased. Directly on the threshold energy, $\sqrt{s} = 2 \cdot m_{\tilde{\tau}_1} \approx 220\,\text{GeV}$, the spectrum has the shape of an equilateral triangle.

Figure 8.7(c) shows the pion energy spectra for a τ polarisation P_τ above 60 % for the fixed centre-of-mass energy $\sqrt{s} = 500\,\text{GeV}$. As the different graphs demonstrate, a change in P_τ affects in first place the rising edge of the spectrum. To determine P_τ accurately, these low energy pions have to be reconstructed and identified robustly in the ILD detector. The analysis, which is presented in chapter 10 is focused on this channel, because the measurement is more challenging in terms of detector performance than the measurement in the alternative ρ-channel (see below). In addition, energy losses prior to the e^+e^- interaction, like initial state radiation and beam energy losses, have to be considered, because the pion energy spectrum depends on the centre-of-mass energy $\sqrt{s}$ (see equation 8.6). This is discussed in section 9.2 of the following chapter.

Decay $\tau \to \rho\nu_\tau \to \pi^\pm\pi_0\nu_\tau$

In the decay channel $\tau \to \rho\nu_\tau \to \pi^\pm\pi_0\nu_\tau$ the degree of τ polarisation affects the energy ratio $R = {}^{E_{\pi^\pm}}/_{E_\rho}$. A positively polarised tau decays preferentially to a longitudinally polarised ρ. In its decay, one of the pions gets a large, the other one a small energy share. The ${}^{E_{\pi^\pm}}/_{E_\rho}$-ratio distribution peaks at 0 and 1 in this case and is proportional to $\sim (2 \cdot R - 1)^2$. A negatively polarised tau decays dominantly to a transversal polarised ρ and in its decay both pions get a equal energy share. In this case the ratio spectrum has a shape $\sim 2 \cdot R(1-R)$.

Process	cross-section for beam polarisation (P_{e^+}, P_{e^-}) (+1,-1)	(-1,+1)	(-0.6,+0.8)	(-0.3,+0.8)
$\tilde{\tau}_1\tilde{\tau}_1 \to \chi_1^0\chi_1^0\tau\tau$	74.0	222.6	162.8	132.8
$\tilde{\tau}_1\tilde{\tau}_1 \to \chi_1^0\chi_1^0\tau + \pi\nu_\tau$	16.1	48.5	35.5	29.0
$\tilde{\tau}_1\tilde{\tau}_1 \to \chi_1^0\chi_1^0\tau + \pi^\pm\pi_0\nu_\tau$	37.8	113.6	83.1	67.8

Table 8.5: *Cross-sections of the signal processes for different beam polarisations*

Process	Expected rates for 500 fb (P_{e^+}, P_{e^-}) $(-0.6, +0.8)$	$(-0.3, +0.8)$
$\tilde{\tau}_1\tilde{\tau}_1 \to \chi_1^0\chi_1^0\tau\tau$	81400	61900
$\to \chi_1^0\chi_1^0\tau + \pi\nu_\tau$	17750	14500
$\to \chi_1^0\chi_1^0\tau + \pi^\pm\pi_0\nu_\tau$	41550	33900

Table 8.6: *Expected rates of the signal processes for different beam polarisation setups*

8.4.1 The Signal Process at the ILC

The cross-sections for the signal process $\tilde{\tau}_1\tilde{\tau}_1 \to \chi_1^0\chi_1^0\tau\tau$ are summarised in table 8.5 for different setups of the beam polarisation. The process prefers a right handed electron and a left handed positron in the initial state. For the analysis, a polarisation scheme of $-60\,\%$ positron and $+80\,\%$ electron beam polarisation $(-0.6, +0.8)$ is assumed as default. The effect of a minor positron polarisation of only $-30\,\%$, which is under discussion for the ILC, is discussed with the final results. Most standard model and many SUSY processes prefer the opposite polarisation configuration, like $(0.3, -0.8)$. Hence, for the enhancement of the signal process, the ILC must be operated in a beam polarisation scheme which disfavours most SM and SUSY backgrounds.

The expected rate of the signal process and the expected number of tau decays into the two studied channels are summarised in table 8.6.

In the $(-0.6, +0.8)$ beam polarisation setup, the signal process has a cross-section of $\sigma \approx 162\,\text{fb}$ which gives rise to about 81000 $\tilde{\tau}_1$ pair production events for $\mathcal{L} = 500\,\text{fb}^{-1}$. The branching ratio (BR) of $\tau \to \pi\nu_\tau$ is $10.9\,\%$ [12] resulting in an effective cross-section of $\sigma_\pi = 2 \cdot \text{BR} \cdot \sigma \approx 15.5\,\text{fb}$ for this decay channel. An additional factor of 2 is introduced here, because there are two taus in every event. The yield is 17750 pions, distributed over 16300 events with a single decay $\tau \to \pi\nu_\tau$ and 960 events in which both taus decay to a single pion.

The branching ratio $\tau \to \rho\nu_\tau \to \pi^\pm\pi_0\nu_\tau$ is $25.5\,\%$ giving an effective cross-section of $37.8\,\text{fb}$ for signal pions in the ρ-analysis channel. The expected yield is 81400 of these decays in $500\,\text{fb}^{-1}$.

A change to the $(-0.3, +0.8)$ beam polarisation scheme would reduce the signal yield by about $20\,\%$ in both channels.

In the following chapters, the neutralino χ_1^0 is denoted by χ_1 and the stau $\tilde{\tau}_1$ is abbreviated $\tilde{\tau}$, as the second stau, $\tilde{\tau}_2$, is mostly irrelevant for the discussion.

9 ILD Detector Simulation

In this chapter the software tools used for the ILD detector simulation are presented in section 9.1. This software framework was used in comprehensive simulation mass production of signal and background processes in 2008 and 2009. These simulated events are the basis of the study of the τ polarisation (P_τ) measurement, which is the main topic of the next chapter. Preparatory studies for the analysis are discussed in section 9.2, namely the development and evaluation of a fit routine to determine P_τ from the reconstructed simulated data.

9.1 Full Detector Simulation

Full detector simulation is the essential method for detector studies in high energy physics experiments. Before some of its applications are summarised, the technique shall be introduced in general. Figure 9.1 illustrates the following explanations.

A detector simulation is a three step process and each of the three simulation steps is connected to its dedicated software:

In the first step, a generator creates events of the physics process to be simulated. On this generator level, an event is a collection of particles in the final state with appropriate four-vectors. In a second step, a detector simulation software propagates each particle from the interaction point through a virtual detector. Thereby it simulates the particle's interaction with the detector material. The output of this process is simulated raw data which is at best equal to real detector raw data. Consequently, the following event reconstruction software makes no distinction between simulated events and real data. This final step, the event reconstruction, typically comprises several subprocesses, depending on the complexity of the experimental setup and the reconstruction software framework. The outcome of the event reconstruction are measured particles in the detector together with their reconstructed four-vectors.

The development of measurement strategies is one application of detector simulations. In chapter 10, this is demonstrated for the measurement of the τ polarisation P_τ. In this case, simulated $\tilde{\tau}_1$-pair production events and the crucial backgrounds are used to evaluate search criteria for pions coming from the $\tilde{\tau}_1 \to \chi_0\tau \to \chi_0 + \pi\nu$ decays. When this selection is in place and a result for P_τ obtained, the dependence between certain detector performance parameter and the achievable measurement accuracy can be investigated. In this case this is in particular the reconstruction momentum resolution for the pions. Another example is connection between the TPC point resolution and the accuracy of the mass peak in the Higgs recoil analysis, mentioned in section

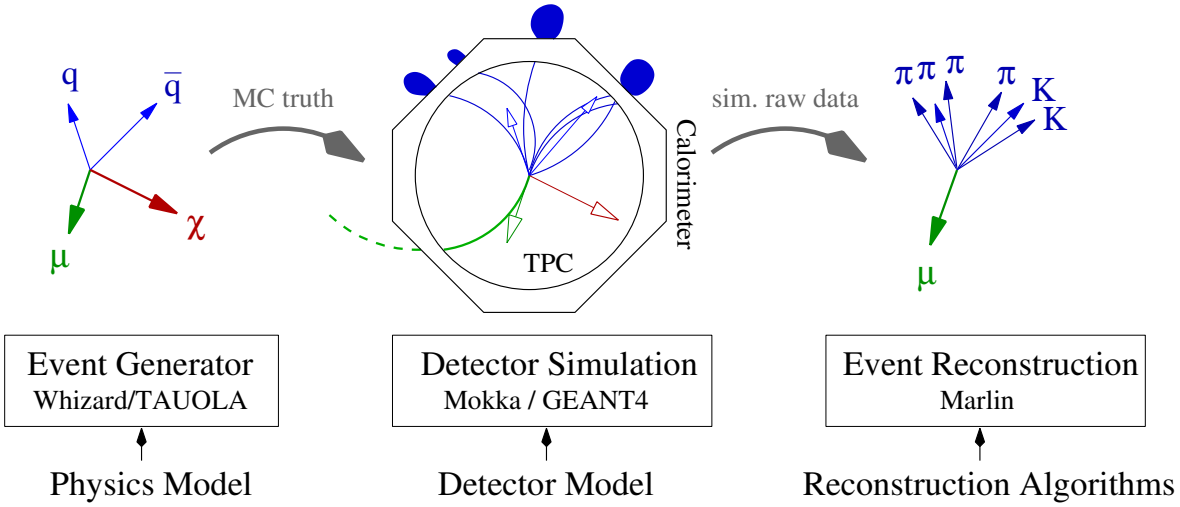

Figure 9.1: *Full detector simulation chain*

2.3.2. Here, the simulation results pose dedicated requirements on the sub-detectors. In addition, the freedom to use different detector models as input to the simulation step allows for a dedicated optimisation of the sub-detectors. One example for this is the optimisation of the calorimeter cell size.

The stated applications so far refer to the detector development. However, once the detector is in operation, simulations will still be needed. In the running phase of an experiment, corrections for limited detector acceptances and reconstruction efficiencies are derived from the simulations. Moreover, as any physics model can be used as an input to the generator, also events of new or exotic physics models can be simulated. In this case the comparison between the measured data and the model dependent simulation can falsify a physics model which has prior been put into the generator.

The software packages for ILD detector are currently being developed and come to operation in the simulation efforts [94]. The event generator Whizard 1.51 [95] has been used for the generation of events, Mokka [96, 97] and GEANT4 [98] for the detector simulation and Marlin [99] for the event reconstruction. A link between the simulation and reconstruction packages is the common data format LCIO (Linear Collider Input Output) [100]. The subsequent sections present these software packages.

9.1.1 Event Generation

Besides generating four-vector files for the simulation, the Wizard event generator also calculates the cross-section of each process. In its default configuration, the generator creates final state particles on the level of single fermions, like quarks, and interfaces Pythia [101] for their fragmentation. In this example, Pythia would fragment the quarks to hadrons. The four-vectors of the fragments enter the list of particles for the simulation.

Pythia however is not adequate for the fragmentation of the taus in the final states

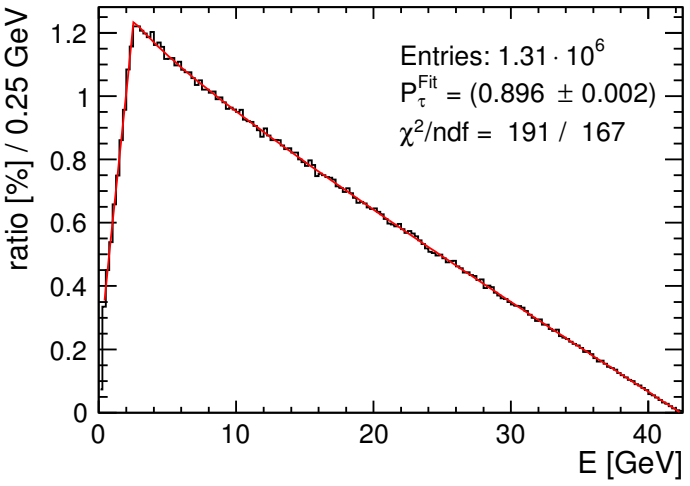

Figure 9.2: *Pion energy spectrum in the decay $\tau \rightarrow \pi\nu_\tau$ on generator level*

of the signal process, because it does not respect particle polarisation. As a consequence the pion energy spectrum in the decay $\tau \rightarrow \pi\nu$ does not reflect the degree of τ polarisation. This problem has been fixed by replacing Pythia with the TAUOLA package[102][1]. In this modified version of Whizard, SM taus are declared stable for Pythia and are left undecayed. Internally Whizard calculates the polarisation state of the final state particles and TAUOLA reads this information. Then it decays the taus in consideration of their polarisation states.

In the SPS1a' SUSY point, the taus in the process $\tilde{\tau}_1 \rightarrow \chi_1\tau$ are polarised to $P_\tau = 97\,\%$, as discussed in section 8.3. Figure 8.4 shows the connection between P_τ and $\tan\beta$ which is equal to 10 in SPS1a'.

However, Whizard generates the taus with $P_\tau = 89.6\,\%$. This number follows from counting how often a positively or negatively polarised tau was found in $2 \cdot 10^6$ $\tilde{\tau}_1 \rightarrow \chi_0 + \tau$ decays. Figure 9.2 shows the resulting pion energy spectrum for the decay $\tau \rightarrow \pi\nu_\tau$ fitted with the theoretical curve. The fit result is $P_\tau = 89.6 \pm 0.02\,\%$. The reason for the difference to the expected value of $P_\tau = 97\,\%$ has not been studied in detail. Of major interest for the analysis is the demonstration of the feasibility of the measurement and an estimation of the achievable accuracy ΔP_τ. The actual value P_τ in the simulated data is of minor importance for this.

Like the $\tilde{\tau}_1$ pair production signal process, also all other supersymmetric processes with taus and standard model τ pair production have been generated with this modified version of Whizard. For the calculation of supersymmetric processes, Whizard needs masses, interaction cross-sections and branching ratios of the involved SUSY particles as an additional input. These parameters have been calculated with SPHENO [103] in the SPS1a' SUSY point.

In the following, the Whizard generated events are called 'Monte Carlo truth'.

[1]The coupling of TAUOLA and Whizard has been done in close cooperation with the authors of both packages.

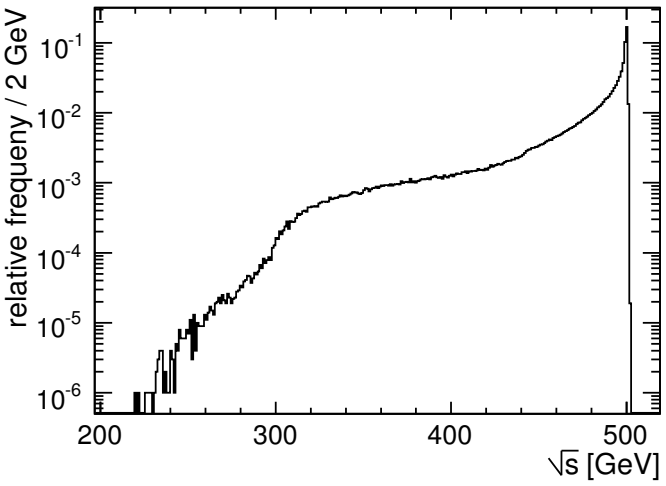

Figure 9.3: *Luminosity spectrum for the process* $e^+e^- \to \tilde{\tau}_1\tilde{\tau}_1$

Luminosity Spectrum

When the ILC is operated at the nominal centre-of-mass energy of $\sqrt{s} = 500\,\text{GeV}$, this full energy will not be available at the primary vertex of each e^+e^- interaction. The reason for this is an energy loss of the beam particles prior to the interaction, mainly due to beam-strahlung and initial state radiation (ISR) [104]. A third contribution is the beam energy spread of the machine but it is negligible compared to ISR and beam-strahlung losses. Figure 9.3 shows the distribution of the effective centre-of-mass energies, $\sqrt{s}$, in the generated events of the signal process $e^+e^- \to \tilde{\tau}_1\tilde{\tau}_1$. In the following, this distribution is called luminosity spectrum $\mathcal{L}_s$.

Whizard respects these energy losses and uses an effective $\sqrt{s}$ in the generation of events. In addition, the generator also adds initial state radiation photons to collection of four-vectors of the event.

However, the effect of the beam-strahlung is not completely respected in the simulation: beam-strahlung photons can interact and produce e^+e^--pairs (see [15]). These pairs are overlaid to every physics event, but are not included in the simulation. The simulation of this background is technically challenging and foreseen in the next iteration of simulation studies.

Beam Polarisation

The ILC will deliver polarised initial beams in different setups as it is mentioned in section 2.2. To have the full flexibility for all ILD physics analyses, all processes have been simulated in four polarisation scenarios, namely $(-1,+1), (+1,-1), (+1,+1)$ and $(-1,-1)$. Here, the first number denotes the positron and the second the electron beam polarisation.

Any intermediate degree of polarisation can be produced by an appropriate mixing of these base states - in the analysis presented in chapter 10 the scenario is $(-0.6,+0.8)$.

beam pol.	event weight for (P_{e^+}, P_{e^-})	weight for $(-0.6, 0.8)$	weight for $(-0.3, 0.8)$
$(-1, -1)$	$(1 - P_{e^+})(1 - P_{e^-})/4$	0.08	0.065
$(-1, +1)$	$(1 - P_{e^+})(1 + P_{e^-})/4$	0.72	0.585
$(+1, -1)$	$(1 + P_{e^+})(1 - P_{e^-})/4$	0.02	0.035
$(+1, +1)$	$(1 + P_{e^+})(1 + P_{e^-})/4$	0.18	0.315

Table 9.1: *Event weight for a mixing of events according to a beam polarisation of* (P_{e^+}, P_{e^-})

In this way, different ILC running scenarios be studied. The mixing is realised by an allocation of event weights. Table 9.1 gives an overview of the weights which are assigned to the different samples to create the polarisation state (P_{e^+}, P_{e^-}).

The resulting cross-section for a beam polarisation state (P_{e^+}, P_{e^-}) can be calculated in a similar way. It is given by the sum of the cross-sections for the fully polarised beams $\sigma(+1, +1)$, $\sigma(-1, +1)$, $\sigma(+1, -1)$ and $\sigma(-1, -1)$ where each is multiplied with the appropriate weighting factor.

In the case of purely s-channel processes, such as the signal process, the cross-section vanishes for equally polarised beams.

9.1.2 Detector Simulation

The simulation framework Mokka is an interface between several different software packages and data formats (see figure 9.1).

As an input, Mokka accepts the generated physics events in the Whizard-format and a geometric description of the detector. The model used for the simulations is called ILD00 [105]. Mokka interfaces the GEANT4 package for the simulation of interactions between particles and the detector material. Besides this, GEANT4 also allows for a decay of unstable particles, like pions or muons, in flight. These particles are stable on generator level.

When the simulation is finished, Mokka converts the GEANT simulated results to simulated raw data. The raw data describes energy deposits in the active detector components. Finally Mokka stores the raw data into files of the LCIO format.

9.1.3 Event Reconstruction

The event reconstruction is performed with in MARLIN framework, which is a collection of software tools specific to LCIO data processing. MARLIN provides access to the detector raw data stored in the LCIO file and allocates it to its modules. These modules are called Marlin Processors.

Each processor carries out a dedicated step of the analysis and stores the processed data back in the LCIO format. After the reconstruction chain is completed, the LCIO file comprises the complete information of the event. This way a reprocessing of certain

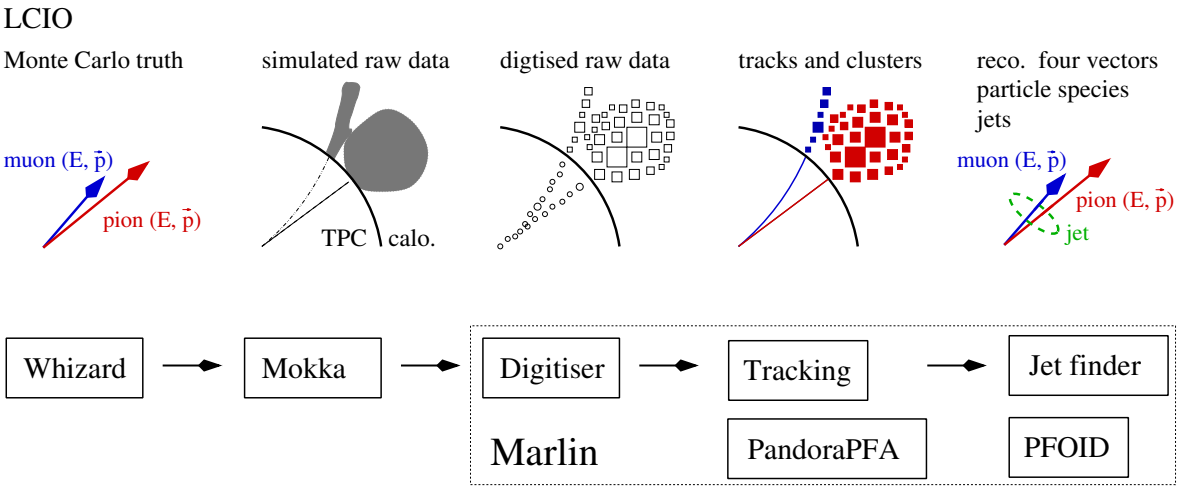

Figure 9.4: *Data processing with MARLIN*

data sets is possible when bug-fixes of a processors become available. Also the scheme allows for a comparative analysis of the same raw data by different reconstruction algorithms.

Figure 9.4 summarises the major steps in the reconstruction chain. As a precondition for data analysis the simulated raw data is digitised. This simulates the sensitive detector elements and the electronics response to the energy depositions in the detector. In the optimal case, the digitised raw data matches real detector raw data.

The event reconstruction follows the particle flow concept (see section 2.3.1). It aims to reconstruct the four vector of all particles which are visible in the detector. Firstly dedicated tracking processors reconstruct the tracks in the TPC and match them to measurements of the silicon tracker. With the reconstructed tracks as an input, the particle flow processor PandoraPFA [106] identifies calorimeter clusters and merges them with the tracks. The outcome is a collection of reconstructed particles, each associated with a measured four momentum vector $(E, \vec{p})$.

Subsequent to these reconstruction steps, additional Marlin processors perform for example a jet finding [107] and a particle identification (PFOID).

In high energetic e^+e^- collisions ($\sqrt{s} \geq 10\,\text{GeV}$), particles coming from the interaction point are frequently bundled in jets. The jet finder analyses the event structure and combines the reconstructed particles into jets.

9.1.4 Detector Coordinate System

The reconstruction algorithms evaluate particle momentum vectors $\vec{p}$ with respect to the detector coordinate system which is depicted in figure 9.5. Commonly a spherical and a Cartesian system are used in parallel and the origin of both system coincides with the interaction point. The two reference frames have a common z-axis which share half the crossing angle with the electron and the positron beam. The positive

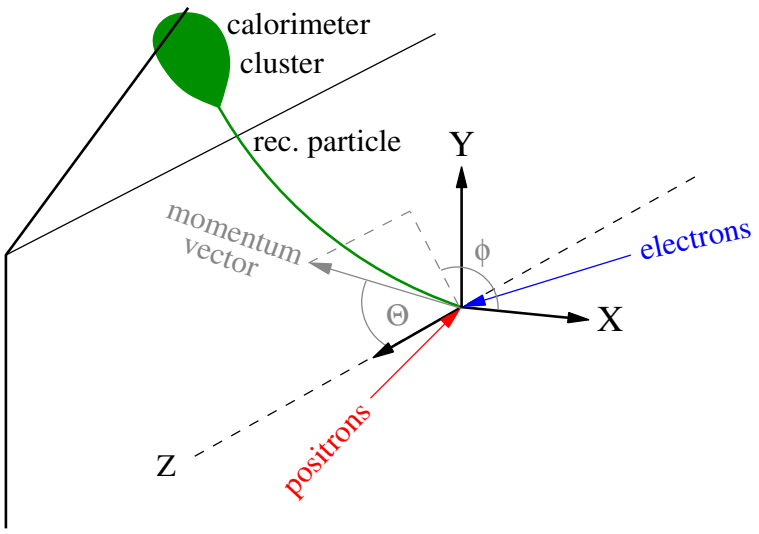

Figure 9.5: *Detector coordinate system*

z-direction is along the outgoing electron beam and the x-axis lies in the plane defined by the beams. The y-axis is arranged such that the system is right handed.

In the spherical frame, momentum vectors are measured by the polar angle Θ and the azimuth angle ϕ where the former refers to the z, the latter to the x-axis. A variable is called 'transverse' in the following, as for example the transverse momentum, if it is calculated after the jets have been projected onto the r-φ (x-y) plane. The according variable is furnished with a '$\perp$'.

9.2 Determination of P_τ on Monte Carlo Level

Preparatory for the study on the P_τ measurement with the ILD detector in chapter 10, this section discusses the final step of the measurement, the determination of P_τ itself.

In the decay channel $\tau \rightarrow \pi\nu$ the P_τ measurement works via the reconstruction of the pion energy spectrum and a fit with theoretical curve (equation 8.6). However the shape of the spectrum is modified by the effect of initial-state radiation and beam-strahlung. The next section discusses these modification and proposes an adaption of the fit function.

In the channel $\tau \rightarrow \rho\nu \rightarrow \pi\pi_0\nu$, P_τ can be determined from a reconstructed $^{E_\pi}/_{E_\rho}$ ratio spectrum. Section 9.2.1 proposes an appropriately constructed function for a fit to such a reconstructed ratio spectrum.

9.2.1 Correction for Initial State Radiation- and Beam-Strahlung in the Channel $\tau \rightarrow \pi\nu$

Due to the energy loss of the beam particles prior to the interaction, which is described by the luminosity spectrum in figure 9.3, the signal process also proceeds at decreased

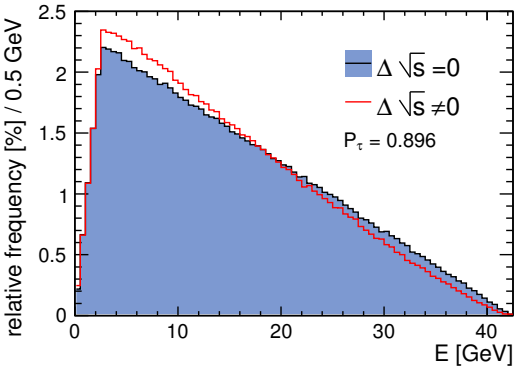

(a) effect of the beam energy loss on the pion energy spectrum

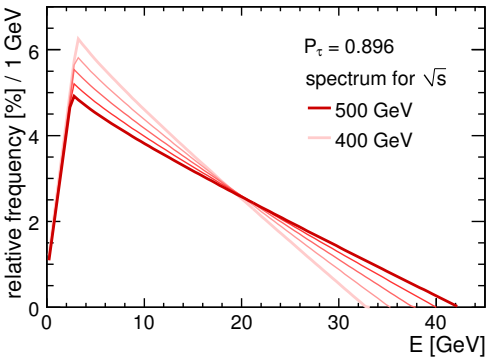

(b) theoretical spectrum for $\sqrt{s}$ between $400 - 500\text{GeV}$

Figure 9.6: *Theoretical spectrum for different $\sqrt{s}$ and effect of ISR and beam energy spread on the pion energy spectrum*

centre-of-mass energies $\sqrt{s}$. These variations in $\sqrt{s}$ propagate to the energy spectrum of the pions in the decay $\tau \rightarrow \pi\nu$ and modify the spectrum's shape.

Figure 9.6(a) illustrates the effect. The diagram compares a pion energy spectrum generated with the beam energy loss ($\Delta\sqrt{s} \neq 0$) with a pion energy spectrum for a fixed $\sqrt{s} = 500\,\text{GeV}$.

The appearance of the modified shape can be explained with the theoretical description (equation (8.6)) of the spectrum. This function depends on $\sqrt{s}$ and figure 9.6(b) shows the function for centre-of-mass energies between 400 GeV and 500 GeV. As the change of the slope demonstrates, with decreasing $\sqrt{s}$ the spectrum's end point shifts to smaller values. At the same time the turnover point moves moderately to higher energies.

The variations $\Delta\sqrt{s}$ produce a superposition of many of these spectra, each one weighted by the relative frequency of the according $\sqrt{s}$ in the luminosity spectrum $\mathcal{L}_\text{s}$. In the sum of these spectra, the falling edge of the energy spectrum acquires the rounded shape shown in figure 9.6(a).

The theoretical description of the spectrum ${}^{\text{d}N(E,P)}/_{\text{d}E}$ however only describes the case of one fixed $\sqrt{s}$. Thus it has to be modified for a fit to data pions which follow the modified shape. For this, two correction methods have been evaluated.

Correction by Superimposing many Spectra

One possibility for an adaption of the fit function ${}^{dN}/_{dE}|_{\Delta\sqrt{s}}$ is to replace it by a superposition of many theoretical spectra

$$\left.\frac{dN}{dE}\right|_{\Delta\sqrt{s}\neq 0} = \int_0^{500\,\text{GeV}} \frac{dN}{dE}(\sqrt{s}) \cdot \mathcal{L}_\text{s}(\sqrt{s})\ \text{d}\sqrt{s}.$$

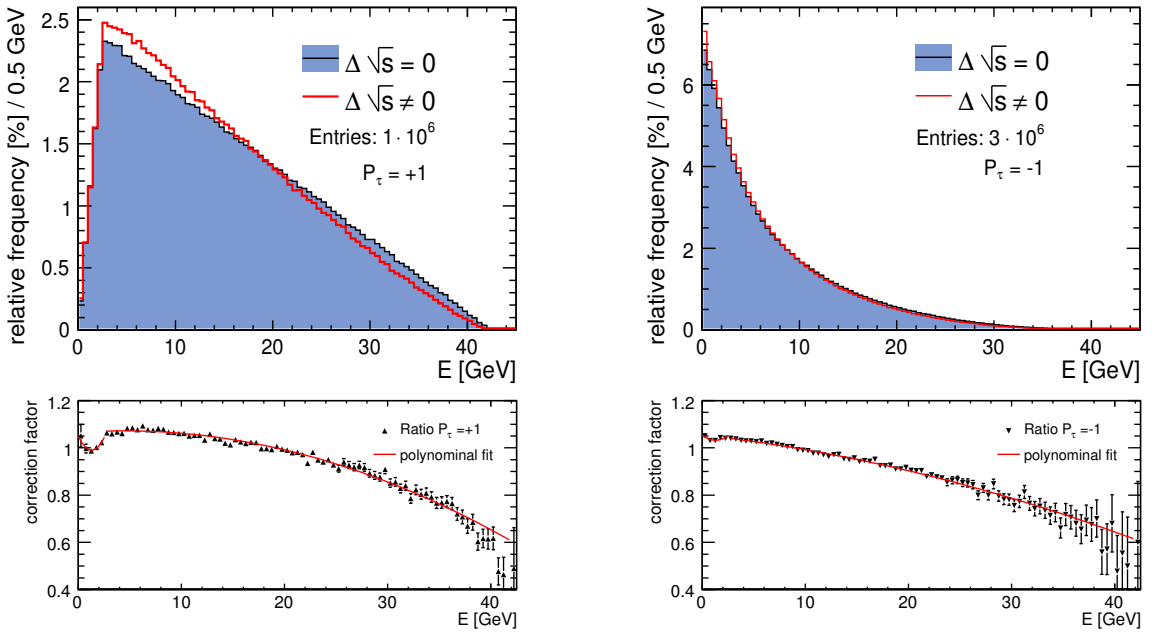

(a) base spectra for $P_\tau = +1$, the lower plot shows the bin-wise ratio

(b) base spectra for $P_\tau = -1$, the lower plot shows the bin-wise ratio

Figure 9.7: *Fully polarised base spectra, with and without beam energy spread and ISR*

This convolution models the appearance of the new shape: the new fit function includes all possible spectra weighted with the relative frequency of their appearance. This weight is given by the luminosity spectrum. Since the latter is not described analytically, the integration needs to be realised as the summation

$$\left.\frac{dN}{dE}\right|_{\Delta\sqrt{s}\neq 0} \approx \sum_{\sqrt{s}=0}^{500\,\mathrm{GeV}} \frac{dN}{dE}(\sqrt{s}) \cdot \mathcal{L}_\mathrm{s} \cdot \delta\sqrt{s}.$$

Here $\delta\sqrt{s}$ is the bin width. In figure 9.3 the luminosity is sampled with $\delta\sqrt{s} = 2\,\mathrm{GeV}$. In the fit procedure a refined $\delta\sqrt{s} = 1\,\mathrm{GeV}$ is used.

Correction with a Correction Factor

The second ansatz is to multiply an additional factor $F(E, P_\tau)$ to the fit function

$$\frac{\mathrm{d}N}{\mathrm{d}E}(P_\tau) \to \frac{\mathrm{d}N}{\mathrm{d}E}(P_\tau) \cdot F(E, P_\tau),$$

which reshapes it to the match the new shape. This correction factor depends on the pion energy and the τ polarisation.

An evaluation of $F(E, P_\tau)$ works via the cases of extreme τ polarisation $P_\tau = \pm 1$. In figure 9.7(a) the upper diagram is equivalent to the one in figure 9.6(a) but denotes the case of $P_\tau = +1$. The lower diagram shows the ratio

$$R(E, P_\tau = +1) = \left.\frac{\text{spectrum generated with } \Delta\sqrt{s} \neq 0}{\text{spectrum generated with } \Delta\sqrt{s} = 0}\right|_{\text{per bin}}$$

For the evaluation of $F(E, P_\tau)$ it is advantageous to describe $R(E, P_\tau = +1)$ analytically. Here this is done with a combination of two polynomials of second order. The first ranges from 0 to $E_{\text{min}} = 2.54\,\text{GeV}$ which corresponds to the rising edge of the spectrum. A separate polynomial is fit to the points corresponding to the falling edge of the spectrum ($E > 2.54\,\text{GeV}$).

If $P_\tau = +1$ was the real polarisation of the taus, these two polynomials would be the right correction factor $F(E, P_\tau)$: they rescale the theoretical fit function from the original spectrum to the modified shape.

Figure 9.7(b) shows the analogue diagrams for the case of $P_\tau = -1$. The quotient of the two spectra is again described by a combination of two polynomials in the same boundaries. Like for the case $P_\tau = +1$, these two polynomials would be the adequate correction factor, if P_τ was -1.

The two correction factors are different but the correction for an intermediate P_τ can be evaluated from the the two cases of full τ polarisation. This follows from the fact that the energy spectrum for any P_τ can be broken up into a $P_\tau = -1$ and a $P_\tau = +1$ contribution. The positively and negatively polarised fraction is p_+ and p_-, respectively:

$$p_+ = \frac{1 + P_\tau}{2} \qquad p_- = \frac{1 - P_\tau}{2} \tag{9.1}$$

Similar, a pion energy spectrum belonging to any intermediate P_τ can be generated by randomly pulling entries, with appropriately adapted probabilities p_+ and p_-, from the two base spectra of figure 9.7 and filling them into a new histogram. As an example figure 9.8(a) depicts a spectrum belonging to $P_\tau = 0.8$. This contains $0.12 \cdot 10^6$ pions from the $P_\tau = -1$ and $1.08 \cdot 10^6$ from the $P_\tau = +1$ base spectrum. Here a non vanishing $\Delta\sqrt{s}$ is included.

Consequently the correction factor $F(E, P_\tau)$ for the intermediate polarisation P_τ is a linear combination of the polynomials $F(E, +1)$ and $F(E, -1)$ with weights p_+ and p_-:

$$F(E, P_\tau) = \frac{1 + P_\tau}{2} \cdot F(E, +1) + \frac{1 - P_\tau}{2} \cdot F(E, -1)$$

As a sum of two polynomials is again a polynomial, the modified fit function assumes the shape

$$\frac{\mathrm{d}N}{\mathrm{d}E}(P_\tau) \to \frac{\mathrm{d}N}{\mathrm{d}E}(P_\tau) \cdot \underbrace{(\mathrm{c}_0 + \mathrm{c}_1 \cdot E + \mathrm{c}_2 \cdot E^2)}_{F(E, P_\tau)}. \tag{9.2}$$

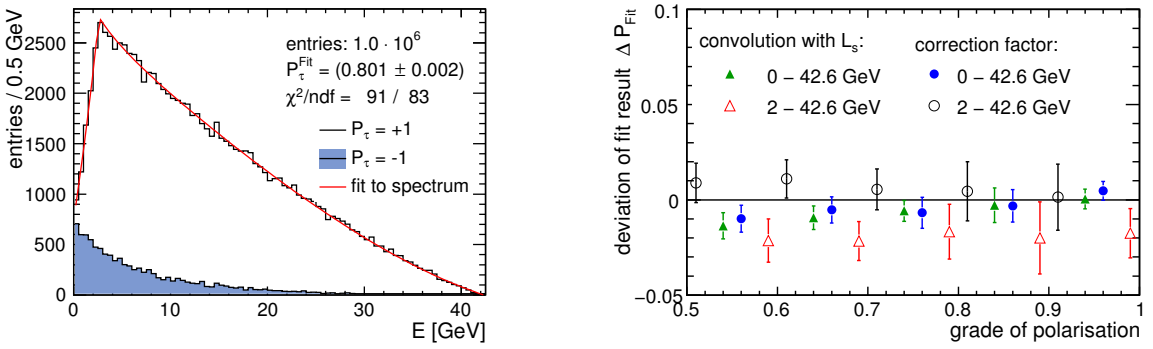

(a) summation of the two base spectra to a spectrum with $P_\tau = 0.8$

(b) fit result for different spectra and P_τ

Figure 9.8: *Test of the fit algorithm at spectra of different* P_τ

with the coefficients

$$c_\mathrm{i}(P_\tau) = \frac{1+P_\tau}{2} \cdot c_\mathrm{i}(+1) + \frac{1-P_\tau}{2} \cdot c_\mathrm{i}(-1).$$

Here $c_\mathrm{i}(\pm 1)$ denotes the according coefficient in the correction polynomials $F(E, \pm 1)$ shown in figure 9.7.

In this scheme, the modifications to the spectrum are parametrised regardless of their origin. The theoretical description of the spectrum and the correction are fitted at the same time to reconstructed data points. This fit method has the advantage that it is comparably simple, but depends to a high degree on an accurate determination of the two base spectra. Figure 9.8(a) also shows an example fit using this method. This yields the expected value of 0.8.

Comparison of the Fit Algorithms

The two fit procedures have been tested at energy spectra belonging to P_τ between 0.5 and 1. For this, the two base spectra shown in figure 9.7 ($\Delta\sqrt{s} \neq 0$) have been combined in the same way as discussed for the example of figure 9.8(a) to create new histograms for the fitting. Each histogram has been filled with 18000 entries, which corresponds to the nominal yield of pions for an integrated luminosity of $\mathcal{L} = 500\,\mathrm{fb}$.

Figure 9.8(b) depicts the difference between the grade of polarisation which has been adjusted by the mixing and the results gained with the two fitting procedures. Here each point corresponds to the mean value of fit results from six independently created dummy histograms. Both methods have been tested with the same histograms for all P_τ. The uncertainty range of each point is the variance of the fit results.

If the fit range is extended over a whole histogram, both methods give correct results for any P_τ. However, below 2 GeV a reconstruction of the spectrum is not possible, as discussed in the subsequent chapter. The analysis does not yield any data points on

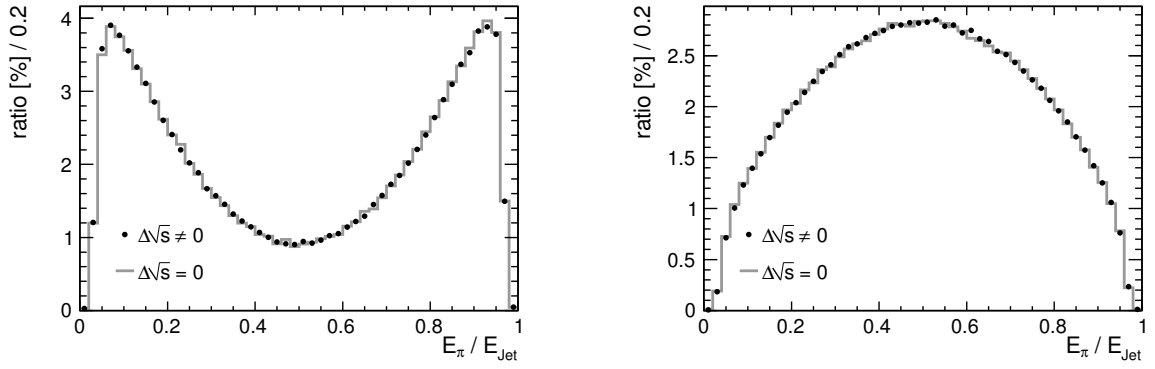

(a) base spectrum for $P_\tau = +1$

(b) base spectrum for $P_\tau = -1$

Figure 9.9: *$E_\pi^\pm/E_{Jet}$-ratio base spectra*

the rising edge of the spectrum and the fitting procedures have to cope with a limited fit range above 2 GeV. In these toy fits, the reduction of the fit range increases the variances, which is expected because the loss of reference points on the rising edge makes the fit less robust. This effect is even enhanced because the falling edge of the spectrum shows a weaker dependency on P_τ (see figure 8.7(c)) than the rising edge of the spectrum.

One peculiarity is that the 'convolution fit method' systematically underestimated the adjusted P_τ. To correct for this, the fit results must be increased by 2 %. The fits done with the polynomial correction factor give unbiased results in average. Therefore this 'correction factor method' is used as a default in chapter 10.

9.2.2 Determination of P_τ in the Channel $\tau \to \rho\nu \to \pi\pi_0\nu$

In the decay channel $\tau \to \rho\nu \to \pi\pi_0\nu$, the τ polarisation is determined from a E_π/E_{Jet}-ratio spectrum, with $E_{\mathrm{Jet}} = E_{\pi_0} + E_\pi^{\pm}$[2]. Figure 9.9 depicts the two base spectra for $P_\tau = +1$ and $P_\tau = -1$ in this channel. The spectra drawn in solid lines correspond to ρ signal jets generated with a fixed $\sqrt{s} = 500\,\mathrm{GeV}$, while the points denote the corresponding spectrum generated with the energy losses prior to the interaction ($\Delta\sqrt{s} \neq 0$).

The energy ratio E_π/E_{Jet} is independent of $\sqrt{s}$. Therefore the points in figure 9.9 agree with the solid drawn spectra and no correction for the effects of the luminosity spectrum is necessary in this measurement channel.

In the same way as discussed along with figure 9.8(a), such an E_π/E_{Jet}-ratio spectrum for any intermediate P_τ can be decomposed into a contribution of the two base spectra. Figure 9.10(a) shows an example for $P_\tau = 0.8$. Again, any spectrum for an intermediate P_τ can be created by mixing entries from the two base spectra in proportions defined by equation (9.1).

[2] the decay $\rho \to \pi^\pm\pi_0$ is exclusive [12]

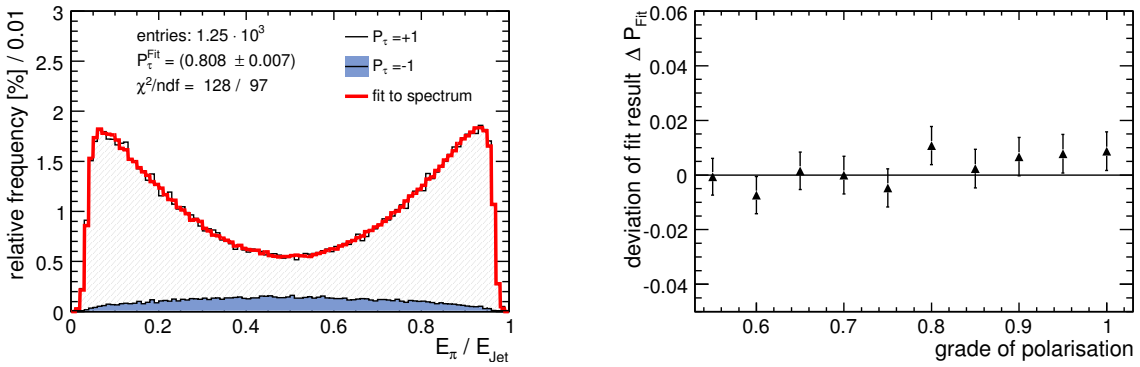

(a) summation of the two base spectra to a spectrum with $P_\tau = 0.8$

(b) fit result P_τ for different ratio spectra and fit ranges

Figure 9.10: *Test of the fit algorithm at $^{E_\pi}/_{E_{Jet}}$-ratio spectra for different P_τ*

Figure 9.10(a) also illustrates a method to determine P_τ from a given $^{E_\pi}/_{E_{\mathrm{Jet}}}$-ratio spectrum. For this a fit function $^{\mathrm{d}N}/_{\mathrm{d}R}$ is constructed, which weights the $P_\tau = +1$ and $P_\tau = -1$ fractions:

$$\left.\frac{\mathrm{d}N}{\mathrm{d}R}\right|_{\mathrm{fit}}(P_\tau) = N\left(\frac{1+P_\tau}{2}\cdot\left.\frac{\mathrm{d}N}{\mathrm{d}R}\right|_{+1} + \frac{1-P_\tau}{2}\cdot\left.\frac{\mathrm{d}N}{\mathrm{d}R}\right|_{-1}\right).$$

Herein $^{\mathrm{d}N}/_{\mathrm{d}R_{\pm1}}$ denotes the shape of both normalised $P_\tau = \pm1$ ratio spectra, as they are shown in figure 9.9. The normalisation constant N and P_τ are free parameters of the fit.

Also this fit procedure has been tested with $^{E_\pi}/_{E_{\mathrm{Jet}}}$-ratio spectra for various τ polarisations. A spectrum for a fit has been created from the base spectra belonging to $\Delta\sqrt{s} \neq 0$ in figure 9.10. The base spectra's shapes $^{\mathrm{d}N}/_{\mathrm{d}R_{\pm1}}$ in the fit function have been determined independently, namely from the $\Delta\sqrt{s} = 0$ spectra in figure 9.10. Figure 9.10(b) depicts the fit deviations. Here the fit uncertainty is 1 %

9.3 Detector and Reconstruction Performance

This section discusses aspects of the detector and reconstruction performance exemplary in terms of three characteristics which are crucial for the measurement of P_τ. These are the energy resolution for low and medium energetic charged particles, the particle identification performance of the reconstruction algorithms and the beam calorimeter veto efficiency.

An accurate determination of low momentum pions energies is crucial for an accurate reconstruction of the pion energy spectrum in the channel $\tau \rightarrow \pi\nu$. In addition, the pions have to be distinguished from other particle species, which requires a clean particle identification.

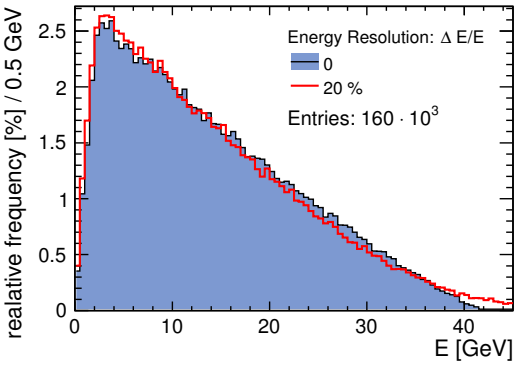

(a) energy spectrum of the pions in $\tau \rightarrow \pi + \nu_\tau$

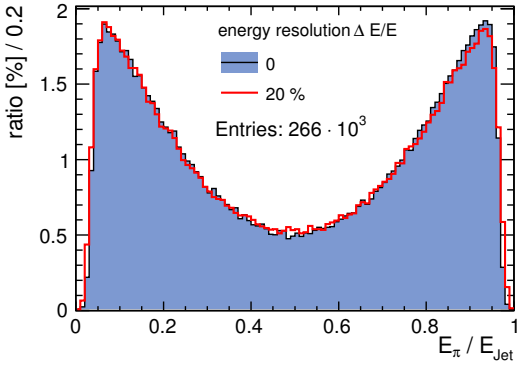

(b) E_π/E_{Jet}-ratio spectrum in $\tau \rightarrow \rho\nu \rightarrow \pi\pi_0\nu$

Figure 9.11: *Influence of a* 20 % *energy resolution on the spectra in both channels*

Standard model scattering processes have the highest cross-sections at the ILC and are the most crucial background for the signal process. The beam calorimeter are dedicated to veto these background events. Thus their efficiency determines the suppression of the background.

The simulated events, considered for the determination of these performances, are listed in 10.2 in the following chapter.

9.3.1 Energy Resolution

The energy resolution R describes how accurate the detector measures the energy of a reconstructed particle compared to the Monte Carlo truth energy in average. It is calculated as

$$R = \sqrt{\frac{1}{n_\text{i}} \sum_{i=0}^{n} \left(\frac{E_\text{i}^{\text{reco.}} - E_\text{i}^{\text{MC truth}}}{E_\text{i}^{\text{MC truth}}} \right)^2}.$$

from n_i reconstructed particles in a certain energy bin

Here $E_\text{i}^{\text{reco.}}$ is the reconstructed and $E_\text{i}^{\text{MC truth}}$ the real particle energy. In the sense of particle flow, the energies of charged particles are reconstructed from the reconstructed momenta. Thus the energy resolution is equivalent to the momentum resolution.

Impact of a decreasing Energy resolution on P_τ

A decrease of the energy resolution alters the shape of a reconstructed pion energy spectrum.

This is illustrated in figure 9.11. Both diagrams in this figure compare a Monte Carlo truth spectrum with the same spectrum for a worsened energy resolution. Here

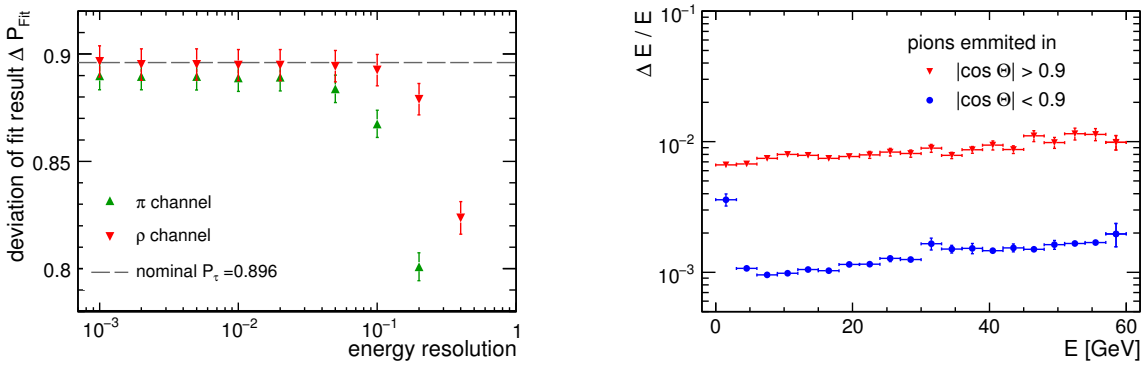

(a) evolution of the fit results for P_τ with degrading pion energy resolution

(b) pion energy resolution in the reconstruction

Figure 9.12: *Energy resolution in the reconstruction and influence on the measurement*

a resolution of 20 % is chosen to illustrate the effect - the achieved energy resolution in the reconstruction is much better and below 10^{-2}. To fake the nonzero resolution, each entry E_i in a histogram has been replaced by a random number pulled from a Gaussian with mean value E with a width of $\sigma = 0.2 \cdot E$. This models a Gaussian smearing of the energy measurement.

In case of the E_π/E_Jet-ratio spectrum, the ρ jet consists of the pion with energy of E_π and two photons from the decay $\pi_0 \rightarrow 2\gamma$. An energy resolution of $15\,\%/\sqrt{E\mathrm{GeV}}$ is assumed for the photons. This is in the range of the envisage energy resolution of the electromagnetic calorimeter.

The energy resolution alters the shape of both spectra and thereby fakes a minor τ polarisation. In case of the $\tau \rightarrow \pi\nu$ spectrum in figure 9.11(a), the maximum of the distribution increases and the falling edge gets stronger rounded. Also some pions are shifted above the kinematically accessible maximum pion energy of 42.6 GeV.

The E_π/E_Jet-ratio spectrum (figure 9.11(b)) becomes more flat which causes a reduced P_τ in the fit.

Figure 9.12(a) shows the influence of a degrading pion energy resolution on the fit result P_τ in both measurement channels. The fit functions have not been modified to take a minor energy resolution into account. In both channels a degradation of the resolution above $\approx 2\,\%$ starts to have an impact on the determined P_τ. The result in the ρ channel is slightly more robust against a degrading pion energy resolution. This is because the measurement resolution of the photon energy has not been worsened and thus the pion energy fluctuations become less pronounced in the ratio.

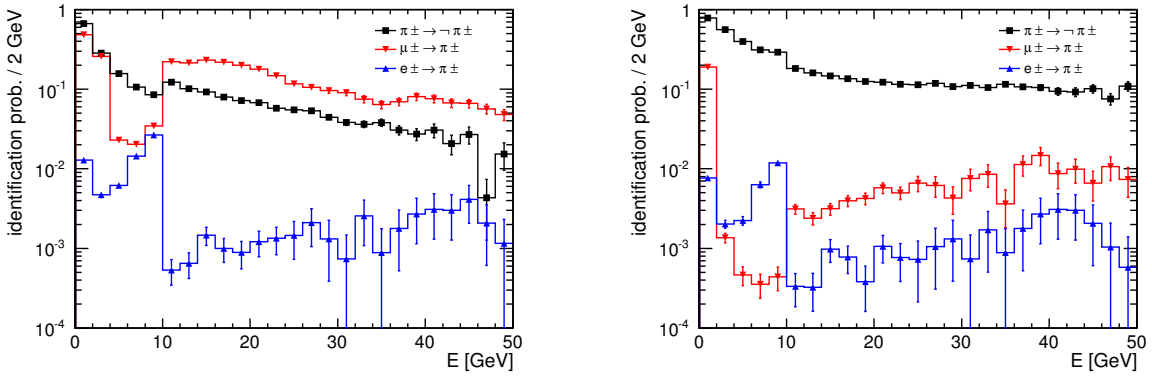

(a) pion identification power

(b) pion identification power with likelihood cut

Figure 9.13: *Particle identification performance without and with likelihood cut*

Energy resolution in the Reconstruction

Figure 9.12(b) depicts the achieved energy resolution for pions in the simulation. The diagram distinguishes between pions emitted in angles with $|\cos\Theta| < 0.9$ and $|\cos\Theta| > 0.9$, respectively. The former is one of the selection criteria in the analysis for both channels. The pions emitted in the forward regions of the detector at $|\cos\Theta| > 0.9$ show a worse energy resolution. This is because particle tracks are not measured over the full TPC radius in this case and thus the momenta are determined less accurate. For $|\cos\Theta| < 0.9$ pion energies are reconstructed with a resolution of $1 - 2 \cdot 10^{-3}$.

As the comparison of figure 9.12(a) and figure 9.12(b) demonstrates, the achieved resolution for pions is about one order of magnitude better than the critical value where it would start to influence the fit result.

9.3.2 Particle Identification

As mentioned above, the PFOID processor assigns a particle species to reconstructed particles together with an identification likelihood[3].

The processor's likelihood method is based entirely on the measured calorimeter information. Prior to the application to reconstructed events, the processor is trained with a set of sample particles. This is done in two different energy ranges, namely for particles with an energy below and above 10 GeV, respectively. The outcome of this training are two likelihood reference distributions - one for each energy range.

Figure 9.13(a) shows the particle identification performance of the algorithm in terms of the probability to identify a real pion as a pion and to misidentify other particles

[3] the identification likelihood is a measure for the reliability of the identification and ranges between 0 for unclear and 1 for a safe identification

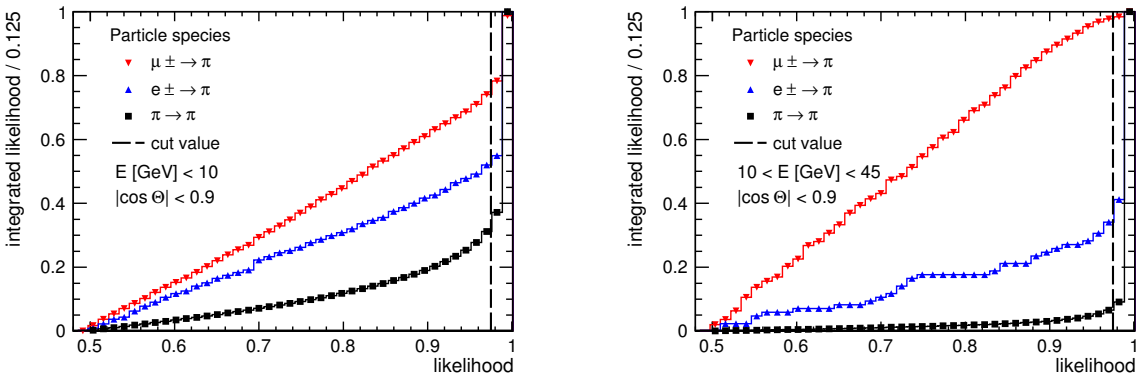

(a) integrated likelihood for E $<$ 10 GeV

(b) integrated likelihood for E $>$ 10 GeV

Figure 9.14: *Particle identification likelihood distributions*

as pions. In this diagram, again particles in the forward region at $|\cos\Theta| > 0.9$ are excluded.

No restriction on the identification likelihood has been taken yet and the misidentification rates are high, except for electrons. For example, 10 % to 20 % of all muons are identified as pions in the energy range above 10 GeV. Below this energy, the PFOID algorithm switches to the other likelihood distribution. This causes an abrupt transition in the identification performances. The misidentification rate $\mu \rightarrow \pi$ improves from about 20 % just above 10 GeV to $3 \cdot 10^{-2}$ just below 10 GeV. The particle identification becomes unreliable for particle energies less than 2 GeV - more than 20 % of all muons are identified as pions. These low energetic muons are partly stuck before they reach the hadronic calorimeter. That makes them harder to separate from pions.

For all particle species, the rate of misidentification can be significantly improved if a minimum identification likelihood is requested. This is illustrated in the diagrams of figure 9.14(a) and 9.14(b). Here the distribution functions of the identification likelihood are shown for all particles which have been identified as pions - in figure 9.14(a) for $E < 10$ GeV and in figure 9.14(b) for $E > 10$ GeV.

If an identification likelihood of at least 0.97 is required to accept the identification as trustworthy (cut value in the figure) 95 % of all muons which have been identified as pions are rejected for $E > 10$ GeV. However, also about 5 % of the real pions have an identification likelihood below 0.97 and are lost. This is even enhanced for $E < 10$ GeV where roughly 30 % of the real pions do not fullfil the cut.

Figure 9.13(b) depicts the equivalent diagram to figure 9.13(a) evaluated with the requirement to have an identification likelihood of more than 0.97. Here, the misidentification rates $X \rightarrow \pi$ are significantly reduced and are below 1 % for particle energies above 2 GeV. For lower energies, 20 % of the muons are still missidentifed as pions.

The likelihood cut requirement also increases the pion rejection rate. Above 10 GeV this is about 15 %, for lower energies it rises up to 70 %. The transition between the two

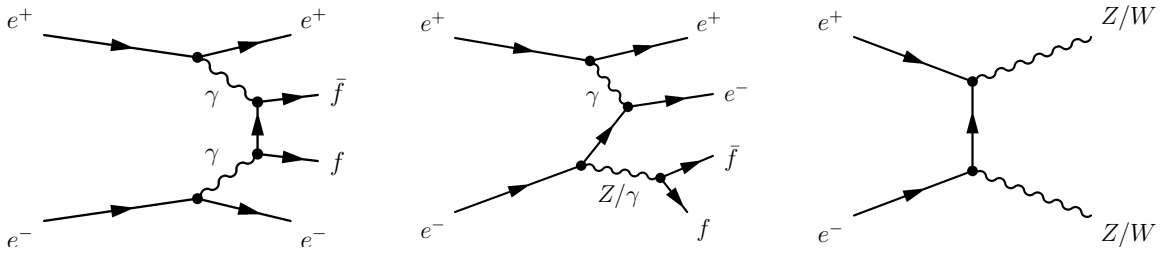

(a) two photon scattering **(b)** Z-Strahlung **(c)** boson pair production

Figure 9.15: *Feynman diagrams of standard model scattering processes*

energy regimes and the change in the likelihood distributions at 10 GeV keeps being visible as a discontinuous step in all curves.

The PFOID processor is currently in the development phase and these identification performances are expected to improve significantly.

9.3.3 Suppression of Background with the Beam Calorimeter

Standard model scattering processes of the kind $e^+e^- \rightarrow e^+e^- + 2f$ and $e^+e^- \rightarrow 4f$ process via three main channels, whose Feynman diagrams are shown in figure 9.15. The two photon process in figure 9.15(a) has a cross-section in the millibarn regime. This is about ten times higher than the cross-sections of Z-Strahlung (figure 9.15(b)) or the boson pair production in figure 9.15(b). Taken together, these processes have the highest cross-sections at the ILC and exceed the cross-section of most SUSY and other SM signal processes by four to six orders of magnitude. The latter are typically have less than 200 fb.

In the two photon scattering and the Z-Strahlungs processes and a fermion pair is emitted with an energy of typically a few GeV, while the beam particles are also present in the final state. The according event signature comprises a low detector activity and a high missing energy, which is also typical for supersymmetric processes. Together with the high cross-sections, this makes SM scattering a crucial background for SUSY searches. But these processes can be suppressed with the help of the beam calorimeters.

Beam Calorimetry

The beam calorimeters are installed at both entrance points of the beam pipes into the detector, which shall detect the beam particles in the final state of $e^+e^- \rightarrow e^+e^-ff$ events and produce a veto on this background. Figure 9.16(a) illustrates one half of the detector with the beam calorimeter in about 3.5 m distance to the interaction point. The incoming and outgoing beams enter through dedicated cutouts in the beam calorimeter. When a beam particle transfers a sufficient momentum to the produced fermion pair, it is deflected in the scattering process and can be detected in a beam

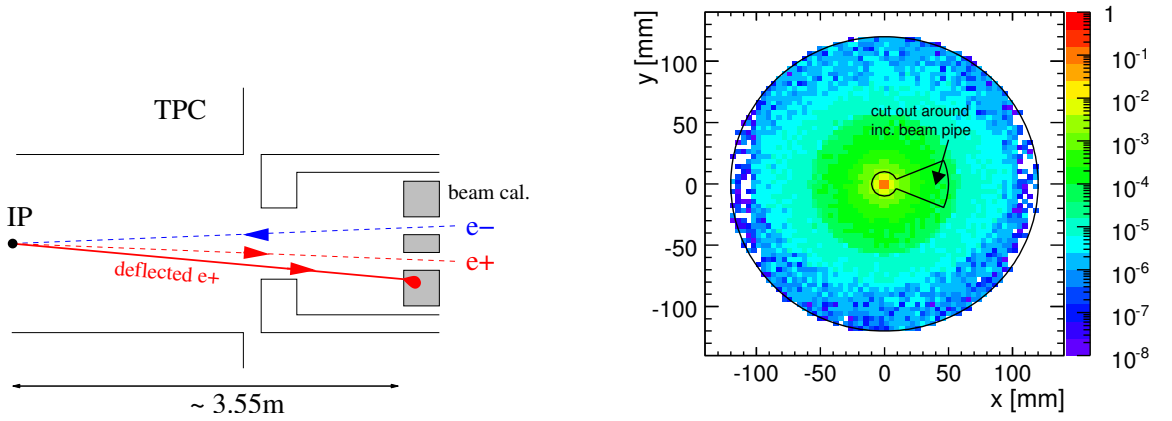

(a) beam calorimeter in the detector

(b) beam calorimeter occupancy distribution

Figure 9.16: *Beam calorimeter occupancy*

calorimeter, as illustrated in the figure. The required momentum transfer is estimated in the next section.

Figure 9.16(b) shows the beam calorimeter occupancy in the simulation. This figure illustrates the shape of the calorimeter together with the rate where deflected beam particles passed its surface. The distribution has a distinct peak in the beam pipe and in total only about 20 % of all scattering events deposit a beam electron in one of the calorimeters. Thus a veto on beam calorimeter activity can only reject a small fraction of the background events and a separated condition against the remaining ones has to be applied. One method for this is discussed in the next section.

In the event reconstruction, a Marlin processor [108] calculates the efficiency to detect a particle in the beam calorimeter in dependence of particle energy and the impact position. Figure 9.17(a) shows this for three different bins of energy. The beam calorimeter's inner hole for the beam pipe has a radius of 2 cm in the simulation. Particles with energies above 200 GeV are detected with a efficiency close to one, almost over the whole surface of the calorimeter. The efficiency degrades close to the inner radius, because photons from the beam induced backgrounds produce an additional occupancy in the calorimeter. Due to this, particles with lower energies are detected with a decreased efficiency, as the curve for $E < 120$ GeV exemplifies. The calorimeters are blind for beam particles with energies below 40 GeV in the simulation, because such low energetic particles are assumed not to be detectable in the background.

Suppression of background events without beam calorimeter activity

One possibility to veto on background events, which do not deposit beam particles in one of the calorimeters requires the calculation of the missing momentum of the event perpendicular to the z axis. This variable is called $\vec{p}_\perp(\text{miss})$ and calculated from all

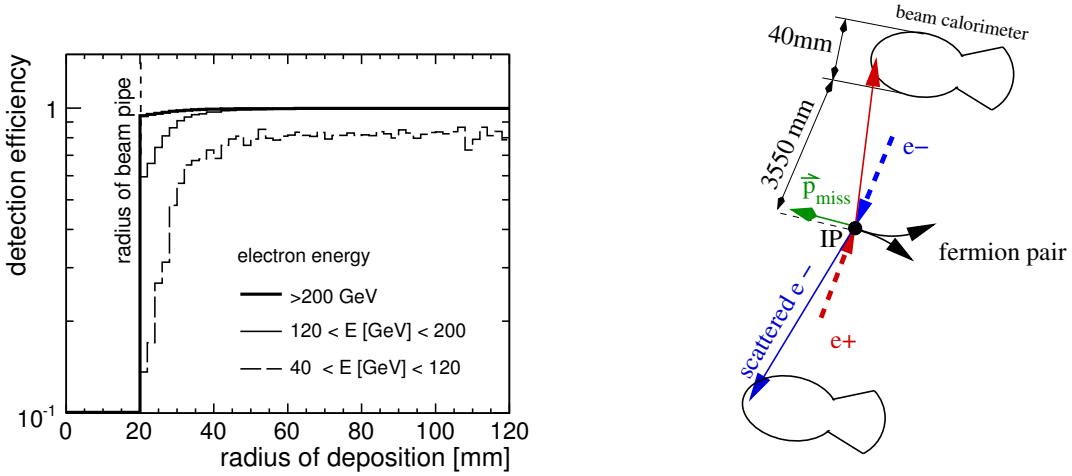

(a) beam calorimeter veto efficiency for different particle energies and radii

(b) deflection of beam particles in a scattering process

Figure 9.17: *Beam calorimeter veto efficiency*

reconstructed particles by

$$\vec{p}_\perp(\text{miss}) = -\sum_{\text{i}} \vec{p}_{\perp,\text{i}}.$$

A non vanishing $|\vec{p}_\perp(\text{miss})|$ is a measure for boosts of the visible system in the $r-\phi$ plane.

Since the initial beams collide under the crossing angle, the centre-of-mass system of all interactions is boosted in negative x-direction. From this $p_\perp(\text{miss}) = 3.5\,\text{GeV} \cdot \vec{e}_x$ is expected in all events. However the crossing angle has not been considered in the simulation and $p_\perp(\text{miss})$ vanishes when all particles in an event become visible in the detector.

A rejection on events which exhibit small $p_\perp(\text{miss})$ is suited to reduce the background together with a veto against beam calorimeter activity. This follows from the geometry of the detector as illustrated in figure 9.17(b). In this sketch, both beam electrons are scattered into the same ϕ angle and stay in the beam pipe. They enter the pipes in diametrically opposed points. In this scenario, the visible system gets the maximal boost in $r-\phi$ plane without that the beam calorimeter show any activity. In this case, $p_\perp(\text{miss})$ is maximal and the magnitude can be estimated from the scattered beam electrons and the detector geometry:

$$\begin{aligned} p_\perp(\text{miss}) &\leq \frac{2 \cdot \text{radius of the beam pipe}}{\text{distance interaction point beam calorimeter}} \cdot E_{\text{beam}} \\ &= \frac{20\,\text{mm}}{3550\,\text{mm}} \cdot 250\,\text{GeV} \lesssim 3\,\text{GeV} \end{aligned}$$

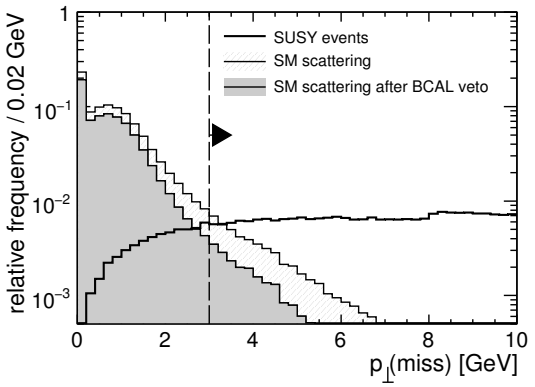

Figure 9.18: *Distribution of $p_\perp$(miss) for SM scattering and SUSY events*

The bending effect of the detector's inner magnetic is neglected here. Hence, the detector geometry divides the SM background in two classes

- if both beam particles e^+e^- vanish in the beam pipe after the interaction
  $\longrightarrow$ small $p_\perp$(miss) below 3 GeV
- if at least one beam particle is visible in the beam calorimeter
  $\longrightarrow$ large $p_\perp$(miss) above 3 GeV

Figure 9.18 depicts the distribution of $p_\perp$(miss) for the SM background and SUSY signal events. For the background, $p_\perp$(miss) peaks towards small values which is expected as in most of the scattering events, only a small momentum is transfered to the fermion pair. A restriction, $p_\perp(\text{miss}) > 3\,\text{GeV}$, together with the beam calorimeter veto rejects more than 97 % of the background events. At the same time less than 1 % of the SUSY signal is lost. Here in addition

$$p_\perp(\text{miss}) > 8\,\text{GeV} \quad \text{if} \quad |\phi_{p_\perp(\text{miss})} - 180\,\text{deg}| < 30 \tag{9.3}$$

is required. This condition compensates the limited acceptance of the beam calorimeter due to the cutouts for the incoming beams.

Supersymmetric processes show a flat $p_\perp$(miss) distribution, because they have neutralinos in the final state which escape undetected. Thus the visible particles typically appear non isotropic and the events usually have an increased $p_\perp$(miss).

Summary of this Chapter

The studies presented in this chapter prepare the measurement of the τ polarisation presented the following chapter. A appropriate ILD detector simulation chain is in place and has been used to produce simulated events of the signal and background processes. For both measurement channels, $\tau \to \pi\nu$ and $\tau \to \rho\nu \to \pi\pi_0\nu$, fit routines are installed to determine P_τ from a reconstructed signal spectrum. In addition a method has been evaluated to reduce the most critical background, coming from SM scattering processes of the class $e^+e^- \to e^+e^- + 2f$.

10 Measurement of τ Polarisation with the ILD Detector

The previous chapter 8 motivates why a measurement of τ polarisation P_τ in the process $e^+e^- \to \tilde{\tau}_1\tilde{\tau}_1 \to \chi\chi\tau\tau$ is interesting from a physics point of view and chapter 9 discusses which aspects of the ILD detector performance are crucial for the measurement.

The following chapter discusses the feasibility to measure P_τ with the e^+e^- data corresponding to an integrated luminosity of $\mathcal{L} = 500\,\mathrm{fb}^{-1}$ at a centre-of-mass energy of $\sqrt{s} = 500\,\mathrm{GeV}$. After an introduction into the selection technique, at first the measurement in the final state $\tau \to \pi\nu_\tau$ is presented in section 10.2. Subsequently the measurement in the channel $\tau \to \pi_0\pi\nu_\tau$ is discussed in section 10.4. The aim is develop a measurement strategy and to estimate the possible measurement accuracy ΔP_τ.

In this analysis signal particles, namely pions, are searched. Throughout the chapter, signal-type events are meant to be events of the signal process $e^+e^- \to \tilde{\tau}_1\tilde{\tau}_1 \to \chi_0\chi_0\tau\tau$. These events are called signal events, if a charged pion coming from a decay $\tau \to \pi\nu_\tau$ or $\tau \to \pi\nu_\tau\pi_0$ is present in the final state. The charged pion is then named signal pion, in both channels. A particle which is at any stage of the analysis considered as a potential signal pion is called a 'signal candidate'.

10.1 Selection Technique

The search strategy for signal candidates is split into two steps: First a preselection algorithm extracts signal candidates from a set of processes which have a similar topology as the signal process. The preselection criteria are almost common for both measurement channels and discussed in sections 10.2.1 and 10.4.1, respectively. After the preselection, most signal pions are among the signal candidates but also a background of fake signal candidates. Initially the background exceeds the signal by four to six orders of magnitude.

The challenge of the measurement is to extract the signal pions out of the high background of false signal candidates. For this, a cut based selection is used in the second step. Section 10.2.4 presents the selection for the single pion channel $\tau \to \pi\nu$ and section 10.4.3 for the channel $\tau \to \pi_0\pi\nu_\tau$.

A cut based selection is simple and thus appropriate for a feasibility study like this one. Moreover, it is robust compared to other selection techniques like a likelihood selection. This means that the exact shape of the distributions used for defining the cuts is of minor importance as long as they show a clear separation between signal

Process	beam polarisation (P_{e^+}, P_{e^-})	statistics in for $\mathcal{L} = 500\,\text{fb}$ expected $[10^3]$	simulated $[10^3]$
$\tilde{\tau}_1^+\tilde{\tau}_1^- \to \chi_1\chi_1\tau^+\tau^-$	$(+1,-1)$	37	56.0
	$(-1,+1)$	113	166.7
	$(-0.6,0.8)$	81.4	$\sum$ 222.7
$\to \chi_1\chi_1\tau + \pi\nu_\tau$	$(-0.6,0.8)$	17.8	49.55
$\to \chi_1\chi_1\tau + \pi\pi_0\nu_\tau$	$(-0.6,0.8)$	41.5	113

Table 10.1: *Simulated statistics of the signal process*

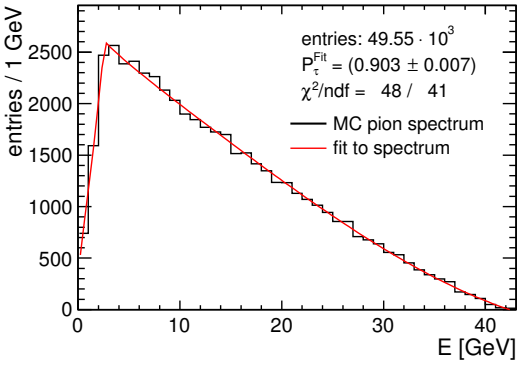

(a) fit to the signal pion energy spectrum in $\tau \to \pi\nu_\tau$

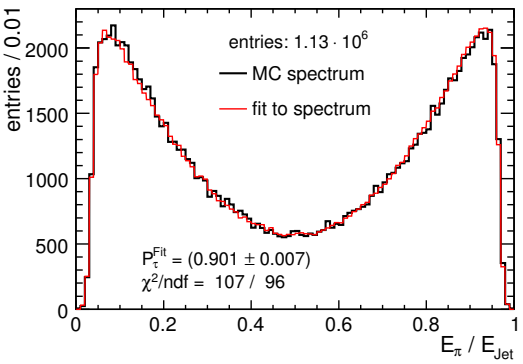

(b) fit to the E_π/E_{Jet}-ratio spectrum for $\tau \to \rho\nu_\tau \to \pi\pi_0\nu_\tau$

Figure 10.1: *Determination of P_τ with the MC spectra extracted from the simulated events*

and background. Systematic effects which change the shape of single distributions do not have a very strong impact on the selection. In addition this is advantageous in another aspect: For some processes less events than expected for an integrated luminosity of $500\,\text{fb}^{-1}$ have been simulated. To compensate for the lack, the weight of these simulated events are scaled up. As a result distributions can have spiky shapes if only few events with large weights enter. Selection techniques which exploit the shape of the distribution, as a likelihood selection, would become unstable in this case.

However, backgrounds can be underestimated in a cut based selection, if cuts are applied to highly weighted events. This is the case, if only single cuts exclude such events or signal candidates. Therefore a consistency check needs to be performed at the end of the selection.

Simulated Signal Process

The cross-section for the signal process is presented in section 8.4.1 and the expected signal-event yield and the number of signal pions in both decay channels are summarised in table 10.1. In total, signal-type events corresponding to an integrated luminosity

of about $750\,\mathrm{fb}^{-1}$ have been simulated for both beam polarisation states $(+1,-1)$ and $(-1,+1)$. Taken together, these are 222700 events. The initial beam polarisation is neglected for the simulated signal-type events and the events of both states are treated equally, to increase the available statistic and reduce statistical fluctuations. This is possible because stau pair production is a pure s-channel process with a single Feynman diagram. In this class of processes, the initial beam polarisation has no influence on the event shape and the distributions in the measurement categories.

The total number of 222700 signal-type events corresponds to an integrated luminosity of about $\mathcal{L} = 1370\,\mathrm{fb}^{-1}$ for ILC operation with $(-0.6,+0.8)$ beam polarisation. To scale down the numbers to the expected yield for $\mathcal{L} = 500\,\mathrm{fb}^{-1}$, each signal-type event gets a reduced weight of 0.366.

Beforehand to the analysis, the τ polarisation has been determined with the generator level output in both measurement channels. The fit procedures used for this are explained in section 9.2. Figure 10.1(a) displays the signal pion energy spectrum in the channel $\tau \to \pi\nu_\tau$ together with a result of the fit. About 49550 signal pions are found in the simulated signal-type events. Scaled down with the event weight this corresponds to 18100 in $500\,\mathrm{fb}^{-1}$ and the branching ratio $\tau \to \pi\nu_\tau$ is 11.1 % in the simulation. The fit gives the results $P_\tau = 90.3 \pm 0.7\,\%$ - in agreement with the Monte Carlo truth value of $P_\tau^{\mathrm{MC}} = 89.6\,\%$.

The determination of P_τ in the alternative channel $\tau \to \rho\nu_\tau \to \pi\pi_0\nu_\tau$ via the ratio of charged pion to the ρ jet energy gives a value of $P_\tau = 90.1 \pm 0.7\,\%$ (see figure 10.1(b)). In this channel, 113000 signal pions are available. The weights scale this number down to 41300 and the branching ratio of $\tau \to \rho\nu_\tau$ is 25.4 % in the simulation.

10.2 Analysis in the Channel $\tau \to \pi\nu_\tau$

As outlined before, the first step of the analysis is a preselection and the enhancement of the signal by selection cuts. This section describes these steps for the channel $\tau \to \pi\nu_\tau$ and further analysis steps are presented which extract a result for P_τ. Figure 10.2 gives an overview of the analysis strategy.

At the beginning, the preselection is applied to the simulated events. The preselected signal candidates are then subjected to the selection cuts. The selection yields about 3300 signal pions. But also some 560 false signal candidates fulfil the cuts and the resulting energy spectrum of the selected signal candidates has an underlying background. Moreover the spectrum's shape is distorted due to an energy dependent selection efficiency. Signal pion are lost mainly at the low energy end because the selection criteria against the SM background are cutting hard against low energetic signal candidates. Two steps are necessary to recover the initial signal pion spectrum: firstly the background shape is parametrised and subtracted. The remaining spectrum describes the yield of signal pions from the selection. It is scaled up to the initial spectrum with an energy dependent efficiency correction. The efficiency denotes the ratio between the number of signal pions after all selection cuts to the initial number

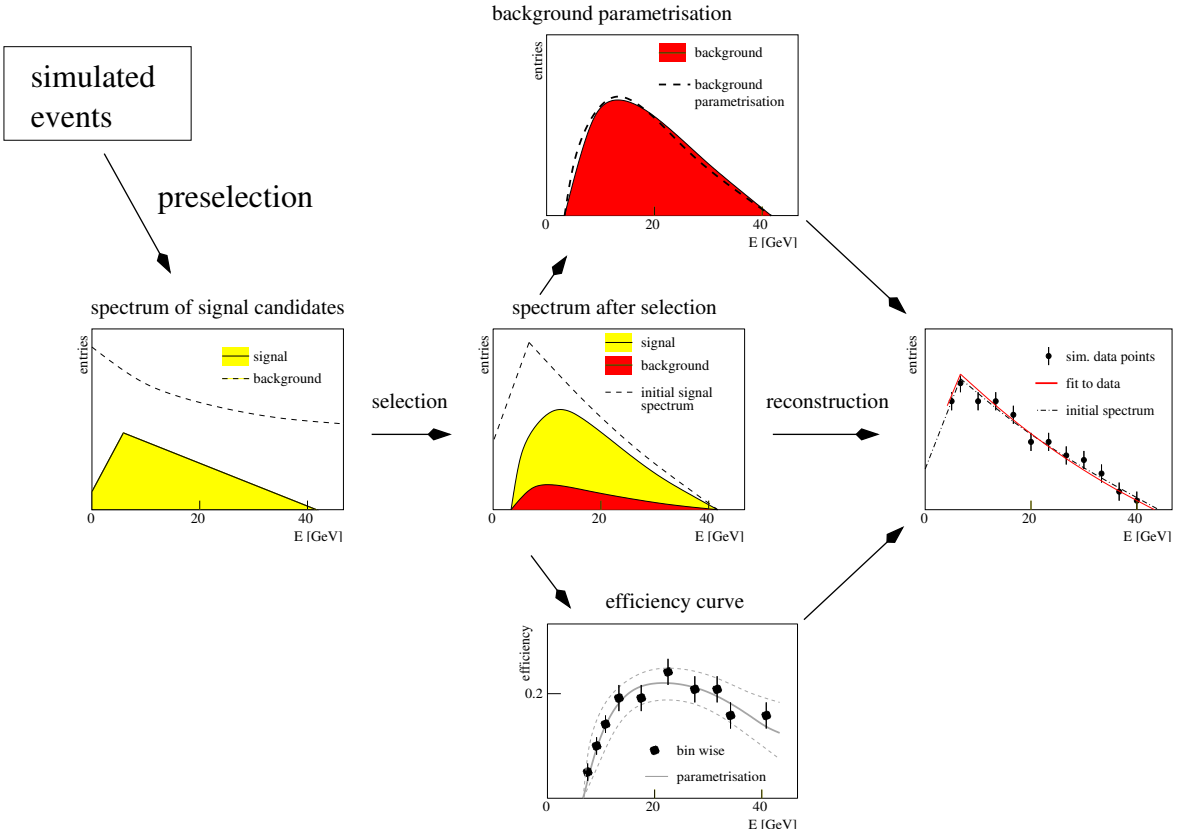

Figure 10.2: *Overview of the analysis steps to measure P_τ in the channel $\tau \rightarrow \pi\nu_\tau$*

in each energy bin. The outcome are simulated data points which scatter around the initial signal pion spectrum (see figure 10.1(a)).

Finally, P_τ is determined by fitting the theoretical description of the spectrum to the reconstructed points. It is assumed that the masses of the stau $\tilde{\tau}_1$ and the neutralino χ_1 are know for the fit. The impact of the mass measurement accuracy on the final result P_τ is estimated within an uncertainty analysis. The fit also yields a result for the number of pions in the reconstructed pion spectrum N_π.

10.2.1 Preselection Criteria

Signal candidates are preselected from two-jet events and are required to appear isolated - as the only charged particle in one of the jets. Due to the kinematic constraints (see section 8.3), the energy of each τ jet is limited to 42.5 GeV. In the preselection, a weaker criterion is required: the energy of each jet in the event must be less than 60 GeV. In addition, the preselection requires that the event exhibits a visible energy of less than 90 GeV, because the weakly interacting neutralinos escape undetected in signal-type events and take away at least 415 GeV. Since only the signal pion together with the decay products of the second tau are visible, signal events show a low activity

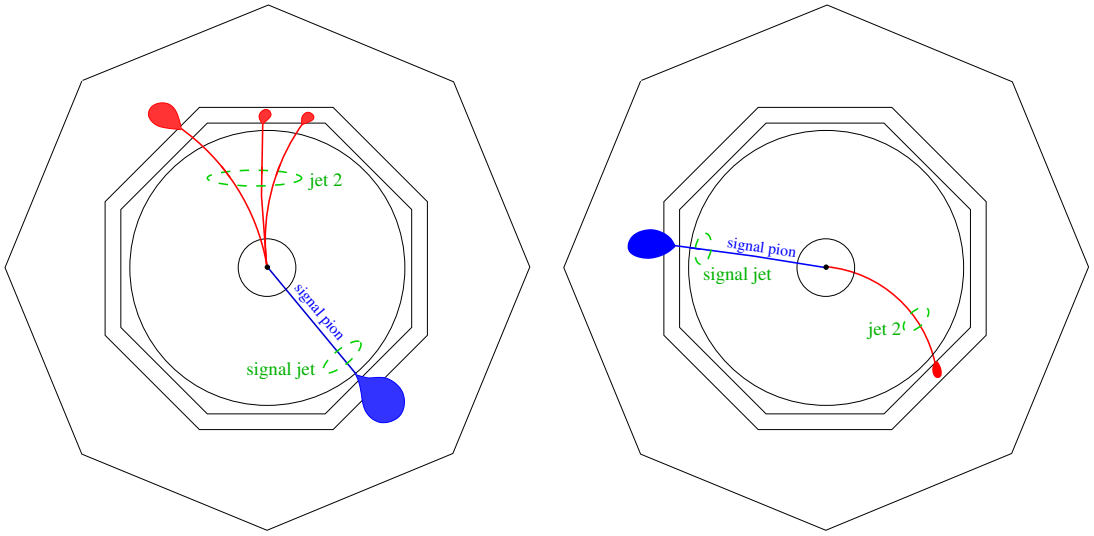

(a) two jets assigned

(b) two charged particles with no jet assignment

Figure 10.3: *Signal event topology in the channel* $\tau \rightarrow \pi\nu_\tau$

in the detector. Thus events with more than 10 reconstructed charged particles are vetoed.

Signal Event Topology

Signal events appear in two topologies schematically displayed in figure 10.3. Both figures show a $r-\varphi$-projection of the detector with the recorded signal event. In figure 10.3(a) the signal pion appears in a distinct jet while the second tau decays to three charged particles. Whenever the second tau decays to more than one visible decay product, the jet finder (see section 9.1.3) assigns two jets to the event. Then the jet with the signal pion is made up of a single track and occasionally additional radiative photons.

If the second tau also features a one prong decay, only two charged tracks are visible, as depicted in figure 10.3(b). In this case, the jet finder does not assign jets to the event. In order to avoid two nomenclatures in the following, a signal jet is always meant to be the jet containing the signal candidate, even if the jet finder does not call it a jet. Analogous to that the decay products of the second tau are always summarised as second jet.

The preselection algorithm accepts a reconstructed particle as a signal candidate if it appears as the only charged particle in one of the two jets. Both particles are accepted in case of events containing no jets and only two charged tracks. Such an event accounts for two signal candidates. However, the appearance of signal events is not always as definite as in figure 10.3 and thus the preselection misses some signal pions. This loss

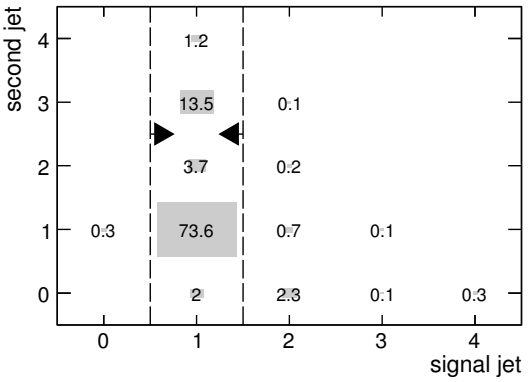

(a) number of tracks in the two jets (numbers in percent of all)

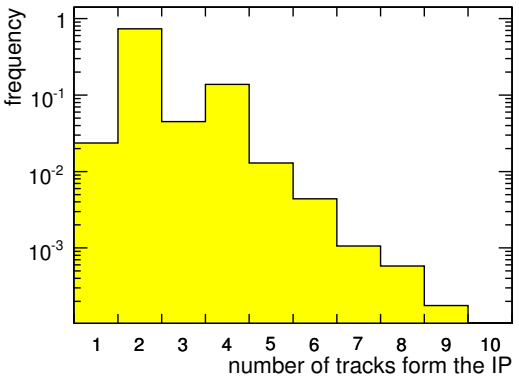

(b) number of track coming from the IP

Figure 10.4: *Track multiplicity in signal events*

can be estimated with figure 10.4(a). The diagram shows the number of tracks which have been reconstructed in the TPC for the signal jet versus this number for second jet.

The predominant case is a 1-1 scenario and the ratio of 72.3 % in this bin agrees with the probability of 72.9 % for both taus to make a one prong decay. In 0.3 % of the signal events the signal pion is invisible due to the limited detector acceptance. In these events the pion was emitted for example almost parallel to the beam pipe and is not visible in the TPC. Also the signal pion can intermix with the decay products of the second tau and then the signal jet contains more than one track. This happens in about 4 % of all signal events. The preselection extracts about 95 % of the signal pions, since it is restricted to the second column in the diagram of figure 10.4(a),

As this diagram indicates, a signal event typically contains less than four reconstructed trajectories. A tau decays to five charged particles at most, thus five charged trajectories is the maximum to be expected in a signal event. Figure 10.4(b) depicts the observed track multiplicity in the signal events. In some rare cases, more than six charged particles are visible. This can happen, for example, when a radiative photon converts into an e^+e^- pair and adds two tracks to the jet. But, the preselection criterion to reject events with more than 10 particles does not affect the preselection efficiency.

Energy Constraints

As mentioned above, the kinematics of the processes restricts the energy of both taus to less than 43 GeV. Hence both jets have a jet energy below this limit, if the reconstruction reflects the kinematics of the event correctly. However photons or tracks can be sorted into the wrong jet and make their energies look unphysical. The scatter

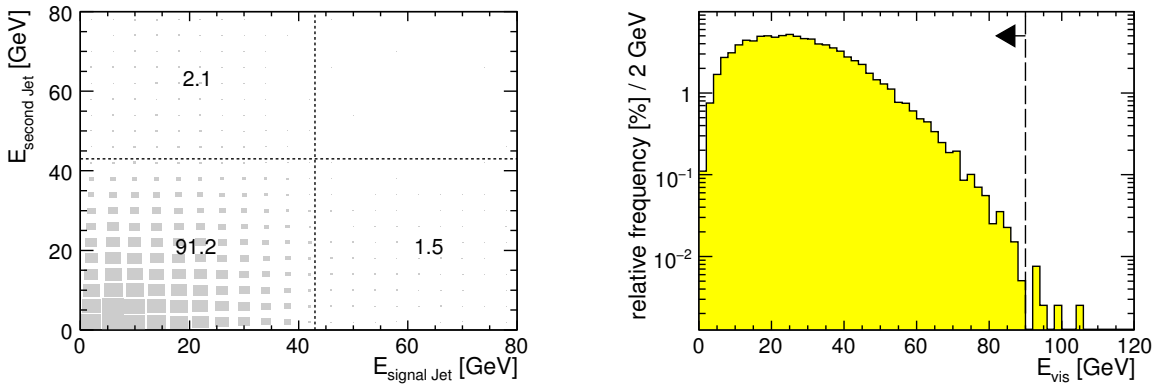

(a) energy of signal versus second jet (numbers in percent)

(b) visible energy in signal events

Figure 10.5: *Jet and visible energy in signal events*

diagram in figure 10.5(a) shows the reconstructed energy of one jet in a signal event on the horizontal axis, while the energy of the second jet is denoted by the vertical axis. The numbers in the cells denote the percentage ratio of all signal events which contribute to the corresponding sector and also contain at least one jet with a single charged particle. A jet energy above the 43 GeV limit in one of the jets appears in about $\sim 3.6\,\%$ of the cases, but a totally unphysical scenario, where both jets have an energy above 43 GeV does not occur. The unphysical jet energies are a due to neutral particles which are sorted into the wrong jet. The preselection vetoes on events, in which one of the jets has an energy of more than 60 GeV and allows for a false allocation of photons. These restrictions limit the visible energy in an event with a signal pion to 90 GeV - the diagram in figure 10.5(b) displays the according visible energy distribution of the signal events.

The preselection conditions extract 16000 out of 18100 signal pions when applied to the signal-type events. This corresponds to a preselection efficiency of 88 %. According to figure 10.5(a), a somewhat higher efficiency of $\sim 92\,\%$ is expected, because 91.2 % of all signal events fullfil the tighter criterion that both jets have less than 43 GeV. The additional loss of $\sim 4\,\%$ arises from technical reasons in the simulation. Occasionally the reconstructed particles could not be mapped to a Monte Carlo particle. In such a case a reconstructed particle can not be identified as a signal pion.

10.2.2 Background Processes included into the Analysis

Potential sources of significant background to the selection are processes which are likely to fulfil the preselection criteria and can contain a pion or a particle with a high pion identification probability.

A process is considered in the analysis if the preselection criteria do not strongly dis-

class	final state $e^+e^- \to ...$	cross-sec. [fb] (P_{e^+}, P_{e^-}) (-0.6, +0.8)	(-0.3, +0.8)
Signal	$\tilde{\tau}_1\tilde{\tau}_1 \to \chi_1\chi_1\tau\tau$	162	133
SUSY	$\tau\tau\chi_1\chi_1\|_{\text{not signal}}$	27.9	26.4
	$\mu\mu\chi_1\chi_1$	167	138
	$\tau\tau\chi_1\chi_1\nu\bar{\nu}$	10.9	16.5
	$e\tau\chi_1\chi_1\nu\nu$	4.0	5.7
	$\mu\tau\chi_1\chi_1\nu\nu$	3.7	5.2
SM (s-channel)	$\tau\tau$	1502	1269
	$\tau\tau\nu\bar{\nu}$	22.9	27.8
	$\mu\mu\nu\bar{\nu}$	22.6	27.4
	$\tau\tau\mu\mu$	4.3	3.7
	$\tau\tau\tau\tau$	4.2	3.6
	$\tau e\nu\nu$	62.0	96.2
	$\tau\mu\nu\nu$	18.7	29.9
	$e\mu\nu\nu$	93.4	147
	$q\bar{q}\nu\bar{\nu}$	151	146
	$q\bar{q}$	13600	11600
(t-channel)	$ee\gamma\gamma \to eef\bar{f}$ $(f \neq \tau)$	$2.00 \cdot 10^6$	
	$ee\gamma\gamma \to ee\tau\tau$	$3.73 \cdot 10^6$	
	$eeZ \to eef\bar{f}$ $(f \neq \tau)$	$0.16 \cdot 10^6$	
	$eeZ \to ee\tau\tau$	$93.5 \cdot 10^3$	
	$eeZZ \to eef\bar{f}$ $(f \neq \tau)$	$4.79 \cdot 10^3$	
	$eeZZ \to ee\tau\tau$	$1.38 \cdot 10^3$	

'f' stands for all standard model fermions except the top quark
'q' stand for all quarks except the top quark

Table 10.2: *Processes considered in the analysis*

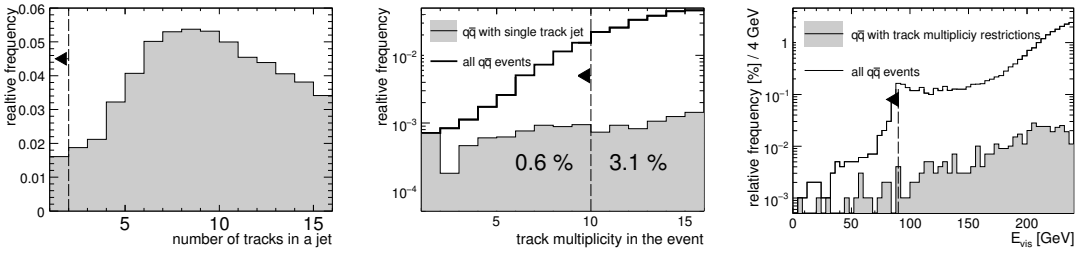

(a) track multiplicity in the jets

(b) track multiplicity in events with a single-track jet

(c) visible energy in the event

Figure 10.6: *Suppression of $q\bar{q}$ events by the preselection criteria*

favour it and its cross-section times pion identification probability of a potential signal candidate is of the order 5 fb. In the following, the potential sources of background are grouped into three classes:

1. signal-type background (signal-type)
2. supersymmetric background (SUSY)
3. standard model background (SM)

The processes taken into consideration are listed in table 10.2.

Signal-type background are signal candidates which are extracted from signal-type events, but do not origin from a decay $\tau \to \pi\nu_\tau$. By construction, signal-type events fulfil the preselection criteria in most of the cases. However, other decays than $\tau \to \pi\nu_\tau$ can produce jets with a single particle. For example charged pions from a decay $\tau \to \rho\nu_\tau \to \pi_0\pi\nu_\tau$ or electrons and muons ($\tau \to \mu + \nu$) can appear isolated and are accepted as signal candidates, since no particle identification is exploited in the preselection.

Like the signal processes, all other supersymmetric processes have neutralinos in the final state and exhibit missing energy. Therefore supersymmetric processes with two fermions or at least one final-state tau and neutrinos are considered. The process $\tau^+\tau^-\chi_1\chi_1|_{\text{not signal}}$ for example includes all other physics processes with the same final state as the signal processes. One of these is $e^+e^- \to \chi_1\chi_2 \to \chi_1\chi_1\tau^+\tau^-$.

The final state $\chi_1\chi_1 ee$ is suppressed strongly by the particle identification and in addition by the $^{\mathrm{d}E}/_{\mathrm{d}x}$ cut (see below). Therefore it is not considered. The process $\chi_1\chi_1\mu\mu$ is included because the misidentification rate of $\pi \to \mu$ is roughly by a factor of 10 higher than $\pi \to e$ (see figure 9.13(b)). Thus the particle identification suppresses muons less effective than electrons and also the specific energy loss in the TPC does not effectively separate muons from pions.

Supersymmetric processes with more than two charged fermions are not considered because these have both small cross-sections ~ 1 fb and produce a four jet signature,

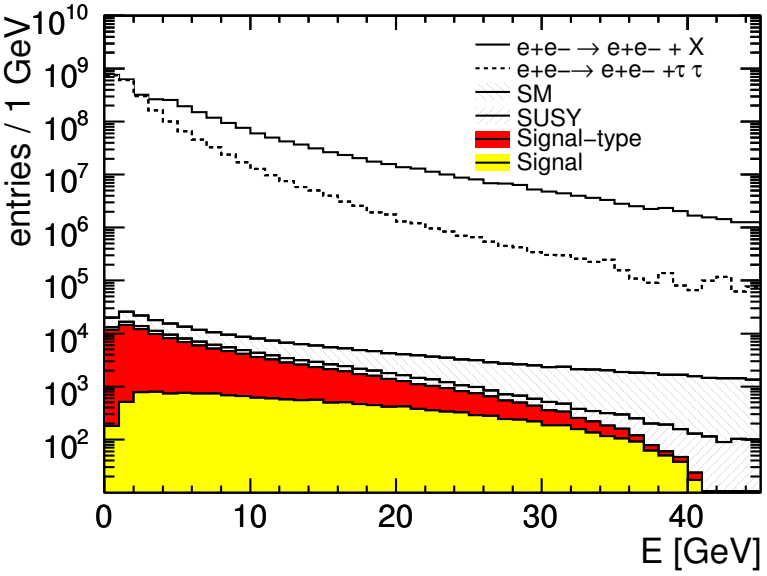

Figure 10.7: *Energy spectrum of the preselected signal candidates*

which distinguishes them from the signal-type events. Squark pair production processes are kinematically not possible at $\sqrt{s} = 500\,\text{GeV}$ because all $\tilde{q}$ are heavier than 250 GeV in SPS1a'.

To consider backgrounds coming from standard model processes, a distinction is made between predominately s-channel and t-channel processes. In s-channel processes, the full centre-of-mass energy enters at the primary vertex. Hence these processes exhibit missing energy only if neutrinos or taus are emitted in the final state. These are in the first place the τ pair production and four fermion final states with leptons.

The preselection vetoes standard model s-channel processes with final state quarks effectively. As an example, figure 10.6 shows this for the $q\bar{q}$ background. A single quark hadronises to a jet with typically more than five tracks (see figure 10.6(a)) - less than 2 % of all jets consist of only a single track. These are a potential source of background. With the restriction that an event must contain at least one single track jet only 3.7 % of all $q\bar{q}$ events account for a signal candidate (see figure 10.6(b)). The additional veto on events with ten tracks or more reduces this fraction to 0.6 %. With the visible energy preselection criterion the $q\bar{q}$ background drops out almost completely (less than 0.01 % is left, see figure 10.6(c)). The visible energy cut criterion is not expected to be that efficient if neutrinos are present, like in the process $q\bar{q}\nu\nu$. But the restriction on the track multiplicity in the preselection suppresses quark final states. Therefore they are neglected except quark pair production and the mentioned $q\bar{q}\nu\nu$ final state.

The most relevant sources of standard model background are four fermion processes of the kind $e^+e^- \rightarrow ee + 2f$, which are discussed together with the beam calorimeter veto in section 9.3.3. To distinguish between the classes in the following, SM background denotes the s-channel contribution and $ee \rightarrow ee + X$ refers to these t-channel processes. Here the 'X' denotes everything produced in the scattering process except τ pairs, which

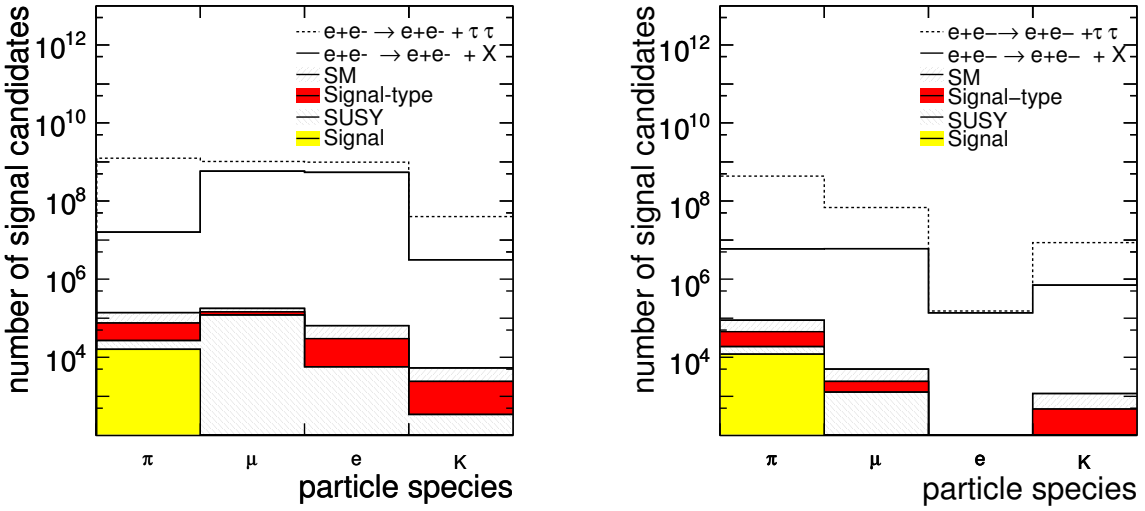

(a) signal candidates sorted by particle species before pion IP

(b) signal candidates sorted by particle species after particle identification and $^{dE}/_{dx}$ cut

Figure 10.8: *Particle species of signal candidates*

are summarised as $ee \rightarrow ee + \tau\tau$.

The energy spectrum of all signal candidates after the preselection is shown in figure 10.7. Superimposed to the signal pion spectrum is a background of 4-6 orders of magnitude. Most signal candidates come from SM t-channel events.

Event Weights

Only a small fraction of the SM t-channel events, which are expected in $500\,\mathrm{fb}^{-1}$, have been simulated because of their high cross-sections. Accordingly the event weights are high: For SM two photon processes the weights are up to 5000 and $10 - 450$ for Z-Strahlungs and boson pair production events, respectively (see figure 9.15). In case of other SM processes, the event weights are between 0.3 and 7 (see section 9.3.3). SUSY background processes have been simulated with sufficient statistics, their event weights are between 0.03 to 0.4.

10.2.3 Particle Identification

The histogram in figure 10.8(a) depicts the number of preselected signal candidates sorted for their Monte Carlo truth particle species. As the first step of background reduction, only signal candidates are accepted which have been identified as pions. To improve the pion identification purity, a cut on the identification likelihood (LH) is set in addition - all signal candidates with an identification likelihood of less than 0.97 are

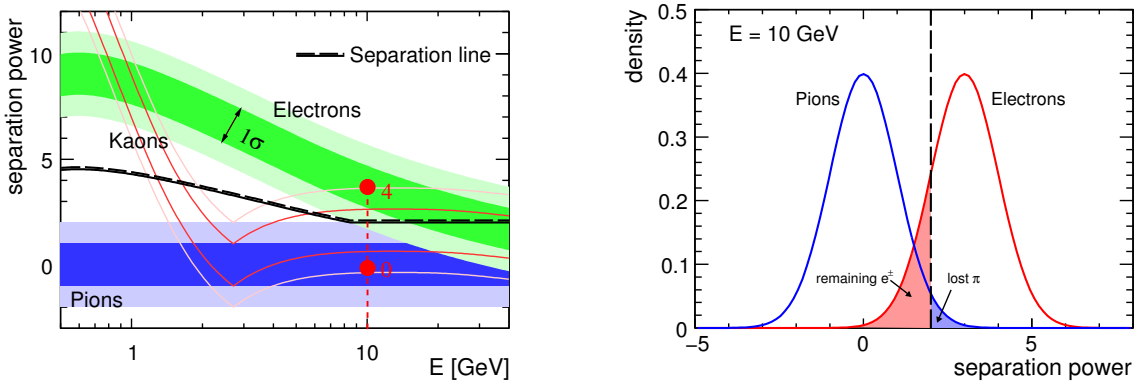

(a) $^{dE}/_{dx}$-separation power for different particle species and energies

(b) reweighting procedure

Figure 10.9: *Exploitation of $^{dE}/_{dx}$-information for particle identification*

rejected (see section 9.3.2).

A different procedure is applied in case of signal candidates with a weight above five: The assigned particle species and the identification likelihood are not subject to a cut, but the weight is reduced by a factor which corresponds to the probability to misidentify the particle as a pion. If the signal candidate is a real pion, the event weight is reduced by the probability to misidentify the pions as something else. This way, no statistics is lost and the description of the background becomes more realistic, as the event weights are smaller. These particle identification probabilities have been evaluated with all signal candidates after the preselection, as discussed in section 9.3.2.

The PFOID processor does not use the measured specific energy loss in the TPC, which also gives an input to the particle identification. To exploit this information, a separation power between pions and different particle species is defined. This is the distance between the band of the other particle species to the pion band in a Bethe-Bloch diagram (see figure 3.7) divided by the $^{dE}/_{dx}$-measurement resolution:

$$^{dE}/_{dx}\text{-pion separation power} = \frac{\text{distance to pion band in Bethe-Bloch plot}}{^{dE}/_{dx}\text{-measurement resolution}}$$

Figure 10.9(a) shows the separation power between pions, electrons and kaons for particle energies below 40 GeV [109]. In this diagram, a $^{dE}/_{dx}$-resolution of 5 % is assumed. The muon band is not shown since it almost overlaps completely with the pion band.

The meaning of the figure becomes clearer with an example: If the separation powers of many pions with a fixed energy of 10 GeV are measured, the results distribute in a Gaussian around zero, whereas for 10 GeV electrons the separation powers distribute in a Gaussian around four. Both have a variance of one. This example is illustrated in figure 10.9(a) - the Gaussians in figure 10.9(b) illustrate the $^{dE}/_{dx}$-separation powers

for the 10-GeV pions and electrons.

A cut on the separation power can reject most of the electrons. However, some electrons in the tail of the distribution fulfil the cut and some pions are lost. The fraction of electrons fulfilling the cut is given by the integral of the according Gaussian below the cut value (remaining $e^{\pm}$ in the figure). In the same way the ratio of pions which are lost is given by the integral over the pion curve above the cut value. Here the integrals over a complete Gaussian is assumed to be unity.

The $^{\mathrm{d}E}/_{\mathrm{d}x}$-condition is again considered by a reweighting procedure: the probability that the signal candidate fulfils the cut is calculated by integrating over a Gaussian from $-\infty$ to the cut value. The mean value of the Gaussian depends on the signal candidate's Monte Carlo truth energy and particle species. It is taken from the bands in figure 10.9(a). Then, the weight of the signal candidate is multiplied with the value of the integral.

The cut chosen in the analysis is indicated in figure 10.9(a). Below 8.5 GeV it is half of the centre of the electron separation band. Above this energy the electron and the pion band start to overlap and the cut is fixed at two.

Figure 10.8(b) shows the signal candidates sorted for their Monte Carlo truth particle species after the application of the particle identification and the $^{\mathrm{d}E}/_{\mathrm{d}x}$-procedure, in comparison to figure 10.8(a). The total background is reduced by almost one order of magnitude (see table 10.3) and especially electrons are effectively vetoed. Their number is reduced by a factor 10^{-4}. But about 4000 signal pions are lost due to misidentification. Although still many non pion signal candidates remain in the sample, most of the SUSY background signal candidates which are no pions are filtered out. The SUSY background is harder to suppress in the selection, because the event topologies are similar to the signal process. Thus the particle identification contributes essentially to the suppression of this background.

10.2.4 Selection Cuts

In the following, the selection cuts are briefly summarised and then their motivation is discussed. A cut flow tabular in table 10.3 shows the effect of each selection step. The result of the particle identification procedure is already listed in this tabular.

Some of the cuts are connected to the acoplanarity angle $\Phi_{\mathrm{acoplan.}}$, which is defined as the angle between the momenta of the two jets projected onto the $r-\varphi$ plane (see figure 10.10).

Some of the cuts are related to properties of the events from which for the signal candidates have been selected. If an event does not fulfil a cut criterion, the signal candidates in this event are skipped. This is meant by 'vetoing an event'. As said above, some events account for two signal candidates and so vetoing a single event can reject two signal candidates at once.

The majority of the SM t-channel events ($ee \to ee + X$) are vetoed by requiring a minimum transverse momentum $\rho_{\perp}$ with respect to a thrust axis. The calculation of $\rho_{\perp}$ is performed with the jets projected onto the $r-\varphi$ plane (e.g. [110]). This is

selection step	Number of signal candidates					
	Signal	Sig-type	SUSY	SM		
				s-channel	e^+e^+X	$e^+e^+\tau\tau$
preselection	16024	100000	23400	149000	$1.1 \cdot 10^9$	$2.2 \cdot 10^9$
pion particle ID	12014	29000	8430	48000	$1.8 \cdot 10^7$	$5.2 \cdot 10^8$
${}^{dE}/_{dx}$ procedure	11834	27440	7400	38300	$1.3 \cdot 10^7$	$5.0 \cdot 10^8$
$\rho_\perp$ cut	6164	14000	4620	1580	195000	271000
total charge =0	5851	...	...	...	158000	236000
beam cal. veto	5780	...	...	...	50600	23900
$\Phi_{\perp(\text{miss})}$ cut	5524	12500	5260	1080	45300	20500
$m_{\text{inv.}}$ (rest)$<$ 2.5 GeV	3810	171	1506	175	378	161
$\lvert\cos\Theta\rvert < 0.9$	3690	...	913	130	94	16
$\Phi_{\text{acoplan.}} > 85\,\text{deg}$	3538	...	531	74	...	...
p_t (1^{st} on 2^{nd}) cut	3310	126	334	16	88	14

Table 10.3: *Cut flow of the selection*

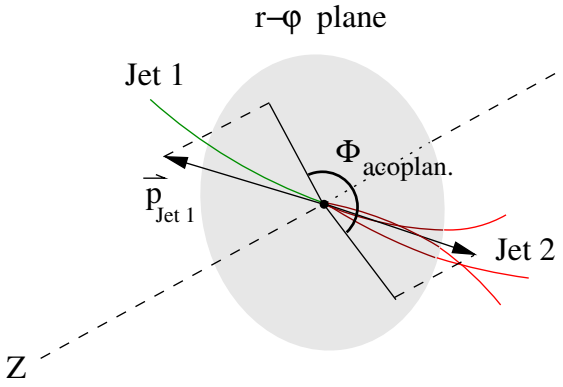

Figure 10.10: *Definition of the acoplanarity angle $\phi_{acoplan.}$*

explained in the following section. The cut criterion is most efficient in connection to the acoplanarity angle $\Phi_{\text{acoplan.}}$:

$$\rho_\perp > (2.7 \cdot \sin(\Phi_{\text{acoplan.}}) + 1.8)\,\text{GeV}.$$

In the scattering process, the two photon rest frame is often boosted along the beam pipe. Hence the jets appear under a small angle Θ with respect to the beam axis and occasionally a charged particle in a jet is undetected. In this cases the sum of the charges of all detected particles does not vanish and such events are rejected.

After the cut on $\rho_\perp$, the remaining SM t-channel signal candidates come from events which have a high missing transverse momentum. In the majority of these events, a beam electron hits one of the beam calorimeter and produces a beam calorimeter veto. An additional treatment is necessary to compensate for the calorimeter's limited

acceptance around the holes for the incoming beam (see section 9.3.3). After the scattering process both deflected beam electrons can escape undetected through these holes and produce a distinct 5-GeV missing momentum signature in the negative x direction. A cut

$$p_\perp(\text{miss}) > 8\,\text{GeV} \quad \text{if} \quad |\phi_{p_\perp(\text{miss})} - 180\,\text{deg}| < 30\,\text{GeV}$$

is effective against these events.

The signal-type background is separated off by an invariant mass constraint. Most of these signal candidates origin from a $\tau \to \rho\nu_\tau \to \pi\pi_0\nu_\tau$ decay. They are found in signal jets which also contain two photons from the decay $\pi_0 \to 2\gamma$ and have the ρ mass as their nominal invariant jet mass. For the cut, the invariant mass of the sum of all particles in the two jets except the signal candidate is calculated. This variable is called $m_{\text{inv}}(\text{rest})$ and the condition is

$$m_{\text{inv}}(\text{rest}) < 2.5\,\text{GeV}.$$

A further reduction of the background is reached by vetoing events in which one of the two jets is emitted with a small angle to the beam pipe

$$|\cos\Theta| < 0.9$$

and constraining the acoplanarity angle

$$\Phi_{\text{acoplan.}} > 85\,\text{deg}.$$

Finally, the remaining SUSY background is reduced further. For this the transverse momentum of the signal jet with respect to the axis of the second jet $p_t(1^{\text{st}}\text{ to }2^{\text{nd}})$ is calculated and vice versa. The cut introduced here limits the sum

$$p_t(1^{\text{st}}\text{ to }2^{\text{nd}}) + p_t(2^{\text{nd}}\text{ to }1^{\text{st}}) < 30\,\text{GeV}.$$

These selection cuts extract 3310 signal pions out of ~ 18100 with a background of 578 false signal candidates.

Suppression of SM-t-Channel Events

In section 9.3.3, the SM t-channel background is classified into events which deposit at least one beam electron in one of the beam calorimeter and events in which both beam electrons stay in the beam pipe. One method to veto the latter is discussed there - it is a cut on the missing momentum in the transversal plane

$$p_\perp(\text{miss}) > 3\,\text{GeV}. \tag{10.1}$$

Here a different method is used against the scattering events with a small transversal momentum transfer to the produced fermion pair, namely a cut on $\rho_\perp$. The effect

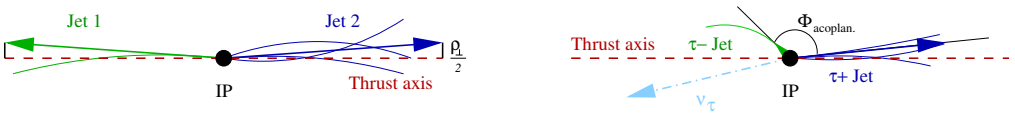

(a) $\rho_\perp$ calculated for a back-to-back event

(b) $\rho_\perp$ calculated for a τ pair with one one-prong decay

Figure 10.11: *Calculation of of the thrust axis and* $\rho_\perp$

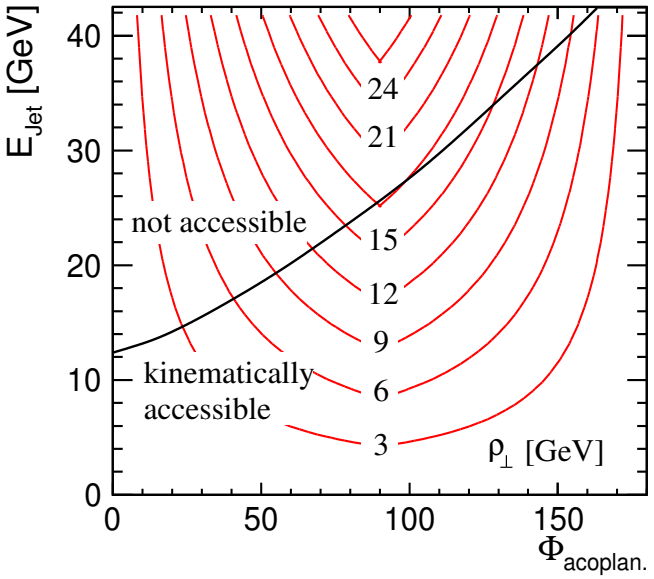

Figure 10.12: $\Phi_{acoplan.}$ *and* p_{jet} *dependency of* $\rho_\perp$ *(* $p_{jet1} = p_{jet2}$*) in signal events*

is similar, because $p_\perp(\text{miss}) \leq \rho_\perp$, but it turns out to be more effective against the background.

The calculations for $\rho_\perp$ are performed in the $r - \varphi$ plane, as indicated by the '$\perp$'. In this plane, the thrust axis is defined as the axis along which the sum of the longitudinal momenta of both jets is minimal. If the angle between the jets, which is the acoplanarity angle $\Phi_{\text{acoplan.}}$, is larger than 90 deg the thrust axis is parallel to $(\vec{p}_{\text{jet}1} + \vec{p}_{\text{jet}2})_\perp$. Otherwise it is parallel to $(\vec{p}_{\text{jet}1} - \vec{p}_{\text{jet}2})_\perp$. A formula for $\rho_\perp$, which is the sum of the transverse momenta of both jets with respect to the thrust axis, is

$$\rho_\perp = 2 \cdot \frac{|\vec{p}_{\text{jet}1} \times \vec{p}_{\text{jet}2}|_\perp}{|\vec{p}_{\text{jet}1} \pm \vec{p}_{\text{jet}2}|_\perp} \quad \text{with} \quad \text{`+' for } \Phi_{\text{acoplan.}} < 90\,\text{deg, `-' else.}$$

Figure 10.11 illustrates the calculation of $\rho_\perp$ for a two jet event.

The magnitude of $\rho_\perp$ depends on the constellation of the jets - via $\Phi_{\text{acoplan.}}$ - and the jet momenta relate it to the jet energies. The dependency is demonstrated in figure 10.12. Here $\rho_\perp$ is calculated for the example case $p_{\text{jet}1} = p_{\text{jet}2}$ and $p_{\text{jet}} = E_{\text{jet}}$. As shown

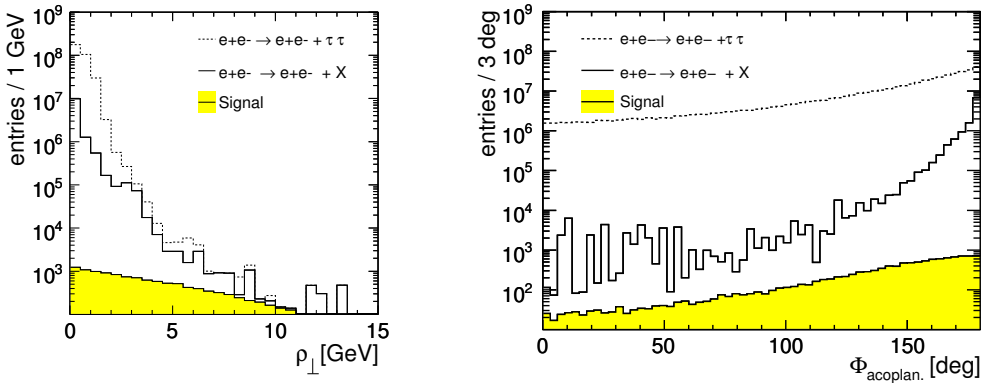

(a) $\rho_\perp$ distribution

(b) acoplanarity angle distribution

Figure 10.13: $\Phi_{acoplan.}$ *and* $\rho_\perp$ *distribution for signal and SM t-channel events*

by the contour lines in the diagram, $\rho_\perp$ is small if the jets are emitted back-to-back or collinear ($\Phi_{\text{acoplan.}} = 0$ or $\Phi_{\text{acoplan.}} = 180\,\text{deg}$). This holds even if both jets have a high energy. In the figure also the accessible kinematic range in signal events is shown - $\rho_\perp$ is less than about 16 GeV for signal events.

The distributions of $\rho_\perp$ for the signal and the SM t-channel background are shown in figure 10.13(a). The distribution is rather flat for the signal, due to the kinematics of the signal process: Each of the two taus is produced with an about fifty times heavier neutralino. From the decay of the $\tilde{\tau}_1$ the τ - χ_1 system is boosted with $\gamma \sim 2$ and therefore the τ decay products appear preferentially back to back. However the heavy neutralino can give a large recoil to the tau which reduces the back-to-back event topology. This flattens distribution.

For the SM t-channel, $\rho_\perp$ peaks stronger towards small values for the following reason: In SM t-channel events, the two outgoing fermions are emitted back-to-back in the rest frame of the initial photons. The two according jets can appear with a small intermediate angle, if the system is boosted along the z axis, but the acoplanarity angle is still close to 180 deg. The projection onto the $r - \varphi$ plane cancels the effect of boosts along z. As said above and illustrated in figure 10.12, $\rho_\perp$ is small if the acoplanarity angle is close to 180 deg and hence $\rho_\perp$ peaks to small values.

The distribution of $\Phi_{\text{acoplan.}}$ is shown in figure 10.13(b), both for the signal and the background. The argument given above does not hold if the produced fermions are taus, as the distribution for $e^+e^- \to e^+e^-\tau\tau$ is flat - $\Phi_{\text{acoplan.}}$ is distributed homogeneously over all possible angles. The neutrinos among the decay products of taus take away momentum and diminish the back-to-back topology. However, in these events a small acoplanarity angle is only possible if in one or both jets the neutrino acquires a great energy share to make the recoil of the visible particle (see figure 10.11(b)). This has the side effect that the associated visible particle is low energetic. This low jet energy keeps $\rho_\perp$ being comparably small.

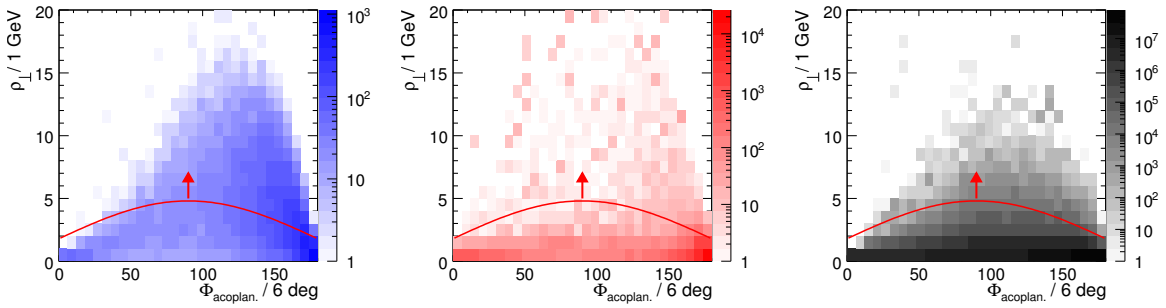

(a) signal events

(b) standard model s-channel events

(c) standard model t-channel events

Figure 10.14: *$\rho_\perp$ cut on signal events and SUSY background*

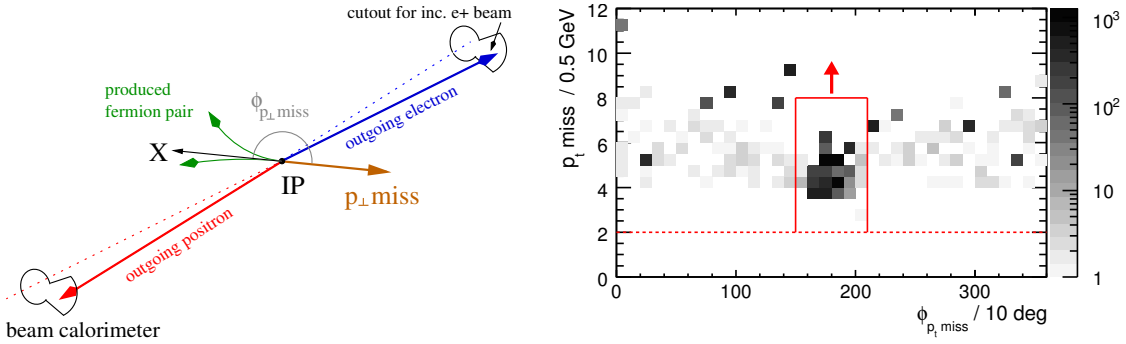

(a) both beam electrons escape undetected

(b) missing momentum plotted versus its direction of emission

Figure 10.15: *Additional cut to compensate for the limited acceptance of the beam calorimeter.*

The distribution of $\rho_\perp$ in figure 10.13(a) would allow for a significant reduction of the background with a cut, for example, $\rho_\perp > 4\,\text{GeV}$. But, this would also be a hard cut against the signal. The two-dimensional cut in a diagram of $\rho_\perp$ versus the acoplanarity angle separates clearer between signal and background. Figure 10.14(a) depicts this for the signal and figure 10.14(c) for the SM t-channel background. The cut introduced here approximates the contour of the background and the separation line is also shown in the diagram.

The SM s-channel background events typically also show a back-to-back topology and are also effectively suppressed by the $\rho_\perp$ cut (see table 10.3). Figure 10.14(b) depicts the according distribution.

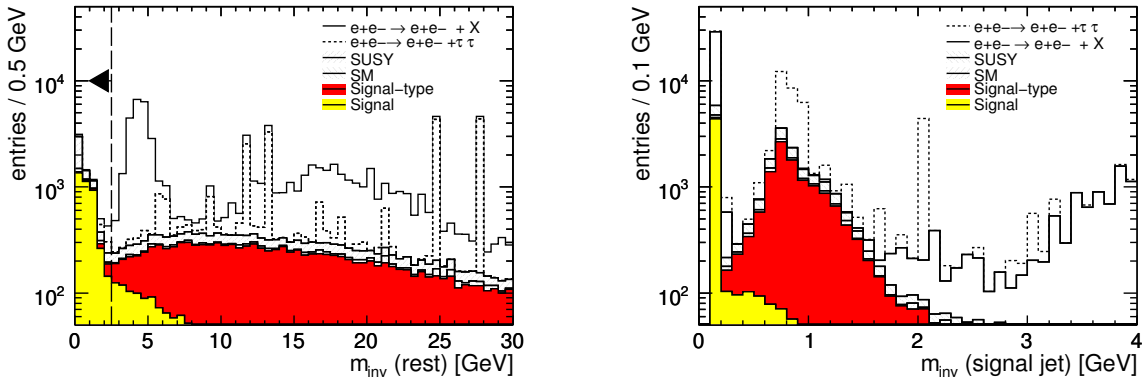

(a) invariant mass of the sum of both jets except the signal candidate

(b) invariant mass of the signal jet

Figure 10.16: *Invariant mass distributions*

Beam Calorimeter Veto

The beam calorimeter veto efficiency P_{veto} is calculated as product of the two probabilities to detect a scattered beam particle in one of the two beam calorimeter in the detector. Similar to the particle identification and the specific energy loss, P_{veto} is used to reduce the event weights: If a non-vanishing P_{veto} is calculated for an event , the weight of the signal candidate coming from this event is multiplied with (1-P_{veto}).

After the scattering processes, both electrons can leave the detector in the direction of the opposite incoming beam and completely avoid a veto. When this happens, the produced fermion pair is boosted in x direction, as sketched in figure 10.15(a). From a similar calculation as discussed in section 9.3.3, $\vec{p}_{\perp}(\text{miss})$ is expected to be $5\,\text{GeV} \cdot \vec{e}_x$ in this case. In the cylinder coordinate system this missing momentum vector has a ϕ angle of $\phi_{p_{\perp}(\text{miss})} \sim 180\,\text{deg}$.

The distribution of $p_{\perp}(\text{miss})$ versus $\phi_{p_{\perp}(\text{miss})}$ is shown in figure 10.15(b). Here, the peak at 5 GeV is visible and vetoed by the cut as shown in the figure. The effect of this cut is not very pronounced in the cut flow table, because only a few events fulfil the criterion. To make the peak more distinct in figure 10.15(b), the following invariant mass cut is already included here.

Further Selection Cuts

After these cuts, the SM t-channel background is reduced by about four orders of magnitude. It is still dominant but the remaining background drops out to a great extend with the following selection cuts.

To reduce the signal-type background, the invariant mass of the sum of all particles

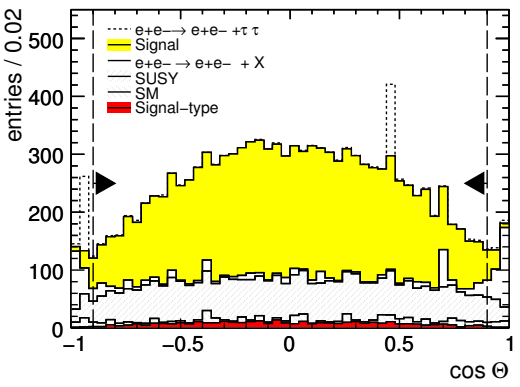

(a) $\cos\Theta$ of both jets in the event

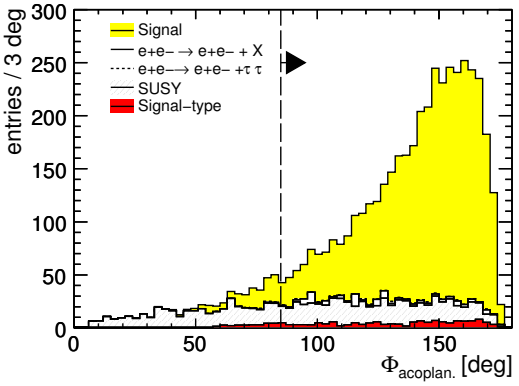

(b) acoplanarity angle $\Phi_{\text{acoplan.}}$ distribution of the remaining events

Figure 10.17: *Cuts on* $\cos\Theta$ *and the acoplanarity angle*

in the two jets except the signal candidate $m_{\text{inv}}(\text{rest})$ is calculated:

$$m_{\text{inv}}(\text{rest}) = \left| \begin{pmatrix} E \\ \vec{p} \end{pmatrix}_{\text{jet1}} + \begin{pmatrix} E \\ \vec{p} \end{pmatrix}_{\text{jet2}} - \begin{pmatrix} E \\ \vec{p} \end{pmatrix}_{\text{signal cand.}} \right|$$

Figure 10.16(a) shows the distribution of $m_{\text{inv}}(\text{rest})$ together with the chosen exclusion cut.

The motivation for choosing this cut variable is the following: If a correct signal pion is picked in a signal-type event, all other visible particles origin from the second tau. As a result, their invariant is smaller than the τ mass because the ν_τ carries away some energy. When $m_{\text{inv}}(\text{rest})$ is calculated for a charged pion coming from a ρ decay, the photons from the π_0 decay are likely be found within the signal jet ('jet1'). They add up to the energy of the second jet but - having an opposite direction - they reduce the momentum. As the result, $m_{\text{inv}}(\text{rest})$ increases. However radiative photons be present in a signal pion jet and cause an increased $m_{\text{inv}}(\text{rest})$. The radiative photons are typically low energetic, but still they produce a tail in the distribution of the signal events in figure 10.16(a).

A direct cut on the invariant mass of the signal jet, for example $m_{\text{inv}}(\text{signal jet}) < 250\,\text{MeV}$, is also suited to separate between signal-type background and the signal. Figure 10.16(b) shows the according invariant mass distribution. This cut would leave a high background of the SM t-channel at small invariant masses and, in addition, the calculation of the invariant jet mass depends to a high extend on other backgrounds present in the detector. In the simulation, beam induced backgrounds have not been considered. If these are included, more particles enter the events and could be sorted into the signal jet. As a result, the tail of the invariant mass distribution for the signal can increase. This reduces the separation to the signal-type background. The latter

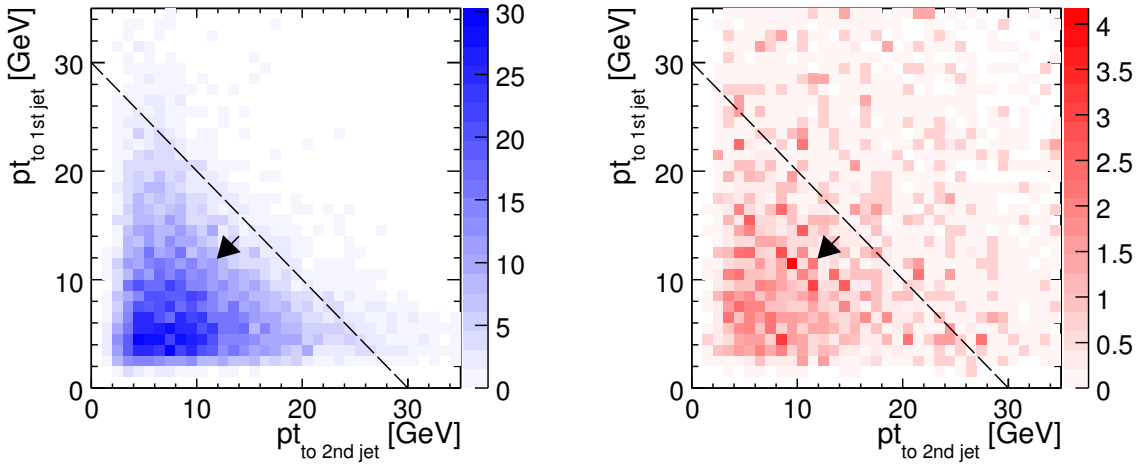

(a) remaining signal events

(b) remaining SUSY background events

Figure 10.18: *$p_t(1^{st}$ to $2^{nd})$ plotted versus $p_t(2^{nd}$ to $1^{st})$*

peaks around the ρ meson mass of 770 GeV and since the ρ peak is comparatively broad, it already partly overlaps with the tail of the signal distribution.

Unlike this direct invariant mass cut, the cut on $m_{\text{inv}}(\text{rest})$ is expected to be robust against additional particles entering the event. If the beam induced backgrounds are added, the $m_{\text{inv}}(\text{rest})$ distribution is expected to be scaled along the x axis because the background particles are equiprobably added to both jets. These additional particles in the jets increase the result while keeping the separation between signal and background, since the $m_{\text{inv}}(\text{rest})$ calculation combines both jets.

After these selection cuts, the signal pions are dominant among the remaining signal candidates (see table 10.3). A further reduction of the background makes the reconstruction of the initial signal pion spectrum more robust, because statistical fluctuations in the background and its uncertainty have a large impact on the reconstructed simulated data points. This is achieved by the three last cuts at a moderate lost of signal pions. The exclusion of events showing a jet with $|\cos\Theta| > 0.9$ reduces the SM background, because SM events typically show more activity in the forward region. In addition, the requirement for a minimal acoplanarity angle of $\Phi_{\text{acoplan.}} > 85\,\text{deg}$ reduces the SUSY background. Figure 10.17 shows the distributions belonging to these two cuts.

The final cut in the selection reduces the SUSY background even further. For this, the transversal momentum of the signal jet with respect to the axis of the second jet is calculated by

$$p_{\text{t}}(1^{\text{st}} \text{ to } 2^{\text{nd}}) = \frac{|\vec{p}_{\text{jet}\,1} \times \vec{p}_{\text{jet}\,2}|}{|\vec{p}_{\text{jet}\,2}|} \approx E_{\text{jet }1} \sin \sphericalangle(\vec{p}_{\text{jet}\,1}, \vec{p}_{\text{jet}\,2}) \tag{10.2}$$

Analogous to that $p_{\text{t}}(2^{\text{st}} \text{ to } 1^{\text{nd}})$ is evaluated by interchanging $1 \leftrightarrow 2$ in the equa-

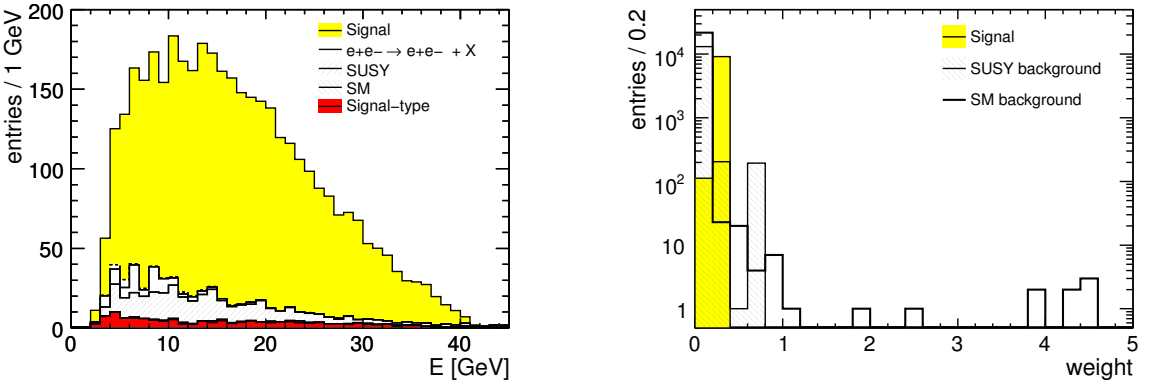

(a) energy spectrum of the selected signal candidates

(b) signal candidate's weights after the selection

Figure 10.19: *Energy spectrum of signal candidates after the selection with event weights*

tion. The cut introduced here follows the edge in the distribution of the signal (figure 10.18(a)). This triangular distribution is a consequence of the limited signal pion energy (see figure 10.5(a)).

In the SUSY background signal candidates can come from completely different physical processes which do not necessarily restrict the jet energy. Therefore the SUSY background scatters more homogeneously over the histogram.

Figure 10.19(a) depicts the energy spectrum of the selected signal candidates. The selection does not yield any signal pions with energies less than 2 GeV. These are lost mainly due to the $\rho_\perp$ cut.

In any case, particles with energies below 2 GeV are not identified robustly by the PFOID processor. For example about 80 % of the muons are identified as pions (see figure 9.13(b)). Thus it is not possible to identify signal pions with lower energies reliably, unless the particle identification performance improves significantly.

Robustness of the Selection

Due to the reweighting procedures, most event weights are smaller than one (see figure 10.19(b)) after the selection and only ten signal candidates in the SM-background are left with weights exceeding unity. Taken together, these make about 6 % of the background (about 35 of 570). The maximum weight of 4.5 is moderate compared to the weights of up to 5000 in the initial sample. Most of the event with high weights are rejected through the cuts - especially by the $\rho_\perp$ and the m_{inv}(rest) cut. This requires a consistency check, because the remaining background could be underestimated. This is the case when highly weighted signal candidates would fulfil the selection, if the cuts are loosened slightly.

To check the robustness of the selection, the $\rho_\perp$ cut has been variated in the range

$\rho_\perp > (3 \cdot \sin(\Phi_{\text{acoplan.}}) + 2)\,\text{GeV}$ to $\rho_\perp > (2.5 \cdot \sin(\Phi_{\text{acoplan.}}) + 1.6)\,\text{GeV}$. This leads to a variation of the number of signal candidates from 3041 to 3568 and the for background from 500 to 730. A variation of the m_{inv} (rest) cut between 2.25 GeV to 3 GeV changes the signal yield in the range 3260 to 3413 and the background in the range 545 to 756. In addition other cuts have been checked in a similar way and in all variables the background increases smoothly with loosening the cuts. Thus the background estimation is considered as trustworthy.

10.3 Determination of P_τ

With the selection being set up, this section describes the remaining analysis steps to arrive at a result for P_τ. Following the overview in figure 10.2, this includes the evaluation of a the background parametrisation $B(E)$ and an energy dependent efficiency correction $\epsilon(E)$. With this input, the initial signal pions spectrum $^{\mathrm{d}N}/_{\mathrm{d}E}|_{\text{initial}}$ is reconstructed bin-wise from the selected spectrum $^{\mathrm{d}N}/_{\mathrm{d}E}|_{\text{selected}}$ in figure 10.19(a):

$$\left.\frac{dN}{dE}\right|_{\text{initial}} = \left(\left.\frac{dN}{dE}\right|_{\text{selected}} - B(E) \right) \cdot \epsilon^{-1}(E) \tag{10.3}$$

The resulting data points are fit with the modified theoretical description of the spectrum, as it is explained in section 9.2.1. The fit determines the polarisation of the taus P_τ and the number of pions in the spectrum N_π.

In the following, the background parametrisation and the energy dependent selection efficiency are derived from the simulated data sample. These could be used as an input when the measurement is performed with real ILD data.

Without real data, the reconstruction chain could be validated with a statistically independent source of simulated signal and background events. For the signal, a partly independent data set is available through the simulated process $\tau\tau\chi_1\chi_1$. This set contains the signal process $\tilde{\tau}_1\tilde{\tau}_1 \to \chi_1\chi_1\tau\tau$ but the signal-type events have been filtered out for defining the cuts. The leftover is included above as the background $\chi_1\chi_1\tau\tau|_{\text{not signal}}$ (see table 10.2). For a cross-check, the additional separated signal-type events are interpreted as a statistical independent Monte Carlo set of hypothetical measured data.

Subsequent to the discussion of these technical aspects of the P_τ determination, the evaluation of the uncertainty ΔP_τ is presented.

Background Parametrisation

Figure 10.20 shows the background after the selection decomposed into its sources. A parametrisation function is fitted to the spectrum; it consists of a Gaussian at the rising edge and an exponential decay to high energies:

$$\left.\frac{dN}{dE}\right|_{\text{back.}}(E) = N \cdot \begin{cases} e^{-\frac{1}{2}\left(\frac{E-E_0}{\sigma}\right)^2} & \text{for} \quad E < E_0 \\ e^{-\lambda(E-E_0)} & \text{for} \quad E > E_0 \end{cases}$$

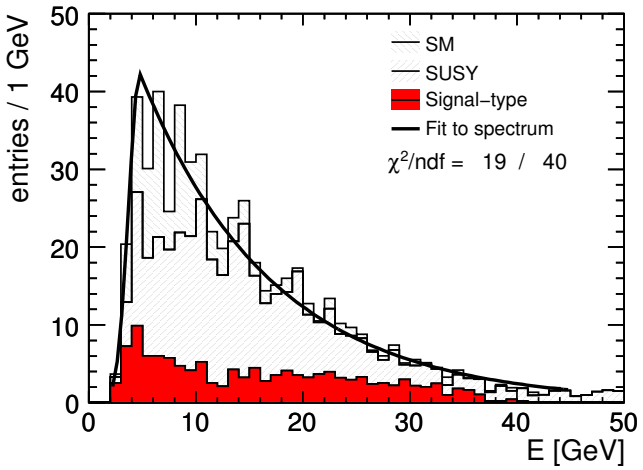

Figure 10.20: *Background after the selection with parametrisation*

Both functions are joined at the energy E_0, σ describes the width of the Gaussian part and λ is the decay constant of the exponential. The Gaussian lacks the factor $1/\sqrt{2\pi}\sigma$ to make the function continuous. The normalisation constant, N, is fixed via the integral over the background spectrum $\mathrm{d}N/\mathrm{d}E|_{\text{back.}}(E)$. This integral must yield the expected number of background particles $N_{\text{back.}}$

$$\int_{-\infty}^{\infty} B(E)\ \mathrm{dE} = N \cdot \left(\sqrt{\frac{\pi}{2}} \cdot \sigma + \frac{1}{\lambda}\right) \approx \int_{0}^{E_{\max}} B(E)\ \mathrm{dE} = N_{\text{back.}}.$$

and from this

$$N = N_{\text{back.}} \cdot \left(\sqrt{\frac{\pi}{2}} \cdot \sigma + \frac{1}{\lambda}\right)^{-1}. \tag{10.4}$$

With $N_{\text{back}} = 578$ (compare table 10.3) the fit yields the following values for the parameters:

$$E_0 = 4.75 \pm 0.40\,\mathrm{GeV} \quad \sigma = 1.03 \pm 0.25\,\mathrm{GeV} \quad \lambda = 0.0808 \pm 0.0042\,\mathrm{GeV}^{-1}.$$

Although the overall fit of the parametrisation to the background has a small $\chi^2/\text{NDF} \sim 0.5$, it does not describe the background optimal for energies below 10 GeV. The reason is the SM-background which shows a spiky shape in this region. This is caused by the 10 remaining signal candidates which have weights between 4 and 5 (see figure 10.19(b)).

Efficiency Correction

The selection efficiency ϵ is defined as the ratio between the energy spectrum of the signal pions being selected by the cuts divided through the spectrum of all signal pions. Figure 10.21(a) depicts these two spectra. The initial weight for the signal pions are set to unity here. The data points in the diagram of figure 10.21(b) represent the bin-wise

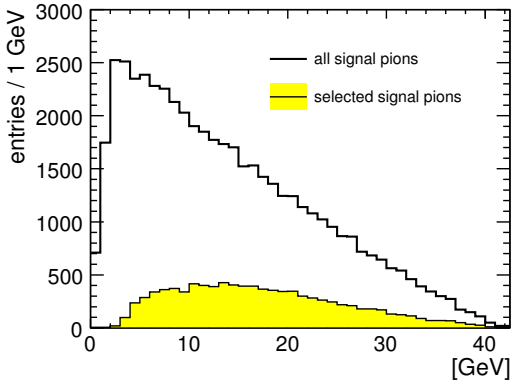

(a) initial and selected signal pion energy spectra

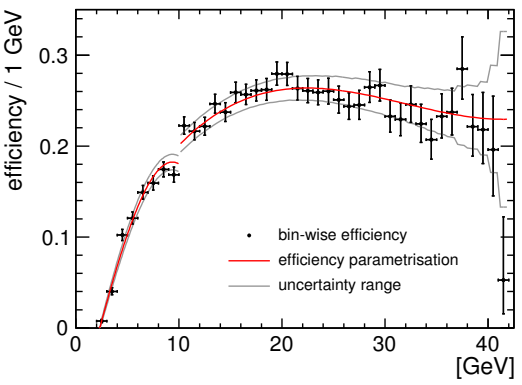

(b) energy dependent efficiency of the signal sample together with efficiency parametrisation

Figure 10.21: *Efficiency correction for the signal sample*

efficiency evaluated from the two spectra and their error bars $\Delta\epsilon_\mathrm{i}$ respect the Bayesian character of the efficiency[1]. For bin contents greater than about six this is equivalent to

$$\Delta\epsilon(E)_\mathrm{i} = \sqrt{\frac{\epsilon(E)_\mathrm{i}(1-\epsilon(E)_\mathrm{i})}{N_{\text{initial, i}}(E)}}.$$

In this equation $N_{\text{initial, i}}(E)$ is the content of the bin belonging to the signal pion energy $E_{\pi,i} \pm 0.5\,\mathrm{GeV}$ in the initial signal pion spectrum. The points scatter around an average efficiency dependency of the selection. Again a parametrisation function is introduced here, to generalise the dependency for the following analysis.

This function is kept more general and depends on the energy and on the τ polarisation P_τ:

$$\epsilon(E, P_\tau) = \left(\frac{1-P_\tau}{2}\right)^2 \epsilon(-1, E) + \left(\frac{1-P_\tau^2}{2}\right) \cdot \epsilon(0, E) + \left(\frac{1+P_\tau}{2}\right)^2 \epsilon(+1, E). \quad (10.5)$$

The three contributions $\epsilon(\pm 1, E)$ are the selection efficiency for signal pions coming from events in which both taus are negatively or positively polarised, respectively. The prefactor is the probability to find the appropriate case in a set of signal events with τ polarisation P_τ. The intermediate case, $\epsilon(0, E)$, denotes the mixed scenario - the selection efficiency for signal pions in events, which contain one positively and one negatively polarised tau. Here, the according prefactor is counted twice, because two combinations of mixed polarisations are possible. The resulting function $\epsilon(0.896, E)$ is illustrated in figure 10.21(b). The uncertainty range of the parametrisation function is adapted to the uncertainty $\Delta\epsilon(E)_\mathrm{i}$ of the points along the curve.

[1] calculated with the ROOT [111] function TGraphAsymmErrors::BayesDivide

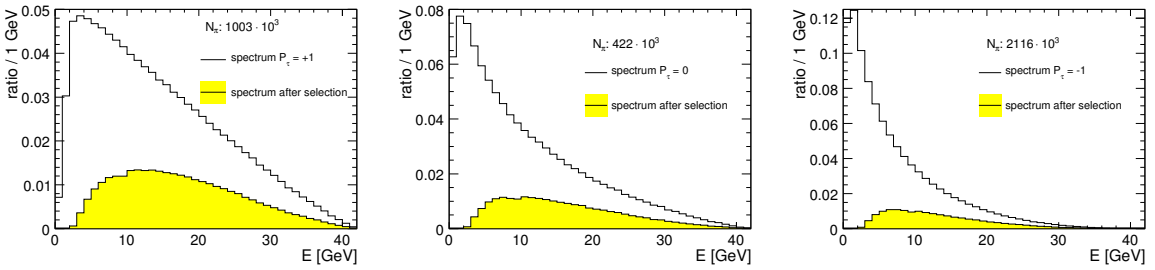

(a) $P_\tau = +1$ **(b)** $P_\tau = 0$ **(c)** $P_\tau = -1$

Figure 10.22: *Initial and selected signal pion spectra of the Monte Carlo generated events for the three possible combinations of the polarisation of the two taus*

Before the appearance of the P_τ dependency is discussed, the evaluation of the factors $\epsilon(\pm 1, E)$ and $\epsilon(0, E)$ is presented in the following. For this, three independent Monte Carlo samples with fixed $P_\tau = 1$, $P_\tau = -1$ and $P_\tau = 0$ have been generated. On these unsimulated samples, the signal pion selection has been performed analogously to the simulated events - by treating the Monte Carlo generated particles as if they were reconstructed particles. A jet finding is faked by combining the visible decay products of each tau to a jet and the particle identification is included by assigning weights to the signal candidates (see section 10.2.3).

Figure 10.22 depicts the generated Monte Carlo signal pion spectra for three cases, together with the corresponding spectra after the selection. Similar to figure 10.21(b) for the simulated signal events, figure 10.23(a) depicts the bin-wise ratio of the histograms belonging together. These curves have a similar shape like to the analogue diagram for the fully simulated set (figure 10.21(b)) but the efficiencies are about 60 % higher. The reason is that the simplified selection on the unsimulated events rejects less signal pions, because, for example, the simplified jet allocation does not sort particles into the wrong jet. Hence no particles are lost in the preselection. Also the initial-state radiation photons have been neglected and therefore practically no signal pions are lost in the cut on $m_{\text{inv}}(\text{rest})$. However the three polarisation cases are treated equally in the faked selection and thus the shape and the ratio between the curves are correct.

To describe these curves analytically, they are fitted with polynomials of third degree in the ranges $0 - 10\,\text{GeV}$ and $10 - 43\,\text{GeV}$. At the transition of these two sections, the PFOID processor changes its likelihood distributions. This causes a discontinuity and requires the piecewise parametrisation. The polynomials are proportional to $\epsilon(+1, E)$, $\epsilon(-1, E)$ and $\epsilon(0, E)$ in equation (10.5). But their normalisation is not correct. To normalise the efficiency parametrisation function, $N \cdot \epsilon(E, P_\tau = 0.896)$ has been fit to the points in figure 10.21(b). The resulting normalisation constant N is included as a common factor $1/N$ to $\epsilon(\pm 1, E)$ and $\epsilon(0, E)$ in equation (10.5).

The P_τ dependency of $\epsilon(P_\tau, E)$ manifests in figure 10.23(a) as the splitting between the efficiency curves below 20 GeV. If these curves were the same, the three contribu-

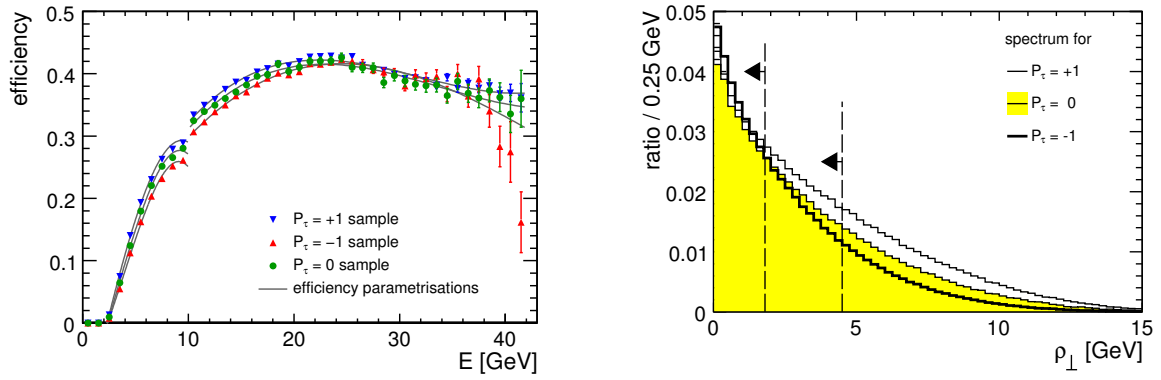

(a) selection efficiency curves

(b) $\rho_\perp$ distributions

Figure 10.23: *P_τ dependency of the efficiency*

tions in equation (10.5) could be simplified to one term $\epsilon(E)$. The splitting is cased by selection cuts, which are harder against signal events containing two negatively polarised taus compared to events which contain at least one or even two positively polarised taus. These are the in first place the $\rho_\perp$, but also the m_{inv}(rest) and the $p_{\text{t}}(1^{\text{st}}$ to $2^{\text{nd}})$ cut.

As an example, figure 10.23(b) illustrates how the $\rho_\perp$ cut differentiates between the three cases. The figure shows the distributions in this variable for the three Monte Carlo samples together with the maximal and minimal cut values. The lower cut at 1.8 GeV is the minimal required $\rho_\perp$ at $\Phi_{\text{acoplan.}} = 0$ or $\Phi_{\text{acoplan.}} = 180\,\text{deg}$, the upper is 4.5 GeV - corresponding to the maximal allowed $\rho_\perp$ at $\Phi_{\text{acoplan.}} = 90\,\text{deg}$. In average the cut is harder against the samples with a small P_τ, because the $\rho_\perp$ distribution for $P_\tau = -1$ and $P_\tau = 0$ decay faster when going to large $\rho_\perp$ compared to the $P_\tau = 1$ case. The reason for the differences lies in the calculation of $\rho_\perp$, which includes the momenta of both jets. In the $P_\tau = -1$ sample, the visible decay products get a small share of the τ energy and the jet energies are low. Both jet energies enter the calculation of $\rho_\perp$ and, averaged over many events, the lower energetic jet in the events with a negatively polarised tau reduces $\rho_\perp$. This causes the lower polarised signal events to peak stronger towards small $\rho_\perp$.

In the form of equation (10.5), the efficiency parametrisation function is valid for any P_τ, but it is not applicable in equation (10.3), because P_τ is unknown before the fit is done. A solution to this problem is an iterative procedure, realised in a bootstrap algorithm: firstly points are reconstructed for an arbitrary initial polarisation and fitted with fit the constructed fit function. With the fit result $P_{\tau,0}$ the efficiency correction is refined and the points newly reconstructed and fitted. The iterated fit result is $P_{\tau,1}$. This iteration is repeated until the fit reaches a stable value and does not change by more than 0.1 % between two iterations.

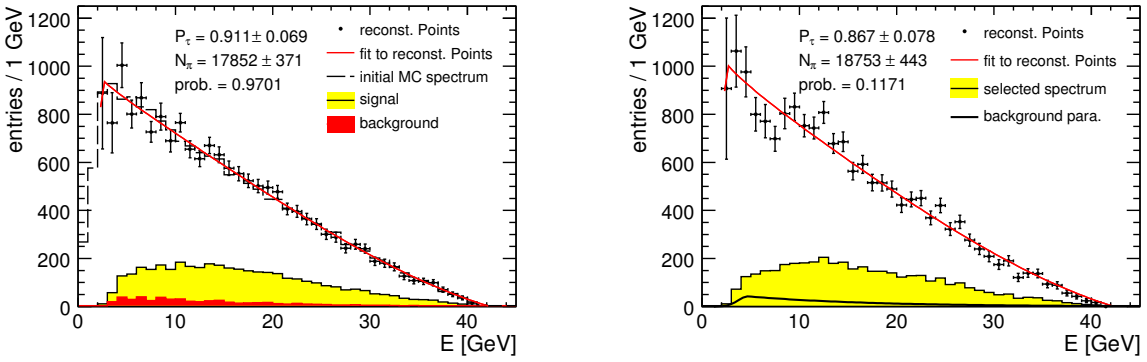

(a) reference data sample

(b) pseudo measured data

Figure 10.24: *Fit to reconstructed data points*

Fit to reconstructed data points

Figure 10.24(a) depicts the reconstructed simulated data points, which have been determined with the background and efficiency parameterisation from the spectrum of figure 10.19(a). The uncertainty of the reconstructed point in the i-th bin is calculated by

$$\Delta N_{\text{reco.}} = \epsilon^{-1}\sqrt{(\Delta N_{\text{selected}})^2 + (\Delta B)^2 + N_{\text{reco.}}\,(\Delta\epsilon)^2}.$$

which follows with error propagation from equation (10.3). In this calculation, N_{selected} is the number of entries in the i-th bin in the selected pion spectrum ${}^{\mathrm{d}N}/_{\mathrm{d}E}|_{\text{selected}}$. The statistical uncertainty $\Delta N_{\text{selected}}$ of this rate depends on the event weights w_{i} of the signal candidates being counted in the bin:

$$\Delta N_{\text{selected}} = \sqrt{\sum_{\text{i}} w_{\text{i}}^2} \qquad \text{with} \qquad N_{\text{selected}} = \sum_{\text{i}} w_{\text{i}}.$$

The contribution coming from the background parametrisation ΔB, depends on the uncertainty of the parameters entering in equation (10.4). The individual contributions are dissolved in ΔB by:

$$\Delta B = \sqrt{\left(\frac{\partial B}{\partial E_0}\Delta E_0\right)^2 + \left(\frac{\partial B}{\partial \lambda}\Delta\lambda\right)^2 + \left(\frac{\partial B}{\partial \sigma}\Delta\sigma\right)^2}.$$

The reconstructed data points are fit with the theoretical description of the spectrum using the polynomial correction fit method (see section 9.2.1). A likelihood fit has been performed and the fit range is limited to the endpoint of the theoretical spectrum, to avoid problems with low statistics in bins close to the spectrum's end. The fit yields

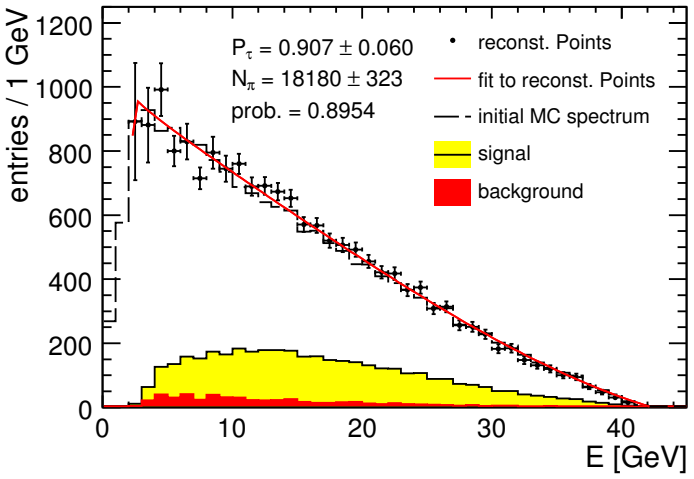

Figure 10.25: *Analysis of the complete simulated data set*

the results $P_\tau = (91 \pm 7)\,\%$ and $N_\pi = 17900 \pm 400$. Both results are in agreement with the expected $P_\tau(\mathrm{MC}) = 89.6\,\%$ and $N_\pi(MC) = 18100$ of the Monte Carlo sample put into the simulation before.

Figure 10.24(b) shows the corresponding result when the reconstruction chain is applied to the independent data sample. Here $P_\tau = (87 \pm 8)\,\%$ and $N_\pi = 18800 \pm 400$. This fit has a worse fit probability of only 11 %, but the results are also compatible with the expectations.

Combination of the Data Sets

In the following section 10.3.1, the contributions to the uncertainties ΔP_τ and ΔN_π are discussed. To have the maximal pool of signal candidates for the determination of the uncertainties, the reference sample used for defining the cuts and the pseudo measured data sample are combined. The former makes up 62 % and the latter 38 % of this complete set. In the combined set, a signal-type event has weight of 0.21. Figure 10.25 depicts the result of the analysis performed with the combined sample. Here P_τ is 0.907 ± 0.060 and $N_\pi = 18180 \pm 320$.

10.3.1 Uncertainty estimation

The statistical uncertainties ΔP_τ(statistical) and ${}^{\Delta N_\pi}/_{N_\pi}$(statistical) describe how fluctuations in a measured sample of signal candidates propagate to the fit results. These numbers are determined in the next section by analysing random subsamples of signal and background which are taken from the complete data set. Each subsample represents a possible outcome of the analysis with the data of $500\,\mathrm{fb}^{-1}$ and is used to determine ΔP_τ and ΔN_π. The scatter of the individual results is a measure for the

statistical uncertainty of the measurement. It is determined to

$$\Delta P_\tau(\text{statistic}) = 10\,\% \qquad \text{and} \quad {}^{\Delta N_\pi}/_{N_\pi}(\text{statistic}) = 3.2\,\%.$$

In addition, there is correlation between P_τ and N_π from the fit. With an independent measurement of N_π - for example derived from a measurement of the cross-section $\sigma(e^+e^- \to \tilde{\tau}_1\tilde{\tau}_1)$ - this correlation can be exploited to reduce ΔP_τ(statistical). For example

$$\Delta\sigma(e^+e^- \to \tilde{\tau}_1\tilde{\tau}_1) = 1\,\% \to \Delta P_\tau(\text{statistic}) = 6\,\%.$$

Additional contributions to ΔP_τ and ΔN_π arise from the uncertainty in the masses of the neutralino m_{χ_1} and the stau $m_{\tilde{\tau}_1}$, which are needed as an input to the fit function. This is discussed in detail subsequent to the explanations for the determination of the statistical contributions. Instead of the masses $m_{\tilde{\tau}_1}$ and m_{χ_1}, only the neutralino mass m_{χ_1} and the mass difference between neutralino and stau $\xi = m_{\tilde{\tau}_1} - m_{\chi_1}$ are considered as input to the fit function. These quantities are almost uncorrelated in the fit.

Finally, the dominant systematic contribution to the uncertainties comes from a possible false estimation of the background.

Together these uncertainties are

uncertainty:	SUSY background		neutralino χ_1 mass		mass difference $m_{\chi_1} - m_{\tilde{\tau}_1}$
$\Delta P_\tau[\%] =$	5	$\oplus$	$7 \cdot \left(\frac{\Delta m_{\chi_1}}{m_{\chi_1}}\right)$	$\oplus$	$5 \cdot \left(\frac{\Delta\xi}{\xi}\right)$
${}^{\Delta N_\pi}/_{N_\pi}[\%] =$	2.7	$\oplus$	$1.8 \cdot \left(\frac{\Delta m_{\chi_1}}{m_{\chi_1}}\right)$	$\oplus$	$1.3 \cdot \left(\frac{\Delta\xi}{\xi}\right)$

where '$\oplus$' means that the errors are added quadratically.

Determination of the statistic uncertainty

As explained in section 10.1, in total 1370 fb of signal-type events have been simulated and the event weights scale down the signal rates to the expected yield for an integrated luminosity of 500 fb^{-1}. However, the weight of a specific signal-type event can also be interpreted as the probability that the according event is present in a distinct set of events which was simulated for 500 fb^{-1}. With this interpretation, various different outcomes of the selection have been generated, namely by randomly pulling signal candidates with the probability of the event weight out of the pool of all signal candidates, which fulfil the selection cuts. Then the event weights are set to unity in each subset. This random pick produces Poisson fluctuations in the number of signal candidates.

The method fails if signal candidates have weights close to unity or even above. These are selected too often and the fluctuations are too small. Figure 10.19(b) shows the weight of the signal candidates and by far the majority has weights smaller than 0.4. Only about 5 % have higher weights. The 10 signal candidates with weights exceeding unity are treated separately for the random pick. In total they stand for 35. To model

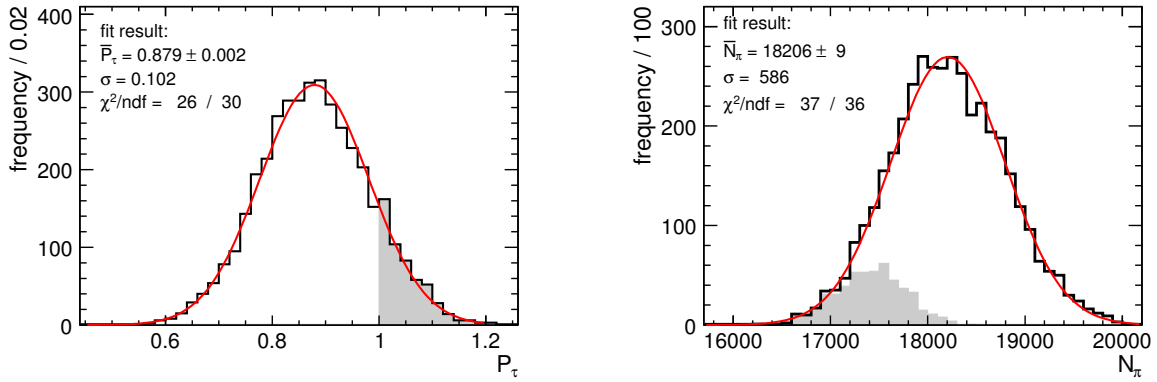

Figure 10.26: *P_τ and N_π distributions determined from 4000 subsamples*

the statistical fluctuations, this number is altered by adding a $\sqrt{35}$ times a random number from a Gaussian with $\sigma = 1$ around 0. Instead of the signal candidates, this number of pseudo signal candidates is add to each picked sample, but redistributed in a range between 2 GeV and 13 GeV. The interval corresponds to the weighted mean energy plus the standard deviation of the 10 signal candidates. The background parametrisation function is used as distribution function. In total, 4000 subsamples have been picked and analysed. Figure 10.26 depicts the resulting distribution for P_τ and N_π. The P_τ distribution in figure 10.26(a) exceeds the physically sensible value of $P_\tau = 1$, because the fit function is not restricted to this maximum.

A Gaussian fitted to the distribution has a mean value 0.879. From the fit to the whole data sample in figure 10.25, a mean value of $P_\tau = 0.907 \pm 0.06$ is obtained. One reason for the discrepancy are the highly weighted signal candidates which are not redistributed in the background spectrum of figure 10.25. However, when the redistribution procedure is applied also to this spectrum, the fit results scatter between 0.875 and 0.890 and are in agreement with 0.879. This has been checked with ten fits, where the redistribution has been applied in addition.

The variance of the the Gaussian P_τ distribution in figure 10.26(a) is 0.10 and this is interpreted as the statistical uncertainty $\Delta P_\tau(\text{statistic}) = 10\,\%$ of a single measurement.

The N_π distribution, shown in figure 10.26(b), peaks at a mean value of $\bar{N}_\pi = 18200$. The ratio between the variance of the Gaussian to this mean value is the relative statistical error $^{\Delta N_\pi}/_{N_\pi} = 3.2\,\%$.

The fit results with the unphysical values $\Delta P_\tau > 1$ are shown in gray in both distributions. In the N_π distributions the gray sub-histogram lies significantly below the mean value, which indicates that a too high P_τ in the fit is connected with a too low N_π. This correlation becomes visible in the diagram in figure 10.27, which shows the result $P_{\tau,\mathrm{i}}$ versus $N_{\pi,\mathrm{i}}$ for each of the 4000 fits. A two-dimensional Gaussian is fitted to the distribution.

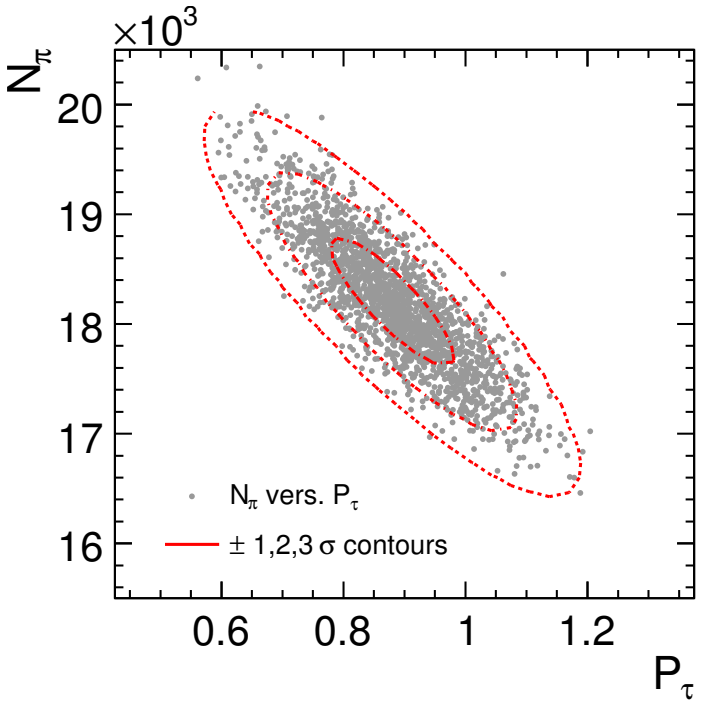

Figure 10.27: *Correlation diagram P_τ versus N_π for 4000 data samples*

From the fit result pairs ($P_{\tau,\mathrm{i}}$, $N_{\pi,\mathrm{i}}$), the correlation coefficient c is calculated as

$$c = \frac{\sqrt{\sum_{\mathrm{i}}(P_{\tau,i} - \bar{P}_\tau) \cdot (N_{\pi,i} - \bar{N}_\pi)}}{\Delta P_\tau \Delta N_\pi} = -0.86$$

where ΔP_τ and ΔN_π are the standard deviations

$$\Delta P_\tau = \sqrt{\frac{1}{N-1}\sum_{\mathrm{i}=0}^{4000}(P_{\tau,i} - \bar{P}_\tau)^2} = 0.102 \qquad \text{and} \qquad \Delta N_\pi = 590.$$

The example diagrams in figure 10.28 illustrate the reason for this correlation. In the energy regime above $\sim$ 15 GeV the background is small and also well described by the parametrisation function $B(E)$. Therefore the simulated data points are reconstructed with a small scatter and they fix the end part of the spectrum in the fit. However, in this range the P_τ dependence is weak (see figure 8.7(c)) and this part of the spectrum contributes weakly to the fit result. Most important for the fit result are the reconstructed points at low energies. In this regime the background is higher and the selection efficiency decreases. Hence the reconstructed points shown an increased scatter.

If the points happen to be reconstructed at too small values at the low energy end, the fit function tends to be bended downwards while the end part is fixed by the robustly reconstructed points at the high energy end. Figure 10.28(a) shows an example for this

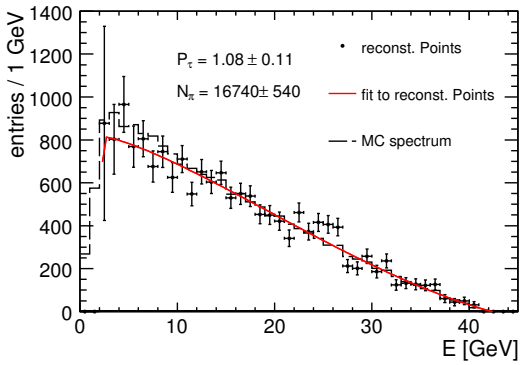

(a) $P_\tau(\text{fit}) > \bar{P}_\tau \rightarrow N_\pi(\text{fit}) < \bar{N}_\pi$

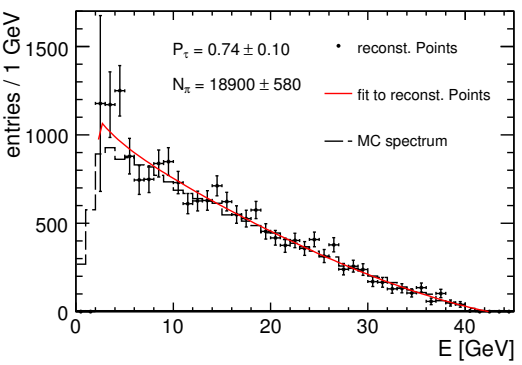

(b) $P_\tau(\text{fit}) < \bar{P}_\tau \rightarrow N_\pi(\text{fit}) > \bar{N}_\pi$

Figure 10.28: *Example fit for two random samples to illustrate the correlation between P_τ and N_π*

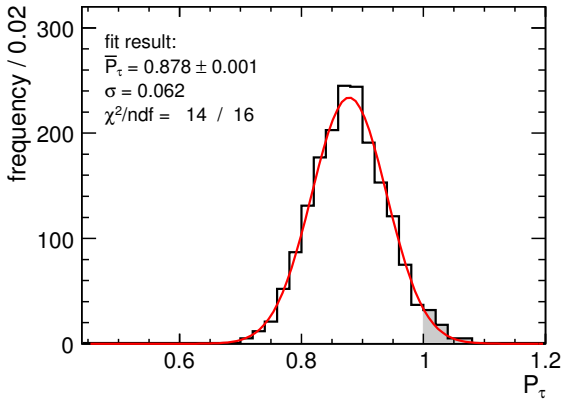

Figure 10.29: *P_τ distribution with restriction on N_π*

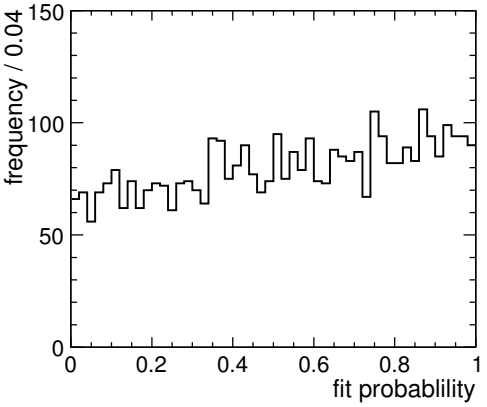

Figure 10.30: *Fit probability distribution*

case. In this scenario, P_τ comes out too high and automatically N_π is too low. The situation is reversed, if the points happen to overestimate the signal pion spectrum, as illustrated in figure 10.28(b).

Without additional input, the correlation cannot be used to reduce the statistical uncertainties, because P_τ and N_π are determined from the same fit. This single result does not fix the location of the N_π versus P_τ distribution in this parameter space. A restriction could come from a statistically independent measurement of N_π via the measurement of the cross-section $\sigma(e^+e^- \rightarrow \tilde{\tau}_1\tilde{\tau}_1)$. If this is for example possible with a relative uncertainty of 1 %, this translates to an uncertainty of $\Delta N_\pi \approx 180$. Using this result, the improvement in ΔP_τ is estimated by cutting out a $\pm 2 \cdot \Delta N_\pi$ band in the distribution of figure 10.27. In this band the $P_{\tau,\text{i}}$ values scatter in a Gaussian with the decreased $\sigma = 0.06$, as shown in figure 10.29. In this case $\Delta P = 6\,\%$ is the reduced

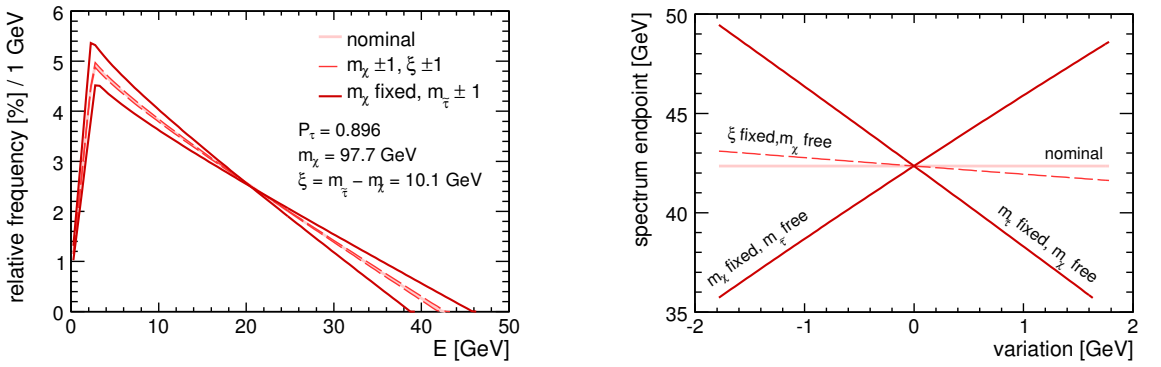

(a) spectrum shape

(b) endpoint of the spectrum

Figure 10.31: *Dependency of the spectrum's shape and endpoint on m_{χ_1}, $m_{\tilde\tau_1}$ and ξ*

statistical uncertainty.

Finally figure 10.30 depicts the fit probability distribution for the 4000 individual fits. The distribution is almost flat but increases slightly towards 1.

Masses $m_{\tilde\tau_1}$ and m_{χ_1}

The masses $m_{\tilde\tau_1}$ and m_{χ_1} of the stau and the neutralino enter into the theoretical description of the pion energy spectrum and have to be known before the fit is done. The mass uncertainties propagate to the uncertainties of the fit by

$$\Delta P_\tau^2 = \left(\frac{\partial P_\tau}{\partial m_{\chi_1}}\Delta m_{\chi_1}\right)^2 + \left(\frac{\partial P_\tau}{\partial m_{\tilde\tau_1}}\Delta m_{\tilde\tau_1}\right)^2 + 2\cdot\frac{\partial P_\tau}{\partial m_{\tilde\tau_1}}\frac{\partial P_\tau}{\partial m_{\chi_1}} C(m_{\chi_1}, m_{\tilde\tau_1})\Delta m_{\chi_1}\Delta m_{\tilde\tau_1}$$

The fit function correlates these masses and the correlation coefficient $C(m_{\chi_1}, m_{\tilde\tau_1})$ in the sum does not vanish. The diagrams in figure 10.31 illustrate this correlation. In figure 10.31(a) the theoretical spectrum is shown for different masses m_{χ_1} and $m_{\tilde\tau_1}$. As the different curves demonstrate, if one of the masses is varied while the other one is fixed, the endpoint of the spectrum is shifted. Thereby a decreasing stau mass is equivalent to an increasing neutralino mass and thus

$$\frac{\partial P_\tau}{\partial m_{\tilde\tau_1}} \approx -\frac{\partial P_\tau}{\partial m_{\chi_1}}$$

Figure 10.31(b) demonstrates the dependency of the endpoint from the input masses and this correlation.

In the following, the neutralino mass m_{χ_1} and the mass difference $\xi = m_{\tilde\tau_1} - m_{\chi_1} = 10.1\,\text{GeV}$ are considered as input to the fit function. In this scheme, $m_{\tilde\tau_1}$ is to be replaced by $m_{\tilde\tau_1} = m_{\chi_1} + \xi$. Both diagrams in figure 10.31 illustrate that the spectrum does not significantly change its shape if ξ keeps being fixed while m_{χ_1} is variated in

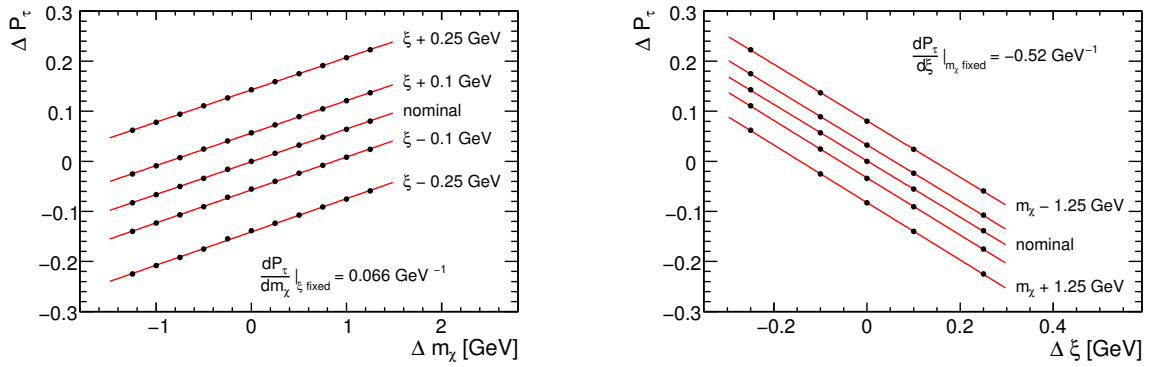

(a) determination of $^{\partial P_\tau}/_{\partial m_{\chi_1}}$ **(b)** determination of $^{\partial P_\tau}/_{\partial \xi}$

Figure 10.32: *Impact of m_{χ_1} and ξ variation on the fit result P_τ*

a range of $\pm 1\,\text{GeV}$. The propagation of the measurement uncertainties Δm_{χ_1} and $\Delta\xi$ to an uncertainty of the fit results P_τ and N_π can now be estimated by

$$(\Delta P_\tau)^2 = \left(\frac{\partial P_\tau}{\partial m_{\chi_1}}\Delta m_{\chi_1}\right)^2 + \left(\frac{\partial P_\tau}{\partial \xi}\Delta\xi\right)^2.$$

Here, a correlation term $C(m_{\chi_1}, \xi)$ is left out, because m_{χ_1} and ξ can be derived from independent measurement. The dependency of the spectrum's endpoint on m_{χ_1} is weak, when ξ is altered.

To estimate the derivatives, the fit to the full data set has been performed for different modified m_{χ_1} and ξ. For this, the fit procedure has been adapted, if the altered fit function required for a new fit range. This has been done by scaling the correction polynomials along the energy axis.

Figure 10.32(a) shows the development of P_τ with m_{χ_1} for different fixed ξ in the range $\Delta m_{\chi_1} = \pm 1.25\,\text{GeV}$ and figure 10.32(b) the corresponding diagram for the reversed case, the fit result's dependency on ξ for several fixed m_{χ_1} in the range are $\Delta\xi = \pm 0.25\,\text{GeV}$.

The dependencies are linear within the expected range. A fit of a straight to the points yields the slopes

$$\frac{\partial P_\tau}{\partial m_{\chi_1}} = 0.066\,\text{GeV}^{-1} \quad \text{and} \quad \frac{\partial P_\tau}{\partial \Delta\xi} = -0.52\,\text{GeV}^{-1}.$$

With the nominal neutralino mass $m_{\chi_1} = 97.7\,\text{GeV}$ and the nominal mass difference $\xi = 10.1\,\text{GeV}$, this results can be rewritten in terms of relative uncertainties:

$$\Delta P_\tau^{m_\chi} = 6.8 \cdot \frac{\Delta m_{\chi_1}}{m_{\chi_1}} \qquad \Delta P_\tau^{\text{mass difference}} = -5.2 \cdot \frac{\Delta\xi}{\xi}.$$

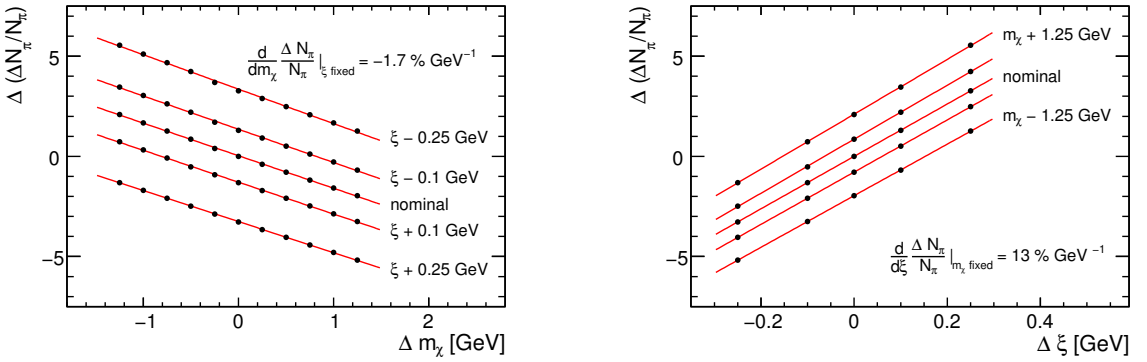

(a) determination of $^{\partial N_\pi}/_{\partial m_{\chi_1}}$ **(b)** determination of $^{\partial N_\pi}/_{\partial \xi}$

Figure 10.33: *Propagation of a variation in m_{χ_1} and ξ to the relative change $^{\Delta N_\pi}/_{N_\pi}$*

Analogue to this, figure 10.33(b) depicts the corresponding diagrams for N_π. Here the derivatives and the uncertainty propagation are

$$\left.\frac{\partial}{\partial m_{\chi_1}}\frac{\Delta N_\pi}{N_\pi}\right|_{\xi \text{ fixed}} = -1.7\,\%\,\text{GeV}^{-1} \quad \rightarrow \quad \frac{\Delta N_\pi}{N_\pi} = -1.8 \cdot \frac{\Delta m_{\chi_1}}{m_{\chi_1}}$$

$$\left.\frac{\partial}{\partial \xi}\frac{\Delta N_\pi}{N_\pi}\right|_{m_{\chi_1} \text{ fixed}} = 13\,\%\,\text{GeV}^{-1} \quad \rightarrow \quad \frac{\Delta N_\pi}{N_\pi} = 1.3 \cdot \frac{\Delta \xi}{\xi}$$

Background Estimation

The SUSY part of the background estimation is subject to model uncertainties. This means that many SUSY parameters like masses and couplings of supersymmetric particles have to be measured before the simulation is performed. Hence this background is understood worse than for example the SM background. SM model uncertainties are negligible because SM parameters needed in the simulation are usually precisely measured. When the data of $\mathcal{L} = 500\,\text{fb}^{-1}$ is available, it will be possible to validate the simulated SUSY background with a measured control sample. The control sample can be extracted from the recorded events with the selection described above, except that cuts which predominantly suppress the SUSY background are inverted. One possible set of cuts is

$$m_{\text{inv}} > 2.5\,\text{GeV} \qquad \Phi_{\text{acoplan.}} < 85\,\text{deg} \qquad p_{\text{t}}(1^{\text{st}} \text{ to } 2^{\text{nd}}) + p_{\text{t}}(2^{\text{nd}} \text{ to } 1^{\text{st}}) > 30\,\text{GeV}.$$

and all other cuts left unchanged. The new selection scheme yields

signal: 26 signal-type: 90 SM: 128 SUSY: 739.

As the new sample is dominated by the SUSY background, the distributions in any measurement category of the simulated events can be used for a comparison to equivalent measured data. One example spectrum, which is suited for a comparison, is the

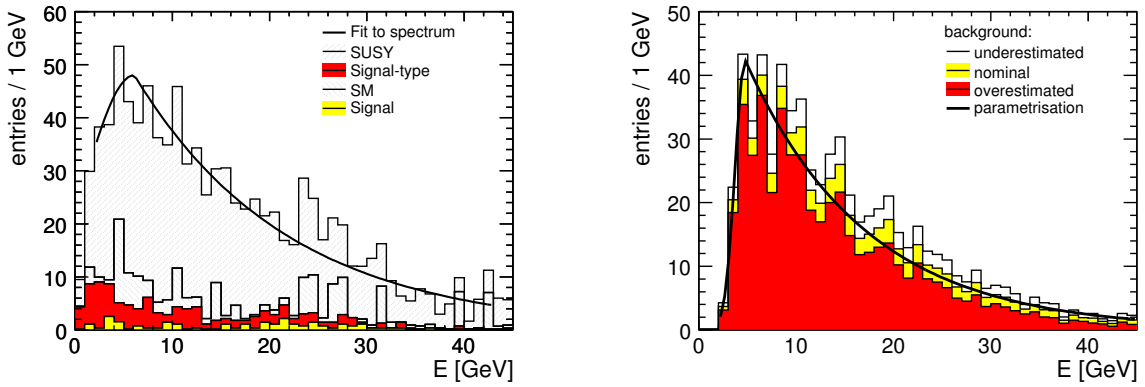

(a) control spectrum

(b) background variation with parametrisation

Figure 10.34: *Background parametrisation with control spectrum*

scenario	P_τ	N_π
nominal	0.91 ± 0.06	18200 ± 300
background overestimated	0.92 ± 0.06	17700 ± 300
background underestimated	0.90 ± 0.06	18700 ± 300
linear rise	0.97 ± 0.06	17800 ± 300
linear decrease	0.85 ± 0.06	18600 ± 300

Table 10.4: *Effect of a false estimation of the background on the fit results*

energy spectrum of the signal candidates. Figure 10.34(a) displays this spectrum, fitted with the background parametrisation B_{control}. Under the assumption that the measured data agrees with this spectrum, the simulated SUSY background which underlies to the signal is considered as reliable.

However, this method can validate the background only within the statistical uncertainties of the control sample. If the control sample validates the simulation, a biased over- or underestimation of the SUSY background within statistical fluctuations is still possible:

$$\left.\frac{\mathrm{d}N}{\mathrm{d}E}\right|_{\text{SUSY}} \cdot \frac{\Delta B_{\text{control}}}{B_{\text{control}}} = \left.\frac{\mathrm{d}N}{\mathrm{d}E}\right|_{\text{SUSY}} \cdot \frac{1}{\sqrt{B_{\text{control}}}}$$

To study the impact of a false estimation of the SUSY background within this range, the event weights $w|_{\text{SUSY}}$ of the simulated SUSY background are scaled by

$$w|_{\text{SUSY}} \to w|_{\text{SUSY}} \cdot \left(1 \pm \frac{1.3}{\sqrt{B_{\text{control}}(E)}}\right).$$

and the fit is performed with the efficiency and background parameterisations unchanged. Here a factor 1.3 is included, because 25 % of the control sample is not SUSY background.

Figure 10.34(b) illustrates the total nominal background and the effect of the possible variation. If the weights are scaled upwards ('+' in the equation) the total background increases and is underestimated by the unchanged background parametrisation. Accordingly, in case of downscaled weights ('-' in the equation) the parametrisation overestimates the background.

Table 10.4 summarises the effect of the SUSY background variation on the fit results. The background variations, as described above, have mainly an impact on the result N_π, because the background shape is not altered compared to the nominal background, as shown in figure 10.34(b). But also a combination of the cases is possible. The case 'linear rise' denotes the fit results gained with the background modified like

$$w|_{\mathrm{SUSY}} \rightarrow w|_{\mathrm{SUSY}} \cdot \left(1 \pm \frac{1.3}{\sqrt{B_{\mathrm{control}}(E)}} \cdot \left(1 - \frac{2 \cdot E}{E_{\mathrm{max}}}\right)\right).$$

This corresponds to an overestimation of the background for small and an underestimation for high energies. Similar to that, the case 'linear decrease' describes the revered case to this, an underestimation for small and an overestimation of the background for high energies.

In summary, the possible variations of the SUSY background lead to variations in P_τ of $\pm 5\,\%$ and in N_π by ${}^{\Delta N_\pi}/_{N_\pi} = {}^{500}/_{18100} = 2.7\,\%$. These numbers add as background estimation uncertainty to the total systematic uncertainties.

10.3.2 Summary of the Analysis in the Chanel $\tau \rightarrow \pi\nu_\tau$

The analysis in the $\tau \rightarrow \pi\nu_\tau$ yields the result

$$\begin{aligned} P_\tau[\%] = \quad & 90.7 \oplus 10\ (\text{statistic}) \oplus 5\ (\text{background}) \oplus \\ & 7 \cdot \left(\frac{\Delta m_{\chi_1}}{m_{\chi_1}}\right)(\chi_1\text{mass uncertainty}) \oplus \\ & 5 \cdot \left(\frac{\Delta \xi}{\xi}\right)(\text{uncertainty on the mass difference } m_{\chi_1} - m_{\tilde{\tau}_1}) \end{aligned}$$

In the SUSY point SPS1a', the neutralino mass is $m_{\chi_1} = 97.7\,\mathrm{GeV}$, while the stau mass is $m_{\tilde{\tau}_1} = 107.7\,\mathrm{GeV}$. The mass difference between the two is $\xi = m_{\chi_1} - m_{\tilde{\tau}_1}) = 10.1\,\mathrm{GeV}$.

At the ILC, the neutralino mass can be measured in sfermion final states $e^+e^- \rightarrow \chi_1\chi_1\tilde{e}_{\mathrm{R,L}}\tilde{e}_{\mathrm{R,L}}$ and $e^+e^- \rightarrow \chi_1\chi_1\tilde{\mu}_{\mathrm{R,L}}\mu_{\mathrm{R,L}}$. The measurement in the $\tilde{\mu}$ channel allows for an accuracy of $\Delta m_{\chi_1} = \pm 1\,\mathrm{GeV}$ [112]. Hence the relative accuracy of the neutralino mass measurement is 1 %. If analogue studies are made in the other sfermion channels, a final accuracy of $\Delta m_{\chi_1} = 0.5\,\mathrm{GeV}$ could be possible - this would reduce ${}^{\Delta m_{\chi_1}}/_{m_{\chi_1}}$

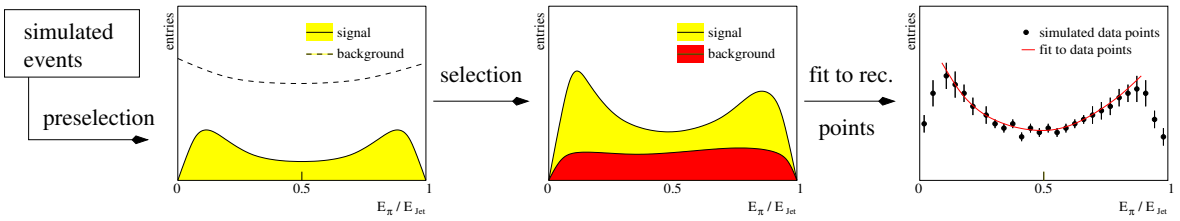

Figure 10.35: *Overview of the analysis steps to determine P_τ in the channel $\tau \rightarrow \rho\nu_\tau \rightarrow \pi\pi_0\nu_\tau$*

to 0.5 %. A measurement of the mass difference ξ is possible by a dedicated endpoint determination in the signal process $\chi_1\chi_1\tilde{\tau}_1\tilde{\tau}_1$. A study on this measurement gives an uncertainty of 0.6 GeV [113], which is a relative accuracy of 6 %. Hence the uncertainty on $\Delta\xi$ gives the dominant contribution to ΔP_τ, namely 30 %. However, the mass difference of stau and neutralino could be measured in other final states and in addition, the masses of the two particles can be determined independently. Assuming that finally measurement accuracies of ${}^{\Delta m_{\chi_1}}/_{m_{\chi_1}} = 0.5\,\%$ and ${}^{\Delta\xi}/_{\xi} = 1\,\%$ are possible, the accuracy estimation for ΔP_τ is

$$P_\tau[\%] = 90.7 \oplus 10\ \text{(statistic)} \oplus 5\ \text{(background)} \oplus 6\ \text{(SUSY masses)}$$

If the beam polarisation scheme of the machine is modified to a setup of only $-30\,\%$ polarisation of the positron beam, while the 80 % for the electron beam is kept, the signal pion yield reduces by 20 %. At the same time, the background after the selection stays constant. The statistical uncertainty rises slightly to $P_\tau(\text{statistic}) = 12\,\%$ (for $(-0.3, +0.8)$).

10.4 Analysis of the channel $\tau \rightarrow \rho\nu_\tau \rightarrow \pi\pi_0\nu_\tau$

This section concentrates on the determination of P_τ in the decay $\tau \rightarrow \rho\nu_\tau \rightarrow \pi\pi_0\nu_\tau$. Figure 10.35 outlines the analysis strategy.

At first, the preselection algorithm selects signal candidates from the simulated events. The preselection criteria are almost similar to the analysis in the channel $\tau \rightarrow \pi\nu_\tau$, but modified to match the changed final state. These modifications are described in the following section. For each signal pion also a signal jet is measured and the ratio between the energy of the signal pion E_π to the energy of the whole jet E_{jet} is used for the determination of P_τ (see section 9.2.2). Directly after the preselection, the background exceeds the signal by about four orders of magnitude. Then, after the application of the selection cuts, the signal to background ratio is about 1 while the selection efficiency for signal pions is $\sim 20\,\%$. Also here, many selection criteria for signal candidates are identical to the measurement via $\tau \rightarrow \pi\nu_\tau$ described above.

Again, the background is subtracted in a parametrised form. The resulting spectrum is fitted with an adapted fit function - here no correction for selection efficiencies is

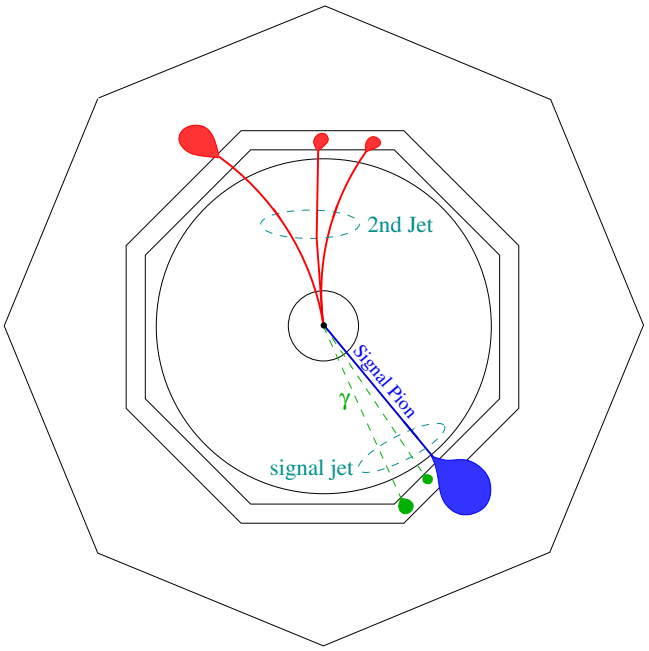

Figure 10.36: *Signal event topology of the channel* $\tau \rightarrow \rho\nu_\tau \rightarrow \pi\pi_0\nu_\tau$

- event contains two jets
- signal candidate appears separated in the detector (jet with single track)
- signal jet contains at least two neutral particles
- the energy of each jet is less than 43 GeV
- energy of the signal candidate less than 43 GeV
- the visible energy in the event is less than 90 GeV
- the event contains less than 10 tracks coming from the interaction point

Table 10.5: *Summarised preselection criteria*

necessary. The fit function is constructed in such a way that it includes the efficiency losses and deformations of the E_π/E_{jet}-ratio spectrum due to the cuts. This is described in section 10.4.4.

The fit yields a result for P_τ and the number of initial signal pions N_π. In the rest of this section the E_π/E_{jet}-ratio spectrum is abbreviated as 'ratio spectrum' and R stands for E_π/E_{jet}.

10.4.1 Preselection

Signal candidates are preselected from two-jet events, similar to the measurement in the channel $\tau \rightarrow \pi\nu_\tau$. The signal jet is required to consist of one charged and at least two more neutral particles (see figure 10.36). Events containing a jet with an energy higher than 43 GeV are vetoed from the beginning, because the jet energy determines

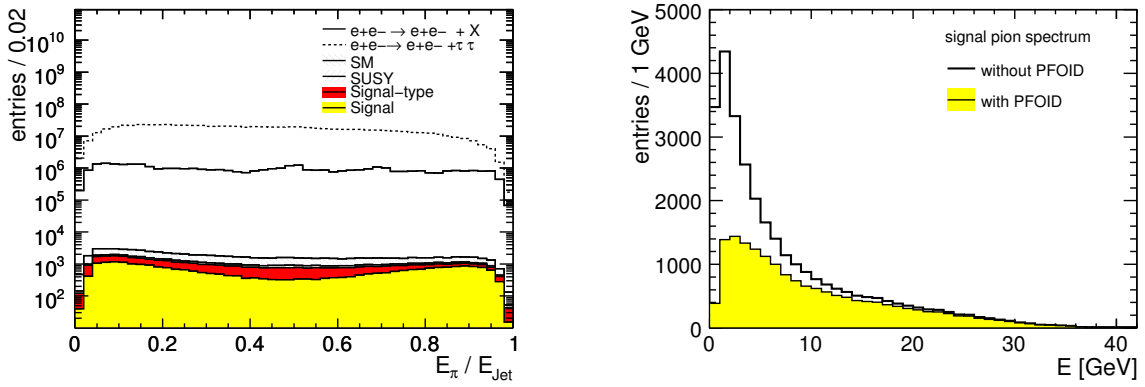

(a) ratio spectrum

(b) energy spectrum of signal pions with and without particle identification constrain (PFOID)

Figure 10.37: *E_π/E_{Jet}-ratio spectrum of all preselected signal candidates and energy spectrum of signal pions*

the ratio E_π/E_{jet} and, as discussed before, 43 GeV is the maximal energy of the taus in signal events. If in a signal event a jet has a higher energy, it is likely that an additional photon has by mistake been sorted into the jet. Then the E_π/E_{jet}-ratio is incorrect.

All other preselection criteria are left unchanged from the single pion channel. They are summarised in table 10.5. The preselection yields 29440 out of 41300 signal pions which is a preselection efficiency of $\sim 71\,\%$.

Compared to the analysis in the channel $\tau \to \pi\nu_\tau$, additional preselection criteria have been introduced and the jet energy constraint has been tightened. Therefore all serious sources of background to this preselection are listed in table 10.2 and no further processes need to be considered. Figure 10.37(b) depicts the ratio spectra of all preselected signal candidates.

10.4.2 Particle Identification

The preselection criteria are constructed to select ρ jets which are jets comprising a charged pion and two photons. After the preselection, 85 % of all signal candidates which are the charged particles in the selected jets, are Monte Carlo truth pions. Therefore no pion identification condition is mandatory. Contrary, a pion identification requirement is disadvantageous for the following reason: the energy spectrum of the signal pions in this channel peaks towards small energies. As discussed in section 9.3.2, the pion identification becomes less robust when going to energies below $\approx 5\,\text{GeV}$. Figure 10.37(b) illustrates the energy dependent rate for a misidentification of pions and a false identification of other particle species as pions.

Vetoing signal candidates which have not been identified as pions or which have an

selection step	Number of signal candidates					
	Signal	Sig-type	SUSY	SM		
				s-channel	e^+e^+X	$e^+e^+\tau\tau$
preselection	29440	15900	7400	32700	$2.0 \cdot 10^7$	$6.1 \cdot 10^8$
t-channel suppr.	13031	7100	3400	670	40000	32000
$0.4 < m_{\text{inv.}} < 1.1\,\text{GeV}$	10207	2500	2300	290	150	20000
$\lvert\cos\Theta\rvert$ (sig. jet) < 0.8	9528	2300	2000	200	3	6000
$\rho_\perp$ cut tightened	8164	2000	1800	200	2	$\sim$3000

Table 10.6: *Cut flow of the selection*

identification likelihood below 0.97 (see section 10.2.3) rejects about half of the signal pions. Figure 10.37(b) also shows the resulting signal pion energy spectrum for this case. Although a particle identification constraint reduces the absolute amount of background, the signal to background ratio does not improve.Even a moderate veto condition on signal candidates which have been identified as something else than a pion with a likelihood greater than 0.97 does not improve the signal to background ratio. Thus only the $^{\mathrm{d}E}/_{\mathrm{d}x}$-reweighting procedure is applied.

10.4.3 Selection Cuts

Like for the preselection, also most of the selection cuts are inherited from the previously discussed selection for the channel $\tau \rightarrow \pi\nu_\tau$ (for this see section 10.2.4). In the following, the selection cuts are reported and table 10.6 gives a cut flow of the whole selection.

Together with the veto on the beam calorimeter activity, firstly the SM t-channel background is reduced with the cut on $\rho_\perp$

$$\rho_\perp > (2.7 \cdot \sin(\Phi_{\text{acoplan.}}) + 1.8)\,\text{GeV}.$$

The requirement to have a vanishing charge in the event and the cut to compensate for limited acceptance of the beam calorimeter,

$$p_\perp(\text{miss}) > 8\,\text{GeV} \quad \text{if} \quad |\phi_{p_\perp(\text{miss})} - 180\,\text{deg}| < 30,$$

are applied in addition. Figure 10.38(a) depicts the invariant mass distributions of the signal jets. Here a cut

$$0.4\,\text{GeV} < m_{\text{inv}}(\text{signal jet}) < 1.1\,\text{GeV}$$

vetoes mainly others than ρ-jets. This reduces the signal-type background, which mostly comes from $\tau \rightarrow K^1\nu_\tau \rightarrow K\pi_0\nu_\tau$ decays. Thereby also most of the remaining $e^+e^- + X$ background drops out, which was made up mostly by six signal candidates with a weight of 5000 and an m_{inv} above 4 GeV.

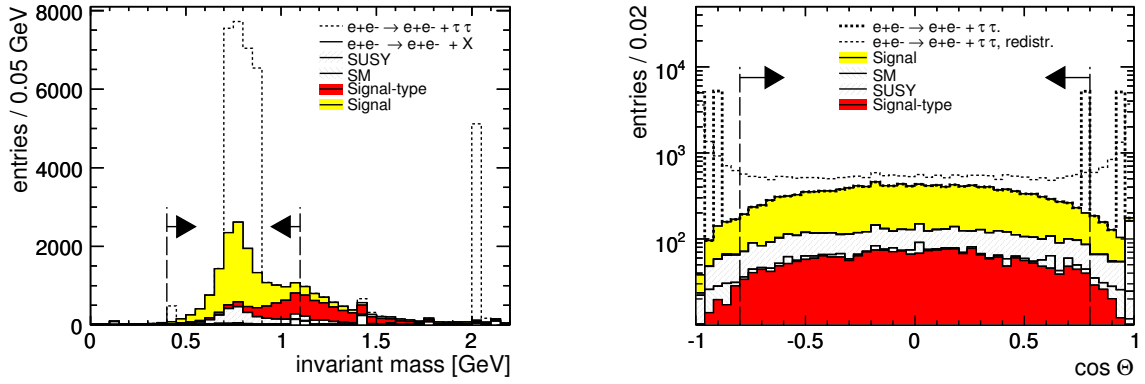

(a) invariant mass of the signal jet

(b) $\cos\Theta$ of the signal jet

Figure 10.38: *Invariant mass and* $\cos\Theta$ *of the signal jets*

After this cut, only the $e^+e^- \to e^+e^- + \tau\tau$ background is left as a significant source of background, but it is made up of 4 entries with weights of the order 5000. Due to these high weights, the background shape is not described correctly in all following distributions. This becomes apparent for example in the $\cos\Theta$ distribution of the signal jet in figure 10.38(b). Here it is possible to veto this background completely with a cut $|\cos\Theta| < 0.7$. But if this is done, the background would be underestimated in the following because the remaining $e^+e^- + \tau\tau$ signal candidates distribute unknown over $\cos\Theta$. Some of them are likely to fulfil the cut. As a remedy, the signal candidates are redistributed according to the initial $\cos\Theta$ distribution of this background. The resulting distribution is also shown in the diagram. The cut introduced here is

$$|\cos\Theta|_{\text{signal jet}} < 0.8.$$

The signal candidates with the high weights are not excluded but their weight is reduced to 30 %. This is the ratio signal candidates left after this cut to the initial number of signal candidates, under the assumption that they were distributed like the initial sample of $e^+e^- + \tau\tau$. Then, the background coming from $e^+e^- + \tau\tau$ is reduced from 20000 to 6000.

Cuts on the acoplanarity angle $\Phi_{\text{acoplan.}}$, $\cos\Theta$ of the second jet and the transverse momenta of the jets with respect to each other, as applied in the $\tau \to \pi\nu$ channel above, are ineffective here. They are left out.

At this stage, the signal to background ratio is about 0.87 and the selection efficiency for signal jets is $\sim$ 23 %. A further suppression of the background is possible by tightening the $\rho_\perp$ cut. With

$$\rho_\perp > (3.5 \cdot \sin(\Phi_{\text{acoplan.}}) + 2)\,\text{GeV}$$

the signal reduces to 8164, while the total background is reduced to 5406. Then the selection efficiency is $\sim$ 20 %. But, with this tighter cut, three of the four highly

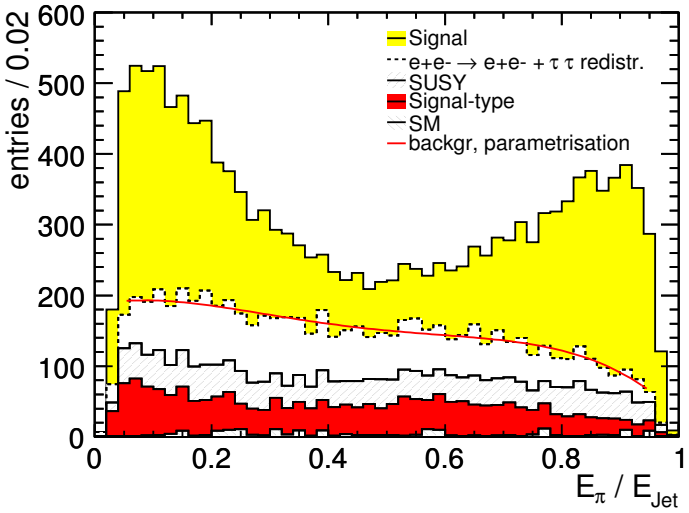

Figure 10.39: *E_π/E_{Jet}-ratio spectrum of all signal candidates after the selection with a background parametrisation*

weighted signal candidates are rejected, the background reduces to 1500 and is likely to be underestimated again. With a similar procedure, as it is applied for the $\cos\Theta$ cut, the background was reevaluated for the tightened $\rho_\perp$ cut and estimated to 3000 signal candidates coming from $e^+e^- + \tau\tau$.

Overall, the selection yields 8164 signal pions at a background of $\sim$ 7000. Figure 10.39 shows the E_π/E_{jet}-ratio diagram of these selected signal jets. Here the $e^+e^- + \tau\tau$ background is again redistributed according to its initial shape.

10.4.4 Determination of P_τ

The reconstruction of simulated data points is done by subtracting the background parametrisation $B(R)$ from the ratio spectrum of all signal candidates:

$$\left.\frac{dN}{dR}\right|_{\text{reco.}} = \left.\frac{dN}{dR}\right|_{\text{selected}} - B(R)$$

In figure 10.39, the background is parametrised with a polynomial of fourth degree. Because of the redistribution of the $e^+e^- + \tau\tau$ signal candidates, the background shape is only estimated. However, when the measurement is done with ILC data, the correct shape can again be derived from high statistic simulations.

Fit Function

A method to determine P_τ via a fit to a E_π/E_{Jet}-ratio spectrum is described in section 9.2.2. The prosed fit function

$$R_{\text{initial}}(P_\tau, N) = N\left(\frac{1+P_\tau}{2}R_+ + \frac{1-P_\tau}{2}R_-\right). \tag{10.6}$$

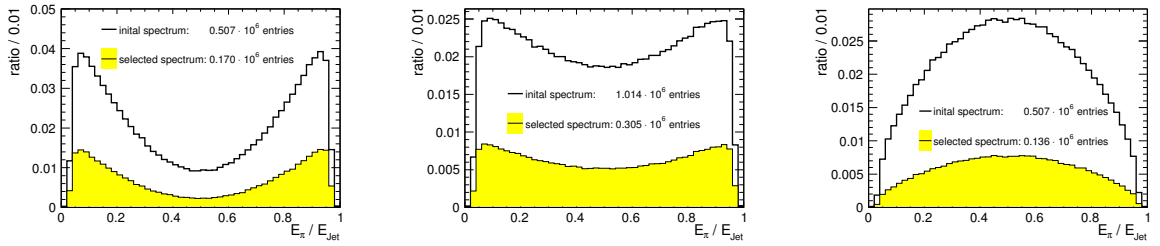

(a) R_{++} and $R_{++}|_{\text{selected}}$ **(b)** R_{+-} and $R_{+-}|_{\text{selected}}$ **(c)** R_{--} and $R_{--}|_{\text{selected}}$

Figure 10.40: *Ratio base spectra entering $R_{reco.}(P, N)$ in equation (10.7)*

includes two normalised $^{E_\pi}/_{E_{\text{jet}}}$-ratio spectra R_+ and R_-. These are made up of signal pions and jets from purely positively or negatively polarised taus, respectively. This R_{initial} is an appropriate fit function for the initial spectrum with P_τ and the normalisation factor N as fit parameter. This fit is shown in figure 10.1(b).

A refinement of the fit function is necessary for a fit to the $^{E_\pi}/_{E_{\text{jet}}}$-ratio spectrum after the selection, because the ratio spectrum of the selected signal pions contains less entries than the initial ratio spectrum and its shape is altered. Both effects have to be accommodated into the fit function. A more general function considers three possible cases, namely

$$R_{\text{reco.}}(P_\tau, N) = N \cdot \left[\left(\frac{1+P_\tau}{2} \right)^2 R_{++} + \left(\frac{1-P_\tau^2}{2} \right) R_{+-} + \left(\frac{1-P_\tau}{2} \right)^2 R_{--} \right] \Bigg|_{\text{selected}} \tag{10.7}$$

Here the $^{E_\pi}/_{E_{\text{jet}}}$-ratio spectrum R_{++} is taken from Monte Carlo events in which both taus have a fixed positive polarisation and R_{+-} and R_{--} are derived in the same way. The lower case 'selected' indicates that the shape of the three spectra after the selection is considered. The prefactors are products of the corresponding probabilities for the combination of the polarisation states to occur (see equation (8.4)), for example $p_+ \cdot p_+$ in front of R_{++}. The intermediate case R_{+-} is counted twice because R_{+-} and R_{-+} is possible.

This extension of the fit function accounts for all possible deformations of the spectrum and, in addition, for a possible polarisation dependency of the selection. This dependency could evolve from the $\rho_\perp$ cut which has a different effect on events with two positively polarised taus (R_{++}) compared to events with one or two negatively polarised taus (R_{+-} or R_{--}). This is the same effect as discussed for the $\tau \to \pi\nu$ channel above (see section 10.3).

The three base spectra are shown in figure 10.40 in each case before and after the selection. In each case the initial spectrum is normalised. Consequently the integral over each 'selected' spectrum results in the selection efficiency for the corresponding combination of polarisation state of the two taus.

For an accurate determination of the base spectra, a large amount of signal events for

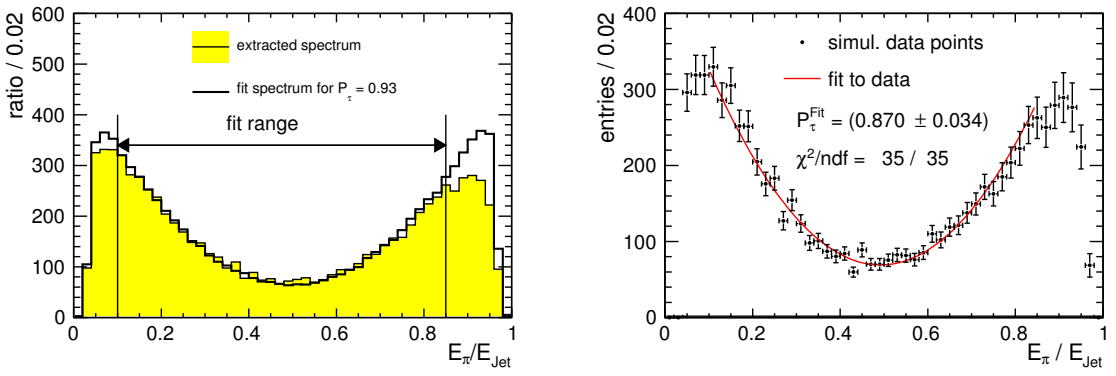

(a) fit range restriction

(b) result of the fit

Figure 10.41: *Fit of $R_{reco.}(P_\tau, N)$ to simulated data points*

the three combinations of tau polarisation is necessary ($\sim 5 \cdot 10^6$ for each case). Here, unsimulated Monte Carlo generated signal events have been used and the application of the selection was done in the same way as described in section 10.3.

The integral over $R_{++}|_{\text{selected}}$ gives 0.335. This means that the selection efficiency for signal candidates coming from signal events with both taus being positively polarised is 33.5 % The efficiencies for oppositely polarised taus in the event is 30.0 % and 26.8 % if both taus are negativly polarised. Due to the individual normalisation, each base spectrum enters with the correct weight into $R_{\text{reco.}}(P_\tau, N)$. The polarisation, P_τ, weights the individual proportions R_{++}, R_{+-} and R_{--} in the reconstructed signal spectrum.

If the assumption

$$R_{+-}|_{\text{selected}} = \frac{1}{2}\left(R_{++}|_{\text{selected}} + R_{--}|_{\text{selected}}\right)$$

was correct, equation (10.7) would simplify to (10.6) with R_+ being replaced by $R_{++}|_{\text{selected}}$ and R_- by $R_{--}|_{\text{selected}}$. Below the fit is done with the correct and this simplified fit function.

However, the base spectra are not perfectly suited, because they have been determined with unsimulated events. Thus detector acceptance and reconstruction effects do not enter correctly, and also the selection cuts do not have the same impact on these unsimulated events as on the simulated ones. Thus the fit function differs from the spectrum of the selected signal jets, as shown in figure 10.41(a). Here, P_τ is fixed to the Monte Carlo truth value of 89.6 % in the fit function and N has been chosen to make both spectra overlap in the central bins.

The fit function deviates significantly from the ratio spectrum at the edges of the spectrum. Therefore the fit range is limited to the interval $0.1 \leq {}^{E_\pi}/_{E_{\text{Jet}}} \leq 0.85$.

Fit to reconstructed data points

Figure 10.41(b) shows the simulated data points, fitted with $R_{\text{reco.}}(P_\tau, N)$ (see equation 10.7). The error range of the point belonging to the i-th bin is calculated by:

$$\delta n_{\text{i}} = \sqrt{\frac{w_{\text{signal}}}{N_{\text{selected}} - N_{\text{background}}} + \frac{1}{N_{\text{background}}}} \qquad \text{and} \qquad \delta R = 0.01.$$

Here δR is set to half the bin width and $N_{\text{background}}$ is taken from the background parametrisation. The contribution δn_{i} is the statistical uncertainty on the number of selected signal and background entries. The former is diminish by the weight of each signal pion of $w_{\text{signal}} = 0.36$ while the event weights are completely set to unity for the latter, because half of the background is made up of the redistributed $e^+e^- + \tau\tau$ signal candidates. These get an unity weight after the redistribution.

The fit yields

$$P_\tau = (87.0 \pm 3.4)\,\%$$

The result for the polarisation is a one-σ agreement with the expected value $P_\tau = 89.6\,\%$. A fit with the simplified fit function, leaving out the case R_{+-}, results in $P_\tau(\text{simplified}) = (86.2 \pm 2.6)\,\%$ and does not significanly differ from the result obtained with the full fit function.

But the fit yields an incorrect number of initial signal jets: the expected number is 41260. while the fit result is only $N = 26100 \pm 450$. The reason for the difference are the base spectra in the fit function. They have the correct shape and relative normalisation, but their absolute normalisation is wrong. This means that the 33.5-% selection efficiency for the case $R_{++}|_{\text{selected}}$ and 30.0 % or 26.8 % for the other cases as stated above are overestimated. This is because the base spectra have been determined with unsimulated events in which less signal pions are vetoed by the selection compared to fully simulated events. For example the preselection loss is not included. A correction of this result is still possible: With the individual efficiencies for each base spectrum the selection efficiency ϵ_{fit} which is modelled by the fit function $R_{\text{reco.}}(P_\tau, N)$ is calculated via:

$$\epsilon_{\text{fit}} = \left(\frac{1 + P_\tau|_{\text{fit}}}{2}\right)^2 \epsilon_{++} + \left(\frac{1 - P_\tau|^2_{\text{fit}}}{2}\right) \epsilon_{+-} + \left(\frac{1 - P_\tau|_{\text{fit}}}{2}\right)^2 \epsilon_{--} \approx 0.312.$$

Here ϵ_{++} is 0.335, $\epsilon_{+-} = 0.300$ and $\epsilon_{--} = 0.268$. From the cut flow in table 10.6, the correct selection efficiency comes out as $\epsilon_{\text{selection}} = {}^{8164}/_{41260} \approx 0.197$. Scaling N according to the false estimation by

$$N_{\text{corrected}} = N \cdot \frac{\epsilon_{\text{fit}}}{\epsilon_{\text{selection}}} = 41200 \pm 700$$

This is in good agreement with the expected number of 41260.

Further studies on systematic effects and the achievable accuracy ΔP_τ are omitted. The estimated background distribution for the $e^+e^- + \tau\tau$ events and the partly inadequate fit function do not allow for reliable statements on systematic uncertainties or detector effects.

11 Summary of the Study on the Measurement of τ Polarisation in $\tilde{\tau}_1$ Decays

The analysis presented in the third part of this thesis is based on a full detector simulation of the ILD. It deals with the measurement of the polarisation of taus, which are produced in supersymmetric stau pair production $e^+e^- \to \tilde{\tau}_1\tilde{\tau}_1 \to \chi_1^0\chi_1^0\tau\tau$. Previous studies of the measurement used only fast detector simulations and less challenging SUSY models (e.g. [80, 81]).

In the SUSY parameter point SPS1a', which is chosen for the analysis, the $\tilde{\tau}_1$ is the next to lightest supersymmetric particle and the decay $\tilde{\tau}_1 \to \tau\chi_1$ is exclusive. The expected yield for $\tilde{\tau}_1$ pair production is 81400 events by the time the ILC has recorded an integrated luminosity of $\mathcal{L} = 500\,\mathrm{fb}^{-1}$ with $-60\,\%$ positron and $80\,\%$ electron beam polarisation at a centre of mass energy of $\sqrt{s} = 500\,\mathrm{GeV}$. The polarisation P_τ can be determined in the decay of the final state taus. In this study, the channels $\tau \to \nu_\tau\pi$ (17800 decays) and $\tau \to \nu_\tau\rho \to \nu_\tau\pi_0\pi$ (41600 decays) have been analysed. On generator level, P_τ is 89.6 %.

Event Signature

Due to the kinematic of the signal process, the taus have an energy between zero and 43 GeV in the detector. Since a neutralino interacts only weakly, it escapes unmeasured and the event signature is two tau jets and a high missing energy. The measurement requires a clean machine and a correct jet allocation. SM four-fermion processes $e^+e^- \to e^+e^-ff$ are a crucial background because their cross-sections exceed the signal cross-section by 4-6 orders of magnitude while the event topology is similar. The reduction of this background requires a hermetic detector and a highly efficient beam calorimetry.

Measurement in the Channel $\tau \to \pi\nu_\tau$

In the decay channel $\tau \to \pi\nu_\tau$, the tau polarisation influences the energy spectrum of the final state pion. This spectrum is described theoretically and the according function is fitted to the measured energy spectrum of the pions in the detector.

In addition, the shape of the pion energy spectrum depends on the centre of mass energy of the interaction and is modified by initial state radiation and beam-strahlung losses. These effects must be accommodated into the fit function, which makes the measurement more sophisticated than in the alternative channel (see below) - also because

the signal yield is about a factor of two smaller. The analysis has been focused on this decay channel, as it is more challenging and hence puts more stringent demands to the detector performance and especially on the precise knowledge of the beam parameters.

In the selection, signal pions in the decay $\tau \to \pi\nu_\tau$ are required to appear isolated in the detector and be identified as pions by a particle identification algorithm. Hence, the analysis probes the particle identification performance. In addition, the specific energy loss in the TPC is exploited to reject particles other than pions.

Besides a veto on calorimeter activity, the rejection cuts against background are based on kinematic variables which are calculated from the measured jet momenta. Here, the analysis benefits from the high momentum resolution of the tracking system. The final selection efficiency is $\sim 20\,\%$, while the signal-to-background ratio is about six to one.

For the determination of P_τ, the remaining background is parametrised and subtracted from the measured energy spectrum of the selected signal pion candidates. The selection efficiency depends on the energy and the polarisation itself. An appropriate efficiency correction, which can adapt to any P_τ, has been installed with a fast simulation study. Finally the modified description of the spectrum function is fitted to the reconstructed spectrum which gives a result for P_τ.

For this channel, statistical (stat), background systematic (bkd) and SUSY mass uncertainties have been analysed which contribute to the achievable measurement accuracy. The final result is

$$P_\tau[\%] = 91 \pm 10\,(\text{stat}) \pm 5\,(\text{bkd}) \pm 6\,(\text{SUSY masses}), \qquad (\pi \text{ channel})$$

while the statistical uncertainty can be reduced to $6\,\%$ if the cross section of the signal process in determined with a $1\,\%$ accuracy in an independent measurement. At the ILC, the background estimation can be validated with an independent measurement.

Measurement in the Channel $\tau \to \rho\nu_\tau \to \pi\pi_0\nu_\tau$

In the decay $\tau \to \rho\nu_\tau \to \pi\pi_0\nu_\tau$, the tau polarisation is transferred to the intermediate ρ, which decays to a charged and a neutral pion. If P_τ is close to $+1$, one of the pions gets a large energy share and the ratio of the pion energies $E_\pi/(E_\pi+E_{\pi_0})$ is preferentially close to one or zero. If P_τ is -1, the energy share is preferentially equal.

The polarisation is determined from measured decay jets including two photons and one charged pion - the π_0 decays to two photons in the detector. The observable is the energy ratio E_π/E_{Jet}. This ratio is independent both of beam energy losses prior to the interaction and the masses of the SUSY particles. Since in addition the signal yield is a factor of two larger than in the signal pion channel, this is the preferred channel to measure P_τ.

With a preselection adapted to the signal jets, the selection uses most of the cuts of the measurement in the channel $\tau \to \pi\nu_\tau$. The selection yields 8000 signal particles with an estimated background of 3000. Again, the background is subtracted in a parameterised form. The polarisation is determined with an adapted fit function. The result is

$$P_\tau[\%] = 87.0 \pm 3.4 \qquad (\rho \text{ channel}).$$

Part IV
Summary and Outlook

This part recapitulates briefly the results of two studies presented in this thesis and gives an outlook on possible following studies. A more detailed summary of the construction of the Large Prototype (LP) Time Projection Chamber can be found in chapter 7, while chapter 11 summarises the simulation study of the τ polarisation measurement.

Development and Construction of a Large TPC Prototype

The LP is the first TPC prototype chamber being built in the research and development phase for the ILD TPC, which has a size in the same order of magnitude as the future chamber. Its inner diameter is 72 cm, similar to the inner field cage of the ILD TPC (~ 70 cm). The design of the field cage - both the mechanical as well as the electrostatic layout - has been optimised with finite element calculations and sample piece tests. The material budget of a field cage wall is estimated to 1.24 % of a radiation length - close to the aspired design goal of 1 % for the ILD TPC. Thus, the LP demonstrates that it is feasible to built a lightweight field cage. The construction took place in 2008 and since the beginning of 2009 the field cage is used in design studies of TPC readout structures for the ILD.

The LP is currently installed in the electron testbeam at DESY. It is planned to install a complete testbeam setup by the end of 2009, with additional silicon detectors and a movable support for the magnet which holds the LP. Then it will be possible to place the electron beam at desired positions in the LP, while the silicon detectors provide external reference points of measured trajectories. This setup will be well suited for optimisation studies of large TPC readout structures.

For manufacturing the LP field cage in a composite construction, reusable tools have been developed and the construction of a second field cage is under discussion. Also, with this setup, more ambitious prototypes in terms of a lower material budget could be built in the future. Their radiation length per wall could even be below the aspired 1 % design goal. In parallel, the field cage can also be used as an infrastructure to develop low material anode end plates.

Measurement of τ-Polarisation in the Process $e^+e^- \to \tilde{\tau}_1\tilde{\tau}_1 \to \chi_1^0\chi_1^0\tau\tau$.

In part III a full reconstruction chain for the measurement of the τ polarisation P_τ in the process $e^+e^- \to \tilde{\tau}\tilde{\tau} \to \chi_1^0\chi_1^0\tau\tau$ is described. Two possible variants of the analysis

have been evaluated. The measurement is robustly possible in the decay channel $\tau \to \rho\nu_\tau \to \pi\pi_0\nu_\tau$, while the main focus of the analysis has been set on the alternative channel $\tau \to \pi\nu_\tau$. This is because the latter channel puts higher demands to the ILD detector performance.

With the current ILD detector setup and reconstruction software tools, it seems possible to measure P_τ with a statistical uncertainty of 10 % ($\tau \to \pi\nu_\tau$) and 3.4 % ($\tau \to \rho\nu_\tau \to \pi\pi_0\nu_\tau$), respectively - assuming the ILC has collected $\mathcal{L} = 500\,\mathrm{fb}^{-1}$. The uncertainty estimation in the channel ($\tau \to \pi\nu_\tau$) acquires additional contributions of a few percent due to SUSY mass uncertainties and background estimations. These results are also summarised in a paper which is about to be published [92].

This analysis has been performed with a full ILD detector simulation. However, a crucial source of background has not been included into the simulation yet, namely e^+e^- pairs coming from the interaction of beam-strahlung photons [15]. These pairs are overlaid on all physics events and need to be removed in the reconstruction. A refinement of the simulation is currently on the way and first studies have started together with the development of strategies to reduce this source of background.

The measurement of P_τ, in particular in the channel $\tau \to \pi\nu_\tau$, could turn out to be very sensitive to the amount of beam background. Many ILC benchmark processes, like $e^+e^- \to t\bar{t}$, produce many trajectories in the TPC and their selection efficiency will not suffer if, accidentally, a real physics trajectory is misidentified as beam background and is removed from an event. The studied polarisation measurement requires a very clean machine. The signal yield depends to a high degree on the robust particle identification of low pions with energies in the range up to a few ten GeV. If the beam backgrounds are too high, the selection efficiency and thus the possible measurement accuracy could degrade substantially. This could be the case in alternative ILC running scenarios, like the low power option [114], which are being discussed. However, if the ILC shall exploit the full physics potential of the e^+e^- interaction, it is necessary that the design of the machine allows for specialised measurements like this one.

Bibliography

[1] OECD, "Science, Technology and Innovation for the 21st Century," *Meeting of the OECD Committee for Scientific and Technological Policy at Ministerial Level, Final Communique, 29-30 January 2004*.

[2] World Wide Study Group for the Physics and Detectors for the Linear Collider, "Understanding Matter, Energy, Space and Time: the Case for the Linear Collider," 2003.

[3] J. Brau *et al.*, "ILC Reference Design Report Volume 1 - Executive Summary," 2007, 0712.1950.

[4] ILD Concept Group, "International Large Detector Letter of Intent," 2009. DESY-09-087, `http://www.ilcild.org/documents/ild-letter-of-intent`.

[5] H. Aihara, P. Burrows, and M. Oreglia, "SiD Letter of Intent," 2009, 0911.0006. `http://silicondetector.org`.

[6] A. Mazzacane, "The 4th Concept Detector for the ILC," *Nuclear Instruments and Methods in Physics Research Section A: Accelerators, Spectrometers, Detectors and Associated Equipment*, vol. In Press, Uncorrected Proof, 2009. `http://www.4thconcept.org`.

[7] M. Gell-Mann, "A Schematic Model of Baryons and Mesons," *Phys. Lett.*, vol. 8, pp. 214–215, 1964.

[8] G. Zweig, "An SU(3) model for strong interaction symmetry and its breaking," 1964. CERN-TH-401.

[9] S. Weinberg, "A Model of Leptons," *Phys. Lett.*, vol. 19, p. 1264, 1967.

[10] L. Glashow, S. "Partial Symmetries of Weak Interactions," *Nucl. Phys.*, vol. 22, p. 579, 1961.

[11] L. Glashow, S. "Weak and electromagnetic Interactions," *Proceedings of the Novel Symposium held 1968 at Lerum, Sweden*, p. 367, 1968.

[12] C. Amsler *et al.*, "Review of particle physics," *Phys. Lett.*, vol. B667, p. 1, 2008.

[13] P. W. Higgs, "Broken Symmetries and the Masses of Gauge Bosons," *Phys. Rev. Lett.*, vol. 13, pp. 508–509, 1964.

[14] P. W. Higgs, "Broken symmetries, massless particles and gauge fields," *Phys. Lett.*, vol. 12, pp. 132–133, 1964.

[15] A. Vogel, *Beam-Induced Backgrounds in Detectors at the ILC*. PhD thesis, University of Hamburg, DESY, 2008. DESY-Thesis-2008-036.

[16] I. J. R. Aitchison and A. Hey, *Gauge Theories in Particle Physics*, vol. I & II. Taylor & Francis, third ed., 2002.

[17] M. E. Peskin and D. V. Schroeder, *An Introduction to Quantum Field Theory* . Perseus Books, 2008.

[18] R. Barate *et al.*, "Search for the Standard Model Higgs boson at LEP," *Phys. Lett.*, 2003, hep-ex/0306033.

[19] LEP and SLD electroweak working group, "web site." `http://lepwwg.web.cern.ch/LEPEWWG/`, 2009.

[20] The LEP Electroweak Working Group, the SLD Electroweak Working Group *et al.*, "Precision Electroweak Measurements on the Z Resonance," 2006, hep-ex/0509008v3.

[21] C. L. Bennett *et al.*, "First year wilkinson microwave anisotropy probe (WMAP) observations: Preliminary maps and basic results," *Astrophys. J. Suppl.*, vol. 148, p. 1, 2003, astro-ph/0302207.

[22] Y. Ashie *et al.*, "Evidence for an oscillatory signature in atmospheric neutrino oscillation," *Phys. Rev. Lett.*, vol. 93, p. 101801, 2004, hep-ex/0404034.

[23] E. Aliu *et al.*, "Evidence for muon neutrino oscillation in an accelerator-based experiment," *Phys. Rev. Lett.*, vol. 94, p. 081802, 2005, hep-ex/0411038.

[24] D. Jackson, J. *Classical Electrodynamics*. Gruyter, 2006.

[25] The ILC Gateway to the Quantum Universe Committee, "The International Linear Collider Gateway to the Quantum Universe Passport," 2007.

[26] G. L. Bayatian *et al.*, "CMS technical design report, volume II: Physics performance," *J. Phys.*, vol. G34, pp. 995–1579, 2007.

[27] A. Koya *et al.*, "Linear Collider for TeV Physics," *KEK-Report-2003-7*, 2003.

[28] M. Thomson, "Particle Flow Calometry and PandoraPFA," *Talk given at the DESY seminar 07/07/2008*, 2008.

[29] E. Accomando *et al.*, "Physics with e^+e^- linear colliders," *Phys. Rept.*, vol. 299, pp. 1–78, 1998, hep-ph/9705442.

[30] H. Murayama and M. E. Peskin, "Physics opportunities of e^+e^- linear colliders," *Ann. Rev. Nucl. Part. Sci.*, vol. 46, pp. 533–608, 1996, hep-ex/9606003.

[31] G. Aarons *et al.*, "International Linear Collider Reference Design Report Volume 2: Physics at the ILC," 2007, 0709.1893.

[32] D. Buskulic *et al.*, "Performance of the ALEPH detector at LEP," *Nucl. Instrum. Meth.*, vol. A360, pp. 481–506, 1995.

[33] T. Behnke *et al.*, "ILC Reference Design Report Volume 4 - Detectors," 2007, 0712.2356.

[34] L. Hallerman. PhD thesis, University of Hamburg, DESY, in preparation.

[35] R. L. Gluckstern, "Uncertainties in track momentum and direction, due to multiple scattering and measurement errors," *Nucl. Instrum. Meth.*, vol. 24, pp. 381–389, 1963.

[36] A. Vogel, "private communication," 2009.

[37] D. R. Nygren, "The Time Projection Chamber: A New 4π Detector for Charged Particles," Paper published in the Proceedings of The 1974 PEP Summer Study, 5-30 Aug 1974, Berkeley, California.

[38] V. Lepeltier, "Review on TPC's," *J. Phys. Conf. Ser.*, vol. 65, p. 012001, 2007.

[39] K. H. Ackermann *et al.*, "The STAR time projection chamber," *Nucl. Phys.*, vol. A661, pp. 681–685, 1999.

[40] T. Lux, "A TPC for the near detector at T2K," *J. Phys. Conf. Ser.*, vol. 65, p. 012018, 2007.

[41] C. Bowdery, *The ALEPH Handbook 1995*. Geneva, Switzerland: European Organisation for Nuclear Research, CERN, second ed., 1995.

[42] G. Charpak and S. B., "New Particle Detectors: The Multiwire Proportional Chamber and Drift Chambers," *CERN-SIS-PU-77-08*, 1977.

[43] Blum and Rolandi, *Particle Detection With Drift Chambers*. Berlin Heidelberg: Springer-Verlag, first ed., 1993.

[44] O. Schäfer, *Ein Monitorsystem für gasbasierte Detektoren am Internationalen Linear Collider*. Diploma thesis, (in german), University of Rostock, 2005. DESY-THESIS-2006-040.

[45] P. Nemethy, P. J. Oddone, N. Toge, and A. Ishibashi, "Gated time projection chamber," *Nucl. Instr. Meth.*, vol. 212, p. 273, 1983.

[46] A. Breskin *et al.*, "High flux operation of the gated multistep avalanche chamber," *Nucl. Instr. Meth.*, vol. 178, p. 11, 1980.

[47] CERN Gas Detector Development Group (GDD). `http://www.cern.ch/gdd/`, 2009.

[48] F. Sauli, "GEM: A new concept for electron amplification in gas detectors," *Nucl. Instrum. Meth.*, vol. A386, pp. 531–534, 1997.

[49] Y. Giomataris, P. Rebourgeard, J. P. Robert, and G. Charpak, "MICROMEGAS: A high-granularity position-sensitive gaseous detector for high particle-flux environments," *Nucl. Instrum. Meth.*, vol. A376, pp. 29–35, 1996.

[50] B. Ketzer, Q. Weitzel, S. Paul, F. Sauli, and L. Ropelewski, "Performance of triple GEM tracking detectors in the COMPASS experiment," *Nucl. Instrum. Meth.*, vol. A535, pp. 314–318, 2004.

[51] H. Fischle, J. Heintze, and B. Schmidt, "Experimental determination of ionization cluster size distributions in counting gases," *Nucl. Instrum. Meth.*, vol. A301, pp. 202–214, 1991.

[52] C. Grupen, *Teilchendetektoren.* (in german), Wissenschaftsverlag, first ed., 1993.

[53] C. Grupen and B. Shwartz, *Particle Detectors.* Cambridge University Press, second ed., 2008.

[54] T. Lohse and H. Witzeling, *Instrumentation in High Energy Physics*, ch. 2. Singapure: World Scientific, 1992.

[55] T. Lux, *Studies for a Time Projection Chamber for the International Linear Collider and Measurement of Beauty Cross Sections in Deep Inelastic Scattering at HERA.* PhD thesis, University of Hamburg, DESY, 2005. DESY-THESIS-2005-019.

[56] P. Schade, "Correction algorithm for TPC operation in inhomogeneous magnetic fields," *LC-Note*, in preparation.

[57] E. Janssen, M. *Performance Studies of a Time Projection Chamber at the ILD and Search for Lepton Flavour Violation at HERA II.* PhD thesis, University of Hamburg, DESY, 2008. DESY-THESIS-2008-011.

[58] LC TPC-collaboration, "TPC R&D for an ILC detector," *LC-Note*, vol. LC-DET-2007-005, 2007.

[59] M. Killenberg *et al.*, "Charge transfer and charge broadening of GEM structures in high magnetic fields," *Nucl. Instrum. Meth.*, vol. A530, pp. 251–257, 2004.

[60] J. Kaminski *et al.*, "Development and studies of a time projection chamber with GEMs," *Nucl. Instrum. Meth.*, vol. A535, pp. 201–205, 2004.

[61] J. Kaminski, B. Ledermann, T. Muller, S. Kappler, and M. T. Ronan, "Study of various anode pad readout geometries in a GEM- TPC," *IEEE Trans. Nucl. Sci.*, vol. 52, pp. 2900–2906, 2005.

[62] R. Diener, "private communication," 2009.

[63] M. Kobayashi *et al.*, "Performance of MPGD-based TPC prototypes for the linear collider experiment," *Nucl. Instrum. Meth.*, vol. A581, pp. 265–270, 2007.

[64] R. K. Carnegie *et al.*, "Resolution studies of cosmic-ray tracks in a TPC with GEM readout," *Nucl. Instrum. Meth.*, vol. A538, pp. 372–383, 2005, physics/0402054.

[65] S. Blatt, *Konstruktion und Inbetriebnahme eines Feldkäfigs für eine TPC*. Diploma thesis, (in german), RWTH Aachen, 2004.

[66] R. Settles and W. Wiedenmann, "The Linear Collider TPC: Revised Magentic-field Requirements," *LD-DET-2008-002, ILC-NOTE-2008-048*, 2008.

[67] EUDET Programme. `http://www.EUDET.org`, 2009.

[68] J. Alozy *et al.*, "First Version of PCMAG Field Map," *EUDET-Memo*, vol. 2007-51, 2007.

[69] C. Gefe, *Magnetic Field Map for a Large TPC Prototype*. Diploma thesis, University of Hamburg, DESY, 2008. DESY-THESIS-2008-052.

[70] S. Hänsel *et al.*, "Silicon Detectors for the LPTPC Test Beam," *Eudet-Memo-2008-16*, 2008.

[71] D. Peterson, "web site." `http://www.lepp.cornell.edu/~dpp`, 2009.

[72] K.-J. Bathe, *Finite Element Procedures*. Prentice Hall, second ed., 1995.

[73] A. Jüngel, "Das kleine Finite-Elemente-Skript," *(in german), Skript zur Vorlesung SS 2001, University of Mainz*, 2004.

[74] ngspice. `http://ngspice.sourceforge.net/`, 2009.

[75] R. Volkenborn and F. Hegner, "private communication," 2009.

[76] DuPont™, `http://www2.dupont.com`, *Kapton®HN Polyimide Film Technical Data Sheet*, 2006.

[77] J. E. Mark, *Polymer Data Handbook*. Oxford University Press, Inc., 1999.

[78] R. Yonamine, "private communication," 2009.

[79] S. P. Martin, "A Supersymmetry Primer," 2008, hep-ph/9709356.

[80] M. M. Nojiri, K. Fujii, and T. Tsukamoto, "Confronting the minimal supersymmetric standard model with the study of scalar leptons at future linear e^+e^- colliders," *Phys. Rev.*, vol. D54, pp. 6756–6776, 1996, hep-ph/9606370.

[81] E. Boos *et al.*, "Polarisation in sfermion decays: Determining tan(beta) and trilinear couplings," *Eur. Phys. J.*, vol. C30, pp. 395–407, 2003, hep-ph/0303110.

[82] The LEP Collaborations, the LEP/SLD Electroweak Working Group, Heavy Flavour Groups, "A Combination of Preliminary Electroweak Measurements and Constraints on the Standard Model," 2004, hep-ex/0312023v2.

[83] P. Bechtle, K. Desch, M. Uhlenbrock, and P. Wienemann, "Constraining SUSY models with Fittino using measurements before, with and beyond the LHC," 2009, 0907.2589.

[84] P. Bechtle, *SUSY Higgs boson searches at LEP and SUSY parameter measurements at TESLA*. PhD thesis, University of Hamburg, DESY, 2004. DESY-THESIS-2004-040.

[85] S. Dimopoulos, S. Raby, and F. Wilczek, "Supersymmetry and the Scale of Unification," *Phys. Rev.*, vol. D24, pp. 1681–1683, 1981.

[86] B. Herrmann, M. Klasen, and K. Kovarik, "Neutralino Annihilation into Massive Quarks with SUSY-QCD Corrections," *Phys. Rev.*, vol. D79, p. 061701, 2009, 0901.0481.

[87] P. Nath, R. L. Arnowitt, and A. H. Chamseddine, "Gravity induced symmetry breaking and ground state of local supersymmetric guts," *Phys. Lett.*, vol. B121, p. 33, 1983.

[88] R. Barbieri, S. Ferrara, and C. A. Savoy, "Gauge Models with Spontaneously Broken Local Supersymmetry," *Phys. Lett.*, vol. B119, p. 343, 1982.

[89] N. Arkani-Hamed, D. E. Kaplan, H. Murayama, and Y. Nomura, "Viable ultraviolet-insensitive supersymmetry breaking," *JHEP*, vol. 02, p. 041, 2001, hep-ph/0012103.

[90] J. A. Aguilar-Saavedra *et al.*, "Supersymmetry parameter analysis: SPA convention and project," *Eur. Phys. J.*, vol. C46, pp. 43–60, 2006, hep-ph/0511344.

[91] H. Baer, C. Balazs, A. Belyaev, and J. O'Farrill, "Direct detection of dark matter in supersymmetric models," *JCAP*, vol. 0309, p. 007, 2003, hep-ph/0305191.

[92] P. Bechtle, M. Berggren, J. List, P. Schade, and O. Stempel, "Prospects for the study of the $\tilde{\tau}$-system in SPS1a' at the ILC," 2009, 0908.0876.

[93] M. M. Nojiri, "Polarization of the τ lepton from scalar τ decay as a probe of neutralino mixing," *Phys. Rev.*, vol. D51, p. 6281, 1995.

[94] ILC software. `http://ilcsoft.desy.de/`, 2009.

[95] W. Kilian, T. Ohl, and J. Reuter, "WHIZARD: Simulating Multi-Particle Processes at LHC and ILC," 2007, 0708.4233.

[96] P. Mora de Freitas, "Mokka, main guidelines and future," Prepared for International Conference on Linear Colliders (LCWS 04), Paris, France, 19-24 Apr 2004.

[97] G. Musat, "Geant4 simulation for the FLC detector models with Mokka," Prepared for International Conference on Linear Colliders (LCWS 04), Paris, France, 19-24 Apr 2004.

[98] S. Agostinelli *et al.*, "GEANT4: A simulation toolkit," *Nucl. Instrum. Meth.*, vol. A506, pp. 250–303, 2003.

[99] O. Wendt, F. Gaede, and T. Kramer, "Event reconstruction with MarlinReco at the ILC," *Pramana*, vol. 69, pp. 1109–1114, 2007, physics/0702171.

[100] F. Gaede, T. Behnke, N. Graf, and T. Johnson, "LCIO: A persistency framework for linear collider simulation studies," 2003, physics/0306114.

[101] Pythia. `http://home.thep.lu.se/~torbjorn/Pythia.html`, 2009.

[102] S. Jadach, Z. Was, R. Decker, and J. H. Kuhn, "The tau decay library TAUOLA: Version 2.4," *Comput. Phys. Commun.*, vol. 76, pp. 361–380, 1993.

[103] W. Porod, "SPheno, a program for calculating supersymmetric spectra, SUSY particle decays and SUSY particle production at e^+e^- colliders," *Comput. Phys. Commun.*, vol. 153, pp. 275–315, 2003, hep-ph/0301101.

[104] S. T. Boogert and D. J. Miller, "Questions about the measurement of the e^+e^- luminosity spectrum," 2002, hep-ex/0211021.

[105] Mokka Detector Model Database Browser. `http://www-flc.desy.de/ldcoptimization/tools/mokkamodels.php`, 2009.

[106] M. A. Thomson, "Particle flow calorimetry at the ILC," *AIP Conf. Proc.*, vol. 896, pp. 215–224, 2007.

[107] S. Catani, Y. L. Dokshitzer, M. Olsson, G. Turnock, and B. R. Webber, "New clustering algorithm for multi - jet cross-sections in e^+e^- annihilation," *Phys. Lett.*, vol. B269, pp. 432–438, 1991.

[108] M. Montull, "Forward Veto MARLIN Processor for ILC beam calorimeter," 2008.

[109] M. Hauschild, "private communication," 2009.

[110] H.-U. Martyn, "Detection of sleptons at a linear collider in models with small slepton neutralino mass differences," 2004, hep-ph/0408226.

[111] A Data Analysis Framework, ROOT. `http://root.cern.ch/drupal/`, 2009.

[112] N. D'Ascenzo, *Study of the Neutralino Sector and Analysis of the Muon Response of a Highly Granular Hadron Calorimeter at the International Linear Collider.* PhD thesis, University of Hamburg, DESY, 2009. DESY-Thesis-2009-004.

[113] O. Stempel, *Messung der $\tilde{\tau}$ Masse am ILC.* Diploma thesis, (in german) University of Hamburg, 2009.

[114] J. Brau *et al.*, "International Linear Collider reference design report. 3: Accelerator," ILC-REPORT-2007-001.

Acknowledgements

During the time while I have worked on this thesis, I got assistance of many people whom I want to thank here. Without their help, I certainly would have been lost ...

At first, I want to mention Prof. Dr. Rolf-Dieter Heuer. Many thanks to you, Rolf, in particular for giving me the opportunity to come to DESY and that you were true to your word 'Für Euch ändert sich nix...', when you left for higher duties.

Alike, I want to thank Ties Behnke. Your supervision and advice, Ties, certainly defined 'the way to go' but I always welcomed the freedom left to spend time on my own ideas. Moreover, the unexperienced cooperation with industry to me sometimes seemed like a struggle against windmills - I appreciated your help at the right times to create sufficient 'pressure' to speed things up.

I am grateful that I had Philip Bechtle as supervisor, in first place for the analysis part. Philip, you really did a great job in keeping the motivation high, in particular when technicalities cause a hard time at the beginning of the analysis effort. Many thanks for all your help.

I also owe many thanks to Prof. Johannes Haller, for being referee to my disputation.

I want to give some special props to people who had an impact also beyond the 'pure' physics. Thanks a lot to you, Lea, Michael and Ralf, of course for the reading and for making me boulder-addict, but also for always having an open ear for my problems. You became real friends to me.

Working in the TPC group was fun from the beginning, mostly because of the people working here - in particular I want to mention Klaus Dehmelt, who was my office mate for a long time and whose humour found to a symbiosis with mine and made the every day work even more fun, Markus Ball, for discussing 'his view of things', and the expert to almost everything in computing, Adrian Vogel.

In the times of analysis work, Mikael Berggren was a great support and endured close to a million of questions, which used to be initiated by a meanwhile infamous 'Mikael, I have a question...'.

Beyond the mentioned persons, I want to thank the whole FLC group and all the people who crossed my way here during my PhD time for the nice time and working atmosphere.

Some pairs of eyes had a look on my text: As mentioned, Ralf, Michael and Lea kindly agreed to provide me with corrections. Likewise, the comments and corrections of Karsten Buesser and Jan Timmermans were more than helpful. Moreover, Karsten, it was and is always nice to learn something 'here and there' from your comments and knowledge on 'odds and ends'. Barbara Warmbein did a great job in ironing out a few 'Germanisms' in the most important parts (I & II) of the text. Finally, Tony Hartin kindly 'agreed' to answer many questions about the 'foreign' language.

Like everyone who worked in the FLC group in the last years, I also have to thank Ramona Matthes. Beyond the help with many organisational things, Ramona, I want to thank you even more just for being the 'good soul' of our group.

Last but by far not least I want to thank my family for the support during the whole time. It is of inestimable value to know that I am always welcome at home.